PROCESS-INDUCED WRINKLING AND WAVINESS IN PREPREG CHARGE-FORMING

by

KYLE ANTHONY FARNAND

B.A.Sc., University of Ottawa, 2011

A THESIS SUBMITTED IN PARTIAL FULFILLMENT OF

THE REQUIREMENTS FOR THE DEGREE OF

MASTER OF APPLIED SCIENCE

in

THE FACULTY OF GRADUATE AND POSTDOCTORAL STUDIES

(Materials Engineering)

THE UNIVERSITY OF BRITISH COLUMBIA

(Vancouver)

January 2016

Abstract

Carbon-epoxy prepreg C-channels were charge-formed by drape forming onto an aluminum tool. Flange lengths, forming temperatures, ply counts, ply sequences, forming methods, and curing bag types were varied and related to wrinkling, waviness, termination profiles, thickness profiles, microstructures, and mesostructures. Post-cure microscopy evaluation revealed wrinkling in parts formed at room temperature. Greater flange lengths and thinner laminates resulted in greater wrinkling severity. Fibre misalignments were more severe for the ply sequence whose 0° plies were located at the surface, taking the form of full-ply waviness after cure. A wrinkling conversion mechanism was proposed to explain the disappearance of externally visible defects after forming and the appearance of full-ply waviness after cure. The extent of conversion was attributed the curing bag tension and the post-formed wrinkled ply's location within the charge with respect to the laminate's outer surface. In all flanges, waviness misalignment angles were equal to or significantly greater than wrinkling misalignment angles. Missing length at the flange termination provided a good approximation of the excess length trapped in the form of wrinkling and full-ply waviness. Additionally, part thickness profiles provided further information on the occurrence of wrinkles. Furthermore, fibre misalignment types and locations were corroborated by non-destructive surface photography. Whether laminates were formed by hand lay-up or by drape forming, waviness gradients were found through the thickness of all 0° plies and attributed to the absence of sufficient intra-ply shear. The differences observed when forming the same ply sequence in alternate orientations may provide insight into the forming compound curvatures. The suggested post-form wrinkle conversion to waviness mechanism provides reason to develop waviness detection capabilities and to improve the understanding of mechanical performance knockdown effects from waviness. This study also proposes that post-forming part surface inspection for externally visible defects can be a critical step in identifying post-cure waviness sites. Defects detected in surface photographs after cure showed promising applicability for locating and identifying types of defects in mould-side surface plies. The occurrence of wrinkling and subsequent full-ply waviness is expected to be reduced if inter-ply slip characteristics are improved, though waviness gradients within individual plies will remain.

Preface

All experimental work was performed, interpreted, and documented by Kyle A. Farnand (author). Dr. Göran Fernlund provided in-depth direction, feedback, and corrections over the duration of this project. A thorough literature review upon which this project was defined was performed in collaboration by Andrew Stewart, Sina Amini Niaki, and Kyle A. Farnand. Kurtis Willden of Boeing Research & Technology contributed significant insights into the charge-forming process.

Table of Contents

List of Tables

List of Figures

List of Symbols

C	Debulk factor
δ_{wa}	Wave height
δ_{wr}	Wrinkle height
δL_{wa}	Excess length trapped as waviness per wave
δL_{wr}	Excess length trapped as wrinkling per wrinkle
Δl	Distance between ply or fibre ends at termination
ΔL	Total excess or missing length trapped within a flange
$\Delta L_{no\ slip}$	Total excess or missing length due to no slip condition
ΔR	Difference in radii between top and bottom of laminate over corner
$\Delta R'$	Post-consolidation difference in radii of laminate over corner
ΔS	Difference in path lengths between top and bottom of laminate over corner
$\Delta S'$	Post-consolidation difference in path lengths of laminate over corner
d	Ellipse height
F_{atm}	Equivalent force from atmospheric pressure
$F_{tension}$	Bag tension force
h	Fibre or ply height
λ_{wa}	Wave length span
λ_{wr}	Wrinkle length span
l	Ellipse length
L_s	Sheared length, ply interface length
ω	Angular forming rate
ϕ_{ideal}	Ideal shear and ideal slip termination angle
ϕ'_{ideal}	Consolidated ideal slip termination angle
$\phi'_{\text{no slip}}$	Consolidated no-slip termination angle
P_{atm}	Atmospheric pressure
R_1	Laminate inner radius over corner, Mould radius
R_2	Laminate outer radius over corner
σ_c	Compressive stress

$s_{friction}$	Interply friction distributed force
s_{wa}	Wave path length
s_{wr}	Wrinkle path length
S_1	Laminate inner path length over corner
S_2	Laminate outer path length over corner
θ	Forming angle
$\theta_{wa,max}$	Maximum waviness misalignment angle
$\theta_{wr,max}$	Maximum wrinkling misalignment angle
v	Forming slip rate
$v_{ideal-shear}$	Linear average forming velocity under ideal shear assumption
$v_{no-shear}$	Linear average forming velocity under no shear assumption
$w_{forming}$	Distributed normal forming force
W_{wr}	Wrinkle width
x_{wa}	Mid-waviness location along the flange length
x_{wr}	Mid-wrinkle location along the flange length

List of Abbreviations

AvgF	Average flange
CPT	Cured ply thickness
HLU	Hand lay-up
LF	Long flange
Offset	$[0/-45/+45/90]_{xS}$ ply sequence
Quasi	$[90/+45/-45/0]_{xS}$ ply sequence
SF	Short flange

Glossary

Bookend	Shape of the flange's or ply's end after forming over a radius provided slip and/or shear is allowed
Out-time	Time spent for a prepreg outside of manufacturer-specified storage conditions
Shear	Deformation mode within the ply during forming
Slip	Deformation mode between plies during forming
Termination angle	Angle of bookend with respect to mould
Waviness	In-plane fibre misalignments
Wrinkling	Out-of plane fibre misalignments
Mid-corner	Middle of the radius section

Acknowledgements

Firstly, I would like to express my sincere gratitude to Dr. Anoush Poursartip and Dr. Göran Fernlund for recognizing my potential despite what appeared on my undergraduate transcript and granting me the opportunity to study at the Composites Research Network world-class research facility. As my supervisor, Dr. Fernlund provided me with a personally tailored balance of freedom and guidance as I navigated through my first foray into research. I would particularly like to thank him for painstakingly revising every iteration of the manuscript with astounding detail.

I thank all my fellow graduate student colleagues with whom I've become good friends through early mornings, late nights, and many a scotch tasting. A particular thanks is owed to Andrew "the human encyclopedia" Stewart for his patience and insightful answers for my endless questions spanning all topics – fibre misalignments above all.

My sincere gratitude is expressed to Kurtis Willden for the many insights and facility tours that helped me gain a practical understanding of composites forming.

I am grateful to The Boeing Company and Torr Technologies Inc. for their generous material donations on which this work was based.

I would like to express deep thanks to my proud and loving family who encouraged me from afar. And last but not least, thank you to my beautiful wife Elizabeth who both held my tail to the flame and whom was endlessly supportive as I wrote, re-wrote, and wrote my thesis anew.

Chapter 1: Introduction

1.1 Composites at a glance

Composite materials are engineered materials made from two or more constituent materials with different physical or chemical properties that remain separate and distinct on a macroscopic level within the finished structure [1]. The constituent materials consist of a matrix phase and reinforcement phase. Common materials are epoxy resin, polyester, or polyurethane for matrices, and, glass, aramid, or carbon for reinforcement fibres. Although less prevalent, natural fibres and thermoplastic matrices are also viable options in many applications. Reinforcement fibres are typically arranged in tows, woven fabrics, unidirectional tapes, non-crimp fabrics (NCF), or short fibre strands prior to impregnation, forming, and cure.

Previously reserved for military and space applications, composites have seen a rapid rise in adoption for commercial products such as commercial aircraft and road vehicles due to their high specific stiffness, high specific strength, and excellent fatigue properties. Additionally, their corrosion resistance properties have led to increasing use in civil infrastructure and in the energy sector. But manufacturing uncertainty, absence of extensive supply chains, high material cost, and non-recyclability have impeded wide-spread adoption of composites [2].

Multi-year delays seen in ambitious composites manufacturing programs such as Boeing's 787 and Bombardier's C-Series programs are examples of the importance of quality control during manufacturing. Hence, recent research efforts have extended toward a better understanding of manufacturing process quality, repeatability, predictability, and flexibility, as well as the impacts of defects on part performance. While manufacturing simulation tools have seen significant improvements, they remain unable to predict defects with enough accuracy to eradicate costly physical testing.

1.2 Composites manufacturing

Composites manufacturing methods can be categorized in one of two generalized workflows. In one case, the fibres are first impregnated and later formed into the desired shape prior to cure. This is the case for all prepreg-based operations wherein resin is deposited onto fibre sheets and

stored in a gel state until needed for manufacturing. The forming methods include hand lay-up and automatic fibre placement (AFP) where plies are deposited individually; and compression moulding, drape forming, lash forming [3], and double diaphragm forming where multiple plies are formed simultaneously and known as charge-forming. Additional methods that follow this workflow which aren't based on prepreg include spray-up, pultrusion, and filament winding. The second workflow consists of first forming the fibrous material, and later infusing the matrix prior to cure. This is shown in resin transfer moulding (RTM), vacuum-assisted resin transfer moulding (VARTM), and wet lay-up. Once formed, cure is most often performed by means of an oven, an autoclave, or in ambient air.

The manufacturing method has a large impact on the final part quality in terms of fibre volume fraction, porosity, fibre alignment, degree of cure, and residual stresses which in turn influence the part's mechanical properties and dimensional tolerances. The chosen method is typically based on consideration of the required part quality, tooling costs, material system, production throughput, and part geometry. In large assemblies such as commercial aircraft, a wide range of materials manufacturing methods may be used to produce sub-components based on the particular part's function, geometry, and certification requirements.

1.3 Fibre misalignments

Fibre misalignment defects are of particular importance due to their impact on mechanical properties and their effects on the part's outer dimensions which often can lead to interference during assembly that can only be rectified by costly trimming and shimming operations or part rejection [4]. Fibre misalignments pose additional risks since they often go undetected. For instance, wrinkling internal to the part cannot be seen from the outside of a part, ultrasonic inspection cannot detect in-plane misalignments and CT scans are not feasible for large structures. Parts are therefore consequently designed with the assumption that defects are always present which results in over-sized parts that are not optimized for weight. An increased understanding of the onset, evolution, and detection of fibre misalignments would lead to manufacturing inspection cost reductions, lighter parts, and increased manufacturing throughput.

Fibre misalignments have been shown to occur during various manufacturing stages: prepreg coiling onto a mandrel during prepreg manufacturing, part forming, cure consolidation, cure shrinkage, and high pressure resin infusion (i.e. fibre wash, particular to the RTM process) [5]–[7]. The buckling of fibres, tows, and plies has been shown to be the driving mechanism of fibre misalignments due to the incompressibility of fibres oriented in compressive strain directions [8], [9].

In much of the available literature, 'wrinkling' and 'waviness' are used interchangeably to describe fibre misalignments. However, this study follows the convention put forward by Bloom, Wang, & Potter where 'fibre misalignments' are defined as any deviations from a nominal fibre or ply path, while subsets 'wrinkling' and 'waviness' refer to out-of-plane and in-plane misalignments in reference to the surface plane (Figure 1-1) [10].

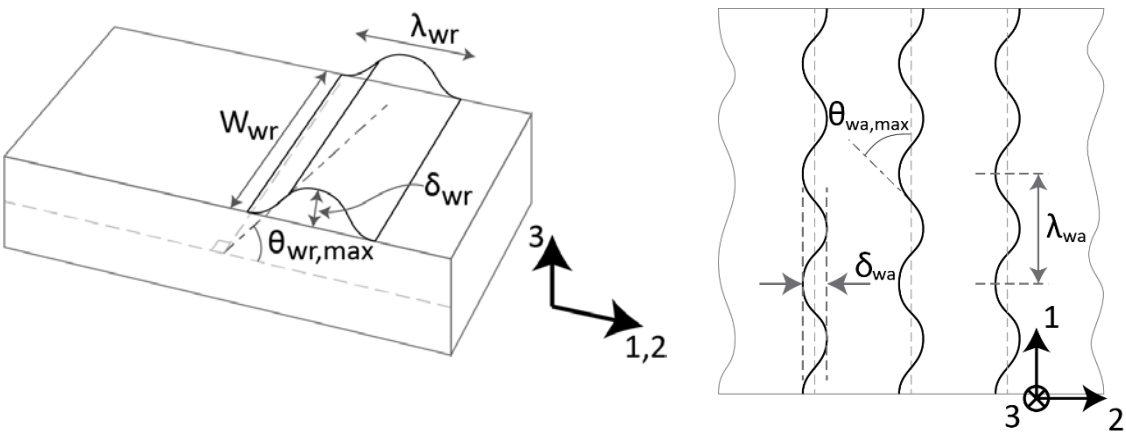

Figure 1-1 Schematics of wrinkling (left) and waviness (right). (Source: Stewart, 2015)

1.4 Fibre misalignments due to forming

Consider a sheet formed to a particular surface. The sheet's ability to conform to the surface – its 'formability' – is a function of the drapeability of a particular sheet material onto a given surface and the application of forming loads determined by the process. Drapeability refers to the ability of a sheet to conform to a particular surface, whereby success is determined by whether or not the sheet has wrinkled, and how the fibres are oriented over the surface[11]. The ability for a single sheet to drape a surface depends on the surface geometry and the deformability of the

sheet in terms of extension, bending, in-plane shear, and through-thickness shear for the particular sheet's orientation with respect to the mould and a given lay-down sequence [12], [13].

Initial research efforts were focused on understanding and characterizing the formability of sheet materials over hemispheres; particularly for woven dry textile fabric [14], [15]. It was shown that the ability to shear within the sheet's plane is of particular importance for the drapeability of fibre-based sheets due to the sheet's inextensibility governed by the fibre stiffness. The drapeability of a textile fabric is thus largely determined by the in-plane shear strain beyond which the in-plane shear of the fabric can no longer occur without wrinkling due to the 'locking' of the fibres. This is termed the 'locking angle' of the fabric. The locking angle for a particular textile fabric can be determined by inducing pure in-plane strain into a fabric by means of a bias extension or picture frame test [16], [17].

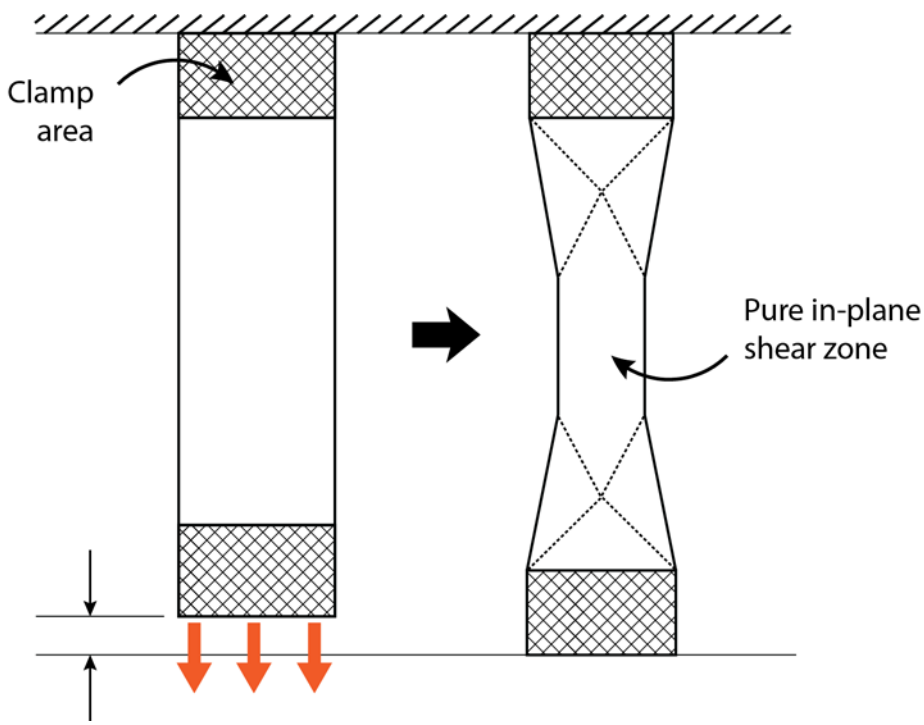

Figure 1-2. Bias extension schematic. (Adapted from Larberg, Åkermo, Norrby, 2011)

Unidirectional fibre sheets do not have interwoven fibres and thus do not have a locking angle. In addition, the bias extension and picture frame tests cannot measure a single prepreg ply's in-

plane shear properties due to its discontinuous nature in the direction orthogonal to the fibres. In pursuit of determining the in-plane shear characteristics for unidirectional prepreg, cross-ply prepreg laminates have been tested in bias extension [18], [19]. The laminates' in-plane shear behaviour was shown to be largely affected by inter-ply slip which in turn was affected by process input parameters such as temperature, deformation rate, and material system, showing differences of an order of magnitude for applied load for laminates tested at room temperature and 70°C [20]. Furthermore, the predictive pin-joint net model that was determined for woven fabrics did not bear much relevance to unidirectional laminates at small strains and thus could not be applied to the prediction of wrinkling in the forming of unidirectional prepreg.

The in-plane shear properties of unidirectional prepreg with regards to wrinkling were further investigated for various requirements of in-plane shear as determined by various doubly-curved mould geometries. For instance, Potter investigated the impacts of concavely and convexly contoured male radii on the occurrence of wrinkles during the forming of cross-ply unidirectional prepreg charges [11]. The part qualities were generally poor in the doubly contoured features whereas the highest quality sections were those which required no in-plane shear. Laminates formed the best contours if they did not have parallel fibres aligned with the tangent of the contour's apex. The part quality also showed a large sensitivity to temperature where the 70°C-formed parts outperformed parts formed at 55°C. The best performing laminate was one where slip characteristics were improved by interleaving adjacent plies with a neat resin sheet. Hallander et al. performed 65°C drape forming tests for a joggled spar configuration varying ply sequence, impregnation level, and ply thicknesses [21]. All defects were found to localize in specific regions of the tool geometry where the plies were locally under in-plane compressive forces and suggested that ply sequences that are more compliant to in-plane shear are less likely to wrinkle. Doubling the ply thickness was found to have an inconsequential effect on the occurrence of wrinkles.

1.4.1 Impact of process parameters on interply slip

Having shown a large impact on the formability of contoured geometry and in-plane shear behavior of formed laminates, the inter-ply slip characteristics have been investigated in isolation via pull-out, lap shear, and slip tests for a range of process conditions.

Early work on thermoset prepregs (the exact material system was not disclosed) saw an inverse correlation between temperature and pull force during qualifying lap shear testing [22]. There was also indication of a quantifiable impact of out-time – the time uncured prepreg is spent outside a refrigerated environment – on pull force was significant, though the trend direction was not published. The effect of out-time on the 65°C-tested samples was however significantly reduced by performing tests at temperatures greater than 89°C.

Measurements of inter-ply forces in carbon fibre-polypropylene thermoplastic composites were done by Scherer & Friedrich via pull-out experiments which saw a strong rate, temperature, and adjacent ply orientation dependence on slip resistance forces [23], [24]. This work was expanded to quantify intra-ply in comparison to the inter-ply slip by Krebs et al [25]. Using a modified pull-out test, a glass-reinforced polypropylene thermoplastic composite was approximately 50 times more resistant to intra-ply shear than to inter-ply slip.

Åkermo et al. performed slip tests to measure coefficients of friction for a variety of adjacent ply orientations in the context of carbon-epoxy prepregs. Trends opposite to those previously reported by Scherer & Friedrich were observed: in this case, 0°/90° and 0°/45°-oriented ply interfaces showed higher friction coefficients than the 0°/0° ply interfaces [26]. Results also showed a stronger contact pressure dependence on friction coefficients for the 0°/90° and 0°/45° ply interfaces than the 0°/0°. Performing slip tests on multiple carbon-epoxy prepreg systems and at various normal pressures, rates, and temperatures, Larberg and Åkermo saw friction coefficient differences on the order of 10 times for different material systems [27]. Rate- and pressure-independent friction coefficients were also reported for certain prepreg systems. Surface roughness, as determined optically and modified with heat treatments, was compared with friction coefficients but few correlations were seen.

Chapter 2: Research Objectives

The Composites Research Network program aims to uncover the mechanics of fibre and ply movement during forming in order to integrate the science into existing process models. Such models would improve the predictive capabilities of simulation software.

This study is a first step in expanding the UBC Composites group's forming and quality assessment capabilities. This study's particular goals were as follow:

a) Design and build a lab-scale charge-forming apparatus;
b) Determine a process parameter window to control the generation of forming-induced misalignment defects;
c) Develop simple and robust methods of measuring and quantifying relevant process outcomes (wrinkling, waviness, flange termination profile, thickness profile);
d) Assess the relative influences of manufacturing input parameters on the measured process outcomes by means of process influence diagrams (Figure 2-1);
e) Uncover the underlying physical phenomena which drive the generation of defects;
f) Build a kinematic framework for the forming process.

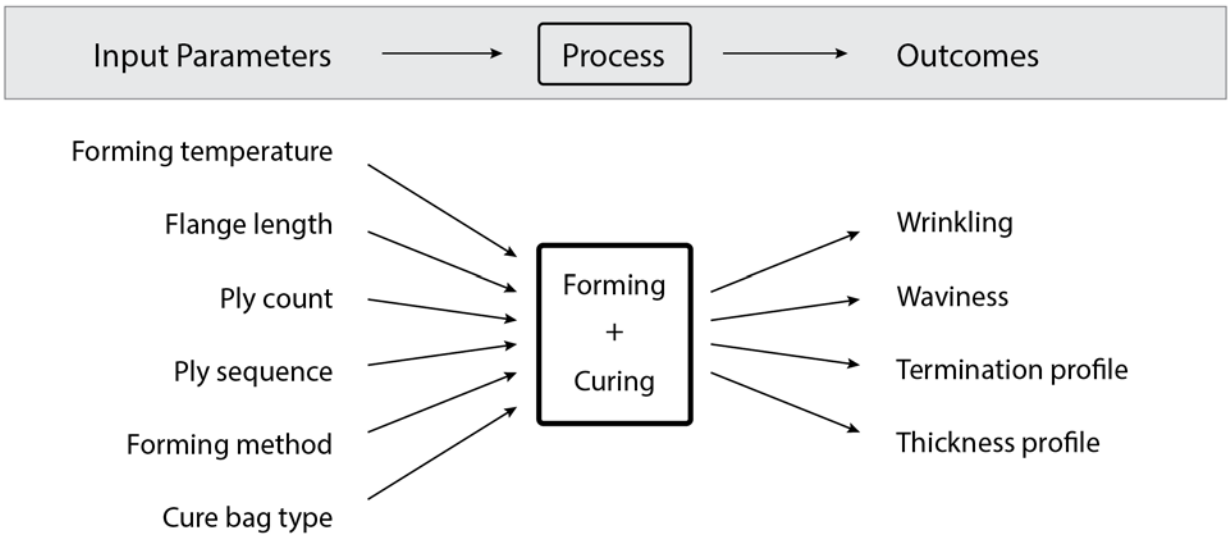

Figure 2-1. Process inputs and process outcomes.

Chapter 3: Kinematics of Charge Forming

The concepts of bookending and excess length have previously been introduced for individual plies, but very little was found in the literature that describes the kinematics of forming multiple plies [8]. A charge-forming kinematics framework is presented below.

3.1.1 Single ply forming

As a ply is formed over a radius, the ply's inner and outer radii are expected to conform to different arc lengths, as shown by the arc length equation where the arc length, S, is dependent on the radius, R, and the angle, θ (Equation (3–1)).

$$S = R \cdot \theta \tag{3–1}$$

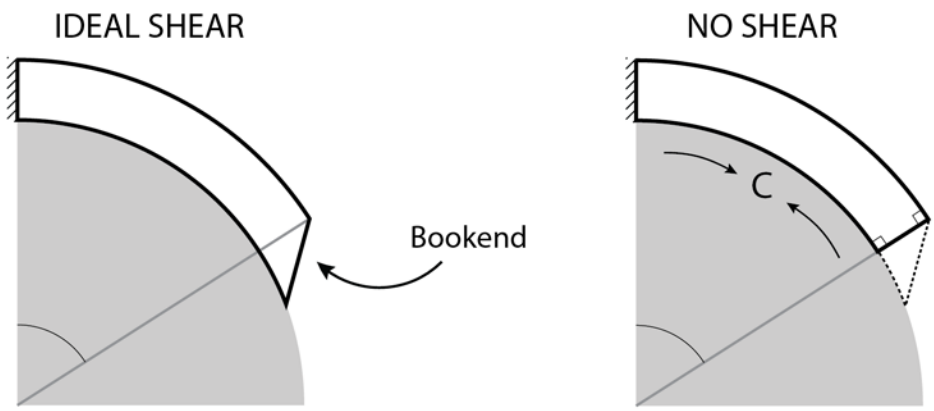

Figure 3-1. Ply deformation and internal stresses within a ply for the ideal intraply shear and no intraply shear conditions.

If the ply shears though its thickness, the ply end will produce a bookend feature at the ply termination and will have no internal stresses (Figure 3-1, on left) [8]. In contrast, if the ply does not shear through its thickness to accommodate this path length difference, the ply's top side will compressive stress and the bottom side (Figure 3-1, on right). Expanding on this concept, the angle of the bookend can be determined from the geometry of the forming process.

3.1.1.1 Ideal shear termination angle

Consider the ideal shear scenario where the lamina shears through thickness as it is formed over a male radius. The flange termination takes the form of a bookend due to the difference in path lengths between the top and bottom of the ply over the radius, where the bottom refers to the mould-side as shown below in Figure 3-2.

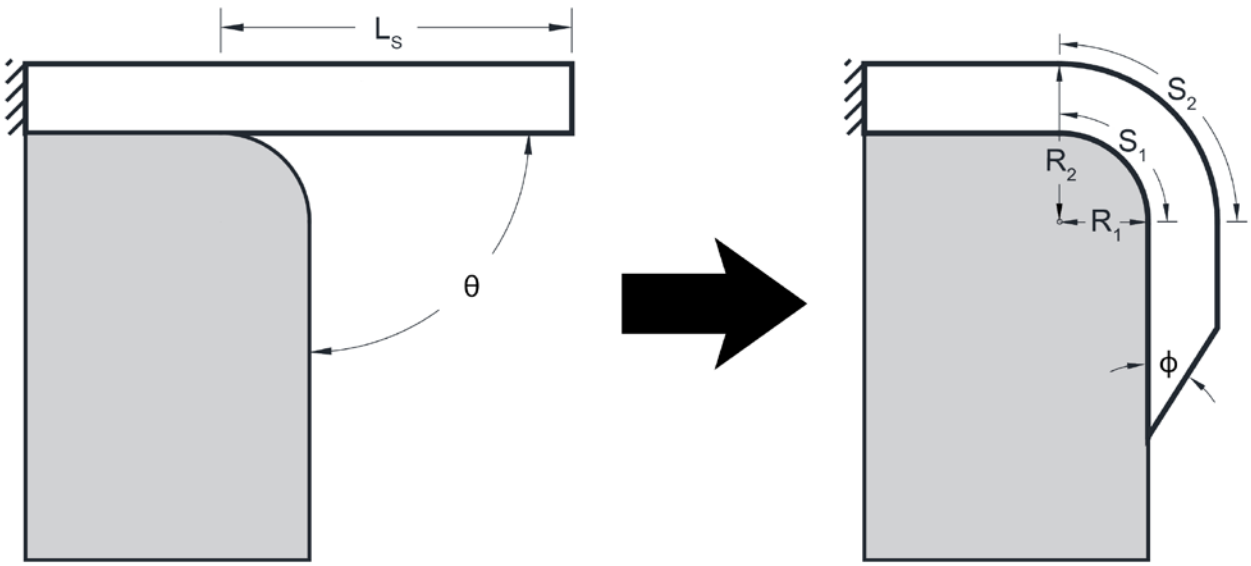

Figure 3-2. Variables considered in the ideal intraply shear forming of a single ply over a radius.

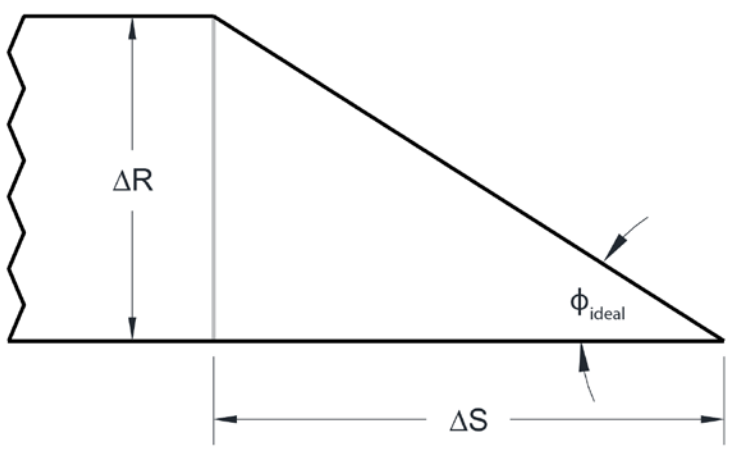

Figure 3-3. Close-up of the ply's bookend after forming under ideal shear conditions.

Figure 3-3 shows a close-up of the ply termination. The plies are assumed to follow concentric arcs at the corner and no buckling is seen in the ply. The forming angle, θ, is the angle between the original position and the formed position of the laminate; the ideal shear termination angle, ϕ_{ideal}, is the angle between the terminations of the top and bottom sides of the ply with respect to the mould line; R_1 and R_2 are the bottom and top radii, respectively; and S_1 and S_2 are the bottom and top ply arc lengths at the corner, respectively. The difference in path lengths between the mould-side and bag-side plies, ΔS, corresponds to the base of the termination triangle, and the difference in radii, ΔR, relates to the thickness of the ply and consequently the height of the termination triangle. The termination triangle height and length are related to the forming angle as follows:

$$\begin{aligned} \Delta S &= S_2 - S_1 \\ &= R_2\theta - R_1\theta \\ \Delta S &= \Delta R \cdot \theta \end{aligned} \tag{3–2}$$

$$\phi_{\text{ideal}} = \tan^{-1}\left(\frac{\Delta R}{\Delta S}\right) \tag{3–3}$$

Combining equations (3–2) and (3–3), we can determine the ideal shear termination angle as a function of the forming angle:

$$\phi_{\text{ideal}} = \tan^{-1}\left(\frac{1}{\theta}\right) \tag{3–4}$$

For a square angle-formed flange where $\theta = \frac{\pi}{2}$, the ideal shear termination angle therefore corresponds to 32.48°.

3.1.2 Laminate forming

Laminate forming involves the simultaneous forming of a flat stack of plies, also known as a charge. Should intra-ply shear (referred to as '*shear*' in this text for simplicity) be impeded, intra-ply slip (referred to as '*slip*' in this text for simplicity) may occur in order for neighboring

plies to accommodate the path length differences over the mould corner. These deformation modes are illustrated in Figure 3-4.

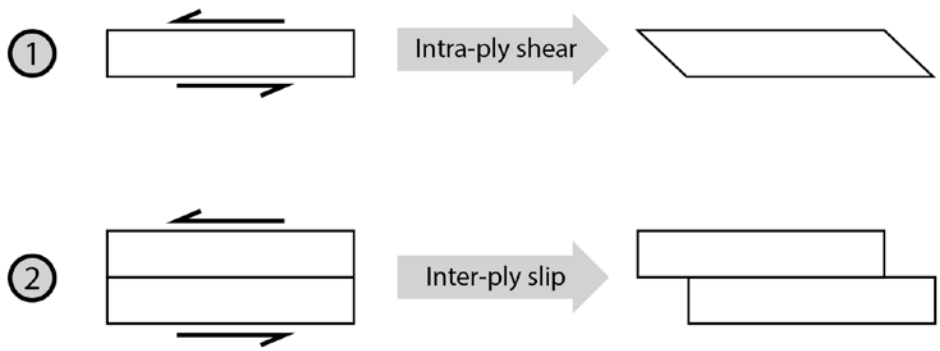

Figure 3-4. Laminate deformation modes during charge. (1) Intra-ply shear, and (2) inter-ply slip.

3.1.2.1 Concepts of excess and missing lengths

Dodwell et al. introduced the idea of excess length whereby a laminate being formed or consolidated to a curved surface (an external radius, for example), will develop an excess ply or fibre path lengths if the generated compressive strain cannot be relieved by shear or slip [8]. The ply's physical characteristics (e.g. fibre architecture, fibre orientation, resin viscosity, impregnation level) as well as its boundary conditions and imposed strain will determine the quantity of excess length that develops as well as the response.

In the case of unidirectional prepreg, fibre orientation is of particular importance in governing the manifestation of excess length. For fibres aligned with the imposed strain (0° plies), the compressive strain manifests itself as buckling since the fibres' slenderness renders them incapable of supporting significant compressive strain. Buckling may then take the form of wrinkling (out-of-plane buckling) and/or waviness (in-plane buckling). For fibres oriented orthogonally to the imposed strain (90° plies), the plies will shear since the fibres are free to shift in a 'log rolling' manner, which can lead to ply thickening. Intermediate ply orientations are expected to respond in a combination of both deformation modes.

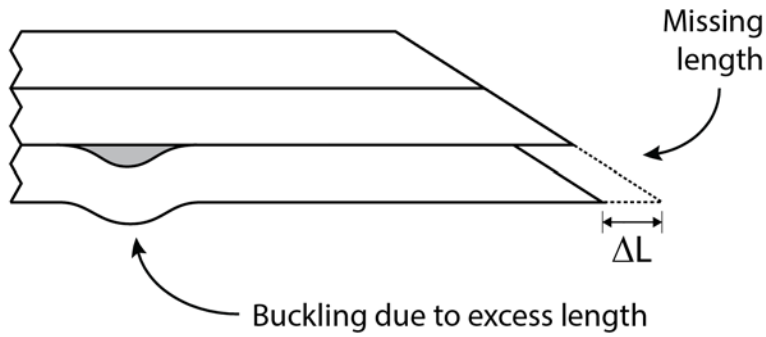

Figure 3-5. Illustration of missing length at the ply termination in relation to excess length from buckling in the ply.

Assuming conservation of volume, should a ply develop an excess length due to buckling or thickness growth, its flange termination profile would therefore show an equal 'missing length', ΔL (Figure 3-5). This missing length is determined from the expected ply termination length, which can be computed given an expected termination angle which was determined in Section 3.1.2.2.2.

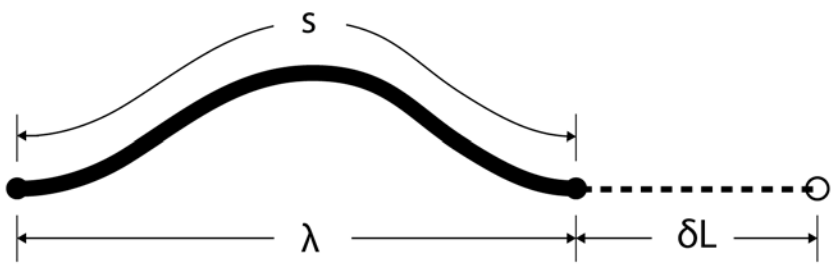

Figure 3-6. Missing length of an individual wrinkle or wave.

For a 0° ply, the 'missing length' – the difference between the expected termination location and the ply's actual termination location – is equal to the total excess length trapped as wrinkling and waviness. The missing length is hence a summation of the excess lengths trapped within individual wrinkles, $\Sigma\delta L_{wr}$, and waves, $\Sigma\delta L_{wa}$ (Figure 3-6):

$$\Delta L = \Sigma\delta L_{\mathrm{wr}} + \Sigma\delta L_{\mathrm{wa}}$$
$$\Delta L = \Sigma(s_{wr} - \lambda_{wr}) + \Sigma(s_{wa} - \lambda_{wa})$$

3.1.2.1.1 Flange termination implications on buckling

Consider a laminate with square ends containing exclusively 0° plies that is formed over a radius such that the plies cannot extend. Depending on the intraply shear and interply slip properties of the laminate subjected to particular forming process parameters, the laminate may accommodate the difference in path length over the radius by shearing and slipping perfectly, partially, or not at all. Slip and shear combinations are illustrated in Figure 3-7 where the extensibility of the plies is considered negligible, as is the case for 0° oriented plies.

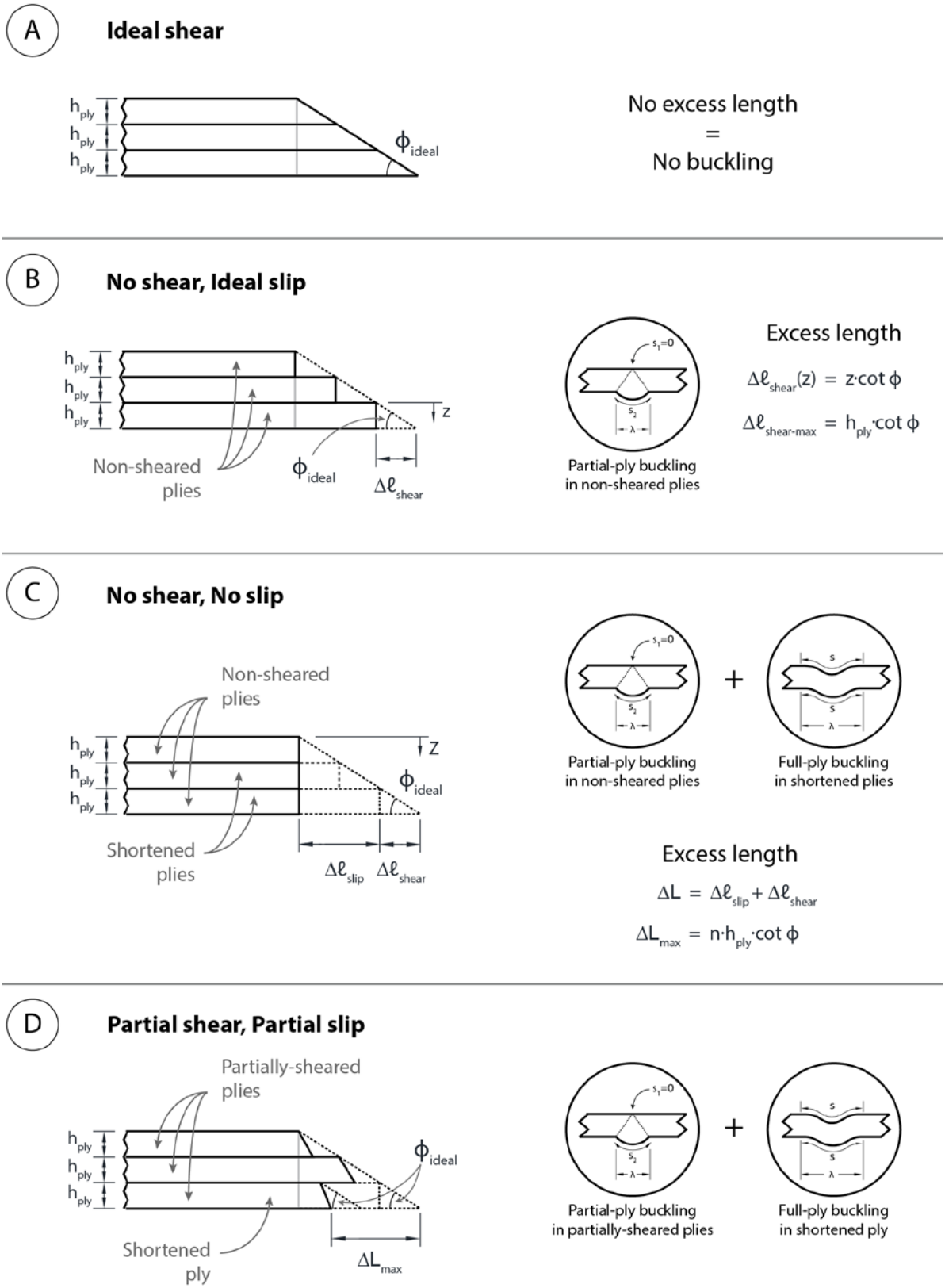

Figure 3-7. Flange terminations as they relate to allowable slip and shear with resulting ply buckling.

For a flange termination whose ply terminations are in line with the ideal shear angle, no ply or fibre buckling is expected to have taken place during forming (Figure 3-7A). For this to be true, it is assumed that the entire laminate did not buckle – a result that would be identified by the flange termination falling short of its expected location on the mould.

In the case where the flange termination shows a '*staircase*' profile, individual plies have not sheared, creating a need for slip at the ply-ply interfaces (Figure 3-7B). The lack of shear manifests itself as compressive strain increasing through the thickness of each ply. The non-compressibility of 0° fibres that make up the ply implies that buckling occurs in the fibres. The magnitude of the excess length that determines the magnitude of buckling which is a function of the ply's thickness and the position of the particular fibre through the ply's thickness. The maximum excess length within a ply due to no-shear is $1.57 \cdot h_{ply}$, at the mould-side.

A third case presents itself when all shear and all slip is restricted (Figure 3-7C). In this case, the excess length within each ply is a function of the contribution from the no-shear condition (gradient shortening for each ply) and of the contribution from the no-slip condition (the entirety of the ply is shortened). The maximum excess length is thus a function of the laminate's thickness. The maximum excess length that can develop for a 90° forming angle due to no-shear and no-slip is $1.57 \cdot n \cdot h_{ply}$, at the mould-side, where n is the number of plies. For a 32-ply laminate, the maximum excess length is on the order of 50 CPT.

In the case where partial shear and partial slip occur, buckling will occur depending on the magnitudes of allowable shear and slip (Figure 3-7D). Given the expected flange termination shape, as determined by the ideal shear case in Figure 3-7A, the level of buckling within each ply due to processing parameters can thus be determined. The angle of the termination determines the excess length allocated to partial-ply buckling whereas the horizontal position of the ply can determine the excess length allocated to full-ply buckling.

Each ply's mechanical properties, geometry, constituent orientation, and boundary conditions will determine their individual response to the compressive strain such as the buckling direction (in-plane, out of-plane), the quantity of wrinkles or waves, and the locations of wrinkles and waves.

3.1.2.1.2 Forming slip rate

In order to determine the forming slip rate, it is practical to first consider the case where no ply shear occurs but where slip is ideal, such as in position 2 of Figure 3-7. Given an angular forming rate, $\omega = \frac{d\theta}{dt}$, we may determine the slip rate, v, seen by adjacent plies at ply interfaces.

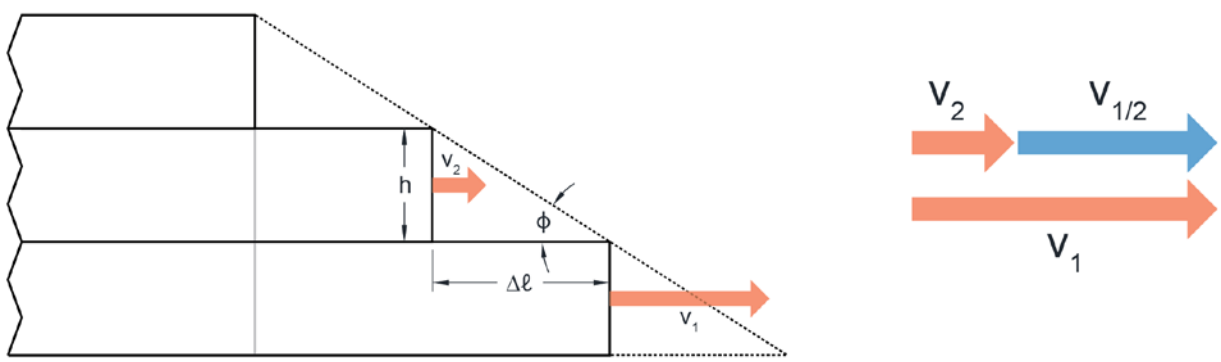

Figure 3-8. Linear ply velocities for the no shear, ideal slip scenario. The orange arrows represent the ply velocities during charge-forming over a radius.

The forming slip rate is shown as relative velocity vector $V_{1/2}$ in Figure 3-8. It is the velocity of the bottom ply with respect to its neighbouring top ply. The angle between ply ends, ϕ, is related to the length difference of adjacent ply terminations, Δl, and the ply height, h in Equation (3–5):

$$\phi = \tan^{-1}\left(\frac{h}{\Delta l}\right) \tag{3–5}$$

Given the same forming conditions, this angle was previously related to the forming angle in Equation (3–4). Combining Equation (3–5) and (3–4), the length difference of adjacent ply terminations can be related to the forming angle:

$$\tan^{-1}\left(\frac{h}{\Delta l}\right) = \tan^{-1}\left(\frac{1}{\theta}\right)$$
$$\Delta l = \theta \cdot h \tag{3–6}$$

Taking the time derivative of Equation (3–6), the forming slip rate can thus be determined as a function to the angular forming rate:

$$v_{1/2} = \frac{d(\Delta l)}{dt} = \frac{d(\theta \cdot h)}{dt}$$
$$\frac{d(\Delta l)}{dt} = \dot{\theta} \cdot h$$
$$v = \omega \cdot h \tag{3–7}$$

For an average angular forming velocity of 0.11 rad/s and a 0.136 mm ply height, the average forming slip rate is 0.015 mm/s. Though, as intra-ply shear increases, the slip velocity decreases. The nominal slip velocity can be used to correlate forming results to linear force measurements obtained from slip tests similar to those performed by Larberg and Åkermo [27].

3.1.2.2 No shear, ideal slip termination angle

The no shear, ideal laminate slip scenario is illustrated in the top row of position 2 of Figure 3-7. The ideal slip termination angle is unaffected by the individual ply termination. Thus, for a 90°-formed flange, the ideal slip termination angle for a laminate is 32.48°.

3.1.2.2.1 Cured termination angle: ‘no slip compaction’ assumption

As the part is cured under vacuum, the ply undergoes consolidation due to the normal force applied by the vacuum bag and the flow of resin. Consider the case where interply slip is inhibited during compaction due to the application of normal force, thus preventing the plies to

slip in order to accommodate the reduced path length over the ply's consolidated radius in the corner. Under this 'no slip compaction' assumption, the height of the flange termination triangle is reduced, but the length remains the same. Thus, the flange termination angle is reduced as shown below in Figure 3-9.

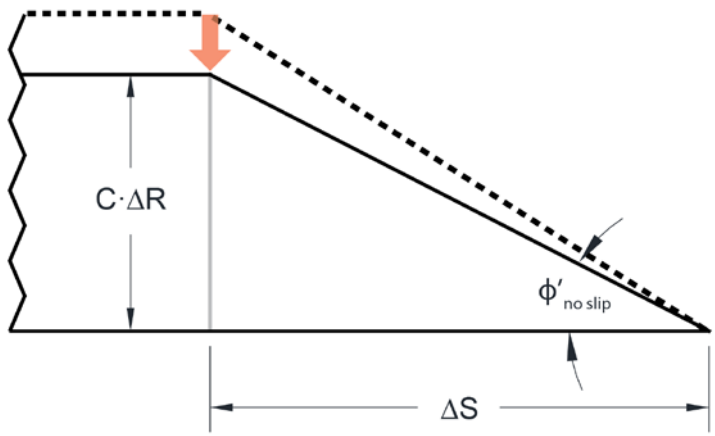

Figure 3-9. Laminate termination after consolidation under the 'no slip compaction' condition. The arrow shows the displacement of laminate's top surface due to cure. The laminate is shown as a homogeneous solid for clarity.

Taking C as the debulk factor, we can determine the no-slip compaction termination angle, $\phi'_{\text{no slip}}$

$$C = \frac{\text{uniform flange thickness after cure}}{\text{laminate thickness before forming}}, \qquad C \leq 1 \tag{3–8}$$

$$\phi'_{\text{no slip}} = \tan^{-1}\left(\frac{C \cdot \Delta R}{\Delta S}\right) \tag{3–9}$$

Combining equations (3–2) and (3–9), the no-slip compaction termination angle is determined as a function of the debulk factor and forming angle.

$$\phi'_{\text{no slip}} = \tan^{-1}\left(\frac{C}{\theta}\right) \tag{3–10}$$

Thus, for a debulk factor of 0.819, a right angle part's end angle is 27.4° under the no slip compaction assumption.

3.1.2.2.2 Cured termination angle: 'ideal slip compaction' assumption

Alternatively, consider the case where slip within the ply is unimpeded during cure. As plies are free to slip past each other as they consolidate to tighter radii over the corner, the laminate termination triangle's length will reduce as its height reduces. The ideal slip compaction termination angle ϕ'_{ideal} is shown below in Figure 3-10.

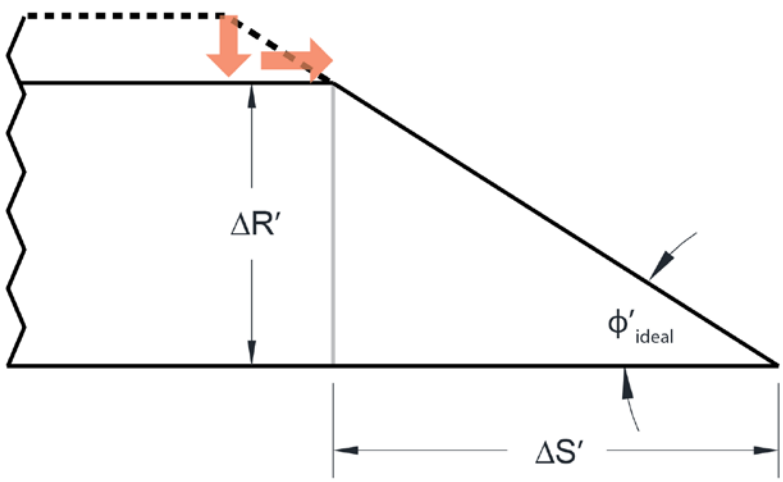

Figure 3-10. Laminate termination after consolidation under the 'ideal slip compaction' condition. The arrow shows the displacement of laminate's top surface due to cure. The laminate is shown as a homogeneous solid for clarity.

Simple kinematics show that the ideal slip compaction termination angle is equal to the ideal slip angle after forming computed in equation (3–4):

$$\phi'_{\text{ideal}} = \phi_{\text{ideal}} \tag{3–11}$$

Chapter 4: Experimental Method

A C-channel is assumed to be a drapeable geometry for all ply orientations since the part is formed over a single curvature without the requirement for in-plane shear deformation, unlike in a contoured (dual curvature) part. Hence, if each individual ply is drapeable, a charge – multiple plies to be formed simultaneously – is expected to be drapeable. Therefore, any defects that arise during the forming of a charge into an L or C-channel are expected to be a direct result of inter-ply interactions, governed in turn by process parameters.

The experiments conducted in this study aimed to recreate process conditions that induced fibre misalignments in industrially-relevant geometries. A single degree of curvature C-channel geometry was chosen in order to eliminate the effects of in-plane shear on fibre misalignment generation to highlight the effect of process conditions on the generation of fibre misalignments.

Optical microscopy was chosen for primary data collection method as it is robust for investigating misalignment defects. However, due to the laminate's soft state after forming, forming-induced defects could not easily be captured due to the difficulty in preparing uncured laminates for microscopy. Thus, laminates were cured in order to provide sufficient rigidity to withstand the grinding and polishing operations in preparation for optical microscopy.

4.1 Part manufacture

'Drape forming' was chosen to charge-form C-channels for this study due to its relevance in the aerospace industry. The process involves laying up a flat laminate and forming it as a charge onto a mould (otherwise known as a mandrel or tool) with atmospheric pressure by means of the pressure differential created by pulling vacuum under an extensible elastomer sheet (Figure 4-1). The benefits of this process include increased processing speed and greater part quality when compared to hand lay-up [22]. It is typically used for high aspect ratio parts with single curvature such as aircraft spars and stiffeners [28].

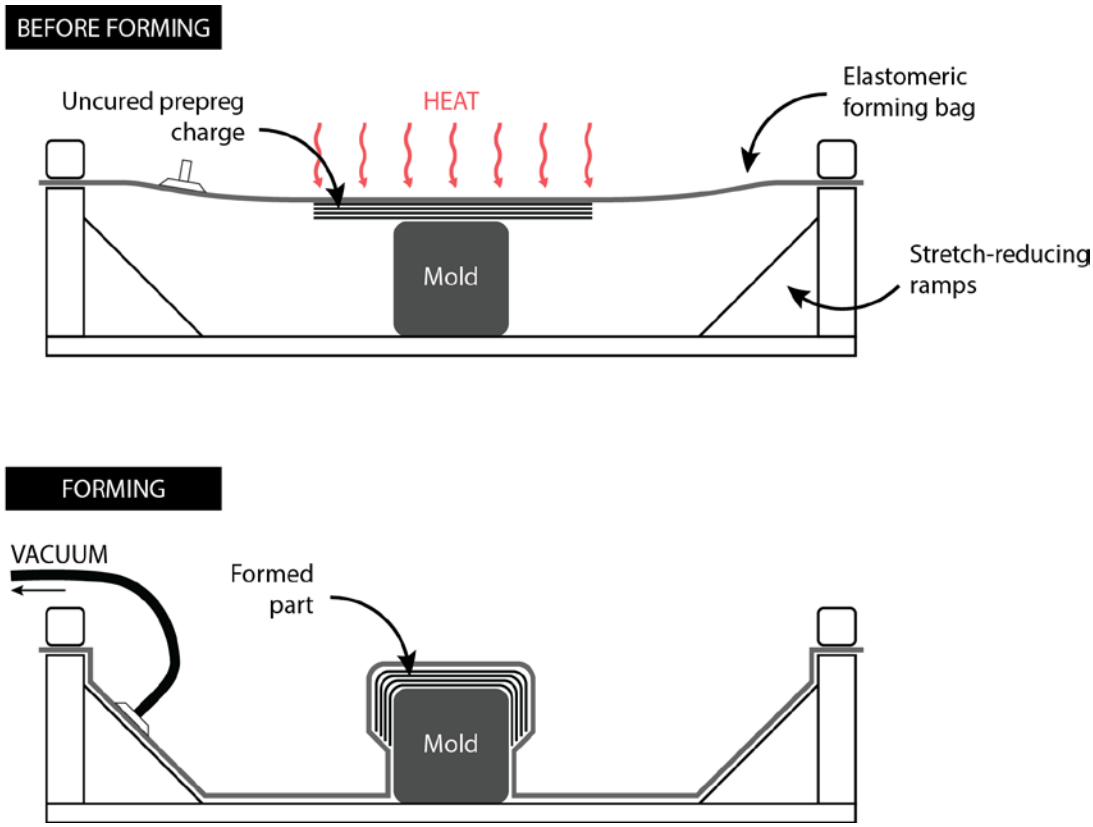

Figure 4-1. Hot drape forming process. Top: heating of the charge in preparation for forming. Bottom: formed geometry. (Adapted from Modin, 1993)

4.1.1 Material preparation

1.2 m x 0.6 m CYCOM 5320/T650-35 unidirectional prepreg sheets were cut from a roll and sealed in a nylon bag with silica moisture absorbing pellets. These intermediate sheets were refrozen until needed for test preparation. Once removed from the freezer, the bags were left to thaw for 30 minutes prior to opening to atmospheric air. 22.2 cm x 7.6 cm laminae were then cut with a utility knife and refrozen in sealable plastic bags for at least 24 hours prior to part manufacture. Once required for part manufacture, the bags were removed from the freezer and were once again left to sit for 30 minutes prior to exposure to atmospheric air. The laminae were then ready for lay-up.

4.1.2 Lay-up

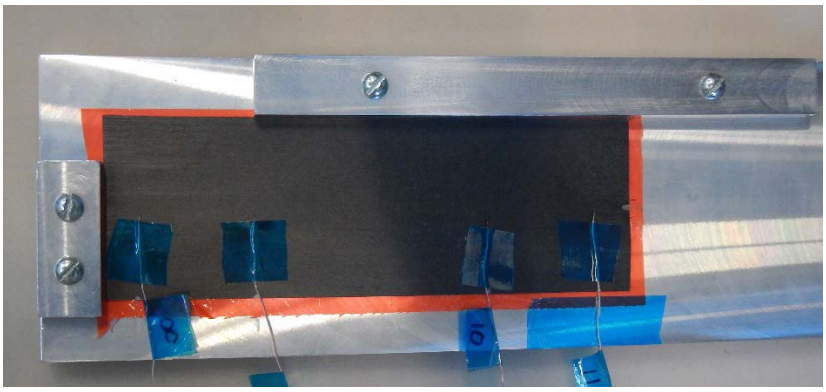

Figure 4-2. Aluminum lay-up plate, fitted with aluminum alignment guides (top and left side) and a sheet of FEP ply. In this photo, thermocouples are shown as part of a thermal qualification test. They were not present during the general manufacturing process.

Quasi-isotropic laminates were laid up onto an aluminum plate wrapped in a sheet of FEP in order to facilitate the removal of the laminate after lay-up (Figure 4-2). The aluminum plate was fitted with two rectangular aluminum alignment guides at right angles from each other at the edge of the lay-up surface to ensure proper alignment of the plies during lay-up. Plies were laid up by facing the backing paper upwards and compacting each ply with a roller prior to the removal of the backing paper. The manufacturer's recommended lay-up procedure did not indicate that intermediate debulk cycles were necessary, thus they were not performed.

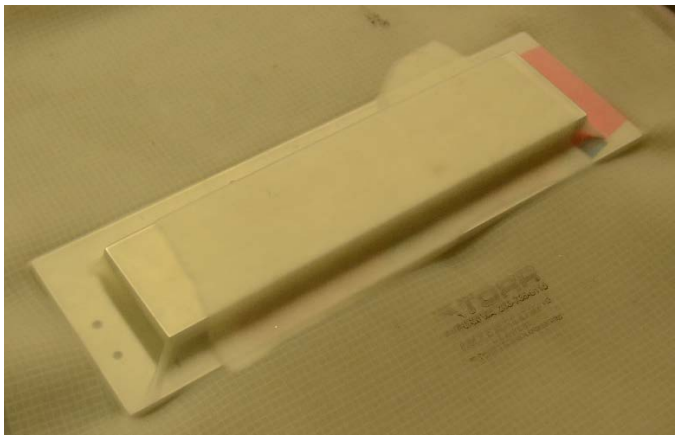

Figure 4-3. Post-layup consolidation in a reusable silicone bag.

Once the laminate was laid up in full, the alignment guides were removed, a second FEP sheet was draped over the top, and a 33 cm x 7 cm x 1 cm aluminum block was placed atop the laminate. The assembly was partially covered with breather ply and placed in a *Torr Technologies Inc.* reusable silicone vacuum bag under full vacuum for 10 minutes (Figure 4-3). The purpose of the aluminum block was to shield the edges of the laminate from additional corner consolidation. Given the block's greater area, the laminate was calculated to have been consolidated with 1.4 atm of pressure.

The laminate was removed and a sonic knife was used to cut a straight edge at the non-buttressed end of the laminate (right side end in Figure 4-2), shortening it to 21.0 cm with a clean edge. A mould centerline was drawn at 13.0 cm from the previously buttressed end.

4.1.3 Forming

A hand lay-up baseline test was first performed in order to compare to the charge-formed parts.

4.1.3.1 Hand lay-up baseline test

Prior to lay-up, the laminae for the hand lay-up baseline C-channel were cut to final length of 21.0 cm x 7.6 cm. Each ply was laid up onto the same aluminum mould by hand with the backing paper side up at room temperature (24°C). Each ply was held into place with both hands for approximately five seconds allowing for adequate adhesion to the previous ply. A roller was used to flatten any bulges and the backing paper was removed. No intermediate debulk was conducted. After lay-up, an FEP sheet was affixed to the top-side of the laminate and the taut silicone forming membrane was used to perform a 10 minute debulk, analogous to the debulking step seen by the charges used for drape-forming after lay-up. The assembly was then moved to the oven in preparation for cure.

4.1.3.2 Drape-formed parts

The oven (a *Thermotron* environmental chamber converted to programmable oven) and the forming assembly were preheated to the forming temperature (either 30°C or 70°C, depending on the specific test conditions). The forming assembly consisting of a forming box (60.0 cm x

60.0 cm aluminum plate, welded aluminum square tubing walls, FEP-wrapped oak ramps), a silicone membrane (*Torr Technologies Inc.* 0.10 cm-thick EL80 flat sheet adhered to a 60.0 cm x 60.0 cm aluminum frame, pierced with a quick-connect vacuum port), and a *FREEKOTE* release agent-covered aluminum mould (10.1 cm x 10.1 cm x 10.1 cm aluminum block) was fitted with thermocouples on the box's sides and on the silicone bag (Figure 4-4 on left). The assembly was then brought up to the desired temperature for forming.

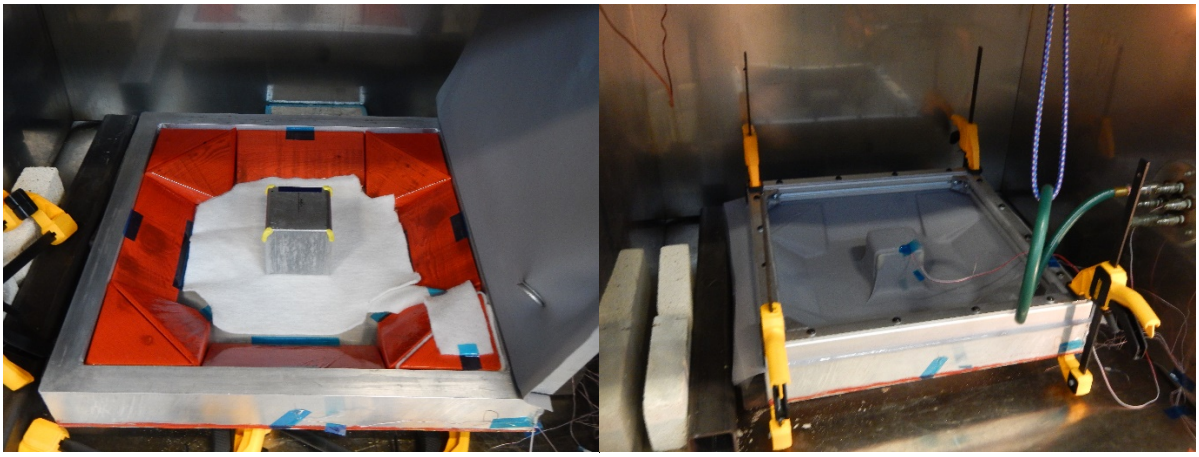

Figure 4-4. Forming assembly in the *Thermotron* oven: (left) prior to forming, and (right) after forming.

To minimize heat loss from the open oven door, care was taken to quickly transfer the laminate to the top of the mould, overlay a 22.2 cm x 8.9 cm FEP sheet, and secure the web section to the mould with *Airtech Flashbreaker* tape. The silicone sheet frame was lowered and clamped down to the forming box walls with Nylon quick clamps. The oven control thermocouple was verified to ensure that it was well-affixed to the silicone bag in the center of the web. The oven door was then closed.

The oven was held at the forming temperature for 30 minutes to ensure temperature uniformity throughout the laminate. The 30 minute requirement was set based on ± 0.75°C uniformity through the thickness of the laminate in separate thermal qualification tests (See Appendix B.6). The vacuum line valve was then opened, initiating drape forming of the flat charge onto the mould. The forming process occurred over 14 seconds, equivalent to an average angular forming velocity of 6.4°/s (0.11 rad/s) as determined by video analysis of forming qualification tests.

5 minutes after the forming was initiated, the oven was reopened and the nylon quick-clamps were substituted one-by-one with steel C-clamps in order to withstand the higher curing temperatures. At this time, a post-form photo survey was taken of the formed C-channel's flanges from the silicone bag's exterior, though no measurements were taken (Figure 4-4 on right). The oven was then re-sealed in preparation for cure.

4.1.4 Cure

In most cases, the parts were cured in the taut silicone bag that was used in forming. But in one instance, a torn bag required the use of disposable pleated Nylon bagging to be used for cure. In both cases, the cure cycle was set to the manufacturer's recommended cure cycle: a 1.0°C/min ramp to 121°C, followed by a 3 hour hold. Once the parts had cooled down, a post-cure photo survey was performed on the part prior to removal from the mould. The part was then removed from the mould by hand and a photo survey of the mould-side surface was taken.

4.2 Post-cure measurements and analysis

4.2.1 Mould-side surface photography

A long exposure photo survey was performed on the mould-side with the intent to capture surface images with a large depth of field and high resolution. This technique was trialed as an inexpensive non-destructive inspection method to identify defect locations and defect types in mould-side surface plies. By setting up the camera, light source, and sample in particular arrangements, it was possible to document the sub-surface features that were visible to the human eye when the sample was oriented at particular angles with respect to the light source. The captured features were later correlated to the locations of defects as seen from optical microscopy on cross-sections of the samples.

The light source consisted of workbench LED lighting covered with breather ply to act as a diffuser. The height and angle of the camera, the part location, and the light source location were constant for each test (Figure 4-5). The angle of the sample with respect to the camera was changed for each part in order to obtain high contrast images of the sub-surface features. In order

to obtain the highest contrast images, the best results were obtained when the samples were angled in the range of -24° to -57° between the camera frame's horizontal axis and the sample's nominal fibre orientation (Figure 4-6).

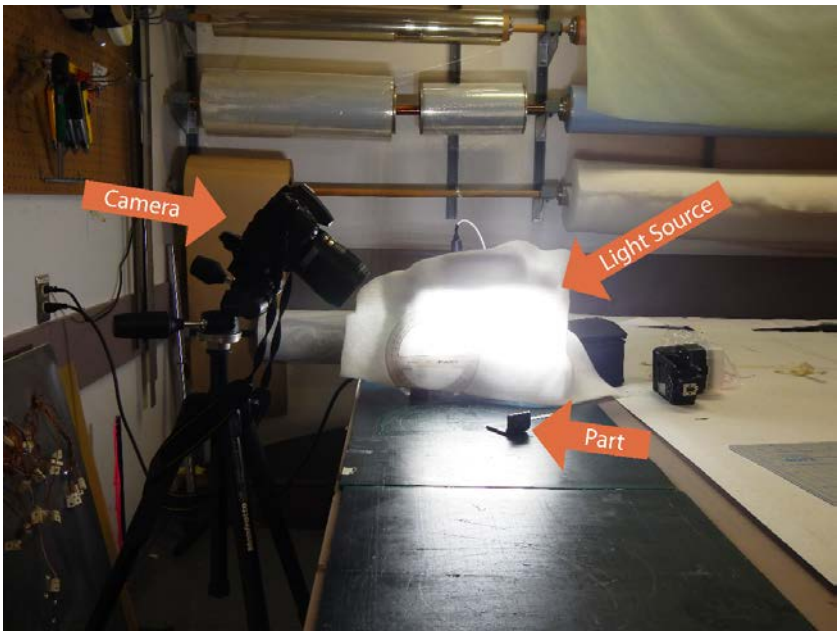

Figure 4-5. Side view of the camera, light source, and part.

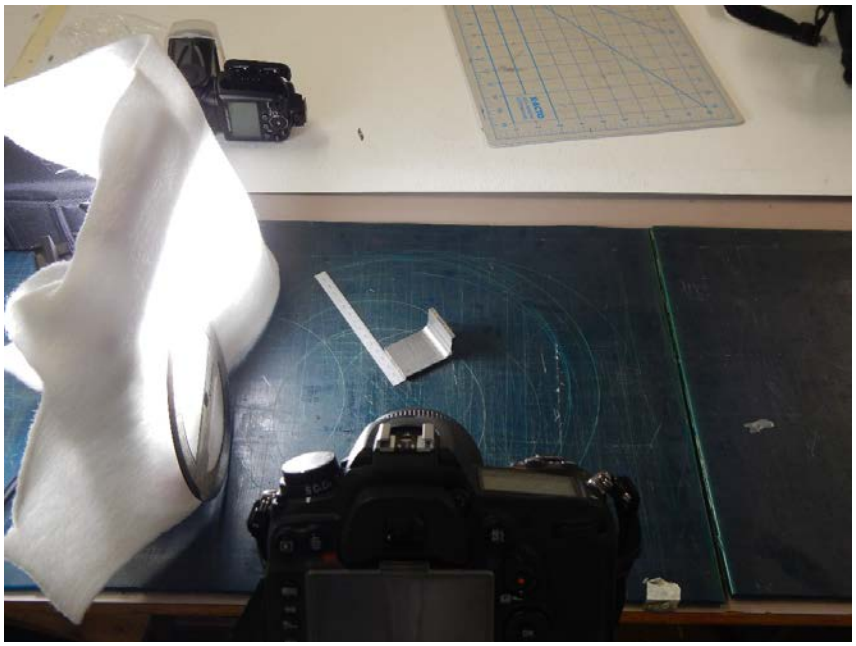

Figure 4-6. Camera perspective for the mould-side surface photography survey.

4.2.2 Measurements from micrographs

4.2.2.1 Optical microscopy image collection

The cross-sectional plane running through the middle of the flange (3.8 cm from the edge of the part) was chosen for microscopy as it was the farthest from either edge. Micrometer thickness readings were taken for each section in order to scale the micrographs. Samples were mounted in room temperature curing epoxy, and polished using a *Buehler* auto-polisher. Micrographs were captured at 200x magnification; images were automatically stitched using the *Keyence* microscope software. The resulting partial mosaics were later manually stitched in Adobe Photoshop. Images were then reduced and imported into *AutoCAD 2015* where they were scaled according to the micrometer thickness readings. AutoCAD provided the means to annotate, save, and revisit all measurements – a major advantage over the single measurement capabilities of other software such as *ImageJ* and *Adobe Photoshop*.

4.2.2.2 Wrinkle quantification

Cross-sectional micrographs were used to quantify the severity of wrinkling in the flange. The measurements are illustrated in Figure 4-7 and the metrics are described in Table 4-1.

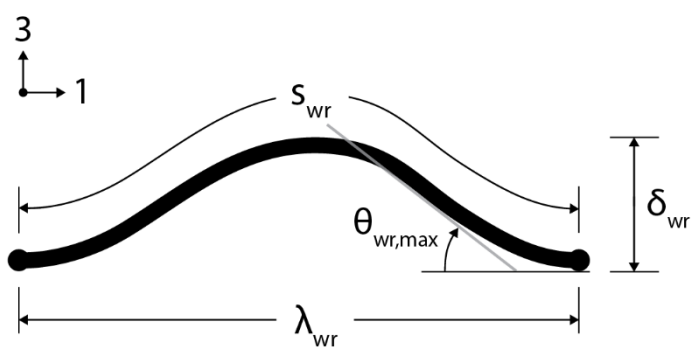

Figure 4-7. Wrinkle quantification measurements based on cross-sectional micrographs.

Table 4-1. Quantification metrics for wrinkling severity

Variable	Given name	Description
λ_{wr}	Wrinkle span length	Length of individual wrinkle along the ply's nominal path
s_{wr}	Wrinkle path length	Path length of individual wrinkle
$\theta_{\mathrm{wr,max}}$	Maximum wrinkle angle	Maximum ply misalignment angle due to wrinkling
δ_{wr}	Wrinkle height	Height of wrinkle peak with respect to the nominal path
δL_{wr}	Wrinkle Excess length	The excess length of a single wrinkle, determined by the following relation: $\delta L_{\mathrm{wr}} = s_{\mathrm{wr}} - \lambda_{\mathrm{wr}}$
$\Sigma\delta L_{\mathrm{wr}}$	Total excess length in flange due to wrinkling	The sum of the excess length from all wrinkles in a particular flange
x_{wr}	Wrinkle location along the flange length	The location of the wrinkle span length midpoint along the length of the flange

4.2.2.3 Waviness quantification

Waviness was quantified using a cross-sectional ellipse survey for all samples. Waviness was additionally quantified by in-plane micrographs for two samples.

4.2.2.3.1 Cross-sectional ellipse survey

Full-ply waviness was quantified for all samples by performing manual ellipse aspect ratio surveys, based on the methodology put forward by Yurgartis relating the fibre angle with the viewing plane to the ellipse's aspect ratio, $\frac{d}{l}$ [29]. An illustration of the ellipses seen in a wavy nominal 0° ply is shown in Figure 4-8Figure 4-8. Table 4-2 tabulates the waviness quantification metrics.

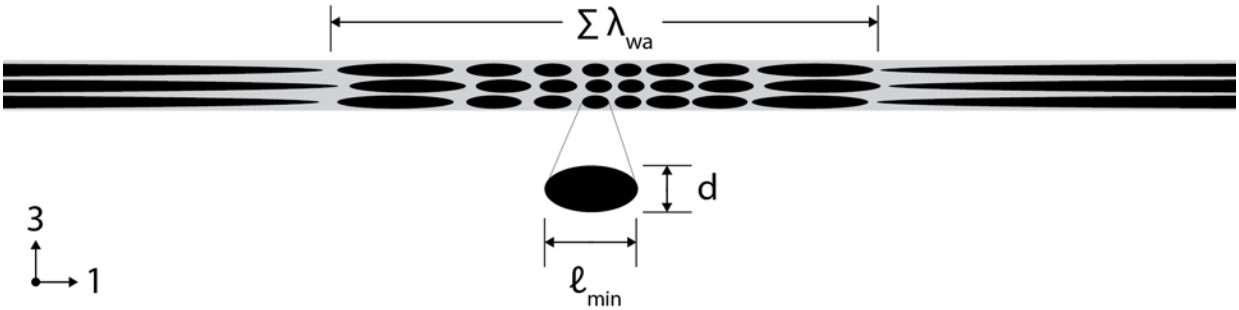

Figure 4-8. Wrinkle quantification measurements based on an illustration of a cross-sectional micrograph of a wavy 0° ply.

Table 4-2. Quantification metrics for waviness based on cross-sectional micrograph ellipse survey.

Variable	Given name	Description
$\Sigma\,\lambda_{\mathrm{wa}}$	Waviness span length	Sum of lengths of full-ply waviness regions within the flange
$\theta_{\mathrm{wa,max}}$	Maximum waviness angle	Maximum fibre misalignment angle due to waviness, as determined by $\theta_{\mathrm{wa,max}} = \sin^{-1}\left(\frac{d}{l_{\mathrm{min}}}\right)$
x_{wr}	Waviness location along the flange length	The location of the waviness span length midpoint along the length of the flange

4.2.2.3.2 In-plane micrograph

Additional in-plane microscopy was performed on two samples. Waviness was quantified in the same manner as wrinkling, but for waviness based on the in-plane micrographs as illustrated below in Figure 4-9. Table 4-3 tabulates the waviness quantification metrics.

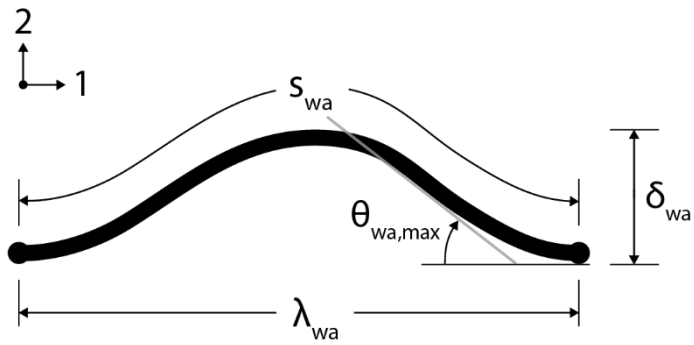

Figure 4-9. Wrinkle quantification measurements based on in-plane micrographs.

Table 4-3 Quantification metrics for waviness based on in-plane micrographs.

Variable	Given name	Description
λ_{wa}	Waviness span length	Length of individual waviness along the ply's nominal path
s_{wa}	Waviness path length	Path length of individual waves
$\Sigma\delta L_{\mathrm{wa}}$	Total excess length in flange due to waviness	The sum of the excess length from waviness in a particular flange $\Sigma\delta L_{\mathrm{wr}} = \Sigma(s_{\mathrm{wr}} - \lambda_{\mathrm{wr}})$

4.2.2.4 Flange termination profiles

Flange terminations were quantified in order to correlate fibre misalignments and missing length seen at the flange termination, as introduced in Section 3.1.2. Two methods were attempted, both relying solely on 0° ply terminations. Measuring every ply was deemed inaccurate due to the tendency of the 90° and ± 45° fibres to flow, obscuring the actual location of the ply termination.

4.2.2.4.1 Local method

Dubbed the *'Local Method'*, the initial flange termination quantification method consisted of measuring ply lengths relative to the origin set at the topmost 0° ply's termination (Figure 4-10). The vertical positions were measured at the ply terminations and are considered negative with respect to the origin.

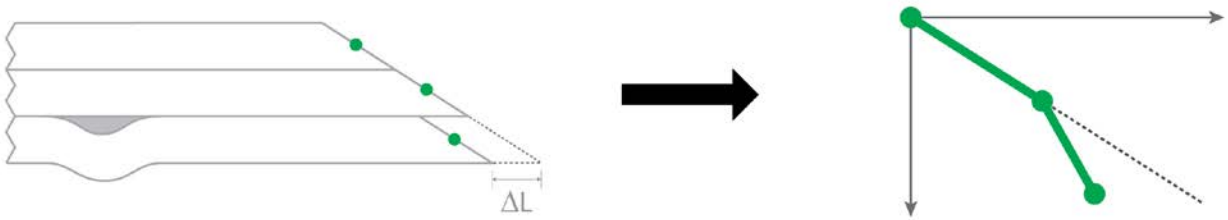

Figure 4-10. Schematic representation of the 'Local method', where all plies shown are assumed to be 0° plies (fibres running left to right).

Due to intensified consolidation at the laminate termination, the plies showed significant vertical displacements resulting in curved ply termination profiles. Although the 'Local method' represented the true termination profile, missing length predictions could not be computed with accuracy.

4.2.2.4.2 End consolidation correction method

The 'end consolidation correction method' was developed to address the issue of curved termination profiles. To compensate for the intensified consolidation at the laminate termination, the 0° ply paths were traced and measured along the flange length beyond the consolidation non-uniformities (Figure 4-11). The corresponding heights for each ply were taken in the uniform region, rather than the termination location. The ply lengths taken from the uniform region were normalized by subtracting the top-most ply's path length. The corrected laminate termination profiles were then plotted with the origin at the top-most ply's corrected termination location, as illustrated in Figure 4-12Figure 4-12 on the left.

Figure 4-11. End consolidation correction method. White lines represent 0° ply traces from the terminations (on right) to the uniform section (on left).

4.2.2.4.3 Part-averaged termination profiles

Given the angular spread between long flange and short flange termination profiles for a given C-channel, the termination profiles were averaged in attempt to remove laminate shifting effects that were seen in all manufactured parts (Figure 4-12 on the left). Short flange results were mirrored about the vertical axis prior to averaging. However, by combining the long and short flange data, no absolute ply termination angle could be determined for any individual flange using this method.

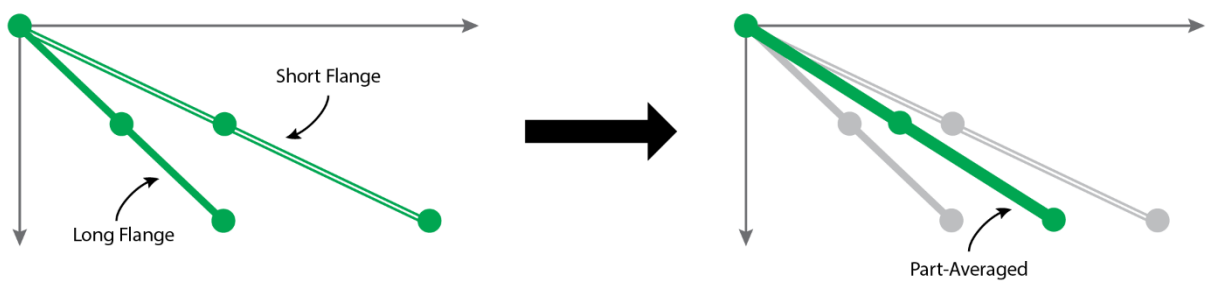

Figure 4-12. Part-averaging of flange termination profiles.

4.2.2.5 Thickness profiles

Part thickness profiles were measured for each flange in AutoCAD 2015 based on cross-sectional micrographs. Measurements were taken perpendicular to the mould surface at approximately 2 mm intervals (1 mm intervals in highly featured regions) along the length of the flange until the termination of the shortest ply (Figure 4-13). The measurement locations were taken with respect to the part's midline with the origin located at the middle of the corner (Figure 4-14). The mid-corner was found by extending the flange and web mould-side edges until they intersect, marking the middle of the corner (blue line in Figure 4-13).

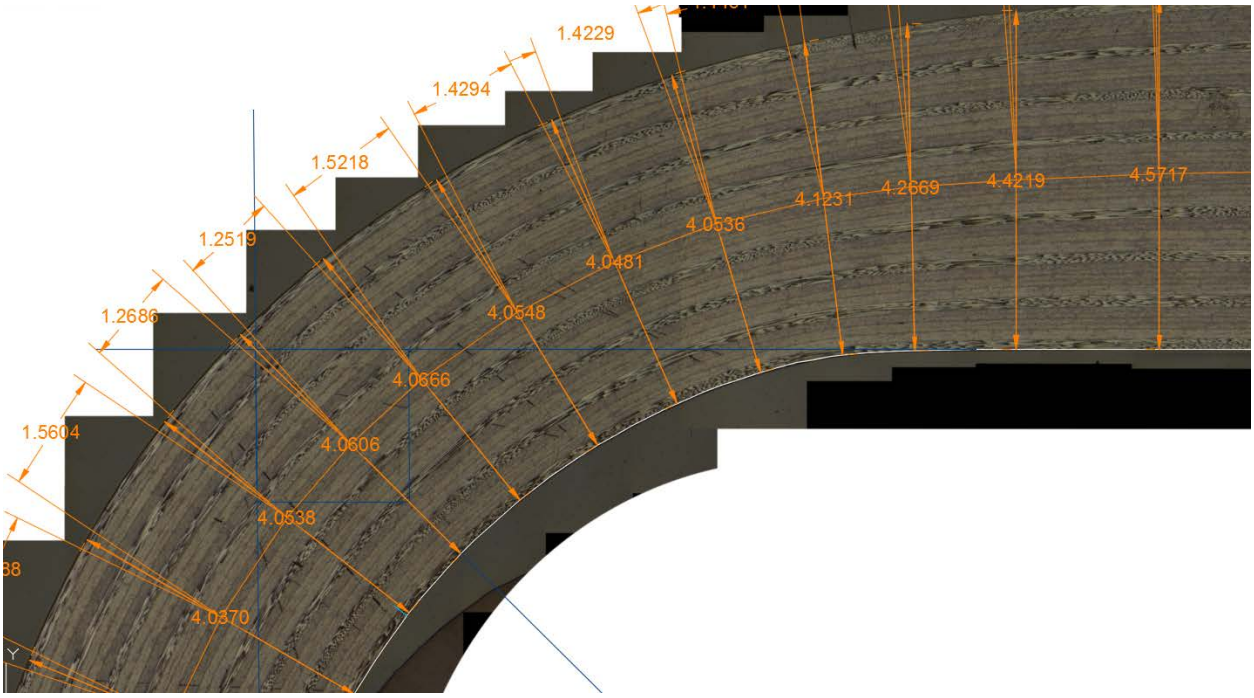

Figure 4-13. Sample image of thickness survey where the blue line shows the determination of the mid-corner location. Units in millimeters.

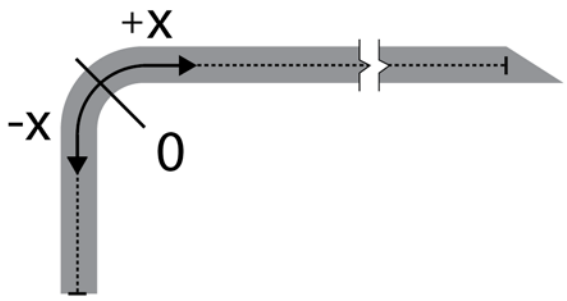

Figure 4-14. Location along the flange length.

In order to directly compare 16-, 32-, and 64-ply thickness profiles, thickness units were normalized with regards to the cured ply thickness ('*CPT*') computed for the particular C-channel. The cured ply thickness for each part was determined by summing the area under the thickness profiles for each flange and dividing by the length of the part.

4.3 Experimental matrix

The process parameters that were used to manufacture all C-channels are summarized in Table 4-4 below.

Table 4-4. Constant process parameters for all manufactured flanges

Material system	CYCOM 5320/T650-35 unidirectional prepreg
Post-lay-up consolidation	10 minutes at 1.4 bar
Geometry	C-channel (90° flanges)
Width	76.2 mm
Short flange '*SF*' (sheared) length	38.1 mm
Long flange '*LF*' (sheared) length	88.9 mm
Nominal web length	101.6 mm
Mould corner radii	9.525 mm
Average forming velocity	6.4°/s (angular) 0.015 mm/s (linear)
Cure cycle	1.0°C/min ramp to 121°C; hold for 3 hours

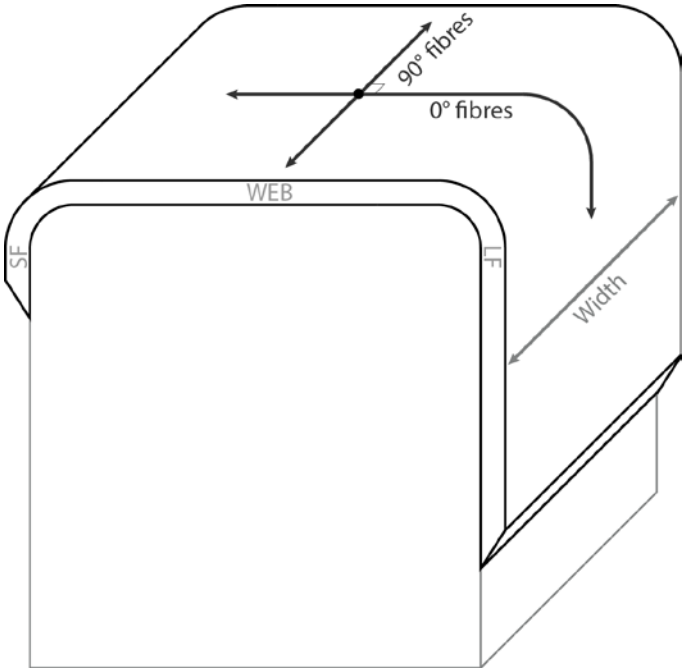

Figure 4-15. Fibre orientations with respect to part geometry.

Table 4-5. Varied process parameters

Forming temperature	24°C (HLU only)	30°C	70°C
Ply count	*'16ply':* 16	*'32ply':* 32	*'64ply':* 64
Ply sequence	*'Quasi':* $[90/+45/-45/0]_{xS}$	*'Offset':* $[0/-45/+45/90]_{xS}$	
Forming method	*'HLU':* Hand lay-up	Drape-formed	
Cure bagging tension	'*Nylon*': Pleated Nylon	'*Silicone*': Taut silicone	

The varied forming process parameters were the forming temperature, ply count, ply sequence, curing bag tension, and forming method (Table 4-5). Forming temperatures were chosen based on the literature which suggested that room temperature forming was more prone to defects than higher temperature forming. 70°C was mentioned as a typical forming temperature for industrial processing [21]. Ply counts were chosen for industrial relevance, based on conversations with industrial partners. The *Quasi* ply sequence, $[90/+45/-45/0]_{xS}$, was chosen as a quasi-isotropic sequence whose surface fibres are oriented along the width of the part. The *Offset* ply sequence, $[0/-45/+45/90]_{xS}$, is the same *Quasi* ply sequence but rotated by 90° with the goal of comparing behavioural differences of the same laminate as it is formed in one direction versus the other.

Nine C-channels were manufactured whose process parameters are specified in Table 4-6 below. Note that Parts c1 and c2 are repetitions of the same conditions. Plot label nomenclature is based on the flange identifier (Long '*LF*', Short '*SF*', or Part-averaged '*AvgF*'– see Section 4.2.2.4.3) for the particular sequential test identifiers (letters a to h). Manufacturing specifications are also noted. Sample plot labels are broken down in Table 4-7.

Table 4-6. Manufactured C-channel process specifications with emboldened parameters of interest

Test ID: Flange IDs	Forming temperature	Ply count	Ply sequence	Forming method	Curing bag material
Part a: LF-a & SF-a	24°C	32	*Quasi* $[90/+45/-45/0]_{4S}$	Hand lay-up	Taut silicone
Part b: LF-b & SF-b	30°C	32	*Quasi* $[90/+45/-45/0]_{4S}$	Drape-formed	Pleated Nylon
Part c1: LF-c1 & SF-c1	30°C	32	*Quasi* $[90/+45/-45/0]_{4S}$	Drape-formed	Taut silicone
Part c2: LF-c2 & SF-c2	30°C	32	*Quasi* $[90/+45/-45/0]_{4S}$	Drape-formed	Taut silicone
Part d: LF-d & SF-d	70°C	32	*Quasi* $[90/+45/-45/0]_{4S}$	Drape-formed	Taut silicone
Part e: LF-e & SF-e	30°C	16	*Quasi* $[90/+45/-45/0]_{2S}$	Drape-formed	Taut silicone
Part f: LF-f & SF-f	30°C	64	*Quasi* $[90/+45/-45/0]_{8S}$	Drape-formed	Taut silicone
Part g: LF-g & SF-g	30°C	32	*Offset* $[0/-45/+45/90]_{4S}$	Drape-formed	Taut silicone
Part h: LF-h & SF-h	70°C	32	*Offset* $[0/-45/+45/90]_{4S}$	Drape-formed	Taut silicone

Table 4-7. Sample plot label nomenclature

Sample label	Sample details
LF-b (32ply, 30°C, Quasi, Nylon)	*88.9mm (long) flange* *Part 'b'* *32 plies* *formed at 30°C* *$[90/+45/-45/0]_{xS}$ repeating ply sequence* *Cured in pleated Nylon bag*
SF-h (32ply, 70°C, Offset, Silicone)	*38.1 mm (short) flange* *Part 'h'* *32 plies* *formed at 70°C* $[0/-45/+45/90]_{xS}$ *ply sequence* *Cured in taut Silicone bag*
AvgF-f (64ply, 30°C, Quasi, Silicone)	*'Part-averaged' flange* – see Section 4.2.2.4.3 *Part 'f'* *64 plies* *formed at 30°C* *$[90/+45/-45/0]_{xS}$ ply sequence* *Cured in taut Silicone bag*
AvgF-a (32ply, HLU, Quasi, Silicone)	*'Part-averaged' flange* – see Section 4.2.2.4.3 *Part 'a'* *32 plies* *formed by hand lay-up ('HLU') at 24°C* *$[90/+45/-45/0]_{xS}$ ply sequence* *Cured in taut Silicone bag*

Chapter 5: Results

Quantified wrinkles, waviness, flange termination profiles, and thickness profiles for all manufactured flanges are summarized in the sections that follow. Raw data for all manufactured flanges can be found in Appendix A .

5.1 Wrinkling and waviness

5.1.1 Externally visible defects

Immediately after the parts were formed, images of the top part surface were taken in order to document the occurrence and locations of externally visible defects prior to cure. Once cured, similar images were taken. Table 5-1 shows a summary of under which process conditions externally visible defects were seen. Figure 5-1 to Figure 5-4 below show photographic examples of externally visible defects after forming and after cure.

Table 5-1. Occurrence of externally visible defects on the bag-side surface after forming and after cure

Part identifier '*n*'	Process parameters (# of plies, forming temperature, ply sequence, cure bag type)	Occurrence of externally visible defects **after forming**		Occurrence of externally visible defects **after cure**	
		Long flange 'LF-*n*'	Short flange 'SF-*n*'	Long flange 'LF-*n*'	Short flange 'SF-*n*'
a	32ply, HLU, Quasi, Silicone	–	–	–	–
b	32ply, 30°C, Quasi, Nylon	•	–	•	–
c1	32ply, 30°C, Quasi, Silicone	–	–	–	–
c2	32ply, 30°C, Quasi, Silicone	–	–	–	–
d	32ply, 70°C, Quasi, Silicone	–	–	–	–
e	16ply, 30°C, Quasi, Silicone	•	–	–	–
f	64ply, 30°C, Quasi, Silicone	•	–	–	–
g	32ply, 30°C, Offset, Silicone	•	–	–	–
h	32ply, 70°C, Offset, Silicone	–	–	–	–

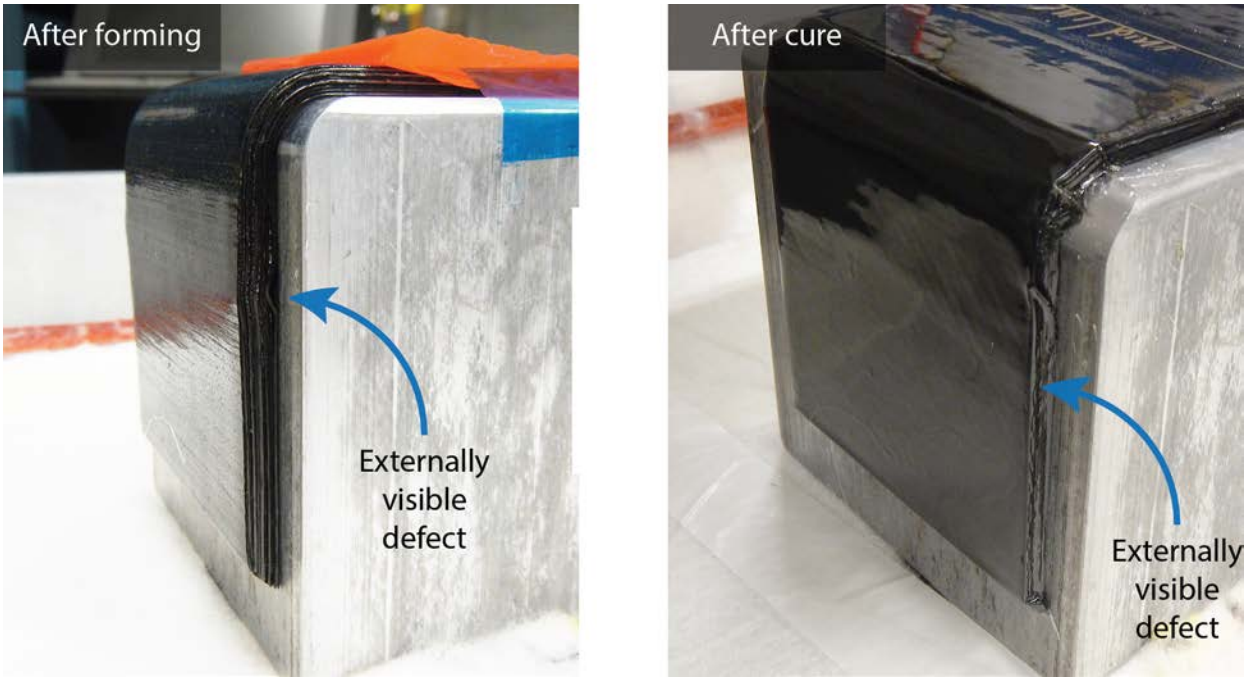

Figure 5-1. Left: long flange with an externally visible defect after forming (shown without forming bag) spanning the entire width of the part. Right: the same defect remained visible after cure in a pleated Nylon bag. (Shown flange is 'LF-b')

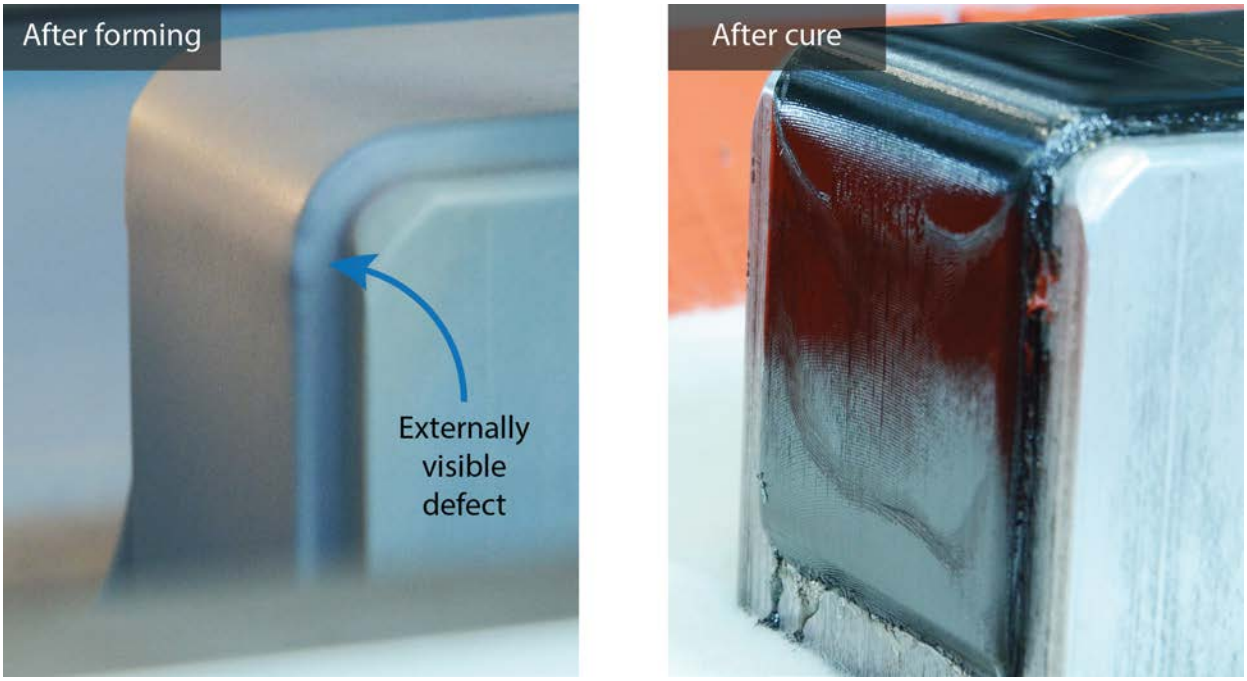

Figure 5-2. Left: long flange with an externally visible defect after forming spanning the entire width of the part. Right: the same defect was no longer visible after cure in a taut silicone bag. Minor surface imperfections can be seen. (Shown flange is 'LF-g')

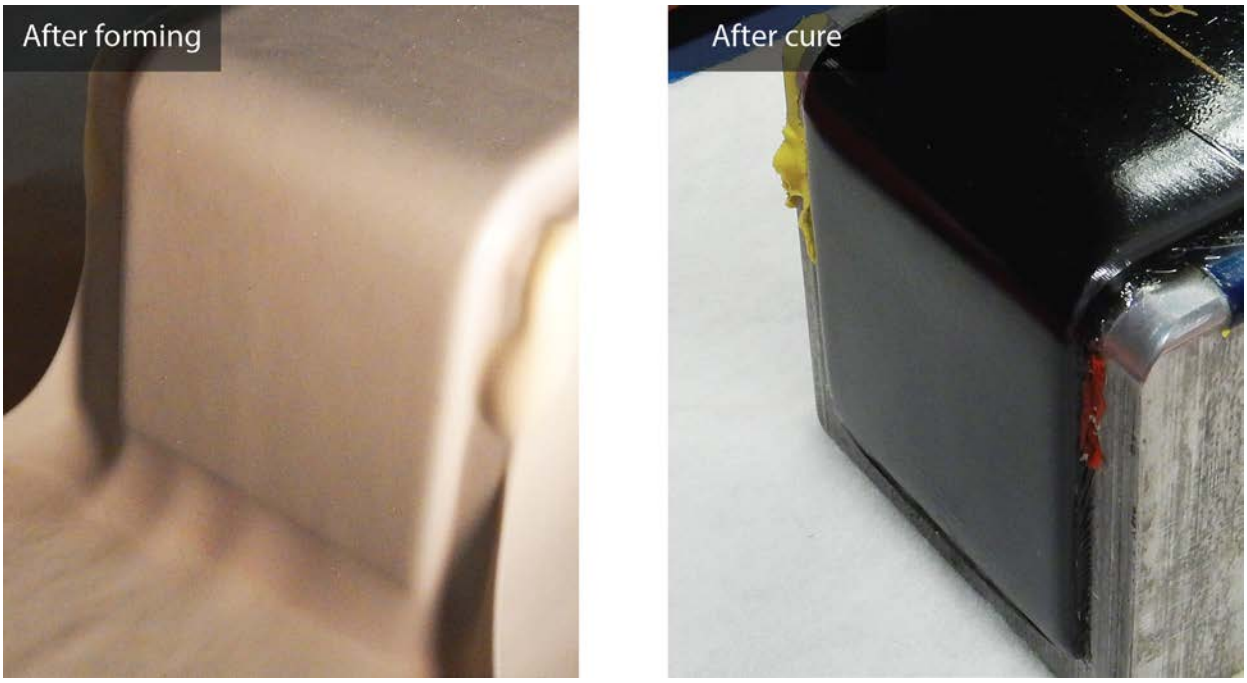

Figure 5-3. Left: long flange with no externally visible defects after forming. Right no externally visible defects after cure in a taut silicone bag. (Shown flange is 'LF-c1')

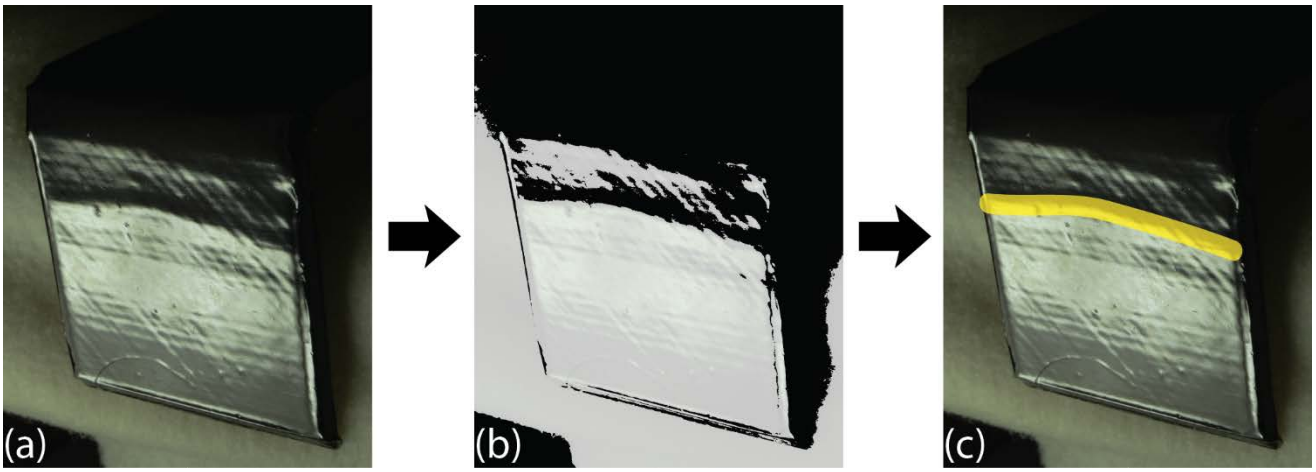

Figure 5-4. Bag-side surface photography of a nylon bag-cured long flange illustrating near-uniform externally visible defect behaviour through the width of the flange. (a) direct lighting photograph accentuating surface reflection b) binary image overlay showing a distinct region where the surface protrudes along the width of the flange, (c) manual trace of the protrusion highlighting the near-uniform widthwise wrinkle profile. ('LF-b' is shown)

Externally visible defects spanning the entire width of the part could be seen in the long flanges near the corner region after forming for 'LF-c1', 'LF-e', 'LF-f', and 'LF-g' (Table 5-1). Only the sample cured in the pleated Nylon bag showed any externally visible defects after cure (Figure 5-1) whereas all taut silicone-cured flanges appeared defect-free after cure, aside from minor surface blemishes (Figure 5-2). In the case where no defects were seen after forming, no defects were seen after cure (Figure 5-3). Short flanges showed no externally visible defects at any point during manufacturing.

5.1.2 Internal fibre misalignments

After cure, the parts were cross-sectioned and examined by optical microscopy which revealed three types of internal fibre misalignment defects within 0° plies: wrinkling, partial-ply waviness, and full-ply waviness. The morphology of the region surrounding wrinkles was largely dependent on the part's ply sequence. The internal defect morphology was compared to surface photography.

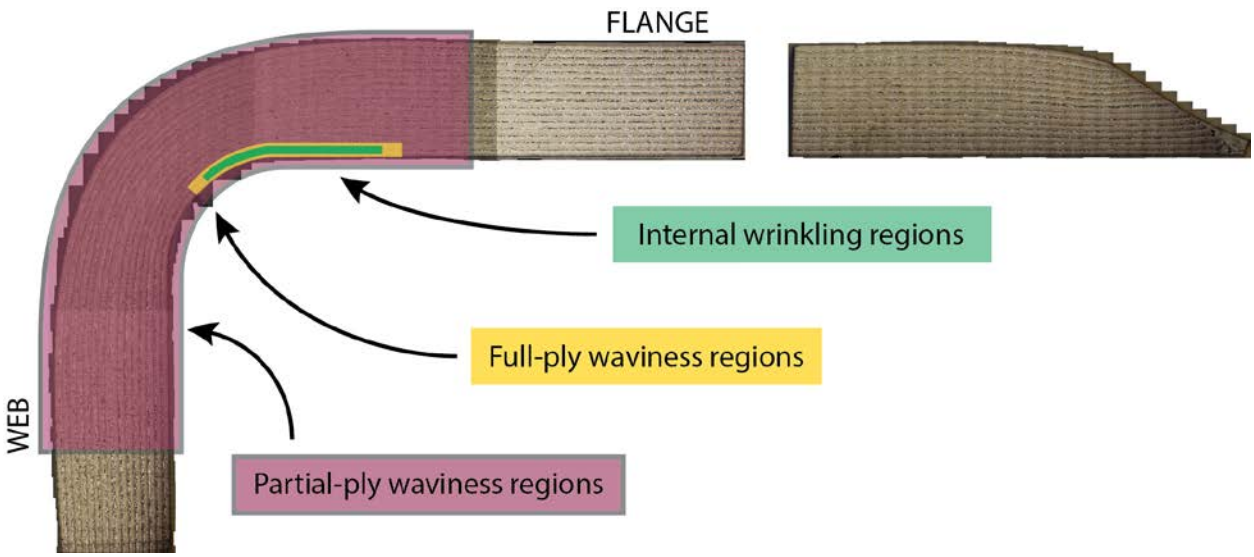

Figure 5-5. Micrograph showing internal fibre misalignment regions of partial-ply waviness, full-ply waviness, and internal wrinkling in a wrinkled part. (Shown flange is 'LF-f')

5.1.2.1 Waviness morphology

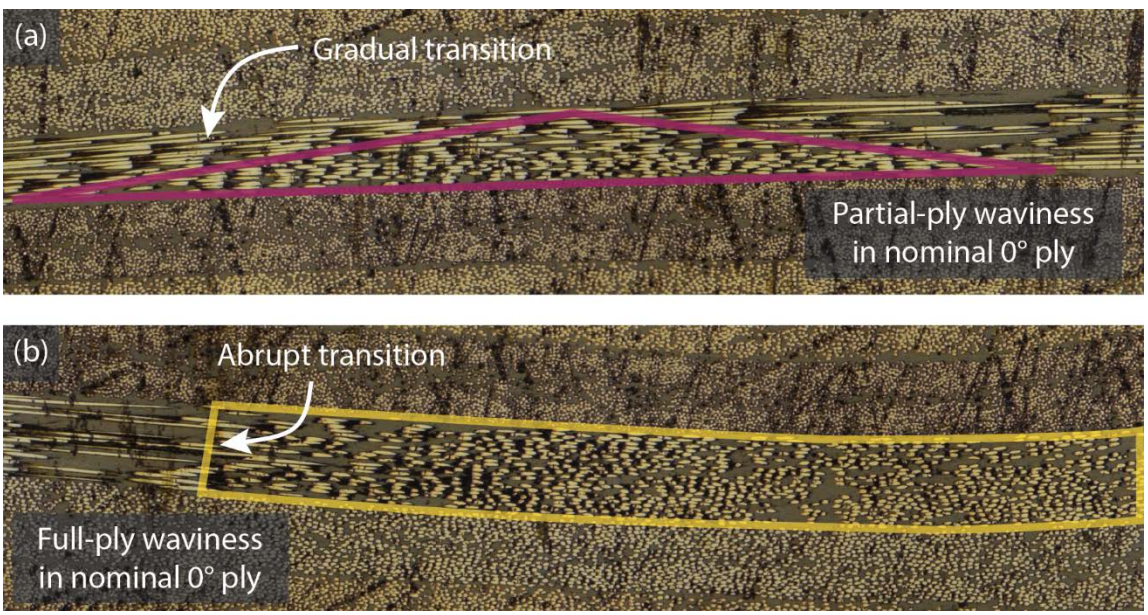

Figure 5-6. Micrographs of (a) partial-ply waviness in 0° plies, and (b) full-ply waviness in 0° plies. The 0° fibre direction spans left to right.

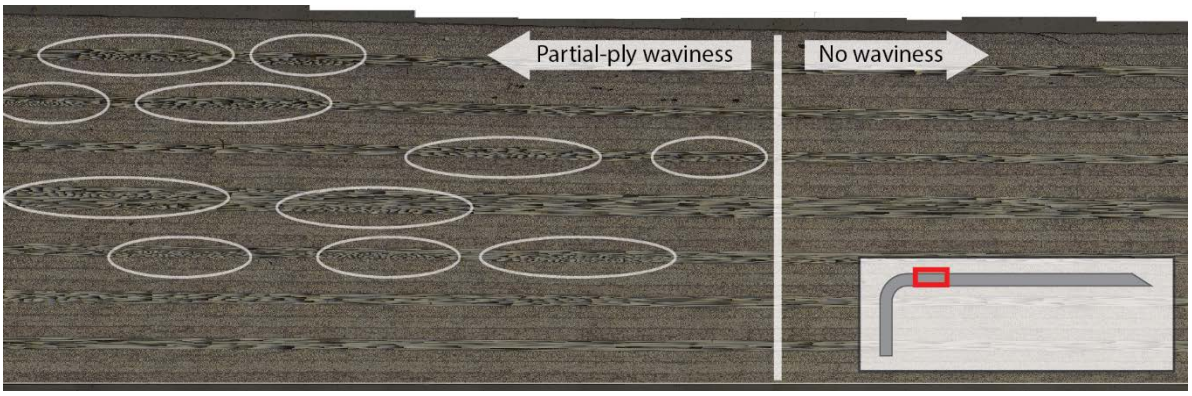

Figure 5-7. Illustration of the partial-ply waviness locations, typical of all manufactured parts.

Waviness could be seen in two forms: '*partial-ply waviness*' and '*full-ply waviness*' (Figure 5-6). Partial-ply waviness is characterized by a gradient of waviness through the thickness of the ply and a gradual transition from a non-wavy state (Figure 5-6 (a)). The top side of the ply retained its approximate nominal fibre orientation whereas the lower part showed waviness. This type of ply waviness was present in all manufactured parts in the corner and nearby web and flange regions throughout all 0° plies in the laminate (Figure 5-5). Partial-ply waviness regions were not found in the remainder of the webs or flanges (Figure 5-7).

Full-ply waviness is characterized by an abrupt transition from a non-wavy ply state for the entirety of the ply (Figure 5-6 (b)). It occurred in 0° plies near the mould-side and was associated with internal wrinkling sites (Figure 5-5).

5.1.2.2 Wrinkle region morphology: *Quasi* flanges

Figure 5-8. Characteristics of a non-wrinkled hand lay-up *Quasi* baseline flange. (Image of 'LF-a')

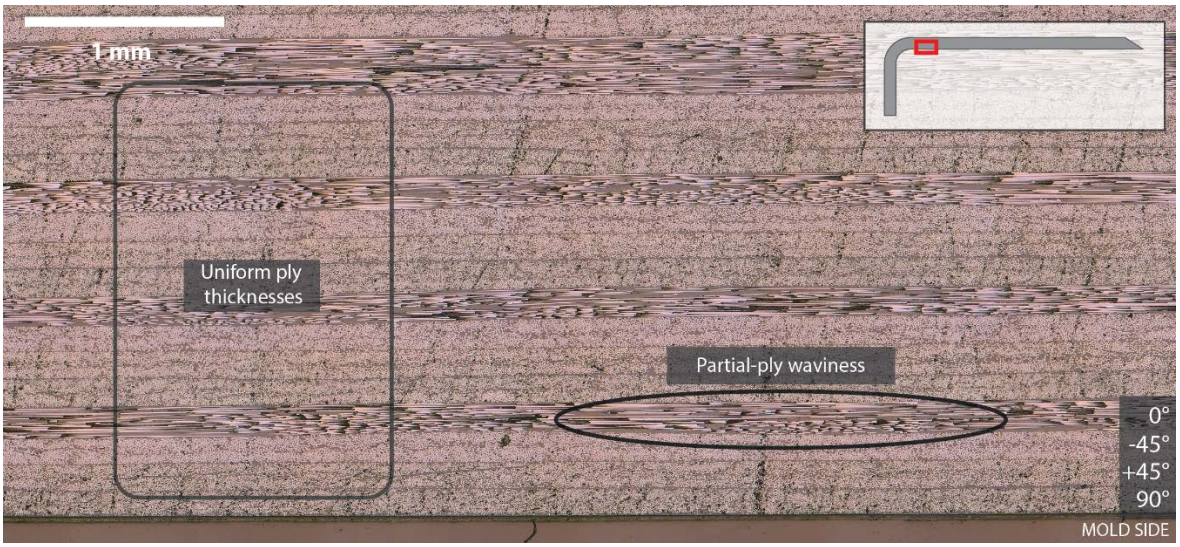

Figure 5-9. Characteristics of a non-wrinkled drape-formed *Quasi* ply sequence flange. (Image of 'LF-d')

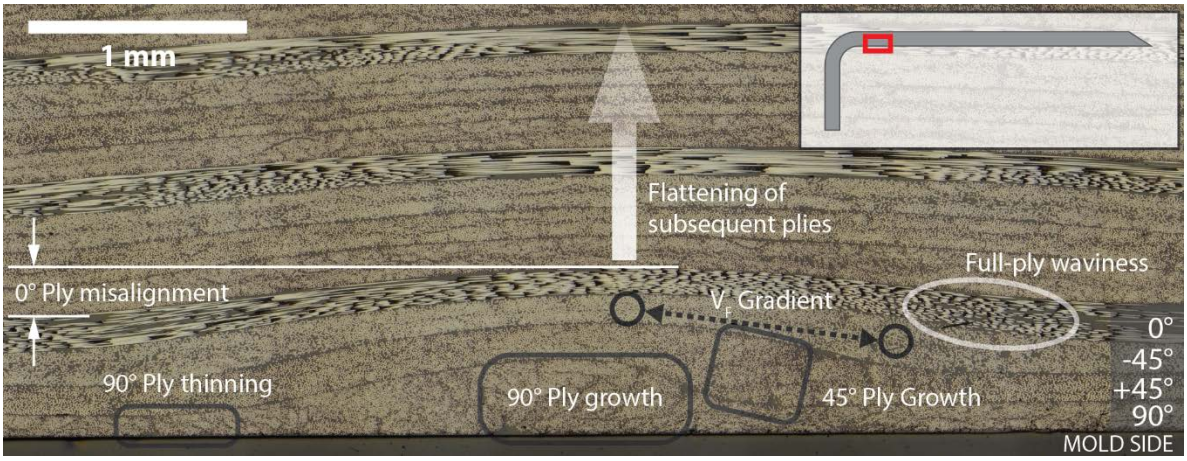

Figure 5-10. Typical wrinkle characteristics of a wrinkled *Quasi* ply sequence flange (Image of 'LF-f')

Flange quality for the baseline hand laid-up part is presented in Figure 5-8 for the region that showed wrinkling in other samples. The plies exhibit uniform thickness and alignment. Multiple regions of partial-ply waviness could be seen in the 0° plies (only one is circled), but the part was otherwise devoid of defects. A non-wrinkled drape-formed part exhibited similar part quality as the hand lay-up baseline flange (Figure 5-9).

The micrograph in Figure 5-10 shows a wrinkled *Quasi* long flange. The 0° ply closest to the mould-side (ply #4 of 32) exhibited the most significant path deviation through the thickness of the laminate. This wrinkled ply also exhibited severe full-ply waviness over the entire span of the wrinkle which was not present in the other 0° plies. Like the baseline hand lay-up flange, partial-ply waviness was seen in the other 0° plies. The adjacent -45° ply (ply #3 of 32) followed a similar misaligned path and showed changing thicknesses. Fibre volume fractions of the +45° and -45° plies (plies #2 and #3 overall) showed significant gradients between the peak region of the wrinkle (greater than average V_F) and the wrinkle's end where the wrinkle straightens out (lesser than average V_F). The 90° ply on the mould side (ply #1 overall) showed significant thickening at the wrinkle peak location and thinning near the wrinkle's end. Ply folding and resin swirling patterns could be seen within this 90° ply's thickest region. Subsequent plies of all orientations showed gradual levelling towards their nominal path.

Wrinkling through the width of the laminate (looking into the page of the micrographs) was generally uniform such that any parallel cross section would show a similar wrinkle profile. This observation was based on the externally visible defects of the laminates after forming and after cure (Figure 5-4) and in-plane microscopy of the 'LF-c1' flange. This was corroborated by multiple cross sections taken of similar parts manufactured in a previous study [30].

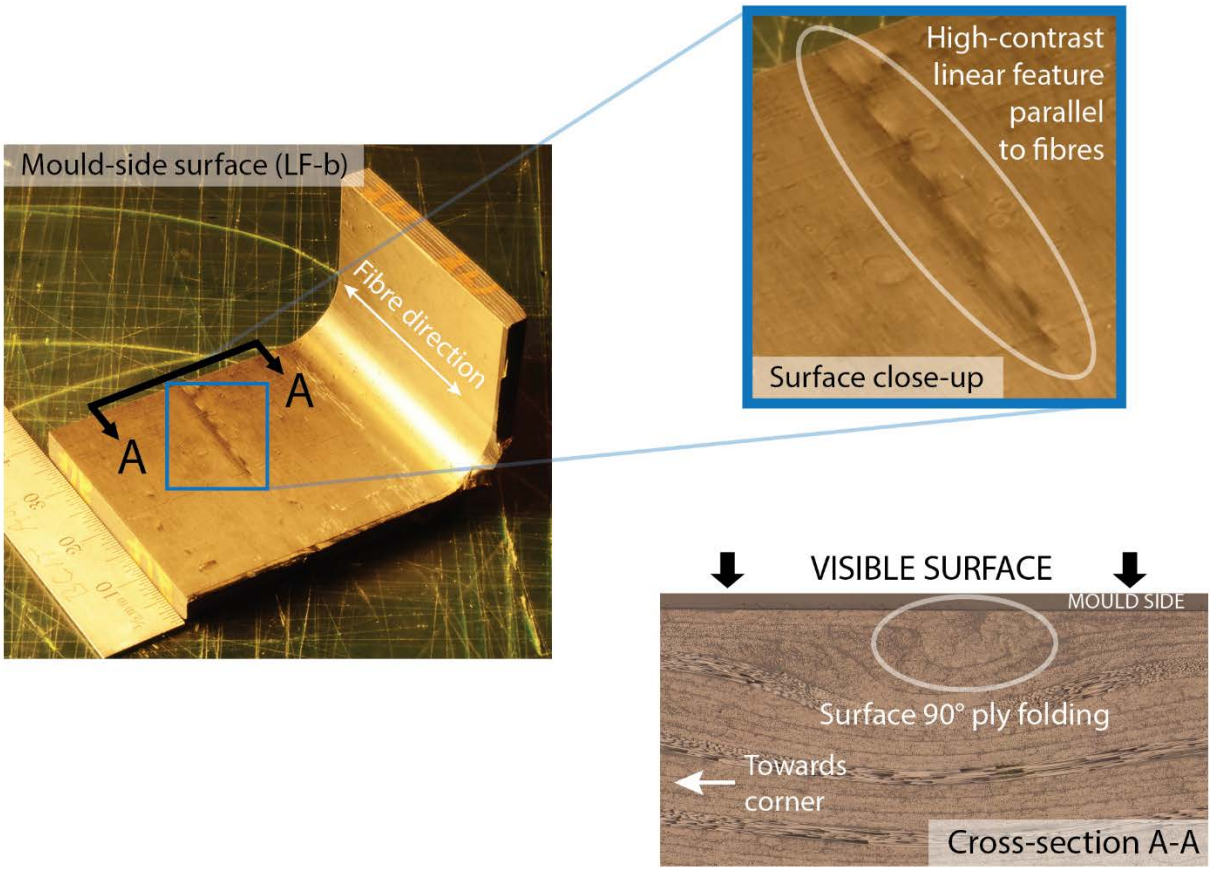

Figure 5-11. Surface photography of a wrinkled flange's mould-side and its corresponding cross-sectional micrograph. ('LF-b' is shown)

To further characterize the *Quasi* flanges' wrinkles, the flange's mould-side surface was photographed as detailed in Section 4.2 (Figure 5-11). The image on the left shows a linear high-contrast feature parallel to the surface fibres. This feature corresponded directly with the location of the flange's wrinkle. In particular, the fold line relates to the location of the surface 90° ply's thickest region, showing resin pooling at the surface where the ply had folded in on itself.

5.1.2.3 Wrinkle region morphology: *Offset* ply sequence flanges

The 90° offset-formed laminate's flanges showed a different wrinkle morphology. Micrographs are shown below.

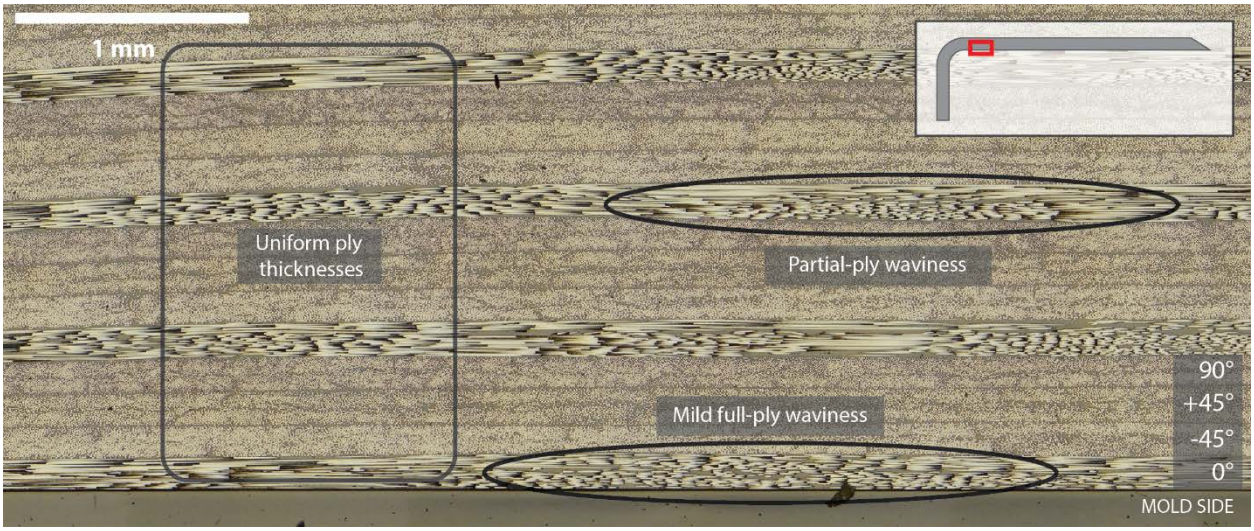

Figure 5-12. Characteristics of a non-wrinkled drape-formed *Offset* ply sequence flange. (Image of 'LF-h')

Figure 5-13. Wrinkle characteristics for the *Offset* ply sequence wrinkled flange ('LF-g' shown)

The non-wrinkled *Offset* ply sequence flange exhibited similar quality to the baseline hand laid-up part: uniform ply thicknesses with no through-thickness path deviations (Figure 5-12). Partial-ply waviness could be seen in the mould-side 0° ply with intermittent regions of mild full-ply waviness. Partial-ply waviness was also found throughout the other 0° plies.

The wrinkled *Offset* ply sequence flange showed significant differences in wrinkling morphology from the *Quasi* ply sequence wrinkles (Figure 5-13 and Figure 5-10). The mould-side 0° ply (ply #1 overall) did not show any appreciable through-thickness misalignments after cure. It did, however, display local thickness growth in a region of severe waviness. Wrinkles were seen in the successive 0° ply in the same region (ply #5 overall). Unlike in the wrinkled *Quasi* flanges,

fibre volume fractions in the adjacent 45° plies did not appear to show appreciable gradients around the 0° ply wrinkling sites.

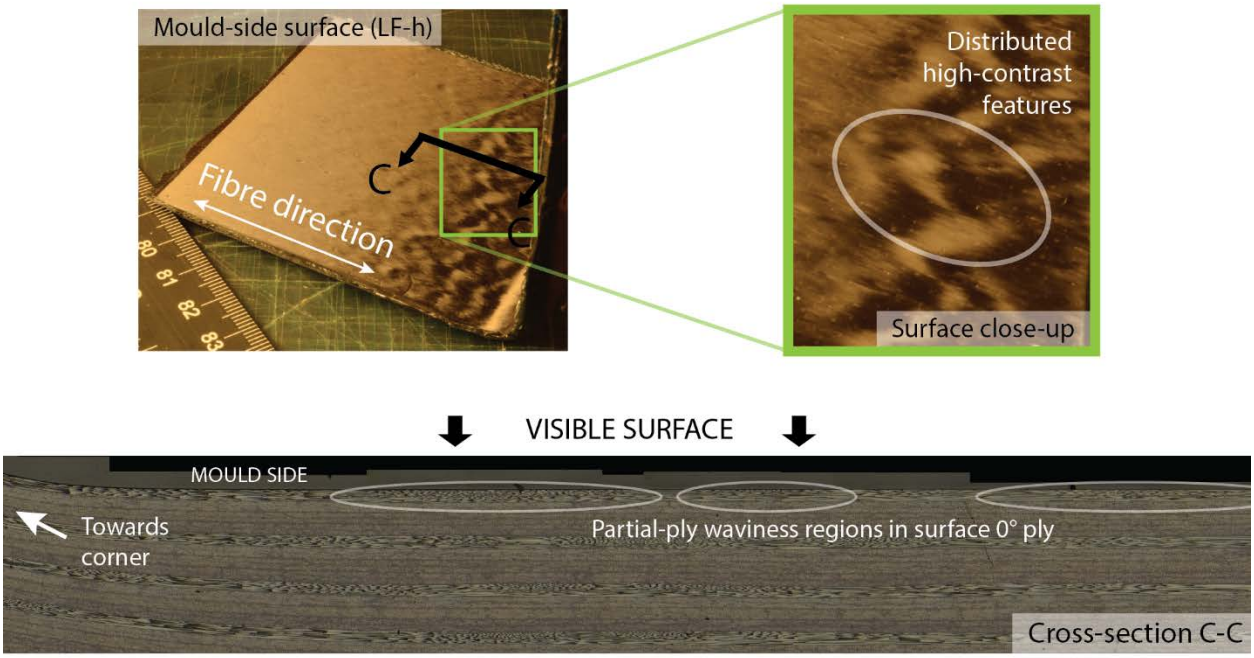

Figure 5-14. 0° ply irregular waviness as it appears from the surface photo survey which corresponds to partial-ply waviness, as seen from cross-sectional micrographs. ('LF-h' shown)

Surface photographs were compared to the micrographs for the non-wrinkled *Offset* ply sequence sample (Figure 5-14). The mould-side part surface showed distributed high-contrast features. A comparison to the cross-sectional micrograph reveals that these features relate directly to partial-ply waviness and mild full-ply waviness. The surface close-up image reveals irregular waviness that does not have a common periodicity.

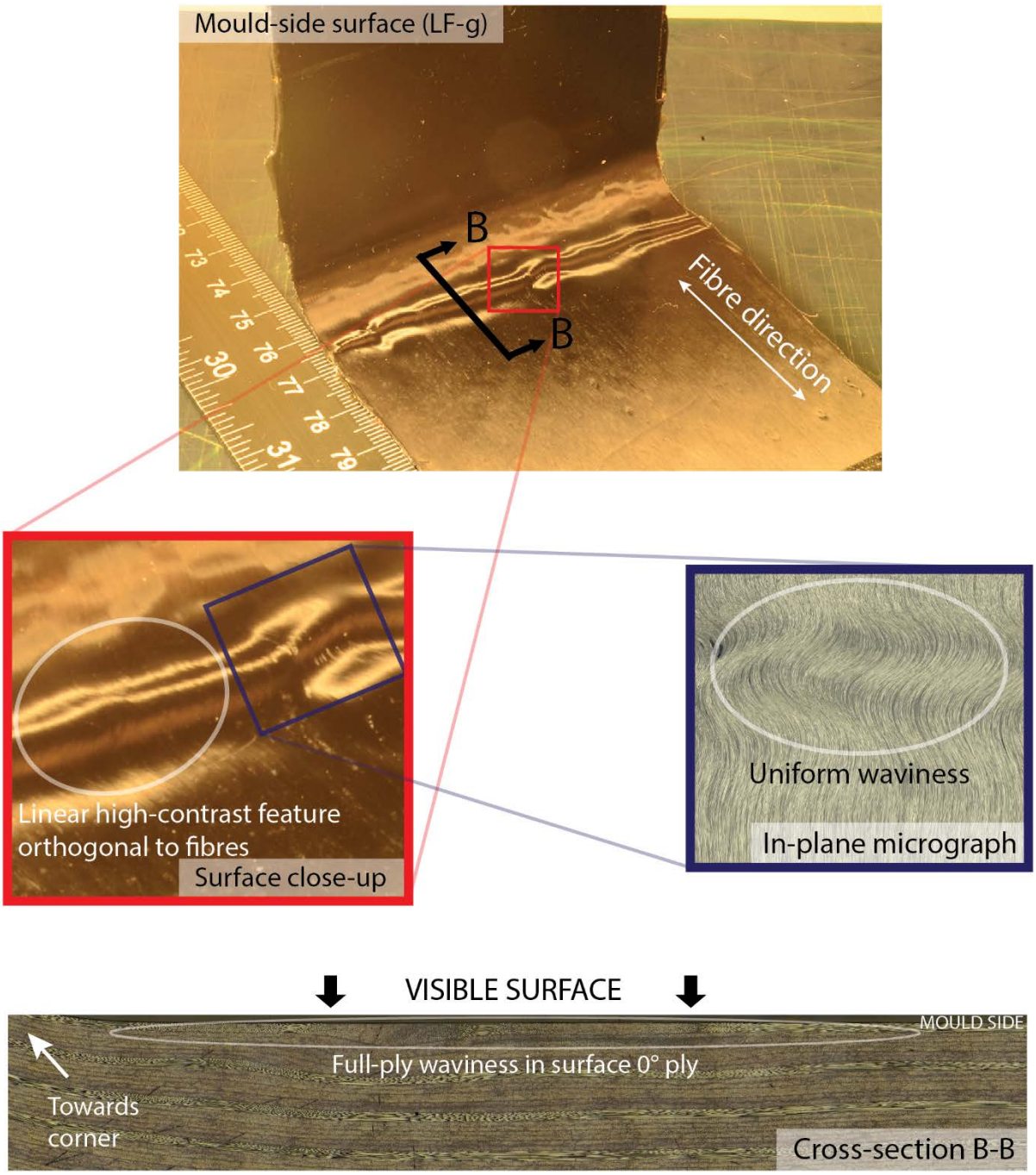

Figure 5-15. 0° ply uniform waviness as it appears from the surface photo survey corresponding to full-ply waviness, as seen from a cross-sectional micrograph. ('LF-g' is shown)

Linear high-contrast features oriented 90° to the surface fibre direction were observed on the mould-side surface for the wrinkled and heavily wavy *Offset* ply sequence flange (Figure 5-15).

The in-plane micrograph correlated these linear features to waviness with a common periodicity which corresponded to full-ply waviness from the cross-sectional micrograph.

5.1.3 Effects of process input parameters on wrinkling

Internal wrinkles have been quantified using the methodology in Section B.1 and are compared against manufacturing input parameters. Table 5-2 compares the occurrence of externally visible defects after forming with the number of internal wrinkles seen from the micrographs.

Table 5-2. Number of internal wrinkles after forming and after cure

		Occurrence of externally visible defects after forming		Number of internal wrinkles after cure	
Part Identifier '*n*'	Process parameters (# of plies, forming temperature, ply sequence, cure bag type)	Long flange 'LF-*n*'	Short flange 'SF-*n*'	Long flange 'LF-*n*'	Short flange 'SF-*n*'
a	32ply, HLU, Quasi, Silicone	–	–	–	–
b	32ply, 30°C, Quasi, Nylon	•	–	2	1
c1	32ply, 30°C, Quasi, Silicone	–	–	3	1
c2	32ply, 30°C, Quasi, Silicone	–	–	2	1
d	32ply, 70°C, Quasi, Silicone	–	–	–	–
e	16ply, 30°C, Quasi, Silicone	•	–	3	1
f	64ply, 30°C, Quasi, Silicone	•	–	1	1
g	32ply, 30°C, Offset, Silicone	•	–	2	–
h	32ply, 70°C, Offset, Silicone	–	–	–	–

It was observed that the externally visible defects that appeared to ‘iron out’ after cure were still present in same region in the form of internal wrinkles (Table 5-2). Additionally, some parts that showed no signs of externally visible defects after forming and cure revealed internal wrinkling (‘LF-c1’ and ‘LF-c2’). This was also true for many of the short flanges, none of which had shown external signs of wrinkling after forming and after cure. The hand lay-up baseline part and both 70°C drape-formed parts (‘Part a’, ‘Part d’, and ‘Part h’) showed neither externally visible defects after forming and cure nor internal wrinkling.

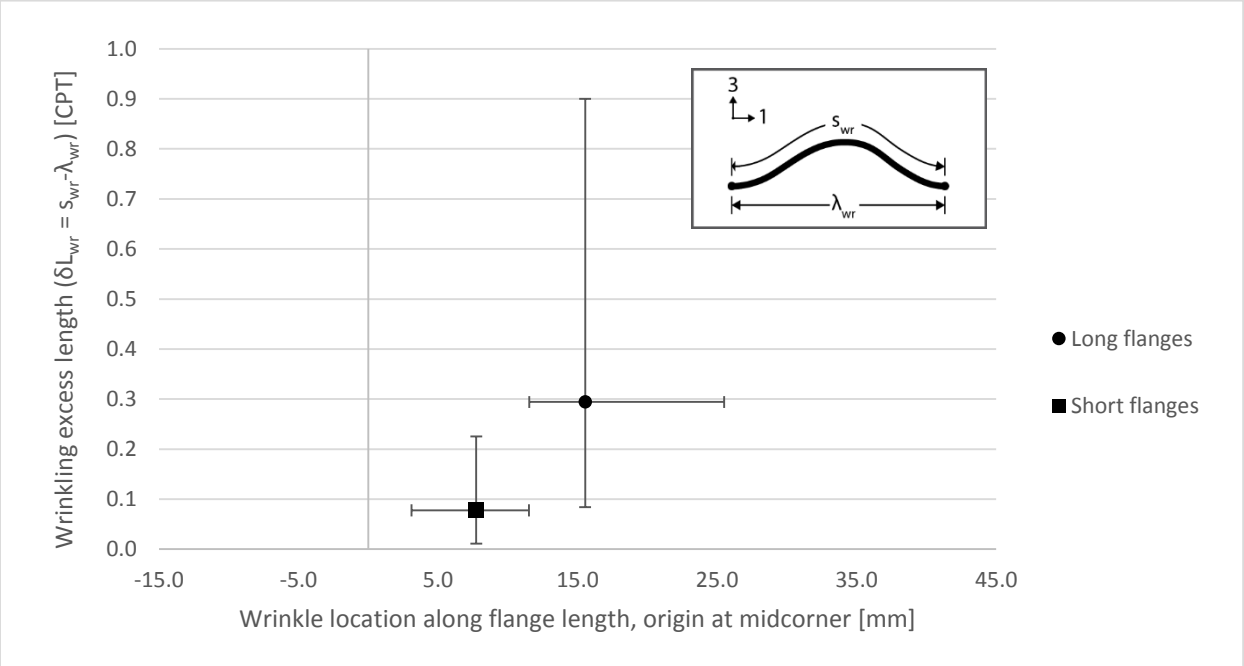

Figure 5-16. Wrinkle severity (trapped excess length) and location for the short and long flanges’ largest wrinkles. Error bars represent the range of the data.

The effects of flange length can be seen by comparing the number, the location, and the severity of wrinkles. For each wrinkled short flange, the corresponding long flange showed an equal or greater number of wrinkles (Table 5-2). Figure 5-16 compares the wrinkle severity – in terms of trapped length in the flange, introduced in Section 3.1.2.1 – and the wrinkle location for the largest wrinkles found in long and short flanges. The short flange wrinkles were always less severe than longer flanges’ largest wrinkles and the position of short flange wrinkles were nearer to the mid-corner.

The absolute wrinkle heights were similar for the 16-ply, 32-ply, and 64-ply flanges' largest wrinkles (Figure 5-17). However, the wrinkles were proportionately larger for the thin laminate when compared to the laminate thickness. This was true for both long and short flanges.

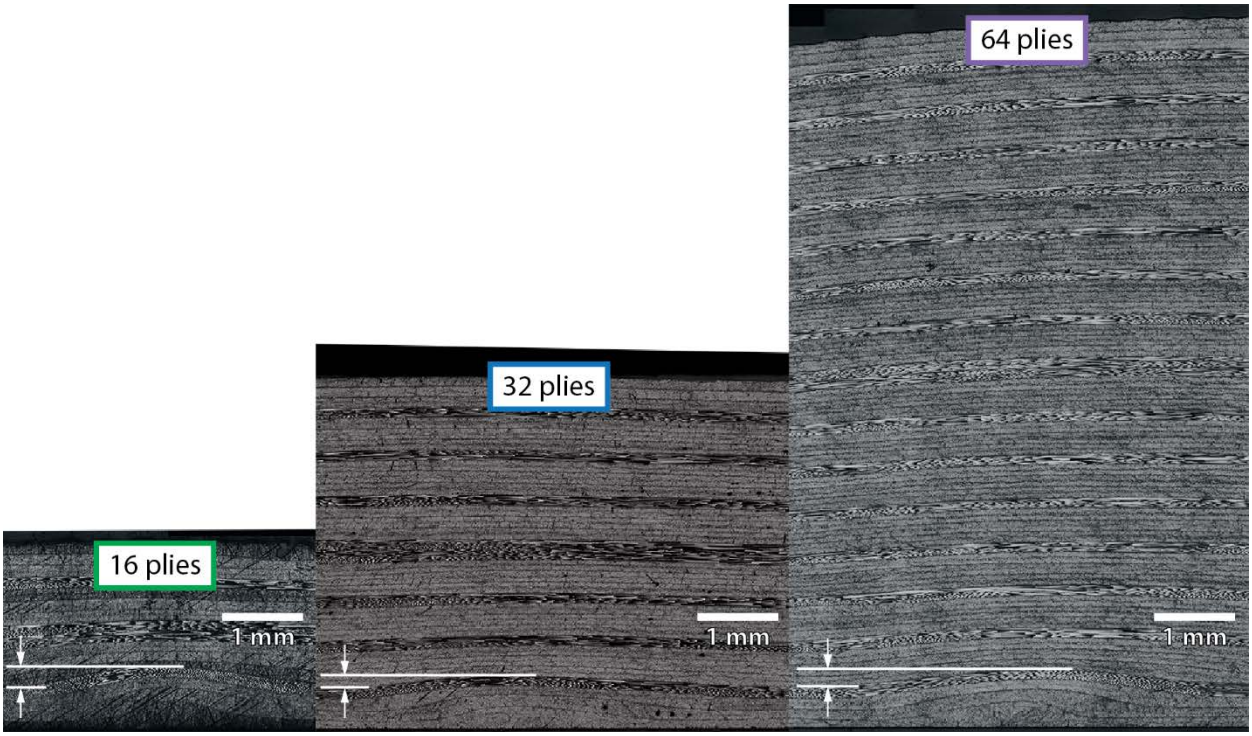

Figure 5-17. Absolute sizes of largest wrinkles found in 16-ply, 32-ply, and 64-ply long flanges. Flanges shown are 'LF-e', 'LF-c1', and 'LF-f'.

Figure 5-18 shows the total excess length trapped as wrinkling for each flange for the 16-ply, 32-ply, and 64-ply flanges. As corroborated by the greater number of wrinkles for the thinner plies and the similar size of maximum wrinkles, the thin flanges show greater excess length trapped as wrinkling than the thicker flanges. The difference is most apparent between the 16-ply and 32-ply flanges.

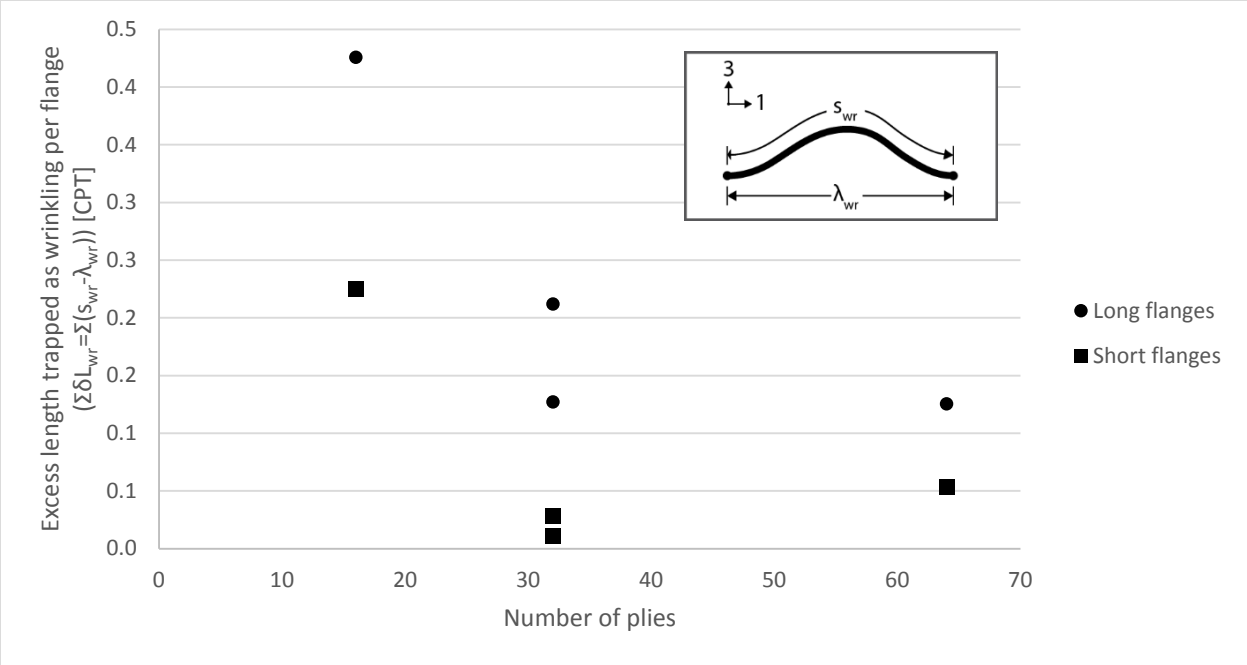

Figure 5-18. Severity of total wrinkling (in terms of excess length trapped within the flange as wrinkling) for 16-ply, 32-ply, and 64-ply flanges.

The forming method had a large impact on the occurrence of wrinkling: the hand lay-up (ply-by-ply) baseline part showed no wrinkling whereas the 30°C drape-formed parts were generally wrinkled (Table 5-1).

With regards to the effect of curing bag tension, it was previously shown that the pleated Nylon-cured wrinkled long flange was the only sample to show an externally visible defect after cure (Table 5-1). Internally, the pleated Nylon-cured long flange's largest wrinkle was significantly more severe than the taut silicone-cured equivalent flanges ('LF-c1' and 'LF-c2'): it was 3 times taller, trapped 6 times more excess length, and was 2.5 times more misaligned. Though the number of wrinkles was approximately the same. The short flanges showed no notable differences between pleated Nylon-cured or taut silicone-cured parts.

5.1.4 Wrinkling and full-ply waviness relationships

Wrinkles and full-ply waviness showed a coupling with regards to occurrence, location, and severity. Table 5-3 tabulates the occurrence of wrinkles, full-ply waviness, and partial-ply waviness in all manufactured flanges.

Table 5-3. Occurrence of wrinkles, full-ply waviness and partial-ply waviness from cross-sectional micrographs after cure.

	Part identifier '*n*'	Process parameters (# of plies, forming temperature, ply sequence, cure bag type)	Internal wrinkles	Full-ply waviness	Partial-ply waviness
Long flanges 'LF-*n*'	a	32ply, HLU, Quasi, Silicone	–	–	•
	b	32ply, 30°C, Quasi, Nylon	•	•	•
	c1	32ply, 30°C, Quasi, Silicone	•	•	•
	c2	32ply, 30°C, Quasi, Silicone	•	•	•
	d	32ply, 70°C, Quasi, Silicone	–	–	•
	e	16ply, 30°C, Quasi, Silicone	•	•	•
	f	64ply, 30°C, Quasi, Silicone	•	•	•
	g	32ply, 30°C, Offset, Silicone	•	•	•
	h	32ply, 70°C, Offset, Silicone	–	•	•
Short flanges 'SF-*n*'	a	32ply, HLU, Quasi, Silicone	–	–	•
	b	32ply, 30°C, Quasi, Nylon	•	•	•
	c1	32ply, 30°C, Quasi, Silicone	•	•	•
	c2	32ply, 30°C, Quasi, Silicone	•	•	•
	d	32ply, 70°C, Quasi, Silicone	–	–	•
	e	16ply, 30°C, Quasi, Silicone	•	•	•
	f	64ply, 30°C, Quasi, Silicone	•	•	•
	g	32ply, 30°C, Offset, Silicone	–	•	•
	h	32ply, 70°C, Offset, Silicone	–	•	•

While partial-ply waviness was present in all flanges, a correlation was seen between wrinkles and full-ply waviness in all flanges, with the exception of *Offset* ply sequence flanges which showed waviness without wrinkling ('LF-h', 'SF-g', and 'SF-h') (Table 5-3). For the wrinkled flanges, the cross-sectional micrographs indicated that wrinkles and full-ply waviness were located in the same regions and in the same 0° plies. The severities of wrinkling and full-ply

waviness are compared below with respect to span length (Figure 5-19) and misalignment angles (Figure 5-20).

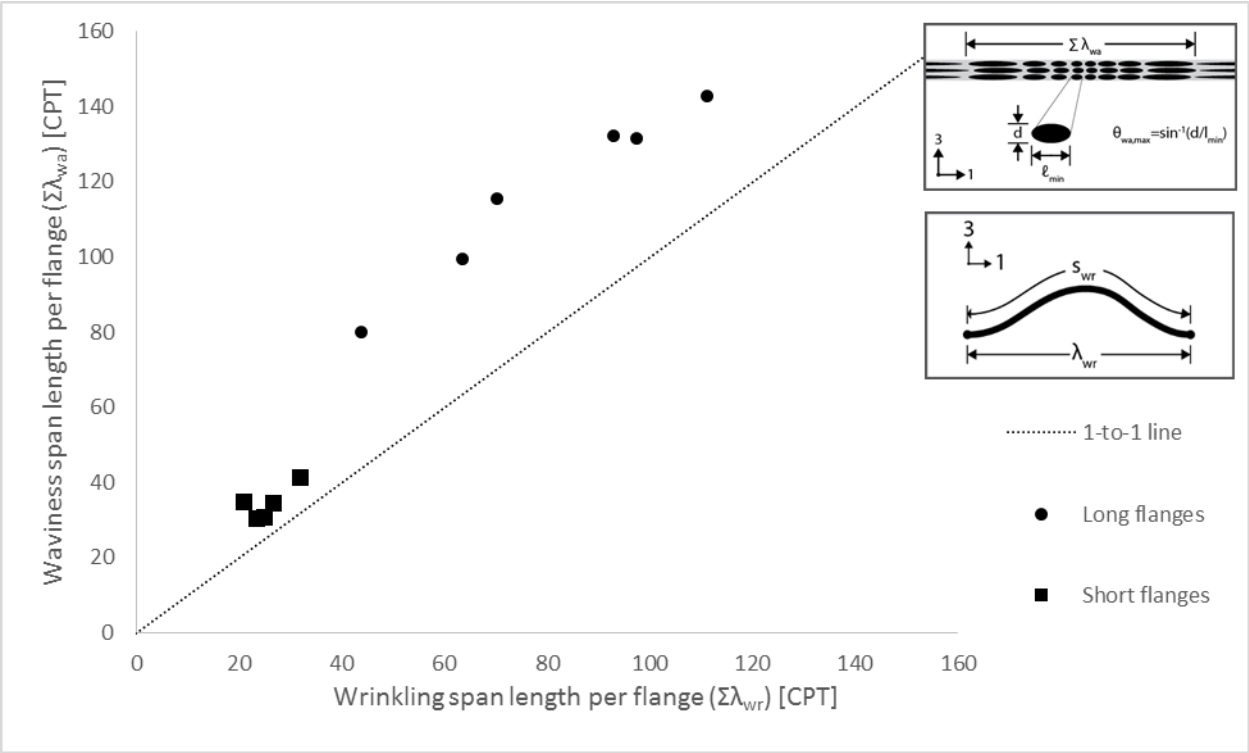

Figure 5-19. Total wrinkle and full-ply waviness span lengths.

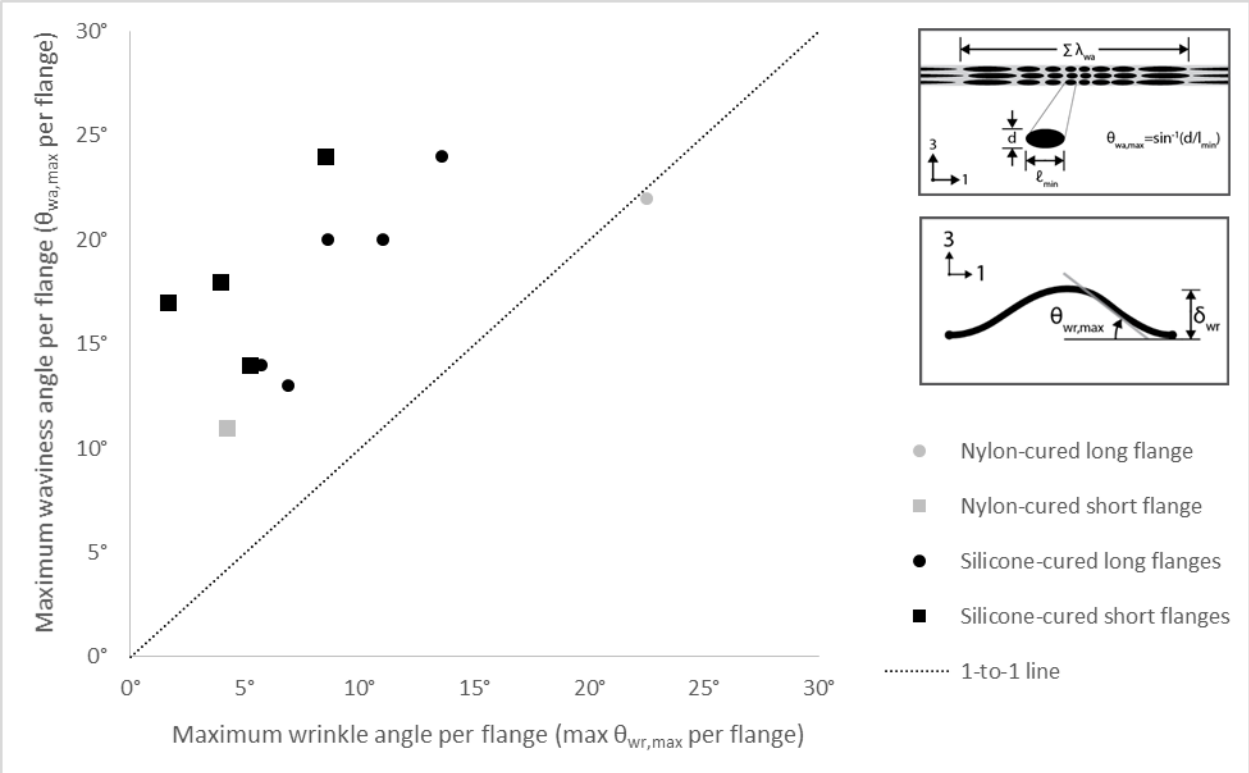

Figure 5-20. Maximum misalignment angles for wrinkling and full-ply waviness of wrinkled flanges.

Total waviness span lengths were greater than total wrinkling span lengths for all parts (Figure 5-19). The long flanges show greater absolute span lengths for wrinkling and waviness than the short flanges. Given that each wrinkled 0° ply shows full-ply waviness over the entire wrinkle span and greater, this indicates that the post-cure wrinkles have a wave component with the waves acting over a slightly longer distance.

Similar trends with regards to misalignment angles were seen (Figure 5-20). While the pleated Nylon-cured long flange showed approximately equal maximum wrinkling and waviness misalignment angles, the taut silicone-cured flanges had significantly greater waviness angles.

Waviness severity with respect to excess length could not be accurately determined from cross-sectional micrographs. A method of reconstructing full-ply waviness paths from cross-sectional ellipse aspect ratios (‘waviness path reconstruction’ method explained in Appendix B.5) was evaluated to address this but did not provide reliable results. Thus, an in-plane micrograph was

taken as a verification step for the visualization of the full-ply waviness severity of the 'LF-c1' flange's wrinkle region (Appendix B.3. and Appendix C.7). The resulting excess length trapped as waviness was measured as 0.62 CPT where the excess length trapped as wrinkling was 0.13 CPT. Hence, the severity of waviness in the 'LF-c1' flange with regards to excess length was 5 times greater than the severity of wrinkling. This result further confirms the greater severity of waviness seen in the angular misalignment comparison (Figure 5-20).

5.1.5 Waviness in *Offset* ply sequence flanges

While waviness in *Quasi* flanges was always accompanied by wrinkling, waviness in the *Offset* flanges was independent of wrinkling (Table 5-3). *Offset* ply sequence flanges showed no wrinkling after cure in the mould-side 0° ply (ply #1 of 32). The only wrinkle was in the subsequent 0° ply (ply #5 of 32) for the 30°C-formed long flange. The effect of ply sequence on maximum full-ply waviness angles is shown in Figure 5-21 below.

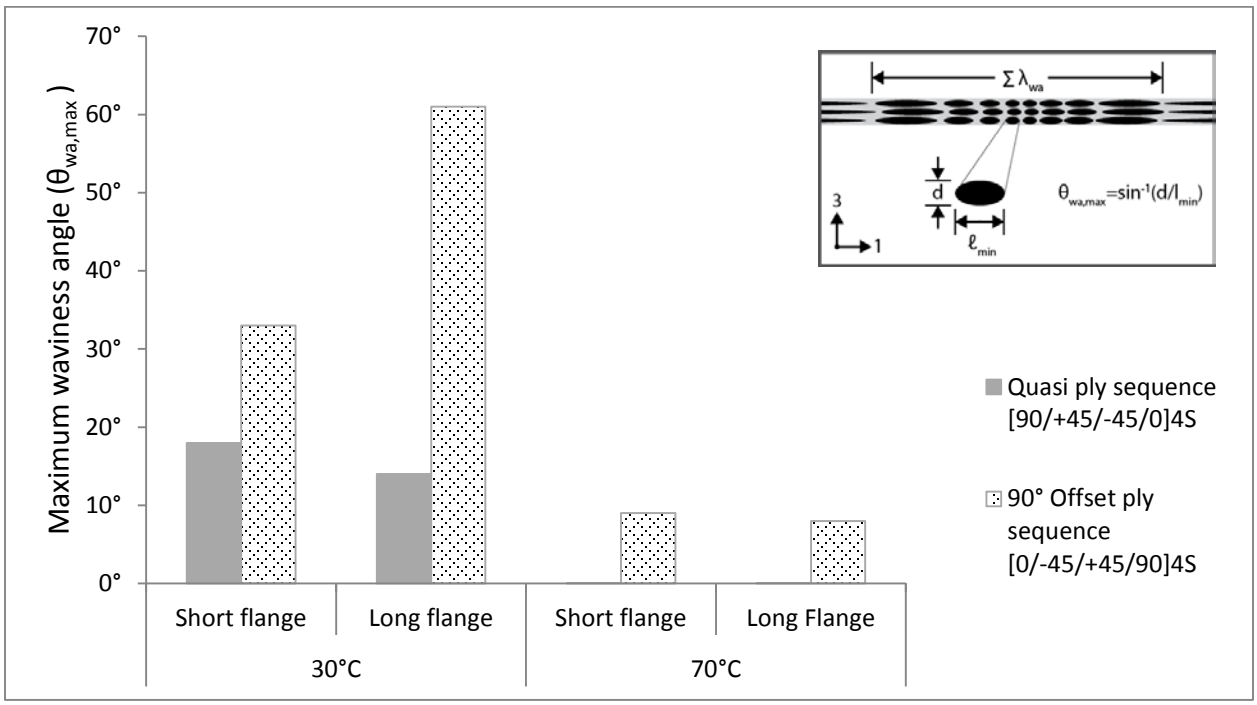

Figure 5-21. Maximum full-ply waviness angle for *Quasi* and *Offset* ply sequences for plies #3 and #1, respectively.

All *Offset* ply sequence flanges showed waviness in their mould-side ply (ply #1 overall). Neither ply sequence showed any wrinkling when formed at 70°C (Table 5-3), though only the *Offset* ply sequence showed waviness, albeit minor. The 30°C-formed *Offset* flanges exhibited significantly greater waviness than the *Quasi* flanges.

5.2 Termination profiles

Individual ply terminations were examined for each ply orientation. Flange terminations (the entire laminate) were examined and quantified using the methodology presented in Section 4.2.2.2. The fibre misalignments severity is compared to the missing lengths of certain plies.

5.2.1 Individual ply terminations

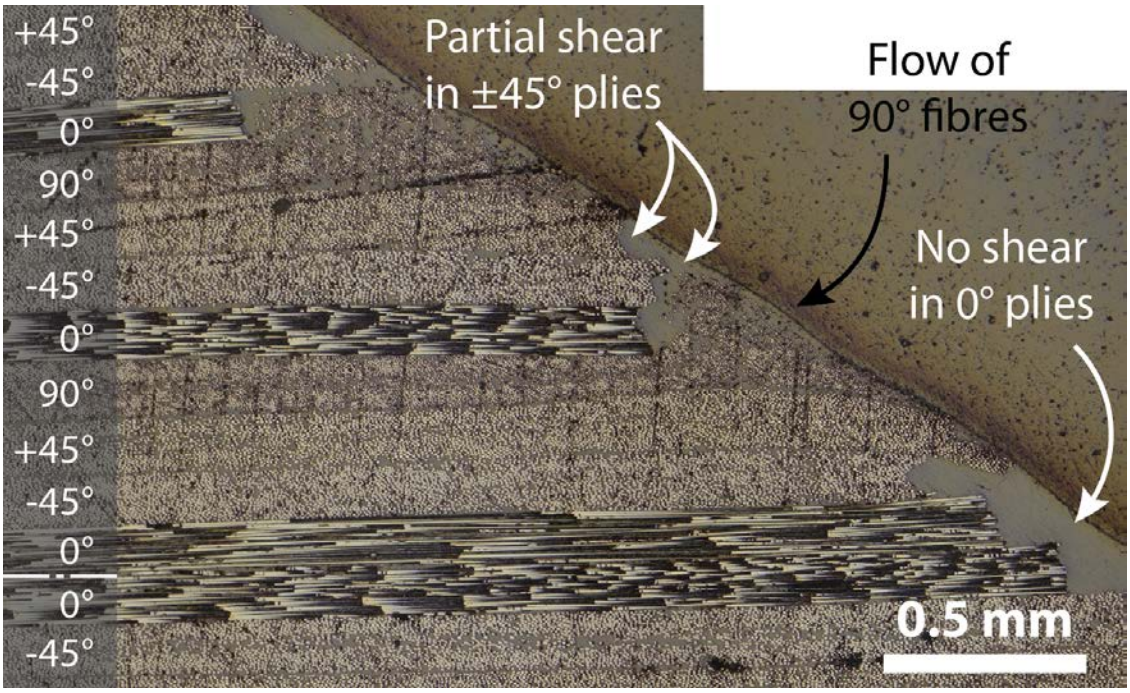

Figure 5-22. Typical ply terminations for 0°, ±45°, and 90° plies. *Quasi* ply sequence is shown.

Individual ply terminations, typical of all flanges are shown in Figure 5-22. It can be seen that 0° plies have not sheared, though they have slipped with respect to neighbouring plies. 0° plies showed nearly square ends whereas the 90° plies showed significant flow into empty cavities. ±45° plies showed varying levels of shear. These characteristics were seen in all flanges.

5.2.2 Laminate terminations and termination profiles

5.2.2.1 End consolidation effects

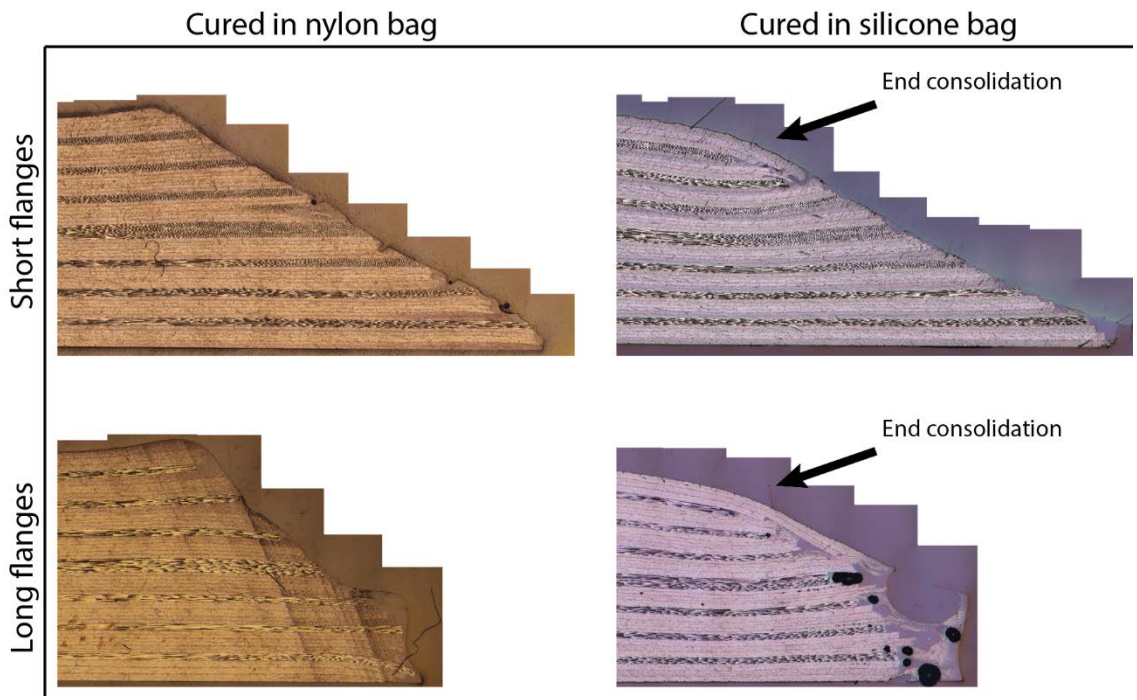

Figure 5-23. Typical flange terminations of pleated Nylon-cured and taut Silicone-cured short and long flanges. (Samples shown are SF-a (top left), LF-a (bottom left), SF-c1 (top right), and LF-c1 (bottom right).

Typical terminations of taut silicone bag-cured flanges are shown in Figure 5-23 in comparison to the pleated Nylon-cured flanges. Consolidation intensification at the ends, was seen in the flanges cured using a taut silicone bag. The pleated Nylon bag-cured flanges showed the reverse trend where the plies appeared to slightly increase in thickness at the end of the flange. This prompted the use of the 'end consolidation correction method' in order to account for the effect of consolidation on profile angles (detailed in Section 4.2.2.2).

5.2.2.2 Laminate shifting

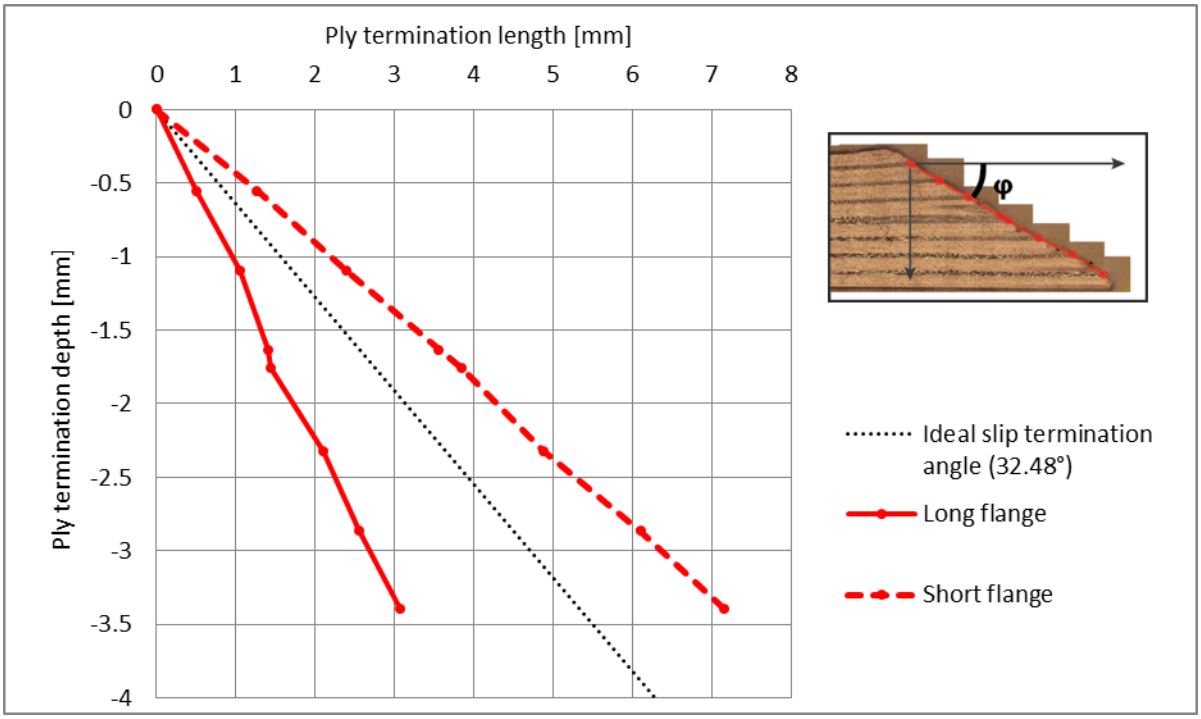

Figure 5-24. Typical individual flange termination profiles for long and short flanges (Shown for 'LF-d' and 'SF-d').

The termination were quantified from the 0° plies' terminations and a typical part's individual flanges is plotted in Figure 5-24 (the short flanges are mirrored about the vertical axis). The short flanges (dashed lines) showed shallower slopes than the long flange (solid lines) in all parts. When comparing a particular test's long and short flanges, they appeared to show similar but opposite offsets with respect to the ideal slip line. Though, the degree of this offset showed no correlation with respect to any input parameter, including the hand lay-up baseline part.

The effects of laminate shifting have been removed by averaging the short flange and long flange termination profiles, shown below (detailed in Section 4.2.2.4.3).

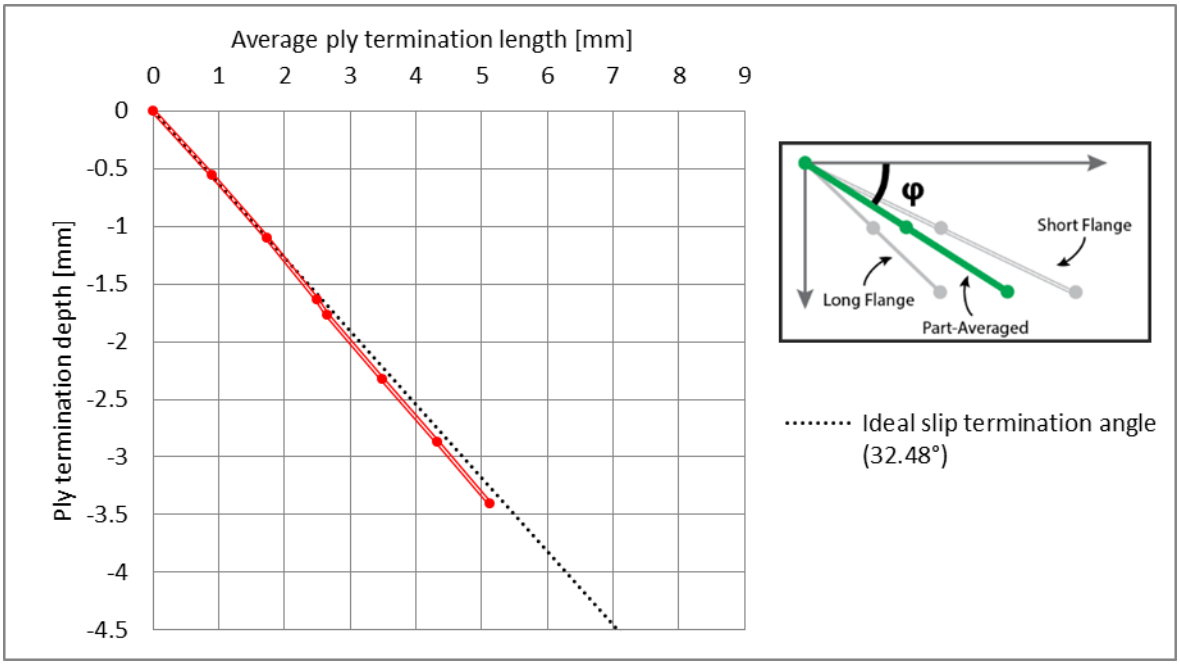

Figure 5-25. Average termination profile for a non-wrinkled and non-wavy silicone cured part. ('Part d' is shown).

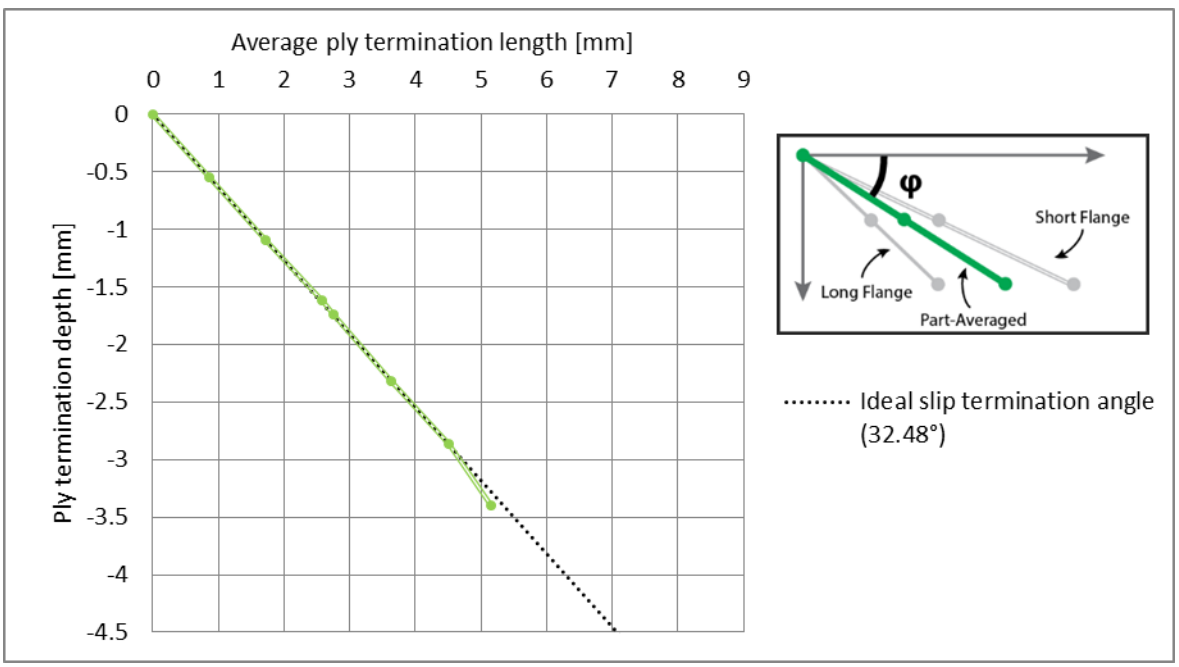

Figure 5-26. Average termination profile for a pleated Nylon-cured and wrinkled part ('Part b' is shown).

Figure 5-25 and Figure 5-26 show the average curves for a defect-free taut silicone-cured part and the wrinkled pleated Nylon-cured part, respectively. The ideal slip termination angle is illustrated for comparison (introduced in Section 3.1.2.1).

The overall curves are straighter and more similar to the ideal slip angle. The taut silicone-cured 'test-averaged' curves undershot the ideal slip line by an average of 1.2° (Figure 5-25). The Nylon-cured flanges showed a close alignment with the 32.48° line.

5.2.3 Effect of fibre misalignments on flange termination profiles

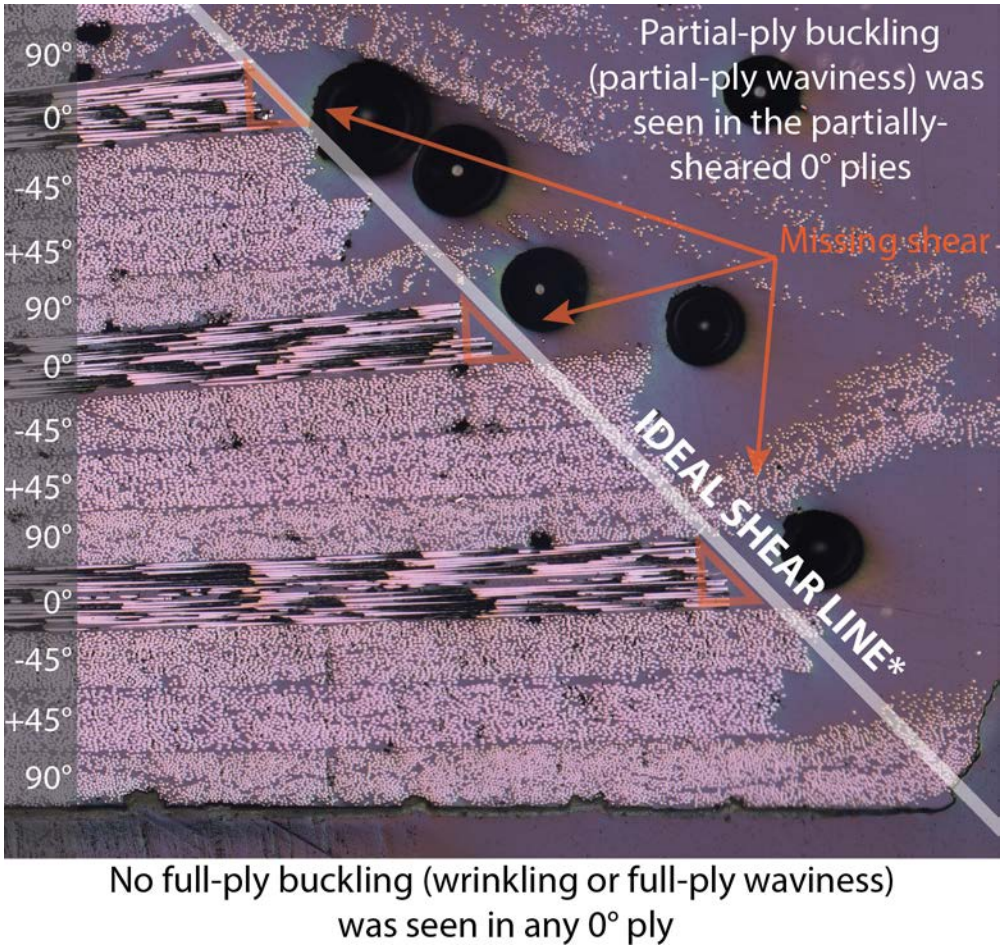

Figure 5-27. Termination of a part with no full-ply buckling. Ideal shear line adjusted for laminate shifting. ('LF-d' is shown)

A portion of a flange termination is shown for a typical flange that contained no wrinkling or full-ply waviness is shown in Figure 5-27. It did, however, contain partial-ply waviness in all 0° plies which was also the case for all flanges. Evidence of partial shear in the 0° plies can be seen.

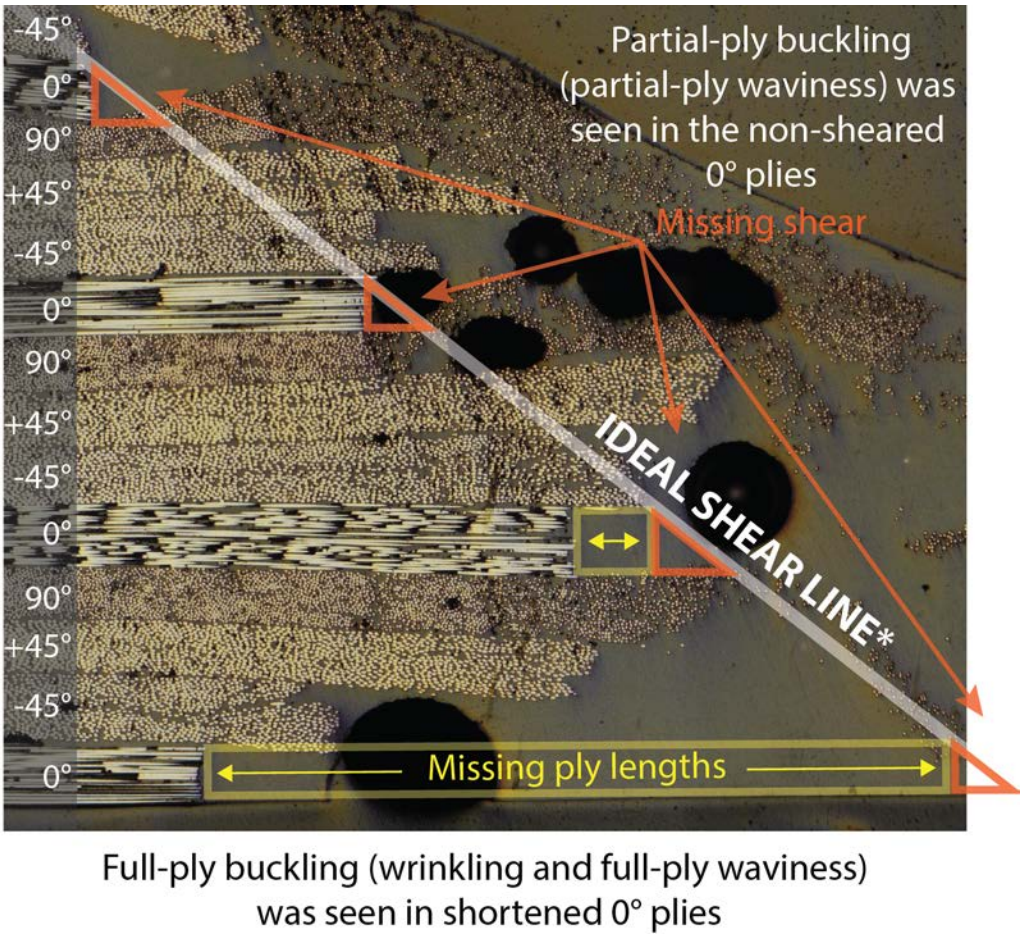

Figure 5-28. Flange termination of a part with full-ply buckling. Ideal shear line is adjusted for laminate shifting. ('LF-g' is shown)

Figure 5-28 shows the lower portion of a flange termination for a flange with significant wrinkling and full-ply waviness. Missing ply lengths can be seen in the heavily misaligned plies. As with all flanges, the non-sheared 0° ply ends corresponded with the presence of partial-ply waviness.

Flange termination images were quantified for parts with full-ply misalignments and are plotted in the figures that follow.

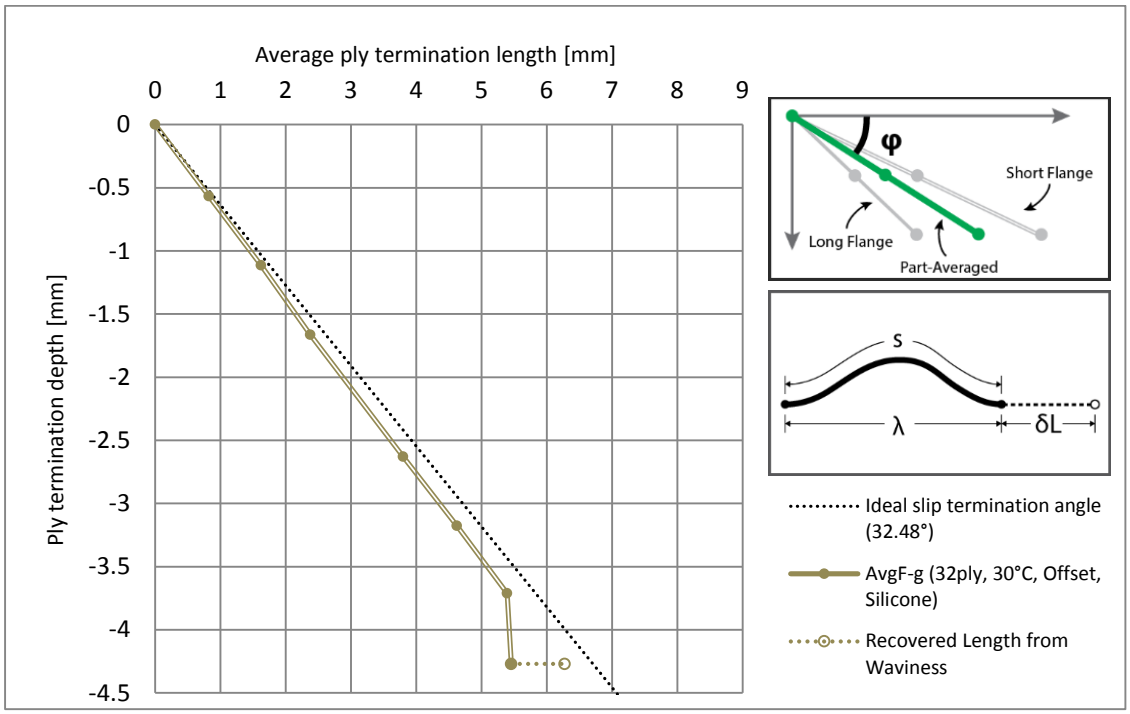

Figure 5-29. Average termination profile with added recovered length from wrinkling and waviness in tail. 'Part g' is shown.

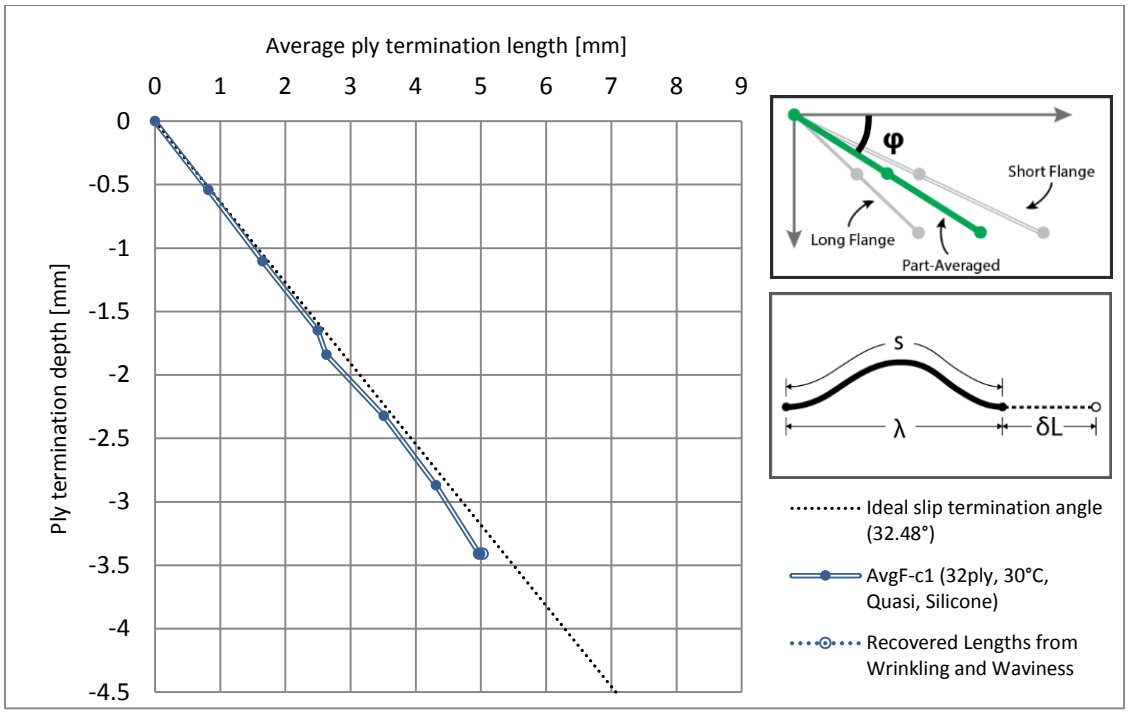

Figure 5-30. Averaged termination profile with added recovered length from wrinkling and waviness in tail. 'Part c1' is shown.

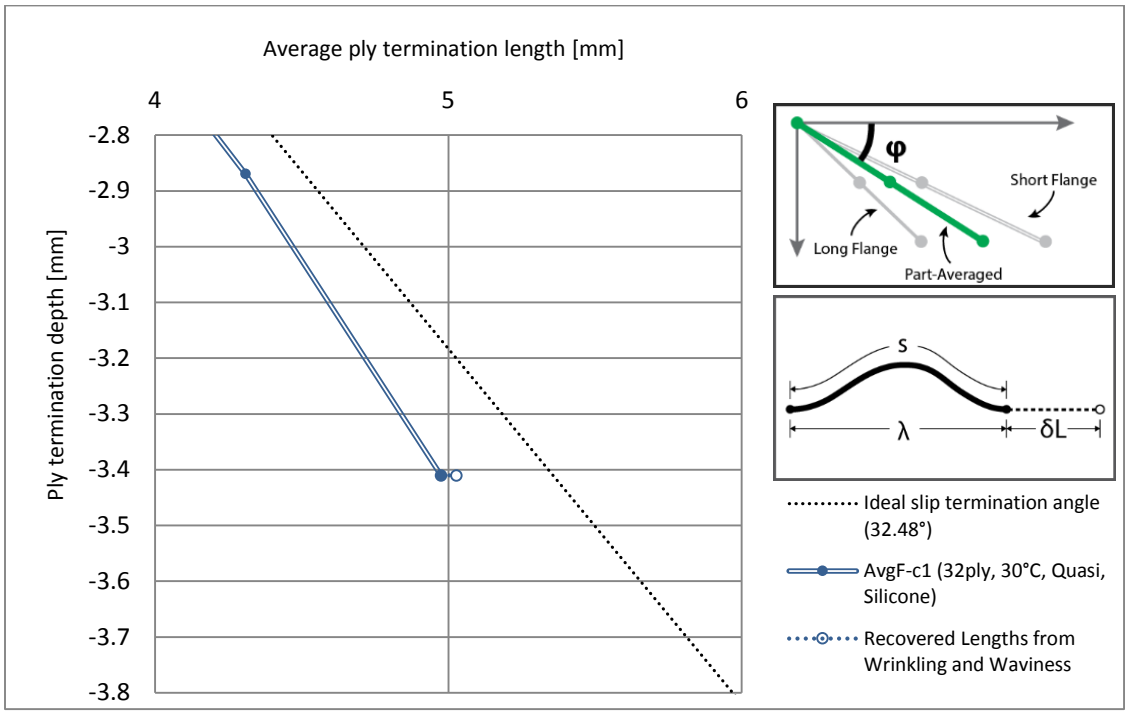

Figure 5-31. Close-up of Figure 5-30.

If the flange termination profile is linear and sloping along the ideal slip line, one can assume that all plies have slipped perfectly within the laminate in both the short and long flanges (Figure 5-25). However, if the flange's termination angle is non-linear, it suggests that there has been imperfect slip within the laminate and a portion of the ply remains within the laminate. This trapped length has been shown to take on the form of wrinkling, full-ply waviness, or both. Parts with prominent wrinkling or waviness exhibited a 'tail'-like feature in the laminate termination profile: a sudden increase in slope at the mould-side (Figure 5-29). The plies involved correlated with wrinkled and wavy plies, suggesting that the tail was the result of the end-to-end shortening of the ply due of fibre misalignment.

This correlation was tested by adding the trapped excess length that was measured from wrinkles and waviness to the corresponding ply's termination x-position. Two samples were chosen to for in-plane microscopy: '*LF-c1*' and '*LF-g*' (method detailed in Section B.3). The excess lengths for wrinkling and waviness are added to the mould-side ply termination length in Figure 5-29, Figure 5-30, and Figure 5-31.

The most significant tail feature was seen in the 30°C-formed *Offset* ply sequence long flange ('*LF-g*') which showed severe waviness in the mould-side 0° ply (ply #1 overall) without wrinkling after cure. The trapped length due to waviness in the long flange was determined to be 1.64 mm (11.9 CPT) by in-plane micrograph measurements. Waviness in the short flange was not measurable due to the waviness' location within the radius, but appears to be of little consequence.

The same process was applied to the 30°C-formed *Quasi* long flange '*LF-c1*' which showed excess length as both wrinkling (0.017 mm or 0.13 CPT) and waviness (0.084 mm, or 0.62 CPT). In this case, the total trapped length (0.10 mm or 0.75 CPT) was one order of magnitude less than that of the heavily wavy 'LF-8' sample. Figure 5-30 and Figure 5-31 show the result of the recovered length from waviness and wrinkling.

5.3 Thickness profiles

Part thickness profiles were measured from micrographs and plotted in the sections below (detailed in Section 4.2.2.2). They are analyzed in terms of corner thinning and as proxies for the occurrence of wrinkles.

5.3.1 Corner thinning

Typical short flange normalized thickness profiles are shown for the pleated Nylon and taut silicone cured parts in the figure below where the origin is located mid-corner and the flange side is positively oriented (Figure 5-32).

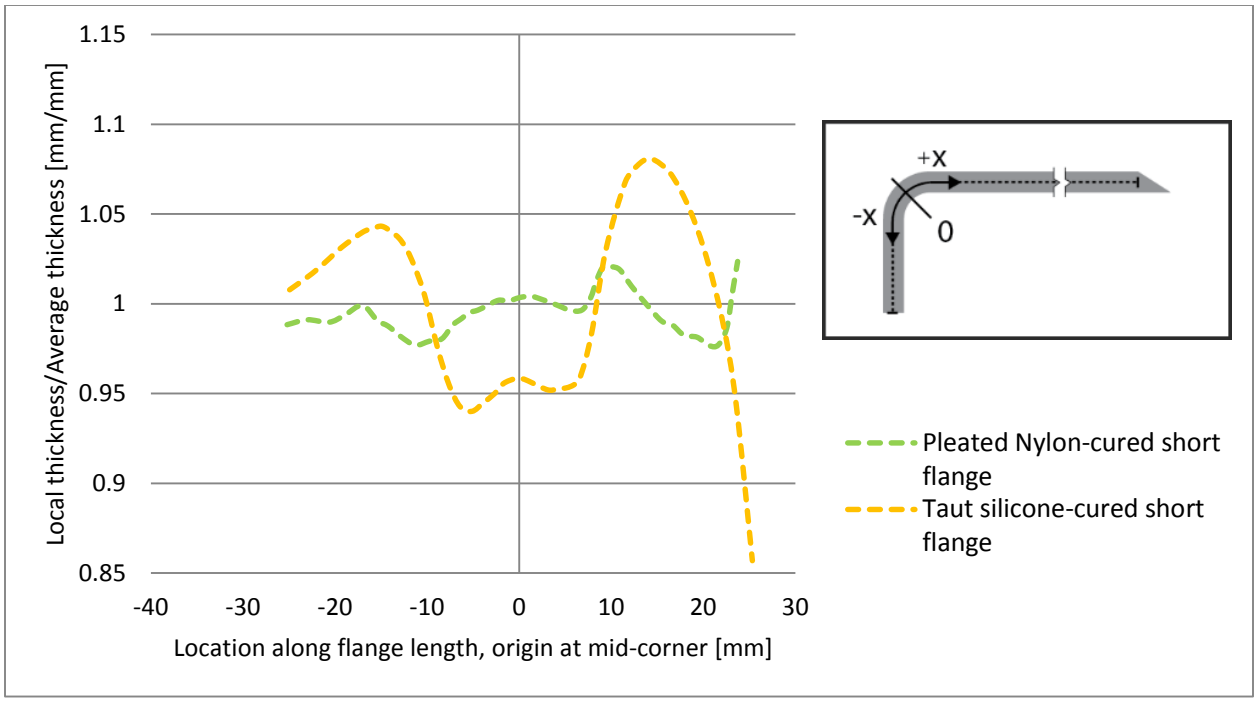

Figure 5-32. Short flange thickness profiles for pleated Nylon and taut-silicone cured parts. ('Part b' and 'Part a' are shown).

Significant corner thinning flanked by thickening is seen in the taut silicone-cured parts. The pleated Nylon-cured parts showed more uniform profiles over the corner, though the surface roughness was greater than that of the taut silicone-cured parts. Near the flange termination (on right), the silicone-cured flanges thins whereas the Nylon-cured flanges thickens. These trends were observed for both the long and short flanges.

Corner thinning was found to be consistently in the range of a 7-9% reduction from average thickness for all taut silicone flanges, regardless of laminate thickness (16-ply, 32-ply, and 64-ply).

5.3.1.1 Material flow from corner thinning

The silicone-cured flanges were further investigated to determine which of the constituents had migrated from the corners to allow thinning. Fibre volume fraction measurements by binary pixel proportions could not be performed due to the differences in lighting in both images that prevented meaningful colour thresholding in order to separate resin and fibre pixels. As a workaround, the individual ply thicknesses for each ply were measured for a non-wrinkled part in the corner (minimum thickness) and in the adjacent flange region (maximum thickness). The ply thicknesses are plotted with respect to ply orientation in Figure 5-33. Greyscale micrographs are shown for the corresponding regions in Figure 5-34.

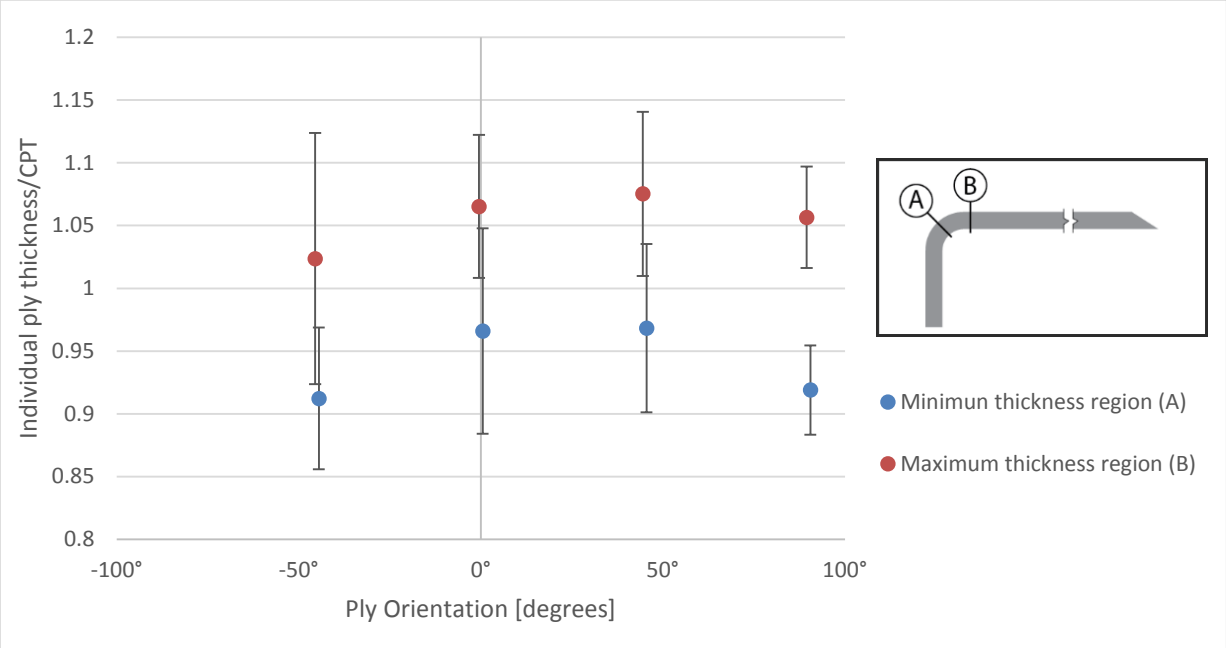

Figure 5-33. Individual ply thicknesses in the maximum and minimum thickness regions versus fibre orientation for a non-wrinkled taut silicone-cured part.

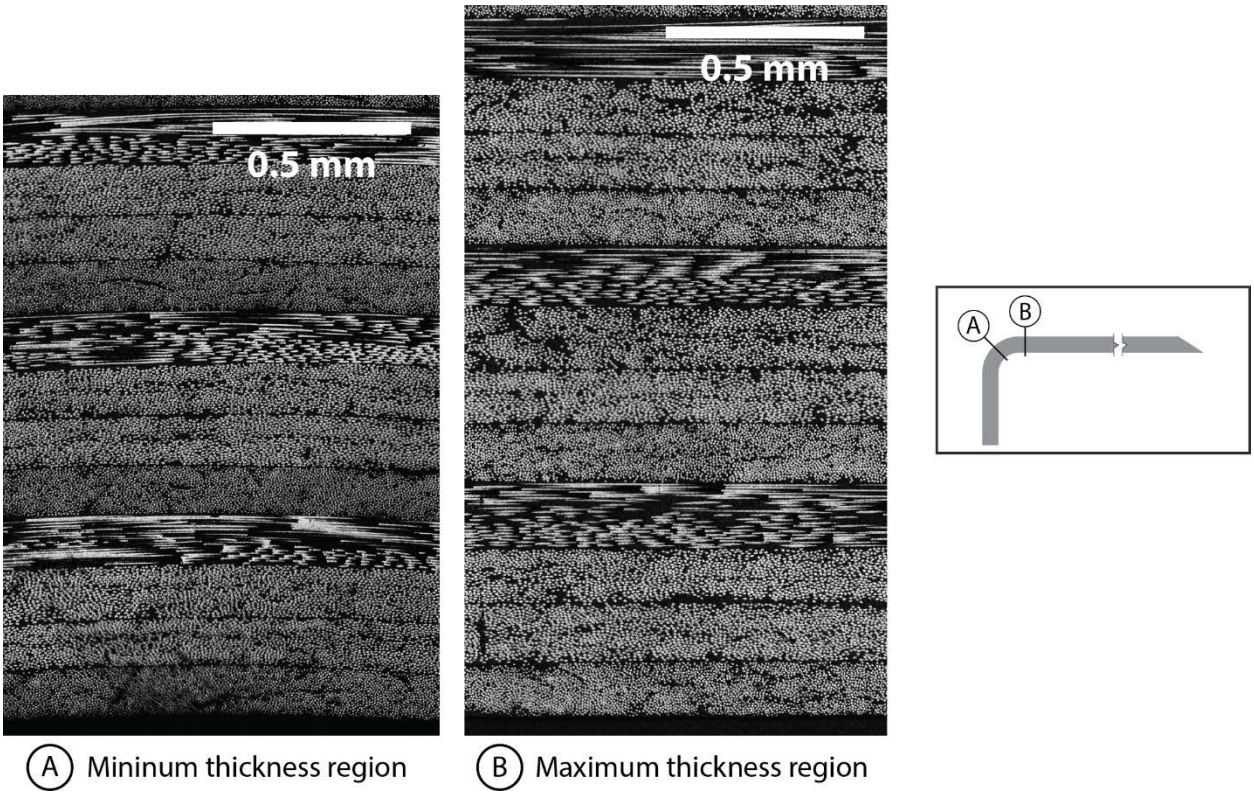

Figure 5-34. Minimum and maximum thickness region micrographs for a non-wrinkled part. 'Part a' is shown.

Each ply orientation saw thickness increases between the corner and the flange region (Figure 5-33). The 0° plies thickness increase indicates that the fibres were not flowing from the corner to the flange and web. A visual inspection of the micrographs suggests that the maximum thickness region features greater resin pooling at the ply interfaces and a lower fibre volume fraction (Figure 5-34).

5.3.2 Wrinkling and thickness profiles in taut silicone-cured long flanges

The relationship between thickness profiles and wrinkles is investigated for the silicone-cured long flanges. Non-wrinkled flange thickness profiles are compared in Figure 5-35 and generalized in Figure 5-36. Wrinkled flanges are compared in Figure 5-37 and generalized in Figure 5-38. Wrinkle locations along the flange have been overlaid onto each curve.

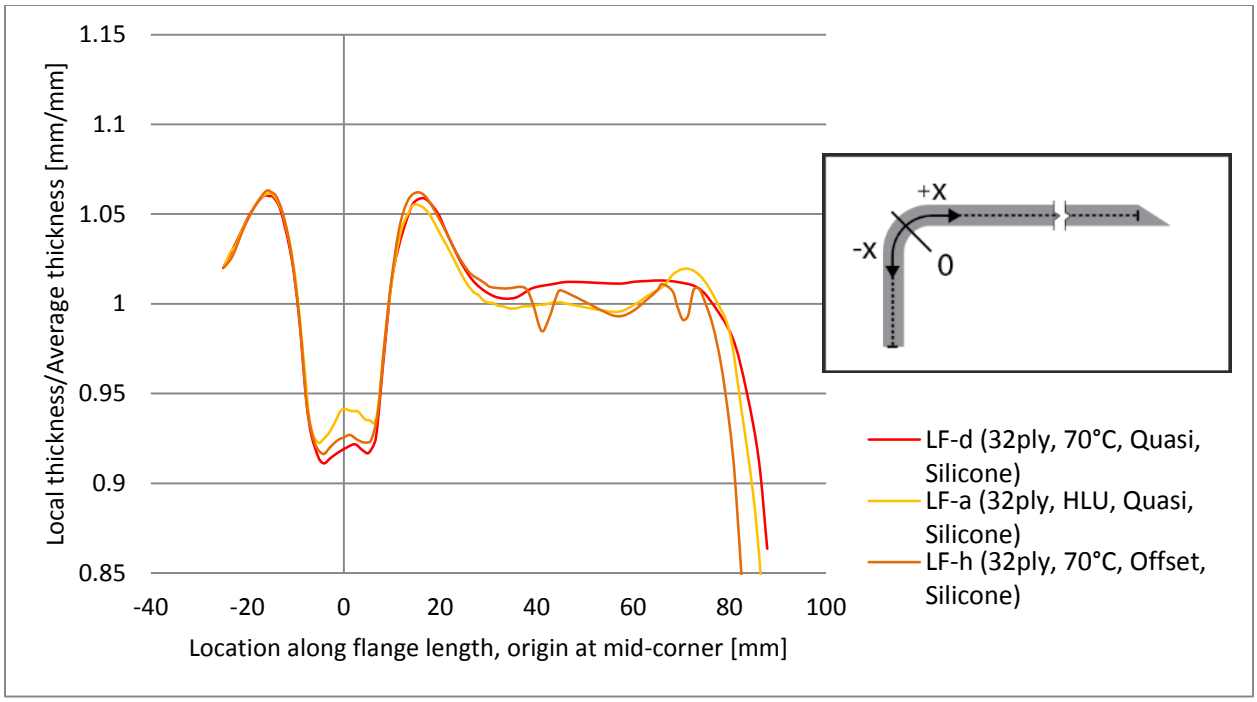

Figure 5-35. Non-wrinkled laminates versus HLU Baseline: Long flanges.

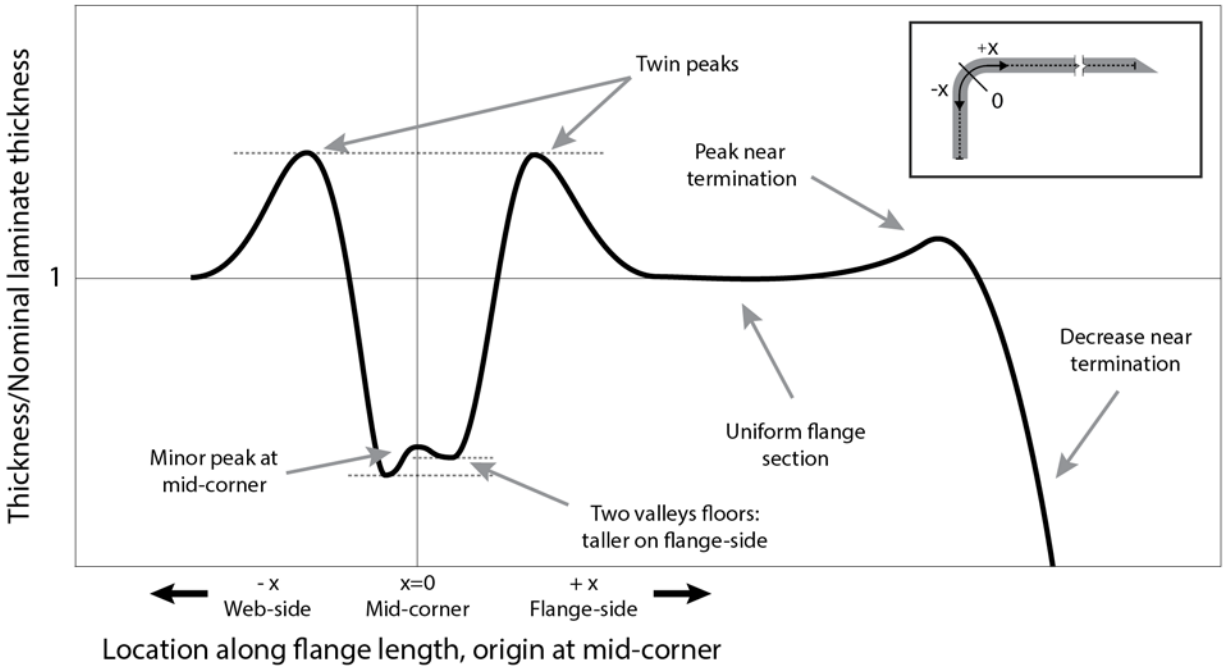

Figure 5-36. Generalized thickness profile of non-wrinkled long flanges cured under a taut silicone bag.

Figure 5-35 compares the non-wrinkled drape-formed long flanges with the hand lay-up control experiment. The corner profiles of the non-wrinkled long flange laminates exhibit common traits which have been generalized in the schematic in Figure 5-36 and summarized below:

- dual valleys in the thinned corner separated by a minor peak;
- equally tall peaks on either side of the corner;
- a region of uniform thickness along the length of the flange which is on the same order as the average laminate thickness;
- an intermediate peak followed by a sharp thickness decrease near the flange termination.

In the flange region, the *Offset* ply sequence flange showed two distinct depressions at 41 mm and at 70 mm. Upon further investigation of the post-manufacturing surface images of the *Offset* flange, two regions where the FEP ply that was used as a low-friction interface between the laminate and the silicone forming bag was noticed to wrinkle appear in the same locations as the depressions in the thickness profile (Figure A.5-9). Hence, the *Offset* flange thickness variations were concluded to be due to manufacturing surface defects, and not due to internal wrinkling caused by forming. They were thus neglected due to their proximity from the corner region.

Wrinkled long flanges are plotted individually in Figure 5-37 and generalized in Figure 5-38. Note that the vertical positions of the wrinkle data on the thickness profile graphs do not relate to the sizes or through-thickness positions of each individual wrinkle; they were given corresponding vertical positions in order to place them onto the part's thickness profile. The purpose of these data is hence to show the wrinkles' positions within the flange.

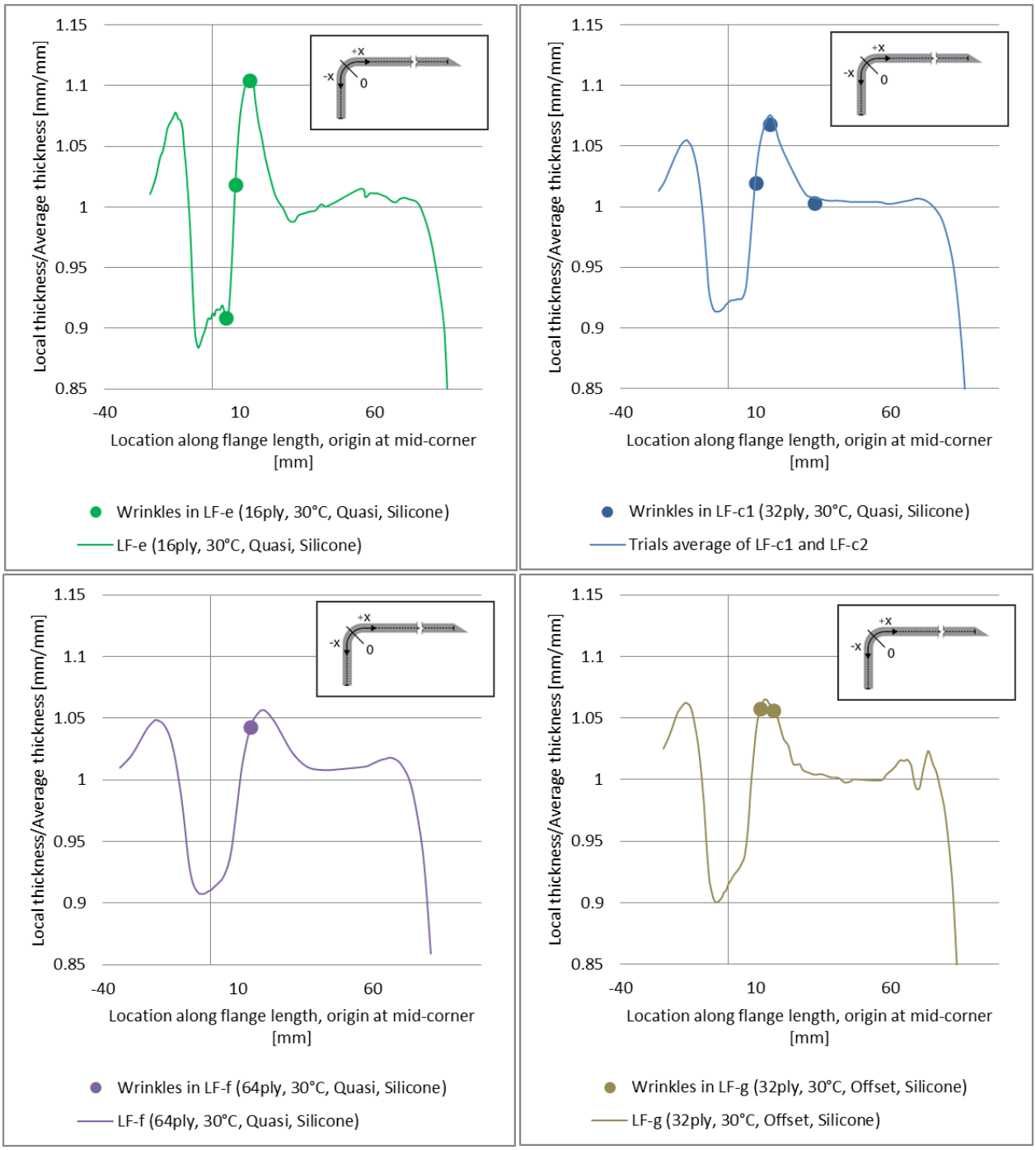

Figure 5-37. Normalized thickness profile of wrinkled long flanges. Wrinkle positions within the flange are overlaid as circles.

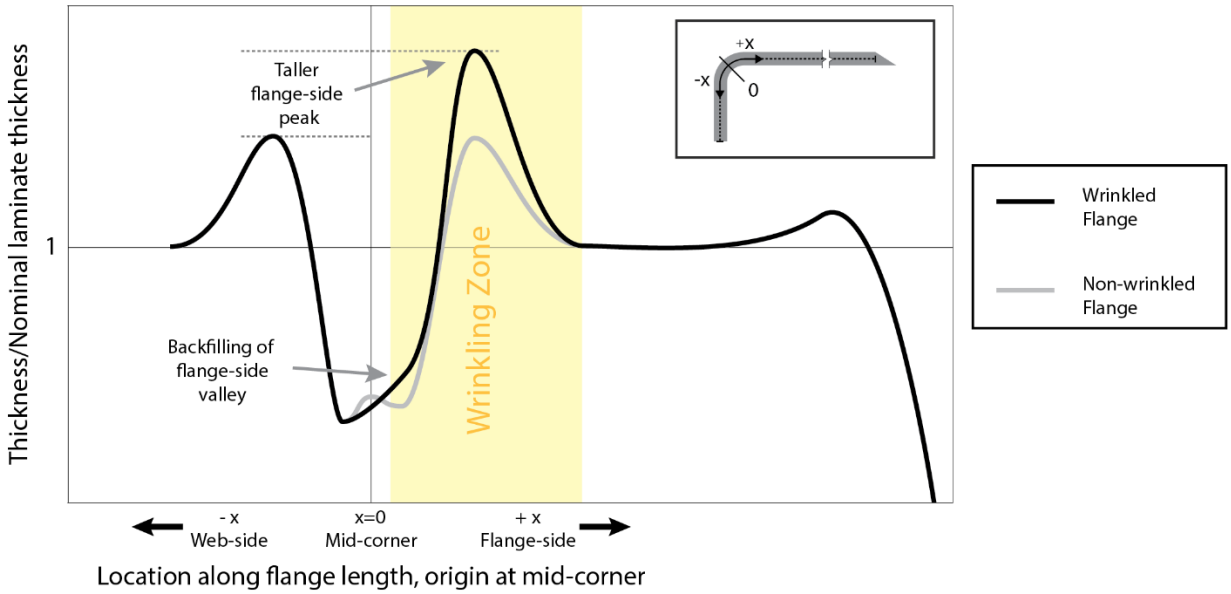

Figure 5-38. Generalized thickness profile of wrinkled long flanges cured under a taut silicone bag showing differences with the non-wrinkled baseline profile.

In most cases, the wrinkling locations appeared to coincide with the location of the flange-side peak near the corner (Figure 5-37). This was not true for all wrinkles, but was true of the largest wrinkle found in each flange. In the cases of the 16-, 32-, and 64-ply laminates (‘LF-e’, ‘LF-c1’, and ‘LF-f’, respectively), the height of the flange-side peak near the corner was measurably greater than that of the web-side peak. In the case of the wrinkled *Offset* ply sequence flange, the peaks were of similar height but the flange-side valley in the corner shows signs of ‘*backfilling*’, where excess material appears to have smoothed out the flange-side valley previously seen in the baseline non-wrinkled thickness profile. Backfilling could also be seen in the other wrinkled flanges to lesser degrees. Farther along the flanges, the flange thicknesses exhibited similar features to the unwrinkled cases. The *Offset* flange showed a significant dip at 71 mm from the mid-corner that could also be attributed to a surface quality defect from bunching of the FEP ply (Figure A.5-8).

Generally speaking, when compared to the non-wrinkled baseline, the wrinkled flanges show either a height increase of the flange-side peak, backfilling of the flange-side valley, or a combination of both (Figure 5-38).

5.3.3 Short flanges

The short flange thickness profiles did not show any distinguishing features for the wrinkled and non-wrinkled flanges. The short flange did not have a regions of uniform thickness between the corner and the termination, unlike in the long flanges. Instead, the flange-side peak and the laminate termination are combined as a single peak feature to the right of the mid-corner.

Chapter 6: Discussion

6.1 Wrinkling and waviness

The effect of input parameters on the occurrence and severity of fibre misalignments, the relationship between wrinkling and waviness, and the effects of ply sequence on fibre misalignment morphology is discussed in the sections that follow.

6.1.1 Wrinkle conversion to full-ply waviness

Three competing mechanisms could explain the disappearance of the externally visible out-of-plane defects after forming: the trapped excess length has been relieved by interply slip, excess material flowed to fill in gaps and smoothen the outer surface, or the wrinkles have been converted to waviness. Given that internal wrinkling was seen in the vicinity of the post-forming defects, the excess length was not completely relieved by interply slip. Neither did plies at the bag-side show any distinct thickness variations that would imply that material migrated to smooth out the surface. And while the excess length may have been somewhat relieved by interply slip much like the plies near the bag-side which appear to have straightened out, severe waviness was present within the wrinkled 0° plies after cure.

From the experimental results, it was not possible to determine if waviness was generated in combination with wrinkles during forming. However, the occurrence of wrinkles without waviness after forming was previously seen in single ply tests performed by Stewart et al. which showed wrinkling to be the preferred buckling mode during forming [30]. Furthermore, for a part whose thickness is significantly less than its width, Euler buckling suggests that it is energetically favourable to buckle in the through-thickness direction. This suggests that only wrinkles were present after forming, and that the post-form wrinkles were converted to full-ply waviness during cure. The conversion mechanism is likely driven by the application of normal force in combination with the increased temperature resulting in a reduction in the resin viscosity allowing for in-plane shear to occur.

The implication that full-ply waviness is only generated from the conversion of wrinkles in a single curvature forming scenario could also explain why these waves are approximately uniform

through the width of the part just as wrinkles were uniform through the width of the part. During the curing process, as the resin viscosity decreases, the wrinkle conversion in one region of the width of the part could have triggered neighbouring fibres within the same ply resulting in ‘unified’ waviness, as seen by the wrinkled and wavy ‘LF-c1’ flange’s in-plane micrograph.

Hence, resulting fibre misalignments are a function of the conditions that led to wrinkling during forming and the resulting conversion to waviness during cure. The impact of process input parameters on the occurrence of wrinkling and waviness are examined in the following section.

6.1.2 Misalignment formation

The wrinkles seen during the forming of charges can be attributed to the force transferred between plies due the requirement to slip with respect to each other in order to conform to different paths. The effect of forming process parameters on the ply-ply interface properties thus control the generation of wrinkles.

During hand lay-up, adjacent plies are decoupled during forming as they were deposited one-by-one. Hence, no wrinkling due to process parameters was expected. This was shown to be the case for both the long and short flanges.

As previously reported by Modin, shorter flanges saw increased part quality over the long flanges during drape forming [22]. The short flange wrinkles were generally less numerous and less severe than in the long flanges. The effect of flange length on inter-ply slip is discussed below.

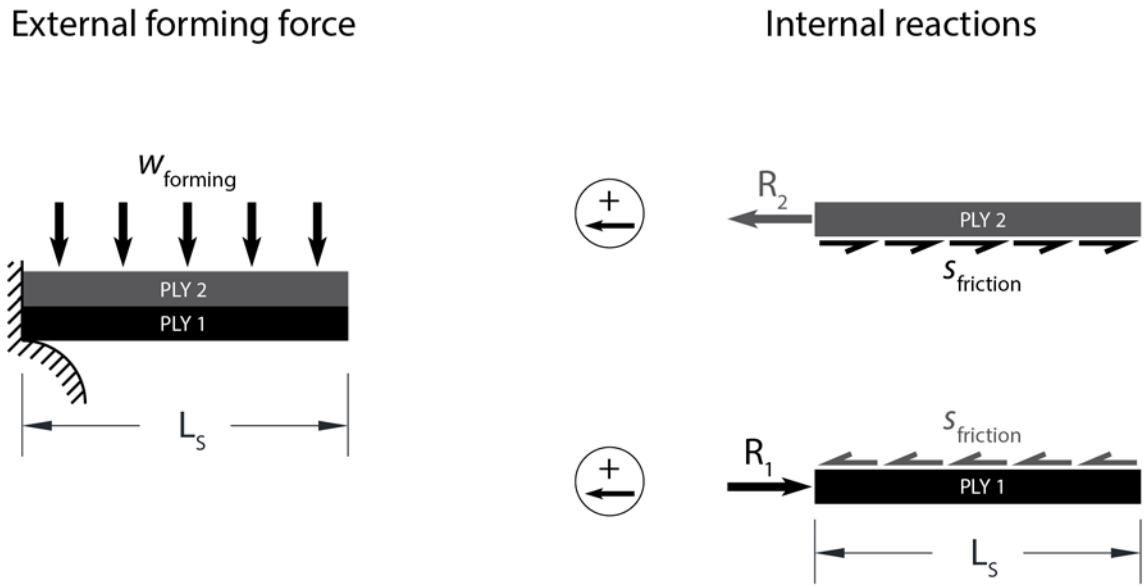

Figure 6-1. Free body diagrams of the forming process (only horizontal forces shown in the figure on the right for the sake of clarity).

Consider two discrete plies loaded in cantilever with a common frictive interface representing the charge forming process (Figure 6-1 on left). A distributed normal force, $w_{forming}$, is applied with the intention to form the laminate over a male radius. The laminate's web end is fixed by the web portion of the laminate. The forming force applies a bending moment to the laminate which results in relative motion between the discrete plies. The interply friction force, $s_{\text{friction}}\left[\frac{\text{N}}{\text{m}}\right]$, acts over the ply contact length L_S [m] opposite to the direction of slip. The rate dependency of the interply friction (resin viscoelasticity) is neglected for the sake of simplicity.

Isolating both plies, a horizontal force balance shows that the top ply undergoes tension and the bottom ply undergoes compression (Figure 6-1 on right). Since the interply friction is a function of contact length, the magnitude of the compressive force is thus directly proportional to the ply interface length as seen in Equation (6–1) below:

$$\begin{aligned} TOP: \quad & R_2 = s_{\text{friction}} \cdot L_S\,, \qquad R_2 > 0 \ \text{(tension)} \\ BOTTOM: \quad & R_1 = s_{\text{friction}} \cdot L_S\,, \qquad R_1 < 0 \ \text{(compression)} \end{aligned} \tag{6–1}$$

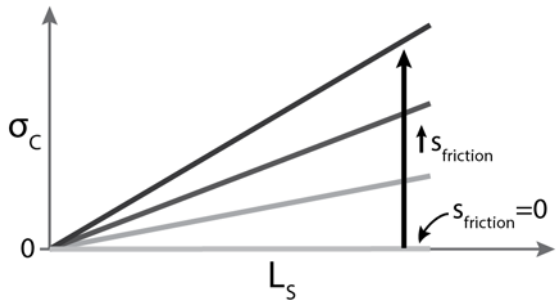

Figure 6-2. Effect of flange length on compressive stress acting on the ply due to frictive forces.

Equation (6–1) also confirms that greater inter-ply friction increases compressive stresses on the bottom ply (Figure 6-2). A frictionless forming operation – where s_{friction} is zero – sees no effect of contact length on compressive stress, which is analogous to the hand lay-up process.
An increase in temperature during charge forming had previously been reported to produce higher quality parts than forming at low temperature [22], [24]. Likewise, the parts manufactured in the current study saw an increase in part quality with increasing temperature for both ply sequences and flange lengths. Therefore, the interply friction force is assumed to decrease with the resin viscosity which was previously reported to decrease by multiple orders of magnitude [31]. Friction slip tests performed on carbon-epoxy prepreg by Larberg & Åkermo saw an increased coefficient of friction with decreasing resin viscosity but it should be noted that these tests were performed at relatively high pressures of the order of 53-120 kPa [27]. The normal pressure experienced by the charge during forming (prior to contact with the mould) are expected to be very low as the laminate readily complies when cantilever loads are applied. The higher pressure results suggests that fibre-fibre interactions due to the migration of low viscosity resin dominated the friction characteristics of the slip test. In contrast, the improved part quality at high temperatures seen in the current study was likely a result of the improved lubrication of the fibres by the resin. Hence, Larberg & Åkermo's conclusions may not be directly applicable to the slip regime in the current study.

If the laminate is treated as a solid beam where plies do not slip, classical bending theory suggests that a thicker beam leads to greater stresses on the bottom face, since the bottom face is farther from the neutral axis. Greater compressive stresses would thus suggest a higher

propensity to buckle with increasing laminate thickness. However, the number of plies was shown to have an inverse effect on the number and severity of wrinkles that were seen in the long flanges (Figure 5-18). This may be attributed to a competing mechanism whereby a thicker laminate provides increased support against buckling in the through-thickness direction. Under this assumption, a well-supported ply in a thick laminate would be more capable of withstanding and relieving the larger compressive stresses whereas an unsupported ply in a thin laminate would be more likely to buckle, even with smaller applied stresses.

The *Offset* ply sequence ($[0/-45/+45/90]_{4S}$) 30°C-formed flanges saw severe unified waviness in the mould-side 0° ply. The excess length from fibre misalignments in the *Offset* 30°C-formed long flange far exceeded those seen in the *Quasi* ply sequence ($[90/+45/-45/0]_{4S}$) flanges. Under the postulation that waves occurred as part of a transformation of wrinkles during cure, this excess length was the result of significant wrinkling that occurred during forming which was later converted to waviness. This assumption is corroborated by the externally visible defects through the thickness of the 'LF-g'part that were seen after forming. Although post-cure wrinkling in the *Offset* ply sequence flanges was of the same order or less than for the *Quasi* ply sequence flanges, waviness was significantly more severe, even presenting itself in the 70°C-formed *Offset* short flange. This could be explained by the relative positions of the 0° plies with respect to the free boundary surface. The *Offset* ply sequence sees a 0° ply at the free surface whereas the first 0° ply is the third ply overall in the *Quasi* ply sequence. Therefore, the free boundary seen by the 0° ply in the *Offset* ply sequence could explain the greater buckling severity that was observed in the *Offset ply* sequence flanges when compared to the corresponding *Quasi* ply sequence flanges.

While it was not possible to determine if the pleated Nylon-cured part featured similar wrinkle characteristics as the corresponding taut silicone-cured parts after forming, it is interesting to note that the pleated Nylon-cured flange contained the largest wrinkle while also exhibiting a maximum waviness misalignment angle that was small when compared to the taut silicone-cured wrinkled flanges. The reduced consolidation pressure applied by the tensionless Nylon bag may have resulted in a smaller proportion of post-form wrinkles converted into waviness.

Overall, it was seen that the waviness severity in most parts was greater than the severity of wrinkling since the maximum misalignment angles due to waviness were approximately twice that of wrinkling (Figure 5-20), the comparative length spans of waviness were comparable to that of wrinkling (Figure 5-19), and the excess length that was attributed to waviness was significantly greater than for wrinkling (by approximately a factor of 5 in the example of 'LF-c1') (Section 5.2.2). Hence, it is possible that the performance knockdown due to waviness was greater than that of wrinkling in the manufactured parts. Though, further testing is required to validate this proposition.

6.1.3 Key takeaways: wrinkling and waviness

- Wrinkles were formed due to the buckling of 0° plies because of compressive stress applied by inter-ply friction loads governed by resin viscosity and flange length.
- The appearance of 'full-ply waviness' (cross section perspective) was related to waviness with a common periodicity through the part's width (in-plane micrograph perspective) and was the result of conversion from post-form wrinkles during cure. Surface photography detected this waviness as linear high-contrast features oriented orthogonally to the surface fibres.
- Surface photography detected 90° surface ply growth due to wrinkling as linear high-contrast features oriented parallel to the surface fibres.
- The appearance of 'partial-ply waviness' was related to waviness without common width-wise periodicity and was the result of the absence of intra-ply shear during forming over corners. Surface photography detected this waviness as distributed high-contrast features.
- Although increasing the number of plies increases the laminate's compressive stress in bending, the added stability provided by the thicker laminate reduced the severity of wrinkling for thicker laminates.
- The free boundary seen by the mould-side 0° ply in the *Offset* ply sequence (ply #1 overall) resulted in more severe fibre misalignments than for the *Quasi* ply sequence whose first 0° ply occurrence (ply #4 overall) is supported on the mold-side by three plies.
- The severity of waviness was greater than that of wrinkling in most parts.

- A smaller proportion of post-form wrinkles were converted to waviness when cured with pleated Nylon bagging.
- The relative influence of the inputs that affected wrinkling during forming are summarized below in Figure 6-3:

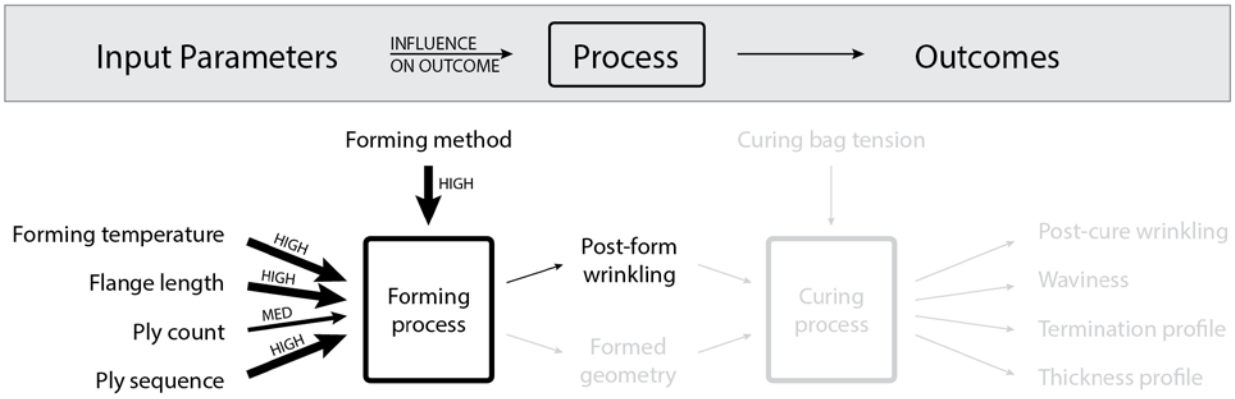

Figure 6-3. Influences of process input parameters on post-forming wrinkling. The light grey portion is assumed to have no effect on the outcome in question.

- The relative influence of the inputs that affected wrinkling and full-ply waviness after cure are summarized in Figure 6-4:

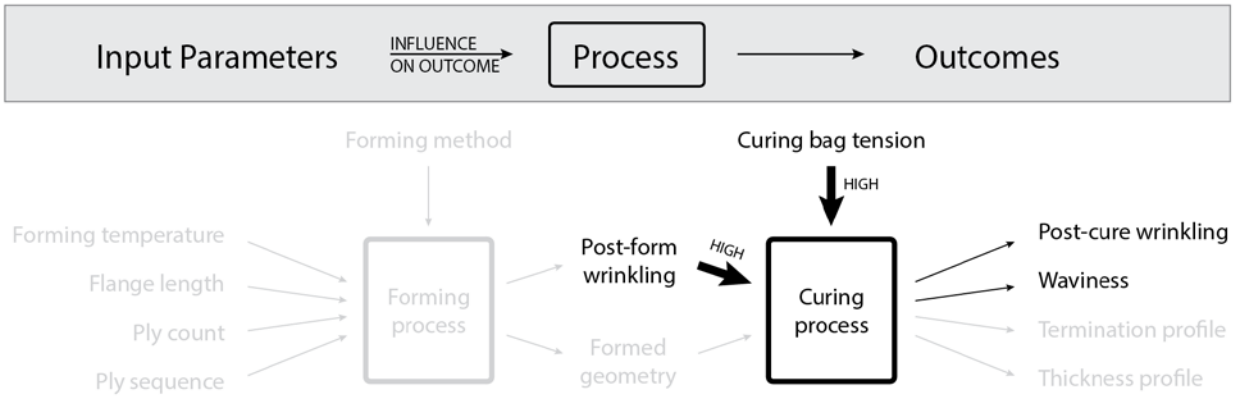

Figure 6-4. Influences of process input parameters on post-cure wrinkling and full-ply waviness. The light grey portion is assumed to have no effect on the outcomes in question.

6.2 Termination profiles and fibre misalignments

Flange terminations were quantified for individual plies and for the laminate, and were related to the fibre misalignments seen in the manufactured parts.

6.2.1 Non-sheared plies and partial-ply waviness

Figure 5-22 showed typical 0° ply terminations whose ends are essentially square, indicating that the 0° plies did not shear, preferring to slip with respect to adjacent plies. This 'staircase' profile was common in all manufactured parts. Partial-ply waviness was also seen in corner regions of all samples. It is plausible that partial-ply waviness is a result of the manifestation of excess length within the ply due to the no shear condition since the top and bottom surfaces are expected to conform to different path lengths.

As previously calculated, the maximum excess length due to a non-sheared ply is 0 CPT at the top surface, linearly increasing to 1.57 CPT at the bottom surface. Although the magnitude of the excess length within partial-ply waviness zones could not be determined experimentally, the partial-ply waviness' gradient appearance – increasing towards the bottom surface – suggests that the absence of shear during forming is a plausible explanation for partial-ply waviness. Although the calculated magnitude of partial-ply waviness may appear negligible at first glance, it is important to note that it is greater than the excess length of individual wrinkles observed in this study which were on the order of 0.01 to 1.06 CPT.

In addition, the absence of intra-ply shear during the forming process validates the linear forming slip rate seen at the ply-ply interface that was determined on the no-shear condition (Section 3.1.2.1.2).

6.2.2 Laminate termination profiles and full-ply buckling

6.2.2.1 Laminate slip during cure

The flange termination profiles for the manufactured C-channels were shown to have approximately equal and opposite angular deviations from the expected ideal profile angle for the long and short flanges. This implies that the laminate shifted towards the long flange during cure, since the effect was noticed in all parts including the hand-layup baseline. Once this effect was accounted for by averaging the long and short flange profiles, the average termination profiles showed good agreement with the ideal slip termination angle that was previously determined in Section 3.1.2.2.2. Since the flange terminations angles were greater than the ideal slip angle, it suggests that plies slip during cure in order to relieve excess length as consolidation occurs, suggesting that the 'ideal slip compaction' assumption from Section 3.1.2.2.2 is a better prediction than the 'no slip compaction' assumption from Section 3.1.2.2.1.

The Nylon-cured part's termination profile showed the best agreement with the theoretical ideal slip termination angle whereas the silicone-cured parts consistently overshot the ideal termination angle by approximately 1.2°. The silicone-cured parts experienced significant corner thinning which may have reduced the path length over the corner for plies closest to the bag. This would have the effect of steepening the test-averaged termination profiles which could explain the higher termination angle.

6.2.2.2 Excess length recovery

The plausibility of relating the missing length seen at the flange termination to the severity of full-ply fibre misalignments was shown by rectifying the 'tail' features with the excess length measured from wrinkling and full-ply waviness in the ply. However, the recovered length that was measured from wrinkling and full-ply waviness did not add up to the entire missing length implying that a small quantity of excess length remained unaccounted for.

The effectiveness of this method decreased when missing lengths were small. Particularly, if they were on the order of the missing length attributed to partial-ply waviness (1.57 CPT), which was the case for 'Part c1'. Given significantly large misalignments, as in 'Part g', this method

could potentially be expanded to provide more information on wrinkles and waviness trapped within a particular part.

The success of the excess length recovery for full-ply buckled plies in combination with the gradient appearance of partial ply waviness as it relates to the non-sheared ply terminations found in all flanges supports the framework proposed in Figure 3-7.

6.2.3 Key takeaways: termination profiles

- Partial-ply waviness occurred in conjunction with non-sheared ply terminations indicating that it was caused by the lack of intra-ply shear.
- All laminates showed termination angles that were within +2° of the ideal termination angle after cure, confirming the assumption that plies slip in order to relieve excess length as consolidation occurs during cure (ie, 'ideal slip compaction' assumption from Section 3.1.2.2.2).
- The part cured in pleated Nylon showed the best agreement with the ideal slip line, likely due to the absence of corner thinning that was otherwise seen in the taut silicone-cured parts.
- The entire laminate shifted towards the long flange during cure for all parts.
- Termination profile 'tail' features were shown to be a useful proxy for the excess length trapped within a ply for a sufficiently large misalignment defects.
- The relative influence of the inputs that affected termination profiles are summarized below in Figure 6-5:

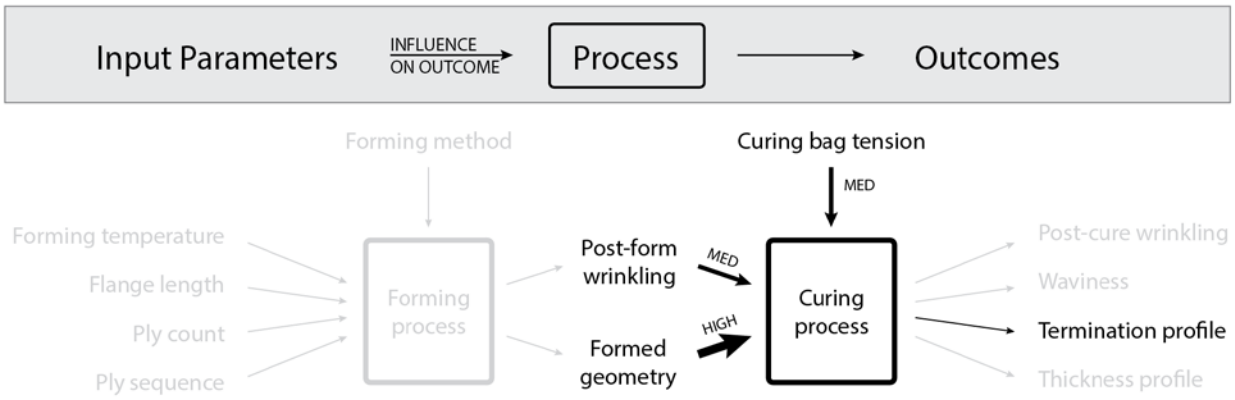

Figure 6-5. Influences of process input parameters on termination profiles. The light grey portion is assumed to have no effect on the outcome in question.

6.3 Thickness profiles

Parts showed corner thickness reductions which had a strong dependency on the bag tension that was applied during cure. Long flange thickness profile features were also related to the occurrence of wrinkles.

6.3.1 Corner thinning

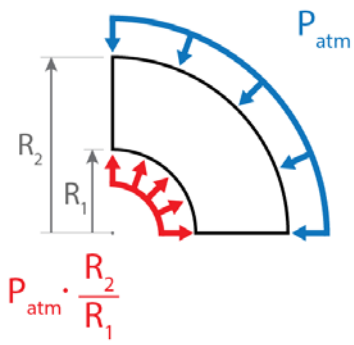

Figure 6-6. Pressure intensification at the mould surface due to surface area differentials between the top surface and the mould surface in male radii.

Corner thinning on the order of 7-9% was seen in all taut silicone-cured parts. Hubert previously proposed that male corners experience pressure intensification due to the difference in area between the outside laminate radius exposed to consolidation pressure, and the inner laminate

radius against the mould [32] (Figure 6-6). However, corner thinning was not seen in the pleated Nylon-cured flanges in the current test series. While the noisiness in the pleated Nylon bag-cured part's thickness profile (due to the pinching of the stiff Nylon bag during cure – see Figure A.1-1 and Figure A.1-2 in the Appendix) could have obfuscated corner thinning features, the greater number of plies and subsequent increase in pressure differential was neither seen to affect the proportions of corner thinning in the 64-ply. Hence, the pressure intensification due to the surface area differentials may not have been significant enough to affect corner thinning in the studied mould radius and laminate thicknesses.

The forming process did not induce corner thinning since the hand lay-up baseline flanges also exhibited corner thinning. The curing bag tension is therefore suggested to have been the cause of the corner thinning seen in this study and is investigated in further detail below.

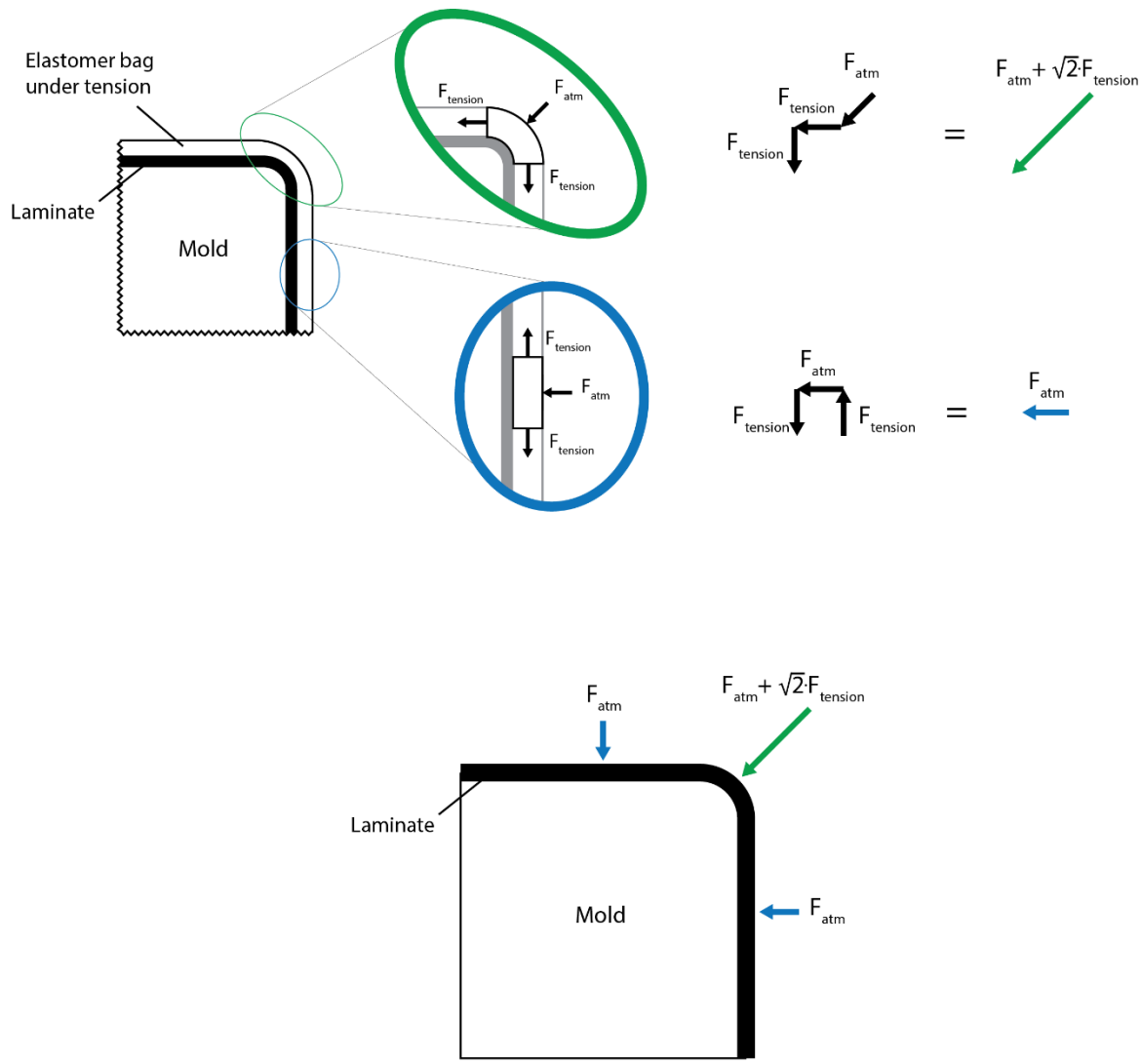

Figure 6-7. Pressure intensification in male corners due to elastomeric bags under tension.

The forces imparted onto the corner by the silicone bag's tension are compared to the forces in a flat section in Figure 6-7. In a flat section, the bag's tension forces are equal and opposite to each other in the plane parallel to the laminate (blue circle). Therefore, the resultant pressure applied to the laminate is simply the atmospheric pressure. Hence, the bag's tension offers no additional contribution to laminate consolidation in the flat sections.

In contrast, the silicone bag tension forces over the corner region of the mould add up to increase the consolidation pressure seen at the corner (green circle). The silicone bag's pressure

contribution over a male 90° angle mould as seen from the mould surface was computed from the stress-strain relation, assuming uniform tension throughout the he bag in Appendix D.2. It showed that the total pressure seen in the corners of the taut silicone-cured parts was on the order of 210 kPa whereas the pressure seen in the corners of the pleated Nylon-cured parts was 160 kPa. Therefore, the pressure difference between the corner and the flat sections were on the order of 110 kPa and 57 kPa, respectively. This additional consolidation pressure likely is the cause of thinning in the corner.

The thickness peaks on either side of the corners are likely due to the migration of material from the corners to the nearby web and flange regions, as shown by the peaks and valley thickness profile features. Since each ply orientation exhibited similar thickness reductions and growth in the corner and adjacent flat sections, respectively, it suggested that 90° oriented fibres did not 'log-roll' out of the corner and into the flat sections, unlike what was previously seen in tests with sharper radii [30]. Rather, the migrant material was suggested to be resin by means of percolation flow. However, since the 90° plies show the largest difference between their average thicknesses in the maximum thickness region and the minimum thickness region in the mid-corner, it is assumed that some 'log-rolling' occurred, but was much less significant than resin flow (Figure 5-33).

The same proposed mechanism can be applied to explain the intensified end consolidation and thickness increases that were seen at the flange terminations (Figure 5-23).

6.3.2 Wrinkling and thickness profiles

The occurrence of wrinkling in taut silicone-cured long flanges was distinguished from thickness profiles as backfilling of the flange-side valley, the increase in flange-side peak height, or a combination of both. The excess length from the wrinkled 0° ply and adjacent 90° and ±45° led to a local increase of volume that translated to the part surface.

Flange profiles for short flanges cured in taut silicone bagging did not exhibit distinct features. The flange's short length meant that the flange-side peak thickness profile feature was combined

with the end consolidation feature which obfuscated the any wrinkling features. Furthermore, the short flange wrinkles were significantly much less severe than those that were found in the long flanges.

Although the Nylon-cured flange wrinkle locations corresponded to thickness profile peak locations, bag pinching (due to poor mould design and bagging practice as seen in Figure A.1-1 and Figure A.1-2 in the Appendix) resulted in additional peaks of similar magnitude that made the detection of wrinkles from the thickness profile implausible.

6.3.3 Key takeaways: thickness profiles

- Bag tension during cure is believed to be the primary driver for corner thinning seen in the silicone bag-cured parts. The same mechanism was likely responsible for the intensified end consolidation at the flange terminations.
- Corner thinning was mainly accomplished by resin flow; 90° fibre ‘log rolling’ was not significant.
- Wrinkles were detectable in long flange thickness profiles. If wrinkles are detectable in parts cured in industrially relevant bags, it could be possible to identify wrinkling occurrences from a high accuracy non-destructive thickness survey.
- Short flange wrinkles were not readily detectable since the wrinkles were smaller and the corner thinning features were blurred with end consolidation features.
- The forming process has no direct impact on the thickness profile. The geometry of the formed part (flange length, thickness, wrinkles) and the curing process conditions (bag tension) determined the final thickness profile.
- The relative influence of the inputs that affected thickness profiles are summarized below in Figure 6-8:

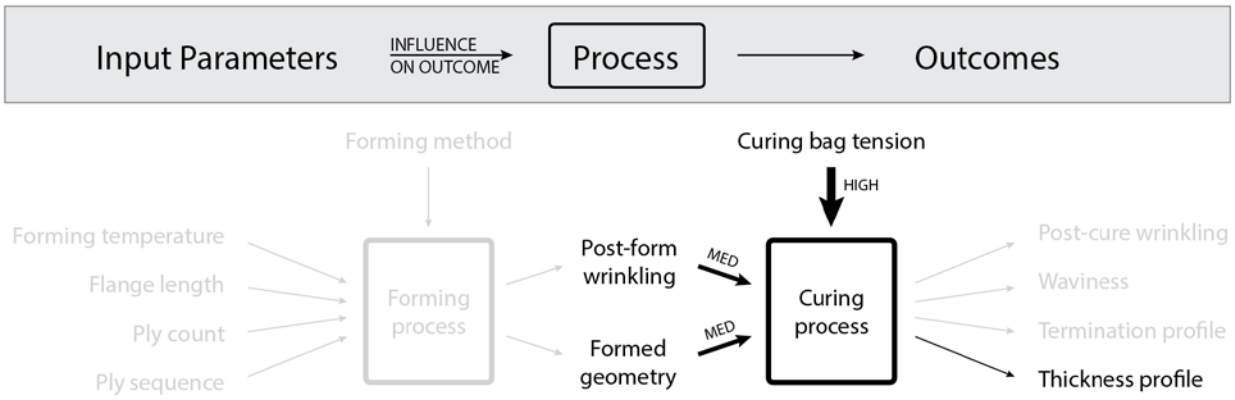

Figure 6-8. Influences of process input parameter on thickness profiles. The light grey portion is assumed to have no effect on the outcome in question.

Chapter 7: Conclusions and Future Work

7.1 Conclusions

This study investigated the effect of process parameters and the mechanisms of fibre misalignment formation and propagation in charge-formed geometries. C-channels were charge-formed under varying flange lengths, forming temperatures, ply counts, ply sequences, forming methods, and curing bag types and were related to wrinkling, waviness, termination profile, thickness profile, and photographic outcomes.

The study substantiated and expanded on previous work done on the impact of process input parameters on forming defects. Cured parts showed wrinkling when formed at room temperature. Increased flange lengths and thinner laminates resulted in greater wrinkling severity. Fibre misalignments were more severe for the cured *Offset* ply sequence ($[0/-45/+45/90]_{4S}$) flanges, taking the form of full-ply waviness after cure.

A wrinkling conversion mechanism was proposed to explain the disappearance of externally visible defects and the appearance of full-ply waviness after cure. The extent of conversion was attributed the curing bag tension and the post-formed wrinkled ply's location within the charge with respect to the laminate's outer surface. In all flanges, full-ply waviness misalignment angles were equal or significantly greater than wrinkling misalignment angles. Missing lengths seen from flange termination profiles were shown to give a good approximation of the excess length trapped in the part in the form of wrinkling and full-ply waviness. Additionally, part thickness profiles provided further information on the occurrence of wrinkles. Furthermore, fibre misalignment types and locations were corroborated by non-destructive surface photography. Whether laminates were formed by hand lay-up or by drape forming, waviness gradients were found through the thickness of all 0° plies and attributed to the absence of sufficient intra-ply shear.

The differences observed when forming the same ply sequence in alternate orientations may provide useful insight into the forming of charges into compound curvatures. The suggested post-form wrinkle conversion to waviness mechanism provides reason to develop waviness

detection capabilities and to improve the understanding of mechanical performance knockdown effects from waviness. This study also suggests that post-forming part surface inspection for externally visible defects can be a critical step in identifying post-cure waviness sites. Defects detected in simple surface photography after cure showed promising applicability to industrial inspection workflows with regards to locating and identifying types of defects in mould-side surface plies. The occurrence of wrinkling and subsequent full-ply waviness is expected to be reduced if inter-ply slip characteristics are improved, though waviness gradients within individual plies will remain.

7.2 Future work

- Improve and enlarge forming and curing equipment in order to reduce variability and to study larger scale parts. Use near-net-shape silicone curing bag (reduces tension force) to better simulate industrial practices and to prevent laminate shifting during cure.
- Perform two-ply forming experiments to investigate the impact of adjacent ply orientations on wrinkling morphology. For example: [0/90], [90/0], and [0/45] ply sequences. Investigate the effect of varying post-layup consolidation pressure and dwell time on the occurrence of wrinkling.
- Develop capabilities for real-time visualization of defect formation during formation. This would be useful for validating modeling in the future. In the interim, post-forming microscopy would prove to be extremely valuable in understanding the defect formation process and the impact of cure on defects, such as the conversion of wrinkles to waves.
- Mechanical testing to investigate the mechanical performance knockdowns of waviness in comparison to similarly severe wrinkles.
- Determine the slip regime (boundary lubrication, etc.) seen during forming with the aim of quantifying the shear stress at the ply-ply interface.

Bibliography

[1] N. Zobeiry, “MTRL 594 - Composite materials course notes.” 2013.

[2] R. Slayton and G. Spinardi, “Radical innovation in scaling up: Boeing’s Dreamliner and the challenge of socio-technical transitions,” *Technovation*, pp. 1–12, 2015.

[3] K. S. Willden, B. P. Van West, and C. G. Harris, “Forming method for composites,” US 8,142,181 B22012.

[4] M. R. Piggott, “The effect of fibre waviness on the mechanical properties of unidirectional fibre composites: A review,” *Compos. Sci. Technol.*, vol. 53, no. 2, pp. 201–205, Jan. 1995.

[5] C. Jochum, J. C. Grandidier, and M. Smaali, “Proposal for a long-fibre microbuckling scenario during the cure of a thermosetting matrix,” *Compos. Part A Appl. Sci. Manuf.*, vol. 39, no. 1, pp. 19–28, 2008.

[6] N. Ersoy, K. Potter, M. R. Wisnom, and M. J. Clegg, “An experimental method to study the frictional processes during composites manufacturing,” *Compos. Part A Appl. Sci. Manuf.*, vol. 36, no. 11, pp. 1536–1544, Nov. 2005.

[7] K. Potter, B. Khan, M. Wisnom, T. Bell, and J. Stevens, “Variability, fibre waviness and misalignment in the determination of the properties of composite materials and structures,” *Compos. Part A Appl. Sci. Manuf.*, vol. 39, no. 9, pp. 1343–1354, Sep. 2008.

[8] T. J. Dodwell, R. Butler, and G. W. Hunt, “Out-of-plane ply wrinkling defects during consolidation over an external radius,” *Compos. Sci. Technol.*, vol. 105, pp. 151–159, 2014.

[9] A. Beakou, M. Cano, J.-B. Le Cam, and V. Verney, “Modelling slit tape buckling during automated prepreg manufacturing: A local approach,” *Compos. Struct.*, vol. 93, no. 10, pp. 2628–2635, 2011.

[10] L. D. Bloom, J. Wang, and K. D. Potter, “Damage progression and defect sensitivity: An experimental study of representative wrinkles in tension,” *Compos. Part B Eng.*, vol. 45, no. 1, pp. 449–458, Feb. 2013.

[11] K. D. Potter, “Beyond the pin-jointed net: maximising the deformability of aligned continuous fibre reinforcements,” *Compos. Part A Appl. Sci. Manuf.*, vol. 33, pp. 677–689, 2002.

[12] K. D. Potter, “Understanding the origins of defects and variability in composites manufacture,” *Univ. Bristol*, 2009.

[13] K. Potter, C. Ward, and K. Hazra, “Improving the manufacture of complex geometries,” no. May, pp. 1–11, 2010.

[14] C. Mack and H. M. Taylor, “The fitting of woven cloth to surfaces,” *J. Text. Inst.*, vol. 47, no. 8, pp. 477–488, 1956.

[15] J. Cao, R. Akkerman, P. Boisse, J. Chen, H. S. Cheng, E. F. de Graaf, J. L. Gorczyca, P. Harrison, G. Hivet, J. Launay, W. Lee, L. Liu, S. V. Lomov, A. Long, E. de Luycker, F. Morestin, J. Padvoiskis, X. Q. Peng, J. Sherwood, T. Stoilova, X. M. Tao, I. Verpoest, A. Willems, J. Wiggers, T. X. Yu, and B. Zhu, “Characterization of mechanical behavior of woven fabrics: Experimental methods and benchmark results,” *Compos. Part A Appl. Sci. Manuf.*, vol. 39, no. 6, pp. 1037–1053, Jun. 2008.

[16] A. G. Prodromou and J. Chen, “On the relationship between shear angle and wrinkling of textile composite preforms,” *Compos. Part A Appl. Sci. Manuf.*, vol. 28, no. 5, pp. 491–503, 1997.

[17] G. Lebrun, M. N. Bureau, and J. Denault, “Evaluation of bias-extension and picture-frame test methods for the measurement of intraply shear properties of PP/glass commingled fabrics,” *Compos. Struct.*, vol. 61, no. 4, pp. 341–352, Sep. 2003.

[18] Y. R. Larberg, M. Akermo, and M. Norrby, “On the in-plane deformability of cross-plied unidirectional prepreg,” *J. Compos. Mater.*, vol. 46, no. 8, pp. 929–939, Oct. 2011.

[19] K. D. Potter, “Bias extension measurements on cross-plied unidirectional prepreg,” *Compos. Part A Appl. Sci. Manuf.*, vol. 33, no. 1, pp. 63–73, Jan. 2002.

[20] Y. R. Larberg and M. Åkermo, “In-plane properties of cross-plied unidirectional prepreg,” in *International Conference on Composite Materials (ICCM) 16*, 2007, pp. 1–7.

[21] P. Hallander, M. Akermo, C. Mattei, M. Petersson, and T. Nyman, “An experimental study of mechanisms behind wrinkle development during forming of composite laminates,” *Compos. Part A Appl. Sci. Manuf.*, vol. 50, pp. 54–64, Jul. 2013.

[22] A. E. Modin, “Hot drape forming of thermoset prepregs,” in *Composites in Mnaufacturing ’93*, 1993, no. 313, p. 23.

[23] R. Scherer and K. Friedrich, “Experimental background for finite element analysis of the

inter-ply slip process during thermoforming of thermoplastic composites," pp. 1001–1006, 1990.

[24] R. Scherer and K. Friedrich, "Inter- and intraply-slip flow processes during thermoforming of CF-PP laminates," vol. 2, no. 2, pp. 92–96, 1991.

[25] J. Krebs, K. Friedrich, and D. Bhattacharyya, "A direct comparison of matched-die versus diaphragm forming," pp. 183–188, 1998.

[26] M. Akermo, Y. R. Larberg, J. Sjölander, and P. Hallander, "Influence of interply friction on the forming of stacked UD prepreg," in *ICCM 19*, 2013, pp. 919–928.

[27] Y. R. Larberg and M. Åkermo, "On the interply friction of different generations of carbon/epoxy prepreg systems," *Compos. Part A Appl. Sci. Manuf.*, vol. 42, no. 9, pp. 1067–1074, Sep. 2011.

[28] T. Ott, "Composite hot drape forming," 1994.

[29] S. W. Yurgartis, "Measurement of small angle fiber misalignments in continuous fiber composites," *Compos. Sci. Technol.*, vol. 30, pp. 279–293, 1987.

[30] A. Stewart, K. Farnand, G. Fernlund, and A. Poursartip, "Experimental study into the parameters affecting the architecture of waviness and wrinkling in prepreg systems," *Can. Int. Conf. Compos. Mater. 2015 Proc.*, pp. 1–8, 2015.

[31] J. Kratz, K. Hsiao, G. Fernlund, and P. Hubert, "Thermal models for MTM45-1 and Cycom 5320 out-of-autoclave prepreg resins," *J. Compos. Mater.*, 2012.

[32] P. Hubert, "Aspects of flow and compaction of laminated composite shapes during cure," University of British Columbia, 1996.

[33] J. S. Lightfoot, M. R. Wisnom, and K. Potter, "A new mechanism for the formation of ply wrinkles due to shear between plies," *Compos. Part A Appl. Sci. Manuf.*, vol. 49, pp. 139–147, Jun. 2013.

[34] J. S. Lightfoot, M. R. Wisnom, and K. Potter, "Defects in woven preforms: Formation mechanisms and the effects of laminate design and layup protocol," *Compos. Part A Appl. Sci. Manuf.*, vol. 51, pp. 99–107, Aug. 2013.

[35] C. Albert and G. Fernlund, "Spring-in and warpage of angled composite laminates," *Compos. Sci. Technol.*, vol. 62, no. October, pp. 1895–1912, 2002.

[36] K. Çınar and N. Ersoy, "Effect of fibre wrinkling to the spring-in behaviour of L-shaped

composite materials," *Compos. Part A Appl. Sci. Manuf.*, vol. 69, pp. 105–114, 2015.

[37] A. Salomi, T. Garstka, K. Potter, A. Greco, and A. Maffezzoli, "Spring-in angle as molding distortion for thermoplastic matrix composite," *Compos. Sci. Technol.*, vol. 68, no. 14, pp. 3047–3054, 2008.

Appendices

Appendix A Supporting Results

A.1 Externally visible defects

Table A.1-1. Post-forming and post-cure outer surface image surveys for each part manufactured flange. Bump features are indicated with blue arrows.

Part Number	Flange	Surface after forming	Surface after cure
1* *Ripped bag case	LF	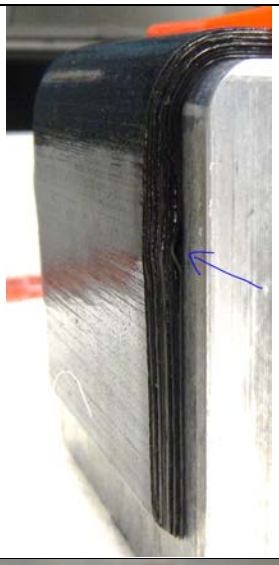	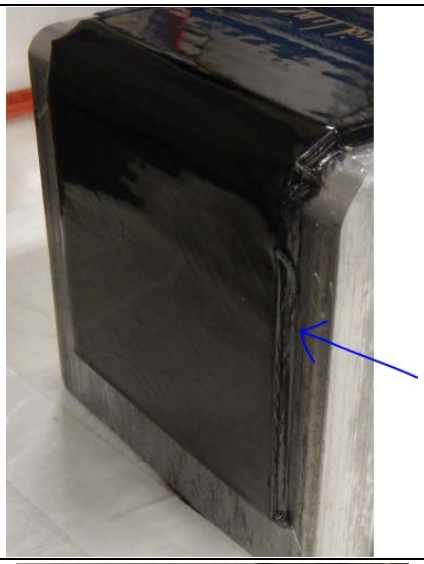
	SF		

Part Number	Flange	Surface after forming	Surface after cure
2	LF		
	SF		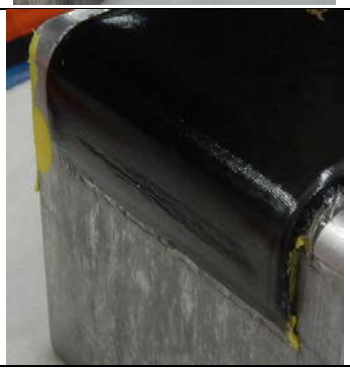
3	LF		

Part Number	Flange	Surface after forming	Surface after cure
	SF		
4	LF	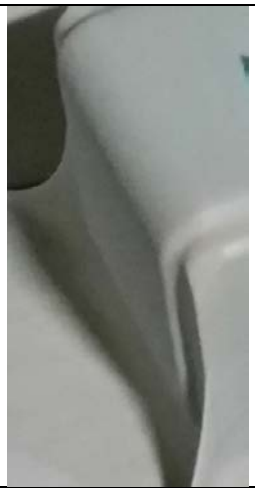	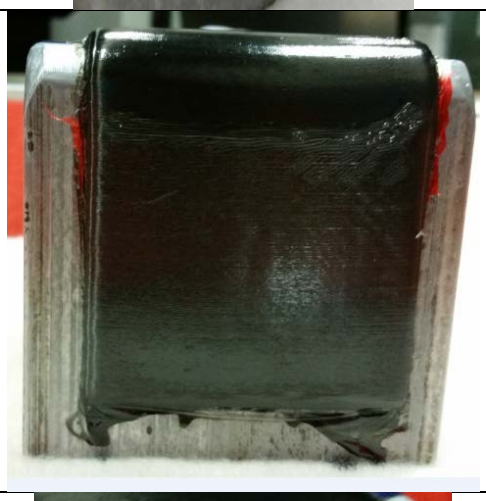
	SF	Not available	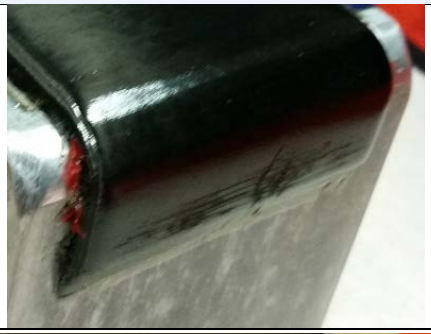
5	LF		

Part Number	Flange	Surface after forming	Surface after cure
	SF		
6	LF		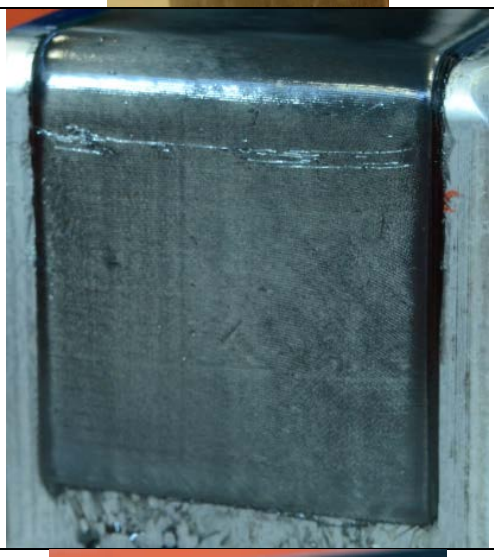
	SF	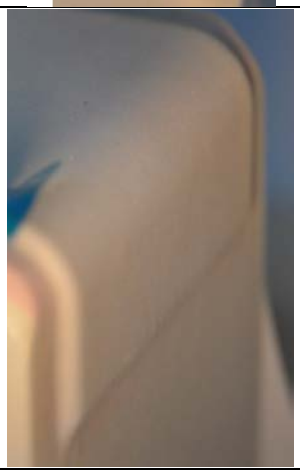	

Part Number	Flange	Surface after forming	Surface after cure
7	LF		
	SF		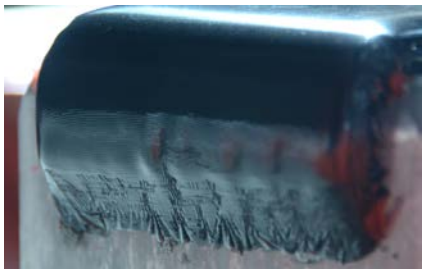
8	LF	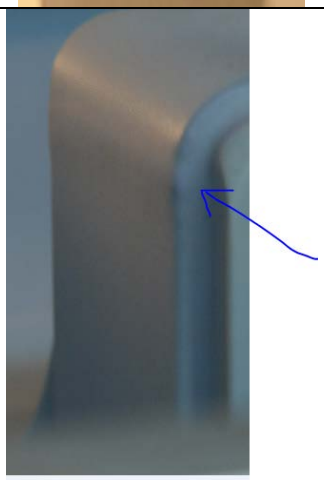	

Part Number	Flange	Surface after forming	Surface after cure
	SF		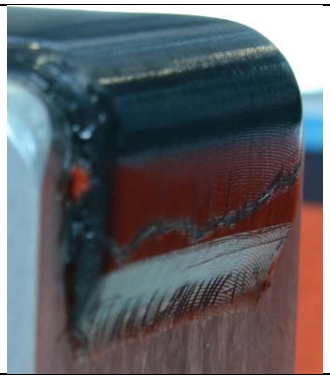
9	LF	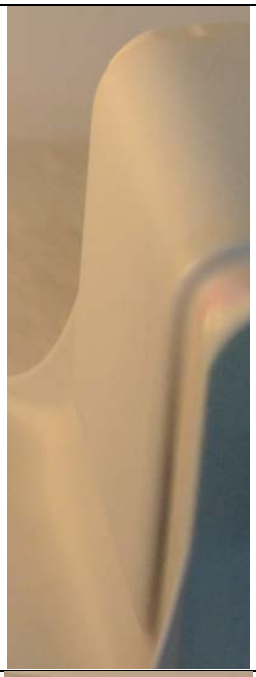	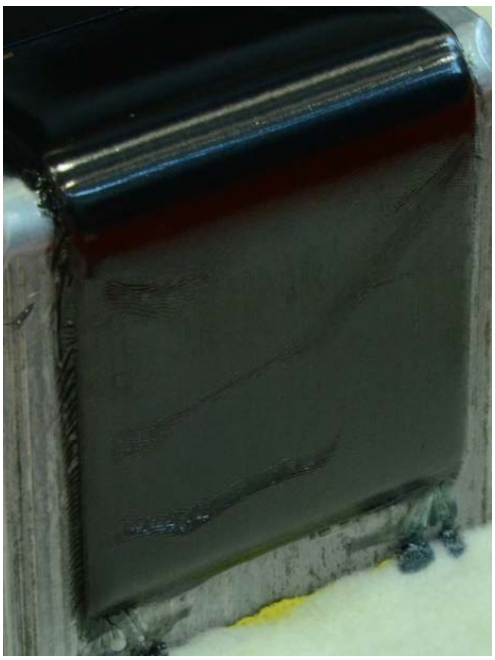
	SF		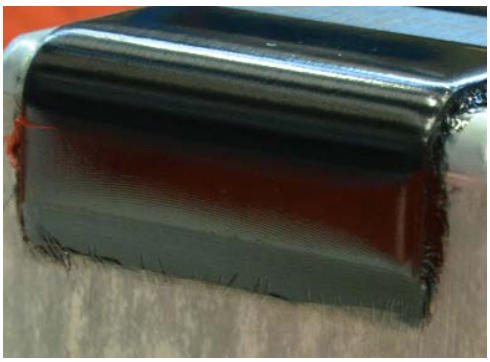

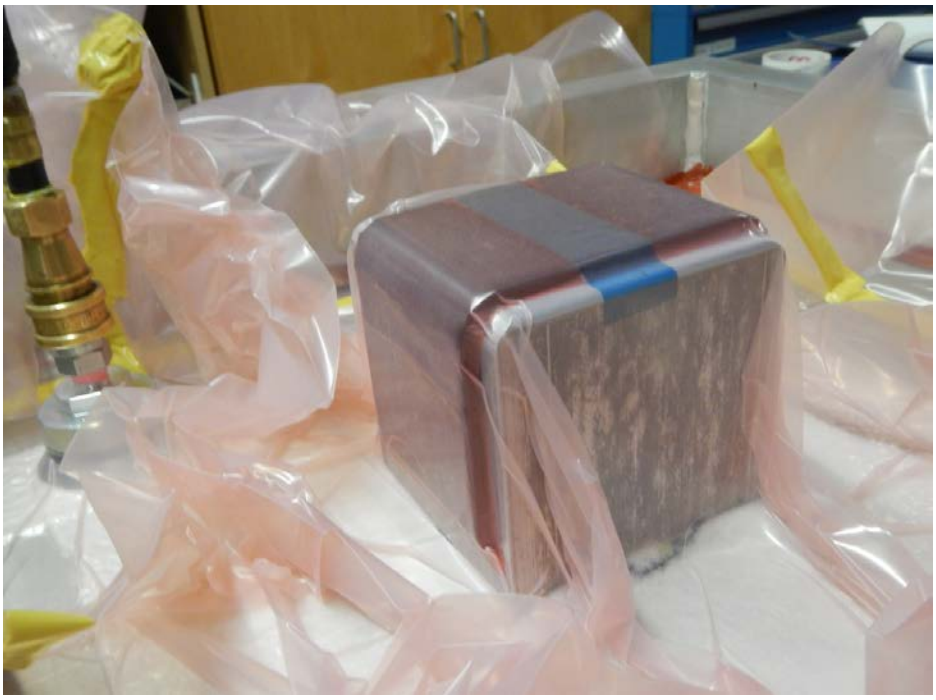

Figure A.1-1. Silicone bag-formed & Nylon bag-cured part prior to cure

Figure A.1-2. Nylon bag-cured corner after cure showing bag pinching leading to poor dimensional control over the corner

A.2 Cured ply thicknesses

The cured ply thickness was averaged over the entire part and is presented in the table below

Table A.2-1. Cured ply thicknesses for all manufactured parts

Part identifier	Cured ply thickness
FE-01	0.135 mm
FE-02	0.135 mm
FE-03	0.136 mm
FE-04	0.136 mm
FE-05	0.135 mm
FE-06	0.136 mm
FE-07	0.137 mm
FE-08	0.137 mm
FE-09	0.137 mm

A.3 Wrinkle quantification

Wrinkles for all manufactured flanges have been characterized for each manufactured part by the methodology detailed in Section B.1 and are tabulated in. Observations on the effect of process input parameters are presented in the following subsections.

Table A.3-1 Wrinkle characterization for all manufactured long flanges. The characterization methodology is detailed in Section B.1.

		A	B	C	D	E	F	G	H	I
		Ply position [#]	Location [mm]	Ply path deviation height [CPT]	Maximum deviation angle [°]	Length span [CPT]	Wrinkling excess length per wrinkle [CPT]	Wrinkling excess length in flange [CPT]	Percent excess length of long flange [%]	Maximum ply thickness growth [%]
Long Flanges	LF-5 (32ply, HLU, Quasi, Silicone)	--	--	--	--	--	--	--	*n/a*	--
	LF-1 (32ply, 30°C, Quasi, Nylon)	3rd	12.0	1.264	8.7	58.1	0.159	1.059	*n/a*	--
		3rd	25.5	4.040	22.5	39.3	0.900			--
	LF-2 (32ply, 30°C, Quasi, Silicone)	3rd	9.1	0.385	3.9	20.1	0.022	0.127	*n/a*	--
		3rd	16.0	1.115	5.7	45.4	0.084			--
		3rd	33.5	0.428	2.4	45.7	0.021			--
	LF-4 (32ply, 30°C, Quasi, Silicone)	3rd	12.5	1.355	8.6	32.1	0.154	0.212	*n/a*	--
		3rd	16.4	0.866	4.8	31.4	0.058			--
	LF-6 (16ply, 30°C, Quasi, Silicone)	3rd	4.6	0.416	4	21.7	0.055	0.426	*n/a*	--
		3rd	8.4	1.056	4.5	32.7	0.048			--
		3rd	13.2	2.158	13.6	38.7	0.323			--
	LF-7 (64ply, 30°C, Quasi, Silicone)	3rd	14.5	1.687	6.9	43.8	0.125	0.125	*n/a*	--
	LF-8 (32ply, 30°C, Offset, Silicone)	1st	11.8	*n/a*	*n/a*	24.0	*n/a*	*n/a*	*n/a*	1.5
		5th	11.5	1.529	11	37.2	0.179	0.219	*n/a*	--
		5th	16.2	0.729	4	33.0	0.040			--
	LF-3 (32ply, 70°C, Quasi, Silicone)	--	--	--	--	--	--	--	*n/a*	--
	LF-9 (32ply, 70°C, Offset, Silicone)	--	--	--	--	--	--	--	*n/a*	--

Table A.3-2. Wrinkle characterization for all manufactured short flanges. The characterization methodology is detailed in Section 3.4.4.

		A	B	C	D	E	F	G	H	I
		Ply position [#]	Location [mm]	Ply path deviation height [CPT]	Maximum deviation angle [°]	Length span [CPT]	Wrinkling excess length per wrinkle [CPT]	Wrinkling excess length in flange [CPT]	Percent excess length of long flange [%]	Maximum ply thickness growth [%]
Short Flanges	SF-5 (32ply, HLU, Quasi, Silicone)	--	--	--	--	--	--	--	--	--
	SF-1 (32ply, 30°C, Quasi, Nylon)	3rd	3.1	0.346	4.2	20.9	0.071	0.071	7%	--
	SF-2 (32ply, 30°C, Quasi, Silicone)	3rd	10.1	0.661	3.9	24.8	0.028	0.028	22%	--
	SF-4 (32ply, 30°C, Quasi, Silicone)	3rd	9.8	0.222	1.6	23.5	0.011	0.011	5%	--
	SF-6 (16ply, 30°C, Quasi, Silicone)	3rd	4.2	0.825	8.5	31.9	0.225	0.225	53%	--
	SF-7 (64ply, 30°C, Quasi, Silicone)	3rd	11.5	0.784	5.2	26.7	0.053	0.053	42%	--
	SF-8 (32ply, 30°C, Offset, Silicone)	--	--	--	--	--	--	--	--	--
	SF-3 (32ply, 70°C, Quasi, Silicone)	--	--	--	--	--	--	--	--	--
	SF-9 (32ply, 70°C, Offset, Silicone)	--	--	--	--	--	--	--	--	--

A.4 Wave quantification

Full-ply waviness in wrinkling regions has been quantified according to the '*ellipse survey method*' detailed in Section B.2 and is tabulated in Table A.4-1.

Table A.4-1 Maximum full-ply waviness characterization using the 'ellipse survey method' for all manufactured flanges. The characterization methodology is detailed in Section B.2.

		J	K	L	M
		Ply position [#]	Waviness-affected region location [mm]	Maximum deviation angle [°]	Waviness-affected region span [CPT]
Long Flanges	LF-5 (32ply, HLU, Quasi, Silicone)	--	--	--	--
	LF-1 (32ply, 30°C, Quasi, Nylon)	3rd	12.0	18°	58.9
		3rd	15.4	22°	72.7
	LF-2 (32ply, 30°C, Quasi, Silicone)	3rd	13.3	14°	142.8
	LF-4 (32ply, 30°C, Quasi, Silicone)	3rd	14.1	20°	99.4
	LF-6 (16ply, 30°C, Quasi, Silicone)	3rd	11.3	24°	132.4
	LF-7 (64ply, 30°C, Quasi, Silicone)	3rd	15.4	13°	80.0
	LF-8 (32ply, 30°C, Offset, Silicone)	1st	10.3	61°	144.3
		5th	14.4	20°	115.4
	LF-3 (32ply, 70°C, Quasi, Silicone)	--	--	--	--
	LF-9 (32ply, 70°C, Offset, Silicone)	3rd	6.6	8°	114.8
Short Flanges	SF-5 (32ply, HLU, Quasi, Silicone)	--	--	--	--
	SF-1 (32ply, 30°C, Quasi, Nylon)	3rd	2.4	11°	34.9
	SF-2 (32ply, 30°C, Quasi, Silicone)	3rd	8.7	18°	31.0
	SF-4 (32ply, 30°C, Quasi, Silicone)	3rd	-1.2	17°	30.5
	SF-6 (16ply, 30°C, Quasi, Silicone)	3rd	1.4	24°	41.4
	SF-7 (64ply, 30°C, Quasi, Silicone)	3rd	9.4	14°	34.7
	SF-8 (32ply, 30°C, Offset, Silicone)	1st	2.9	33°	73.6
	SF-3 (32ply, 70°C, Quasi, Silicone)	--	--	--	--
	SF-9 (32ply, 70°C, Offset, Silicone)	3rd	6.9	9°	66.4

A.5 Surface quality of manufactured parts

The surface quality for all flanges after cure is presented below. The blue lines represent the cross-sectional micrograph viewing planes. Arrows indicate the locations of surface defects due to the bunching of FEP sheeting material.

Figure A.5-1. (FE-01 LF) [30°C-Draped | 88.9mm | 32ply | [90/+45/-45/0] | R9.525mm] showing good bag-side surface quality along the midline

Figure A.5-2. (FE-02 LF) [30°C-Draped | 88.9mm | 32ply | [90/+45/-45/0] | R9.525mm] showing good bag-side surface quality along the midline

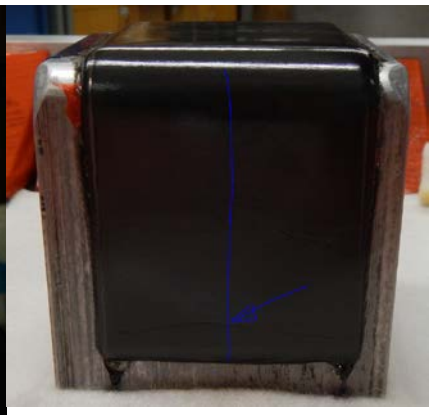

Figure A.5-3. (FE-03 LF) [70°C-Draped | 88.9mm | 32ply | [90/+45/-45/0] | R9.525mm] showing a minor depression near the flange end along the midline due to bunching of FEP ply

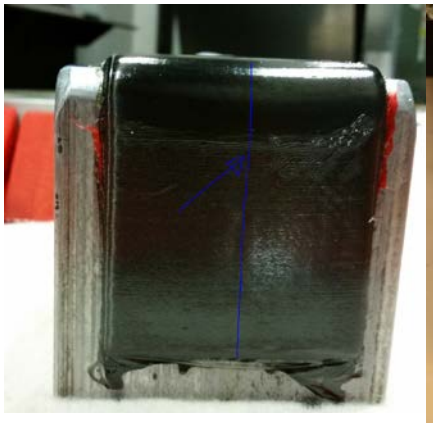

Figure A.5-4. (FE-04 LF) [30°C-Draped | 88.9mm | 32ply | [90/+45/-45/0] | R9.525mm] showing a minor depression near the corner end along the midline due to bunching of FEP ply

Figure A.5-5. (FE-05 LF) [24°C-HLU | 88.9mm | 32ply | [90/+45/-45/0] | R9.525mm] showing good bag-side surface quality along the midline

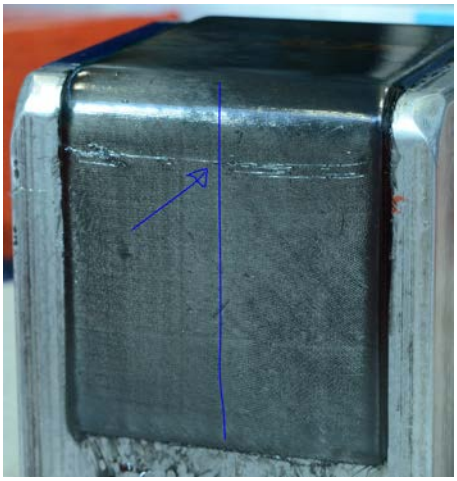

Figure A.5-6. (FE-06 LF) [30°C-Draped | 88.9mm | 16ply | [90/+45/-45/0] | R9.525mm] showing a very minor depression near the corner end along the midline due to bunching of FEP ply

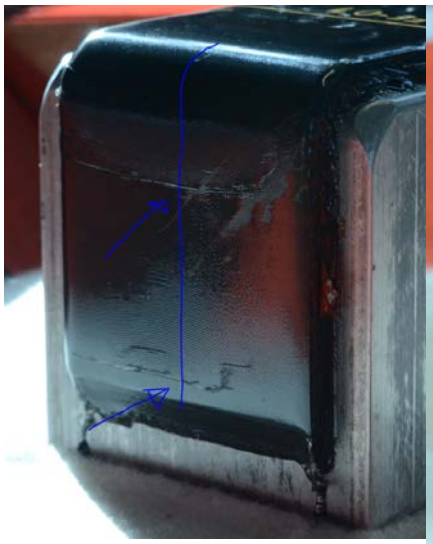

Figure A.5-7. (FE-07 LF) [30°C-Draped | 88.9mm | 64ply | [90/+45/-45/0] | R9.525mm] showing two regions of minor depressions along the midline due to bunching of FEP ply

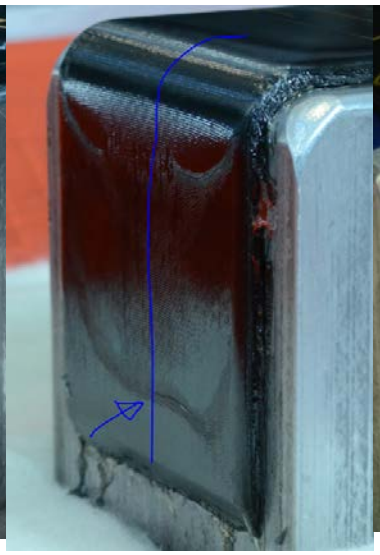

Figure A.5-8. (FE-08 LF) [30°C-Draped | 88.9mm | 32ply | [0/-45/+45/90] | R9.525mm] showing a minor depression near the flange end along the midline due to bunching of FEP ply

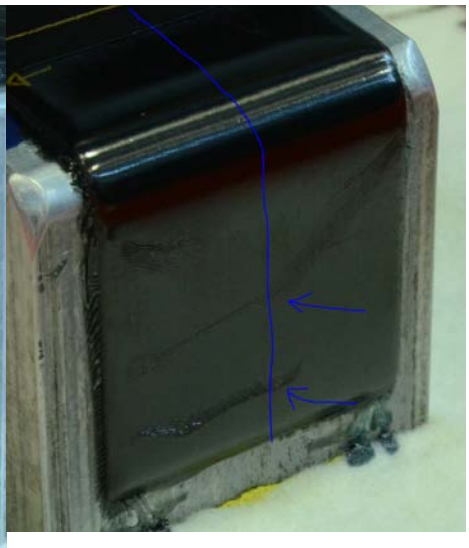

Figure A.5-9. (FE-09 LF) [70°C-Draped | 88.9mm | 32ply | [0/-45/+45/90] | R9.525mm] showing two regions of pressure intensification along the midline due to bunching of FEP ply

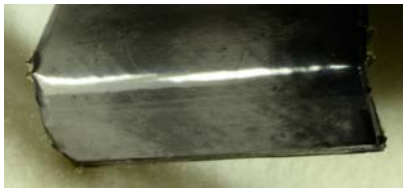

Figure A.5-10. (FE-01 SF) [30°C-Draped | 38.1mm | 32ply | [90/+45/-45/0] | R9.525mm] showing good bag-side surface quality along the midline

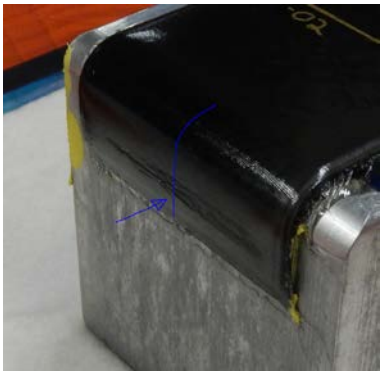

Figure A.5-11. (FE-02 SF) [30°C-Draped | 38.1mm | 32ply | [90/+45/-45/0] | R9.525mm] showing a minor depression near the flange end along the midline due to bunching of FEP ply

Figure A.5-12. (FE-03 SF) [70°C-Draped | 38.1mm | 32ply | [90/+45/-45/0] | R9.525mm] showing good bag-side surface quality along the midline

Figure A.5-13. (FE-04 SF) [30°C-Draped | 38.1mm | 32ply | [90/+45/-45/0] | R9.525mm] showing a minor depression near the flange end along the midline due to bunching of FEP ply

Figure A.5-14. (FE-05 SF) [24°C-HLU | 38.1mm | 32ply | [90/+45/-45/0] | R9.525mm] showing good bag-side surface quality along the midline

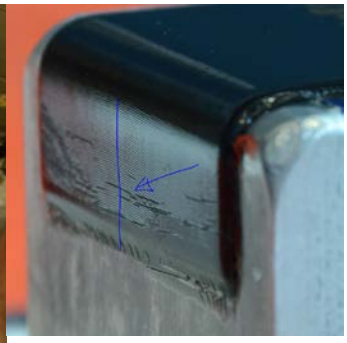

Figure A.5-15. (FE-06 SF) [30°C-Draped | 38.1mm | 16ply | [90/+45/-45/0] | R9.525mm] showing a very minor depression near the flange end along the midline due to bunching of FEP ply

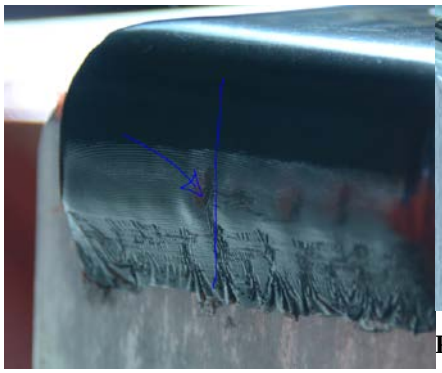

Figure A.5-16. (FE-07 SF) [30°C-Draped | 38.1mm | 64ply | [90/+45/-45/0] | R9.525mm] showing aminor depression and significant transverse wrinkling near the flange end along the midline due to bunching of FEP ply

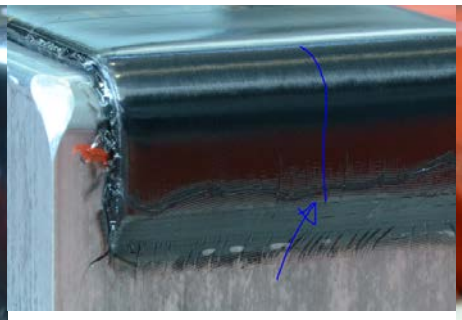

Figure A.5-17. (FE-08 SF) [30°C-Draped | 38.1mm | 32ply | [0/-45/+45/90] | R9.525mm] showing a minor depression near the flange end along the midline due to bunching of FEP ply

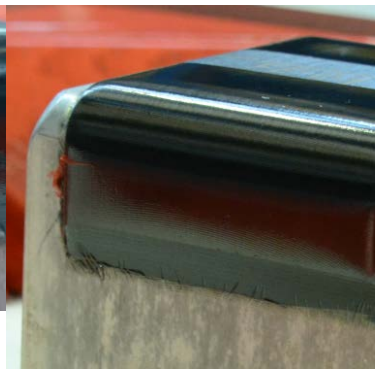

Figure A.5-18. (FE-09 SF) [70°C-Draped | 38.1mm | 32ply | [0/-45/+45/90] | R9.525mm] showing good bag-side surface quality along the midline

Appendix B Additional Methods Details

B.1 Wrinkle quantification

Wrinkling has been characterized in a variety of different ways. In one method, Potter suggests that wrinkles and waviness can be characterized by the mechanisms that formed them via a taxonomy of defects [7], [12].

With regards to specific defects, Lightfoot characterized wrinkles from cross-sectional microscopy in terms of zonal location, number of wrinkles, ply growth height, number of ruptured plies, and number of plies misaligned to more than 20° [33]. Waviness was characterized from the same images using an automated script to determine misalignment angles using the Yurgartis elliptical aspect ratio method and dividing regions into misalignment degree bins [29]. Hallander et al. characterized wrinkles from cross-sectional microscopy in terms of quantity, type, zonal location, defect height, and distance from the radius [21]. Bloom et al. characterized wrinkles from cross-sectional microscopy with multiple misalignment angular spread metrics [10].

A first misalignment analysis was performed on cross-sectional micrographs. Wrinkles were first identified by comparing the bottom-most 0° ply path to the corresponding as-designed (theoretical) ply path. The as-designed path is determined by tracing the mould line, and scaling it to meet the mid-line of the ply's non-wrinkled section. If the ply showed a local rise and drop feature, it was deemed a wrinkle. The 0° plies were chosen because they are columnar with respect to the slip direction – and are the stiffest in that direction – thus being the only plies that could buckle in a single curvature forming scheme. Additionally, they maintain a constant thickness through wrinkled zones, allowing for accurate measurements.

The wrinkles that were produced in these experiments had distinctly similar features that allowed for a standard characterization to be performed across all tests. In particular, wrinkles typically appeared as bell shapes (analogous to the normal distribution curve) rather than fully-reversing waves, thus were treated as a single maximum features. These bells were not always symmetrical from left to write, but did not have any folding features (i.e. each horizontal coordinate is only associated with a single vertical value). The wrinkled ply in question was then traced through its mid-line and characterized by the combinations of the multiple measurements, as illustrated in Figure B.1-1, and explained in Table B.1-1.

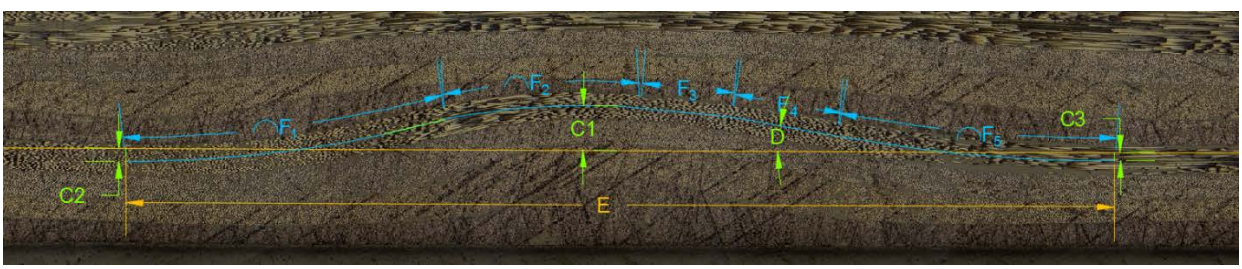

Figure B.1-1.Quantification of individual wrinkles where the yellow line is the intended ply path, as per a non-wrinkled section and the blue line is the actual ply's path, both through the ply's mid-line.

Table B.1-1. Wrinkling characterization breakdown

	Measurement	Description	Method
A	Ply position [#]	Ply's position within the laminate	Counted up from the mould-interfacing ply for all ply orientations – starts at 1 and ends at 32 for a 32-ply laminate.
B	Location [mm]	The wrinkle's location with respect to the origin at the radius's mid-corner (45° into the corner)	Length along the mid-line path of the part from the origin at mid-corner to the middle of the wrinkle (with respect to its length span) where positive (+) locations are toward the flange termination and negative (-) locations are towards the web. The location represents the middle of the wrinkle, with respect to its length span.
C	Ply path deviation height [CPT]	Maximum height of the wrinkle	The mid-height, '$C1$', is measured from the as-designed path to the maximum. The end-heights, '$C2$' and '$C3$', are minor compensations for the height of the 'wrinkle bounds' if their vertical positions aren't directly on the as-designed path (see E: Length span). The end-height is positive (+) if the wrinkle end is below the as-designed path. The ply deviation height, C is calculated from the following equation: $$C = C1 + \frac{C2 + C3}{2}$$ and is represented in units of cured ply thickness (CPT).

	Measurement	Description	Method
D	Maximum deviation angle [degrees]	Maximum ply misalignment angle due to wrinkling	The upward angles of either side of the wrinkle are measured with respect to the as-designed ply orientation. The maximum value is selected.
E	Length span [CPT]	Length of the region affected by a particular wrinkle	Length, termed 'E', along the as-designed path between 'wrinkle bounds' bounds are determined by the region where the fibres change from the as-designed orientation to a given angle, containing a maximum. In other words, from the wrinkle's perspective, the wrinkle is deemed ended if the ply returns to parallel with the as-designed path. The wrinkle bounds are thus a function of the ply angle, and not the vertical position of the ply.
F	Wrinkling excess length per wrinkle [CPT]	Path length excess from the as-designed path due to wrinkling: a defect severity index	For the length span of the wrinkle, the traced wrinkle is measured via individual arc length segments dubbed 'F_n'. The length span, ie the wrinkle's as-designed length, is subtracted from the total wrinkle path length to give the excess length due to wrinkling. The excess length, 'F' is represented by the following equation: $$F = \sum F_n - E$$ $$= F_1 + F_2 + F_3 + F_4 + F_5 - E$$
G	Wrinkling total excess length in flange [CPT]	Total excess length in the flange due to wrinkling : a defect severity index	Summation of excess lengths for all wrinkles in a particular flange.

	Measurement	Description	Method
H	Percent excess length of long flange [%]	Comparison of the short flange's total excess length to the long flange's excess length for the same part	The short flange's total excess length 'G_{SF}' is taken as a percentage of the long flange's total excess length 'G_{LF}': $$H = \frac{G_{SF}}{G_{LF}} \times 100$$
I	Maximum ply thickness growth [%]	Percentage growth of the 0° ply's thickness with respect to the cured ply thickness	With regards only to the 0° ply in question, the thickness increase is determined from the cured ply thickness, CPT, and the ply's local thickness, 't_x' by the following equation: $$I = \frac{t_x - CPT}{CPT} \times 100$$

B.2 Wave quantification

As the detection of waviness is generally quite difficult, the quantification of waviness is often rudimentary if at all performed. Typical waviness measurements are limited to cross-sectional micrograph image analysis surveys of fibre ellipses by the Yurgartis method [29], [34]. Where this approach can produce nominal fibre misalignment values, it does not provide any information on the characteristics of waves such as amplitude and span. However, due to the simplicity of this approach, a similar procedure has been observed in this study under the '*ellipse survey method*' moniker. The specific characterization methodology is detailed in Table B.2-1 below.

Table B.2-1 Waviness characterization breakdown for the 'ellipse survey method'

	Measurement	Description	Method
J	Ply position [#]	Ply's position within the laminate	Counted up from the mould-interfacing ply for all ply orientations – starts at 1 and ends at 32 for a 32-ply laminate.
K	Waviness-affected region location [mm]	The waviness-affected region's location with respect to the origin at the radius's mid-corner (45° into the corner)	Length along the mid-line path of the part from the origin at mid-corner to the middle of the waviness-affected region (with respect to its region span, M) where positive (+) locations are toward the flange termination and negative (-) locations are towards the web. The location represents the middle of the waviness-affected region, with respect to its length span.
L	Maximum deviation angle [degrees]	Maximum ply misalignment angle due to waviness	The in-plane fibre angles of the waviness-affected region is surveyed by means of the Yurgartis method which stipulates that the fibre angle is related to the aspect ratio of the elliptical projection of the fibres which have been cut at an angle other than 0°. The maximum fibre misalignment with regards to the as-designed 0° in-plane orientation is recorded.
M	Waviness-affected region span [CPT]	Length of the waviness-affected region	The waviness-affected region is determined by visual inspection of the cross-sectional micrographs. Regions of severe full-ply waviness were seen in and around the wrinkling sites based on the visual ellipse analysis. The waviness length span is delimited by the regions where the ply returns to full-ply nominal ellipse profiles. The region span is measured along the mid-line of the part.

Two original analysis methods have been tried with the aim to develop new means of quantifying waviness: in-plane microscopy and cross-sectional micrograph ellipse reconstruction. These methods aim to generate information on the characteristics of waves such as amplitude and span which can later help interpret the waviness formation physics during forming. Additionally, they aim to provide data on the trapped length due to waviness.

B.3 Spring-in measurements

Spring-in is a cure-induced phenomena that leads to the final cured part angle to be different from the mould it was cured on. It has been largely attributed to the difference in coefficients of thermal expansion between the part and the mould, and due to the anisotropy of the corner [35]. The relationships between fibre misalignment and spring-in have been investigated by Çınar and Ersoy as they cross-examined spring-in with the occurrence of fibre misalignments in L-shaped corner regions [36]. By inducing waviness in corners, it was determined that the increase in fibre waviness in the corner sections of 4-ply L-shapes decreased the level of spring-in.

Mould-side surfaces were sprayed with an even coat of developer (a solution of acetone, isopropyl alcohol, and talc powder) in preparation for spring-in angle measurements using a coordinate measuring machine (CMM) equipped with a non-contact cross laser scanning head. Using the Nikon Focus software package, planes were best-fitted to approximately 40 measured points on each surface extending through the full length of the flange and web. The dot product of each plane's normal vector was computed to determine the angle between the flanges and the web. The same procedure was utilized for measuring the mould surface whereupon the part angle was subtracted from the mould angle to obtain the spring-in angle. The developer was wiped off and the parts were sectioned in preparation for optical microscopy.

B.4 Method development: in-plane microscopy

In the case of the parts that were manufactured, the bulk of waviness that was seen from the cross-sectional micrographs occurred in the flange. Given that the flanges in these experiments were flat sections, it was possible to perform optical microscopy on an in-plane section of the

part. The planes were chosen based on guidance from cross-sectional microscopy results. Two samples were ground using this method. One sample exhibited pure waviness in its mould-side 0° ply with no wrinkling; the other sample showed a combination of wrinkling and waviness of the same ply.

In order to generate an in-plane micrograph for the non-wrinkled part, grinding planes were taken parallel to the lamina plane, allowing for a full image of the waviness in question. In the case where the 0° ply was wrinkled, no single parallel plane existed that passed through the entirety of the ply since the ply's path wrinkles by more than the ply's thickness. Therefore, in this case, a plane angled through the part's width was taken in order to get a single image that shows waviness data for the entire ply under the assumption that the ply waviness profile is uniform along the width of the part. It is important to note that the grinding plane cannot follow the part's curvature over the radius of the part, thus resulting in waviness data loss in the flange radii.

Unlike wrinkles that typically appeared as peaks rather than fully-reversing waves, waves appeared as fully reversing waves. Thus, in this analysis, a wave has both a minimum and a maximum. The waves were traced following continuous fibres where possible; piece-wise waviness portions in the case of the wrinkled part were aligned to generate a constant fibre path throughout the flange. Waves were then quantified with respect to the following metrics:

Table B.4-1. In plane micrograph quantification method

	Measurement	Description	Method
N	Location of Minimum [CPT]	The wave's minimum's distance from the radius's mid-corner (45° into the corner)	Length along the mid-line path of the part from the origin at mid-corner to the wave's minimum, where positive (+) locations are toward the flange termination and negative (-) locations are towards the web.
O	Location of Maximum [CPT]	The wave's maximum's distance from the radius's mid-corner (45° into the corner)	Length along the mid-line path of the part from the origin at mid-corner to the wave's maximum, where positive (+) locations are toward the flange termination and negative (-) locations are towards the web.
P	Wave amplitude [CPT]	The amplitude of the wave	Given the waves' tendency to be fully reversing (having a maximum and a minimum prior to returning to flat), the wave amplitudes were quantified by taking the average of the maximum's and the minimum's amplitudes.
Q	Maximum deviation angle [degrees]	Maximum fibre misalignment angle due to waviness	The fibre angle through the wave is measured. The maximum value is selected.
R	Length Span [CPT]	Length of the region affected by a particular wave.	Length, termed 'R', along the as-designed path between 'wave bounds'. The wave bounds are determined by the region where the fibres change from the as-designed orientation to a given angle, containing a maximum and a minimum.

	Measurement	Description	Method
S	Waviness excess length per wave [CPT]	Path length excess from the as-designed path due to waviness: a defect severity index	The wave is traced and measured via individual arc length segments, dubbed 'S_n'. The length span, ie the wave's as-designed length, is subtracted from the total wrinkle path length to give the excess length due to the wave. The excess length, 'S' is thus represented by the following equation: $$S = \sum S_n - R$$
T	Waviness total excess length in flange [CPT]	Total excess length in the flange due to waviness : a defect severity index	Summation of excess lengths for all waves in a particular flange.

B.5 Method development: waviness path reconstruction

The second waviness measurement method was inspired by the Yurgartis ellipse diameter ratio method which stipulates that if a fibre is cut at an angle ω from the fibre axis, the angle can be calculated from the ratio of the resulting ellipse minor diameter, d, and major diameter, l, from the sine function [29]:

$$\sin \omega = \frac{d}{l} \tag{7–1}$$

Where the Yurgartis method suggests cutting samples at a 5° offset of the nominal 0° ply's fibres of interest, the cross sections were taken exactly parallel to the 0° ply's fibres in order to avoid skewing the thickness data of the web, since the investigated parts are non-flat. In this case, the calculated angle ω corresponds directly to the misalignment angle of the fibre with respect to the nominal direction. From point-measurements of fibre angles (averaging of 3 measurements) at an average spacing of 0.25 mm along the length of the ply, the local fibre angle is applied as a vector over the distance L_x from the midpoint between the previous point and the current point to the midpoint between the next point and the current point, as per Equation (7–2). Staring the next

vector where the previous vector ended, the in-plane fibre path can be reconstructed piece by piece, under the assumption that the waviness is uniform through the width of the part. The concept is illustrated in Figure B.5-1. It is important to note that the measured fibre angles have the tendency to cycle between reaching a maximum misalignment angle and approach the nominal angle of 0° over the length of the flange. Hence, as the angle measurement reaches the nominal fibre angle, the ensuing angle's sign is changed ($-\omega$ in this case) under the assumption that the fibre waviness takes on a sinusoidal shape as opposed to a staircase shape; a reasonable assumption for the tests conducted in this study, as verified by experimental results. This process is repeated, switching from positive to negative over the length of the zone of interest.

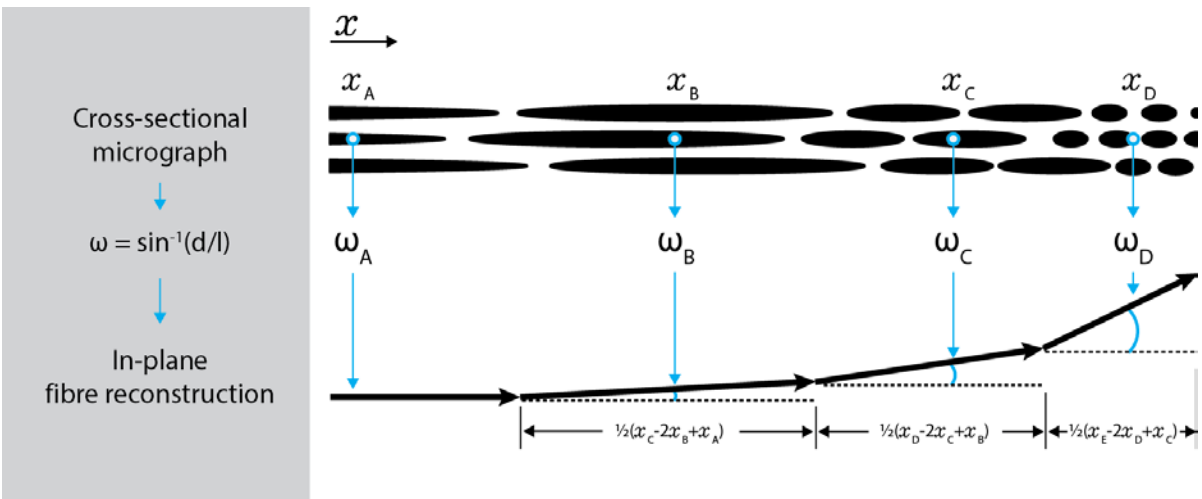

Figure B.5-1. Fibre path reconstruction methodology based on the Yurgartis ellipse aspect ratio to fibre angle relation

$$L_x = \frac{x_{n+1} - x_n}{2} - \frac{x_n - x_{n-1}}{2}$$
$$= \frac{x_{n+1} - 2x_n + x_{n-1}}{2} \qquad (7\text{–}2)$$

Due to the time-consuming nature of these methods, the waviness analyses were only performed on a few samples as proofs of concept of the method, and to gain a first look at the relationships between wrinkles and waviness zones.

B.6 Thermal qualification of forming process

Thermal qualification tests were performed in order to determine the time required for the charge to reach temperature uniformity. Thermocouples were mounted to multiple locations on the forming box, mould, and in the oven as seen in the figures below.

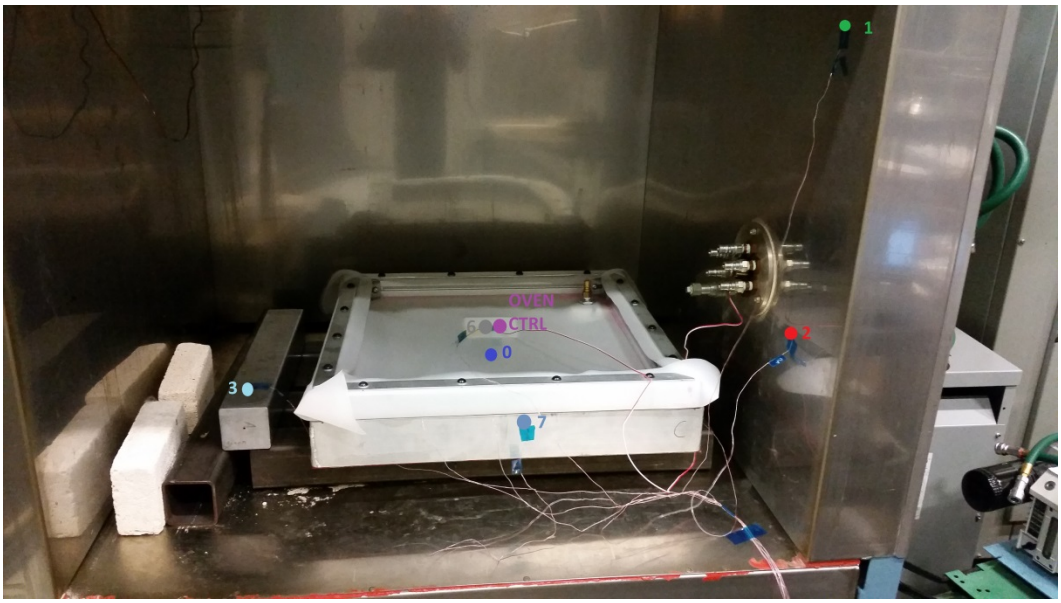

Figure B.6-1. Thermocouple locations within the oven for temperature profiling tests.

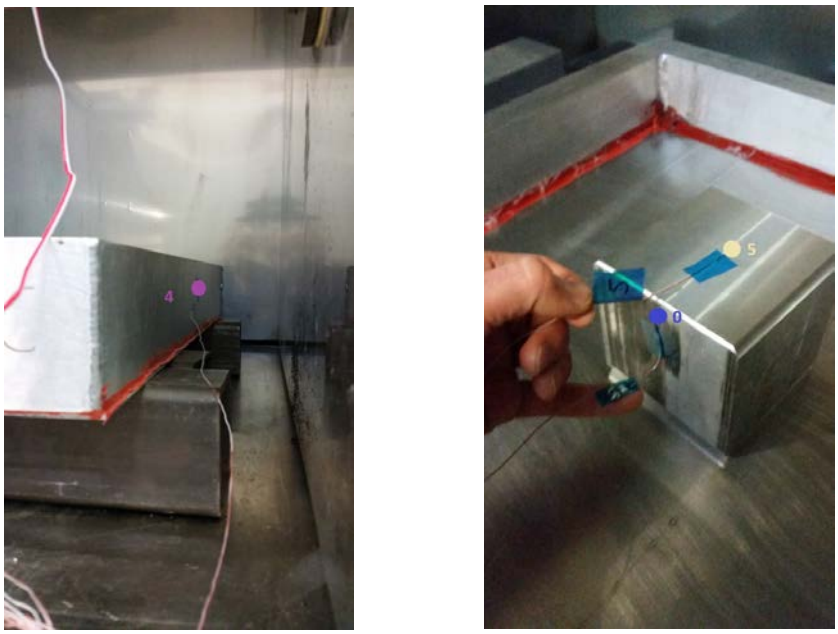

Figure B.6-2 Thermocouple locations on the frame and on the mould for temperature profiling tests.

The oven was first set to 70°C and was left running in order to determine the time required for the oven, forming box, and mould to reach the desired temperature. Environmental temperatures were shown to stabilize after approximately 87 minutes, as shown in Figure B.6-3. The figure shows a drop in temperature due to the opening of the door at approximately 210 minutes.

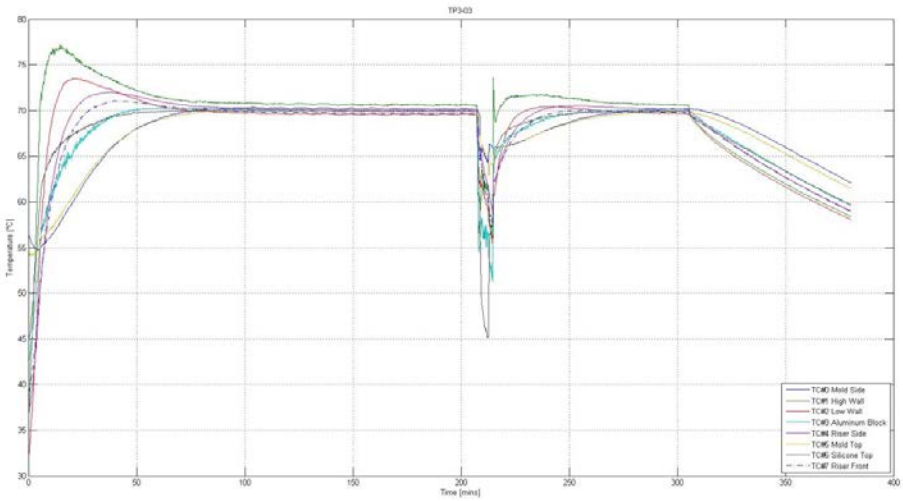

Figure B.6-3. Environmental temperature stability results (Test TP3-03)

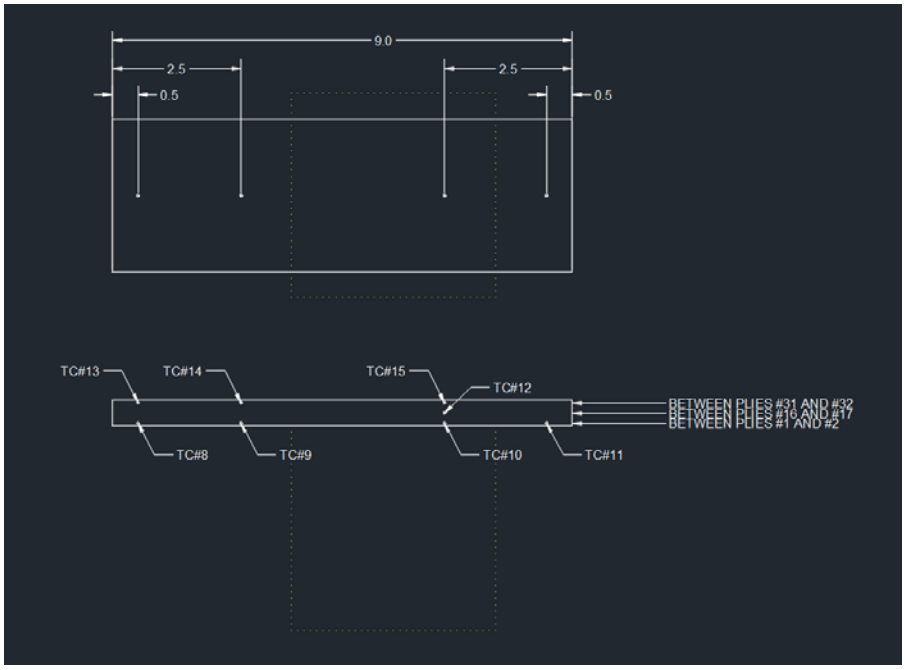

Figure B.6-4. Thermocouple locations within the 32-ply laminate. The mold position is shown in the dotted line.

In a second test, a 32-ply laminate was laid up with thermocouples located near both surfaces and in the middle whose locations within the laminate are sketched in Figure B.6-4. The oven was set to 70°C for 120 minutes to ensure temperature uniformity. The oven door was opened and the charge was quickly transferred to the mould. FEP ply was added and the forming bag frame was clamped in order to simulate the forming preparation process. The oven door was then closed 1 minute and 12 seconds after it had been opened. The laminate temperature data is shown below in Figure B.6-5. Subtracting the minimum thermocouple temperature data from the maximum thermocouple temperature data, the temperature difference within the laminate can be plotted and is shown in Figure B.6-6.

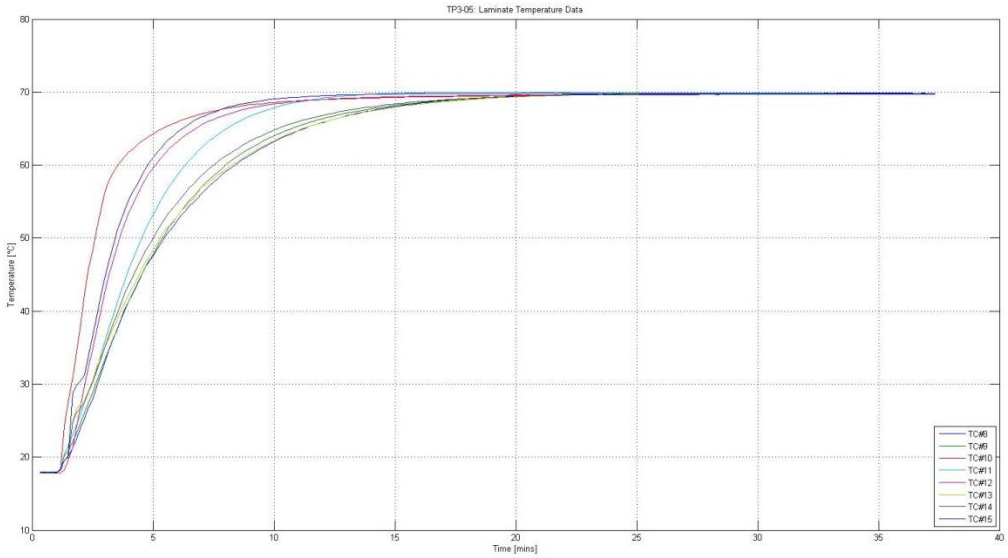

Figure B.6-5. Laminate temperature data after being transferred to the oven, preheated to 70°C.

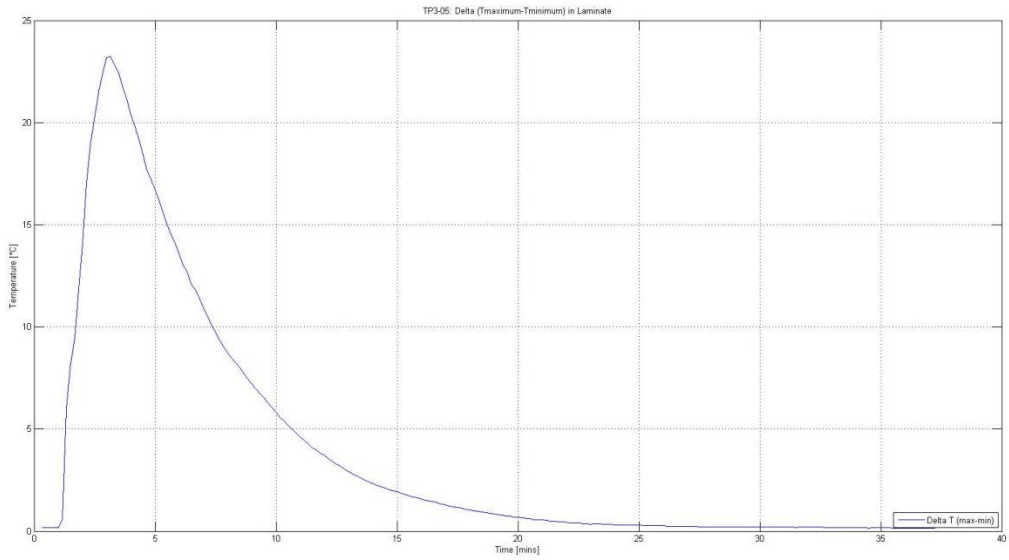

Figure B.6-6. Temperature difference within the laminate

It can be seen that for the laminate to reach maximum attainable temperature a post-transfer heating time of 27 minutes is required. Hence, a heating time of 30 minutes was selected for actual part manufacturing.

Appendix C Additional Analysis

In this section, the outcomes of forming at varying process parameters are presented. Additionally, results from the waviness quantification methods introduced in Sections B.3 and B.5 are examined.

C.1 Ripped bag case

The first part that was drape-formed (‘*Part 1*’) used a slightly thinner silicone membrane (0.030”) and no oak ramps. This led to the tearing of the bag after forming as the nylon quick-clamps were being substituted for the steel C-clamps. Under this circumstance, after forming, pictures were taken of the part directly, rather than from above the silicone membrane. To preserve the part for further analysis and in the absence of a replacement silicone membrane, this part was bagged using a disposable nylon bag in preparation for cure. Given that this bagging material does not stretch significantly, the bag was pleated to conform to the complex geometry of the mould on the plate without tension in order to prevent it from tearing under vacuum

pressure. Special attention was paid to prevent the nylon bagging material from wrinkling on the part.

The equipment was later rebuilt with a thicker silicone bag and oak ramps to prevent bag breakage, as outlined in Section 4.1.3. All further parts were manufactured using the rebuilt apparatus.

C.2 Wrinkling

Effect of forming temperature

The forming temperature has shown to have the largest effect on the occurrence of wrinkling in the manufactured C-channels. As shown in Table A.3-1, no wrinkle was seen in any flange that was formed at 70°C for both the *Quasi* ($[90/+45/-45/0]_{xS}$) and the *Offset* ($[0/-45/+45/90]_{4S}$) ply sequences. The 70°C-formed part quality was thus the same as the hand lay-up baseline. Since the 70°C-formed flanges did not produce any wrinkles, no information is available to address the impact of temperature on wrinkle morphology.

The 30°C-formed long flanges all showed some level of wrinkling. The *Quasi* ply sequence showed minor wrinkling in all short flanges, whereas the *Offset* ply sequence short flange did not wrinkle.

Effect of flange length

Flange length had a significant impact in the occurrence and morphology of wrinkles in the 30°C-formed flanges – the 70°C flanges did not wrinkle. All long (88.9 mm) flanges that were drape-formed at 30°C showed wrinkles whereas all but one of the shorter 38.1 mm flanges showed quantifiable wrinkles. The non-wrinkled short flange belonged to the *Offset* ($[0/-45/+45/90]_{4S}$) ply sequence part.

The short flanges had singular wrinkles whereas the long flanges typically had two or three distinct wrinkles, with the exception of the 64-ply laminate that produced a singular wrinkle. The

short flange wrinkles were generally found nearer to the corner, as illustrated in Figure C.2-1 where the square markers are generally closer to the origin, the mid-corner. By contrast, the long flanges' largest wrinkles were typically found slightly farther along the flange. This is particularly the case when comparing short and long flanges from the same C-channel part, as shown by comparing the same coloured markers in Figure C.2-1. Additionally, the long flanges generally contained wrinkles with greater ply path deviation height, greater maximum deviation angles, and greater trapped excess length than the shorter flanges from the same C-channels, as seen in Table A.3-1, columns C, D, and G and H.

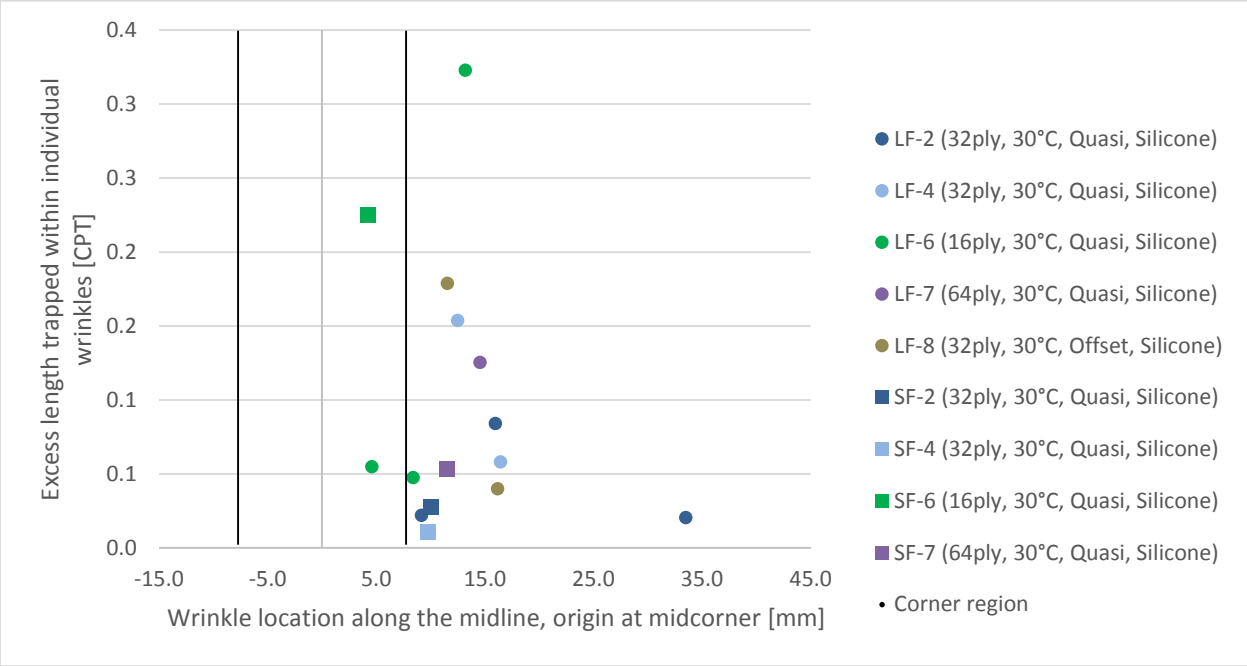

Figure C.2-1. Effect of the flange length on wrinkle locations and wrinkle severity, determined by excess length. The short flanges (squares) generally appear closer to the mid-corner whereas the long flanges generally appear slightly farther along the flange and are typically more severe than the short flange wrinkles of the same part. The region between black bars represents the corner radius region of the mould.

Effect of ply count

16-ply, 32-ply (two trials), and 64-ply laminates of the *Quasi* ($[90/+45/-45/0]_{xS}$) ply sequence can be compared for the long flange and the short flange scenarios in terms of wrinkle severity and wrinkle quantity.

The 16-ply long flange (‘*LF-6*’) contained the most severe wrinkle in terms of ply path deviation height, maximum deviation angle, length span, and trapped excess length due to wrinkling (columns C, D, E, and F in Table A.3-1) when compared to the 32-ply and 64-ply long flange (‘*LF-2*’ and ‘*LF-4*’, and ‘*LF-7*’) wrinkles. Similarly, the 16-ply short flange (‘*SF-6*’) wrinkle exceeded the severity of 32-ply and 64-ply short flange (‘*SF-2*’ and ‘*SF-4*’, and ‘*SF-7*’) wrinkles. It is noteworthy that the severity of the 16-ply short flange wrinkle also exceeded the severity of the wrinkles 32-ply and 64-ply long flanges, particularly in terms of wrinkling excess length trapped in the flange (column G).

No linear relation exists between ply count and trapped excess length in the long flanges considering 16-ply, 32-ply, and 64-ply laminates. Similarly, no linear relation exists between ply count and trapped excess length in the short flanges considering 16-ply, 32-ply, and 64-ply laminates.

With regards to the long flanges, the 16-ply flange shows three distinct wrinkles, the 32-ply flanges show three and two distinct wrinkles, and the 64-ply flange shows one distinct wrinkle. Hence, it would suggest that there may be an inverse correlation between ply count and number of wrinkles in the range of 16 to 64 plies. As all short flanges produced singular wrinkles, no such correlation exists for the short flanges seen in these results.

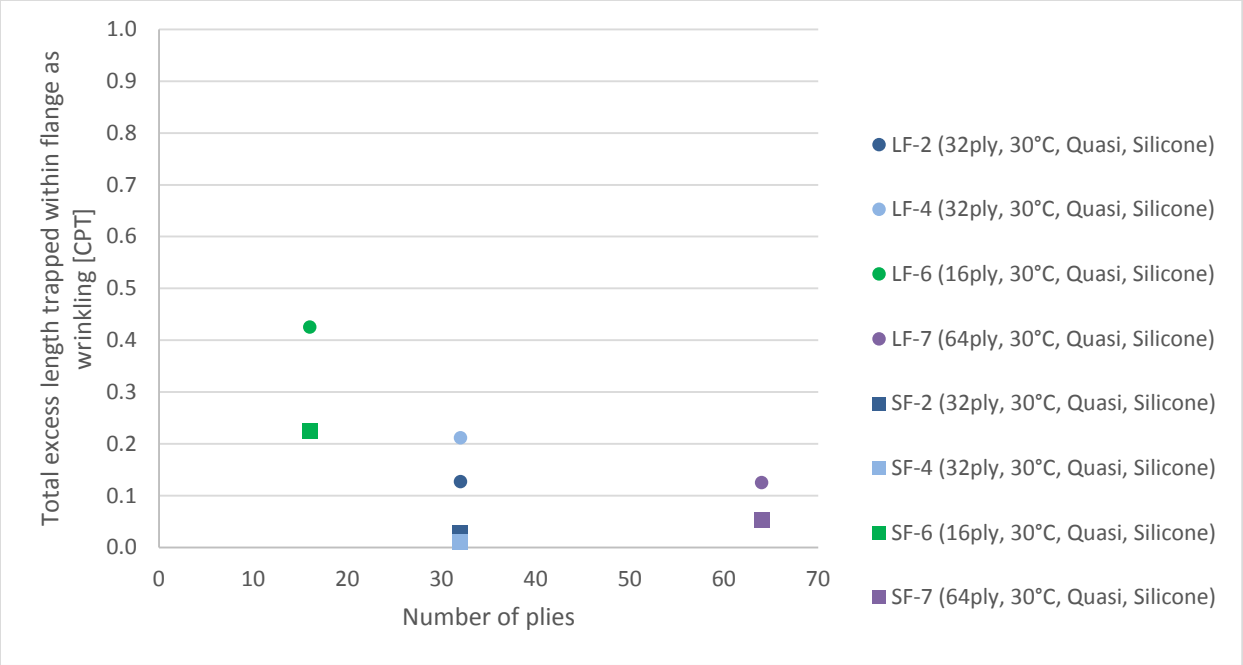

Figure C.2-2. Chart comparing the number of plies to the quantity of excess length trapped as wrinkling within the long (circles) and short (squares) flanges showing the greatest trapped excess length in the thin laminate (16 plies) and in the long flanges.

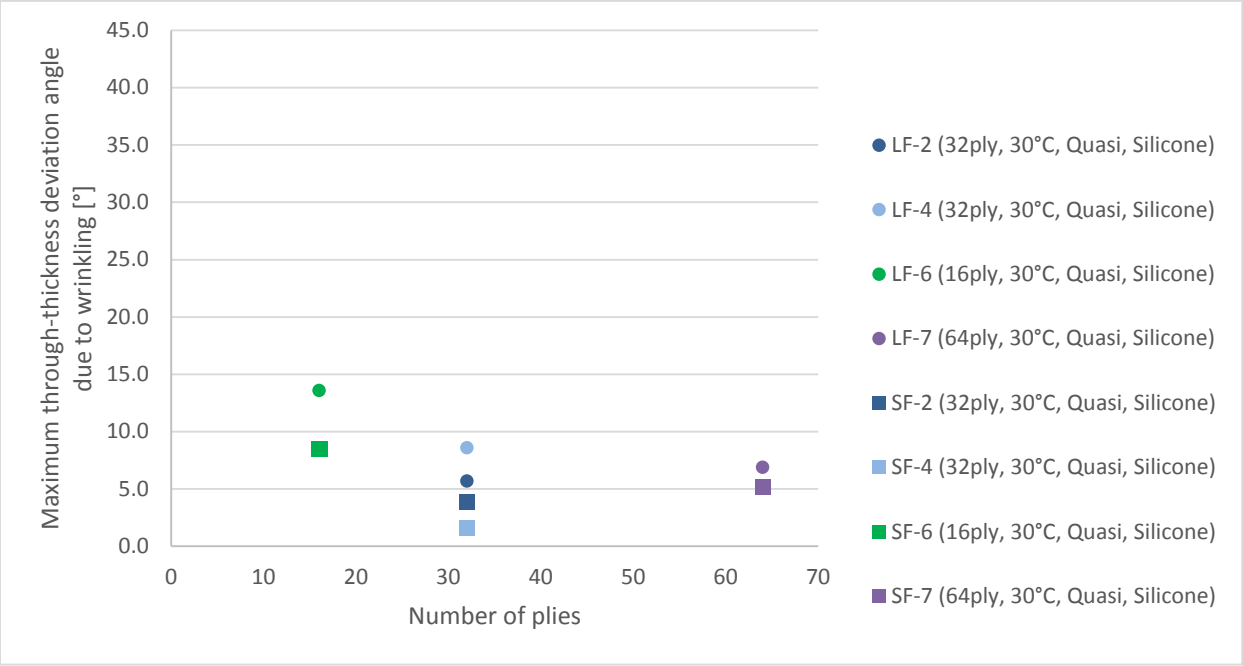

Figure C.2-3. Chart comparing the number of plies to the maximum ply through-thickness deviation angle [°] showing the greatest misalignment of fibres in the thin laminate (16 plies) and in the long flanges.

Effect of ply sequence

The effect of ply sequence on wrinkling severity in long flanges can be investigated by comparing the 30°C-formed *Quasi* ($[90/+45/-45/0]_{4S}$) ply sequence long flanges '*LF-2*' and '*LF-4*' to the *Offset* ($[0/-45/+45/90]_{4S}$) ply sequence long flange '*LF-8*'. It is important to note that the laminate position of the 0° plies cannot be compared directly. The most significantly wrinkled ply in the *Quasi* ply sequence is the ply closest to the mould (ply #4 overall). In contrast, the *Offset* ply sequence shows no wrinkling in the ply closest to the mould (ply #1 overall), but it does show signs of severe waviness. A wrinkled ply is seen the following 0° ply (ply #5 overall) in the same region. With regards to severity, all quantities are of the same order for both ply sequences: number of wrinkles, location, ply path deviation height, maximum deviation angle, length span, and excess length, as seen in Table A.3-1. Figure C.2-4 illustrates the impact of ply sequences (blue versus brown markers) on wrinkling severity, using the maximum deviation angle and trapped excess length metrics. It can be seen that the *Offset* ply sequence did not produce short flange wrinkles whereas the *Quasi* ply sequence flanges showed quantifiable, yet small wrinkles.

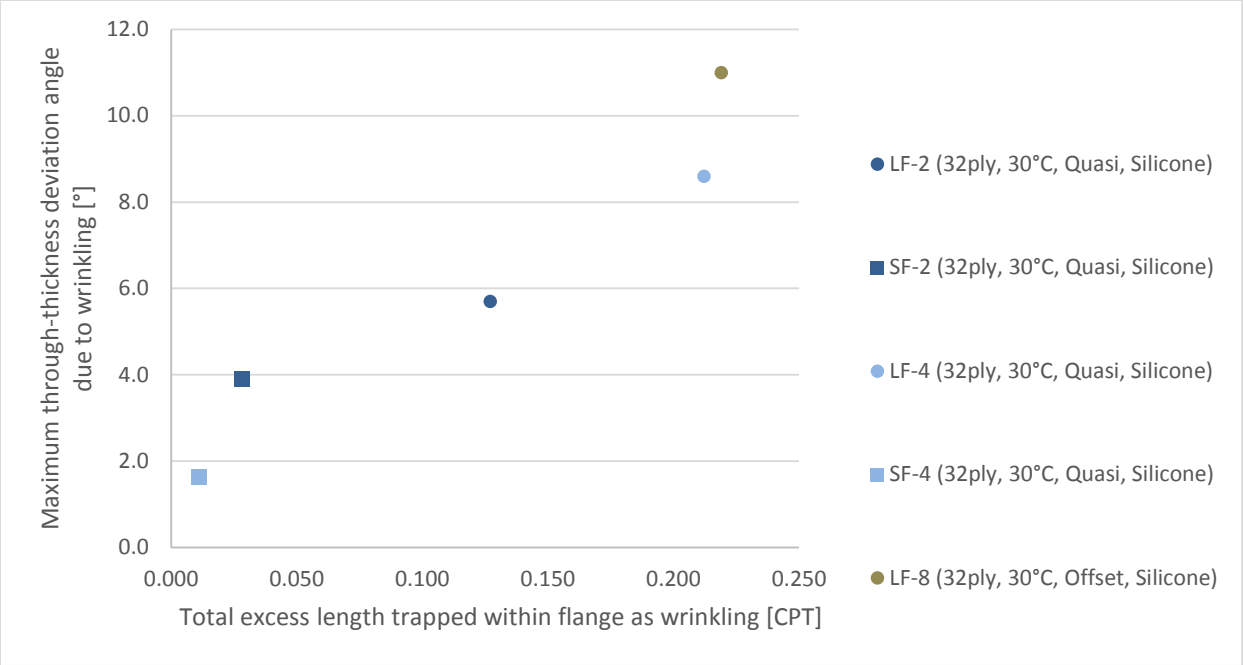

Figure C.2-4. Point cloud comparing the wrinkling severity for Quasi (blues) and Offset (brown) laminates.

Since the 70°C-formed flanges did not wrinkle, nothing can be concluded about the effect of ply sequence on the morphology of wrinkles at high forming temperature.

Effect of forming method

The hand lay-up formed flanges showed no occurrences of wrinkling in either the long or short flanges.

Combined effects of curing bag type and forming bag thickness

The effect of cure bag type on wrinkling severity in long flanges can be investigated by comparing the Nylon-cured flange '*LF-1*' to the otherwise comparative silicone-cured flanges '*LF-2*' and '*LF-4*'. The number of wrinkles and their locations are comparable, but the Nylon-cured long flange wrinkles' ply path deviation height, maximum deviation angle, and excess length far exceed the silicone-cured long flange wrinkles'.

In the case of the short flange counterparts ('*SF-1*' versus '*SF-2*' and '*SF-4*'), the location of the nylon-cured short flange wrinkle is somewhat closer to the mid-corner than the silicone-cured flange wrinkles. All other metrics showing similarities between, the excess length of the nylon-cured short flange wrinkle is several times more significant.

C.3 Waviness

Effect of forming temperature

It can be seen that temperature plays a significant role in the occurrence and severity of waviness in the 0° plies, much as it did for the occurrence of wrinkling. Comparing the 30°C and 70°C-formed long flanges for the *Quasi* ply sequence ($[90/+45/-45/0]_{4S}$), '*LF-2*' and '*LF-4*' versus '*LF-3*' respectively, we see that the 70°C-formed sample did not show any apparent wrinkling. In contrast, measureable waviness of maximum deviation angle (column L) greater than 10° can be seen in both the 30°C-formed long flanges. With regards to the short flanges, the 70°C-formed flange '*SF-3*' also shows no appreciable waviness whereas the 30°C-formed flanges, '*SF-2*' and 'S*F-4*', show waviness whose magnitude is of the same order as their long flange counterparts. The short flange waviness appears to be concentrated nearer to the mid-corner and over a shorter span than in the long (columns K and M). A comparison of the forming temperature and the maximum waviness deviation angle for the *Quasi* ply sequence is shown in Figure C.3-1.

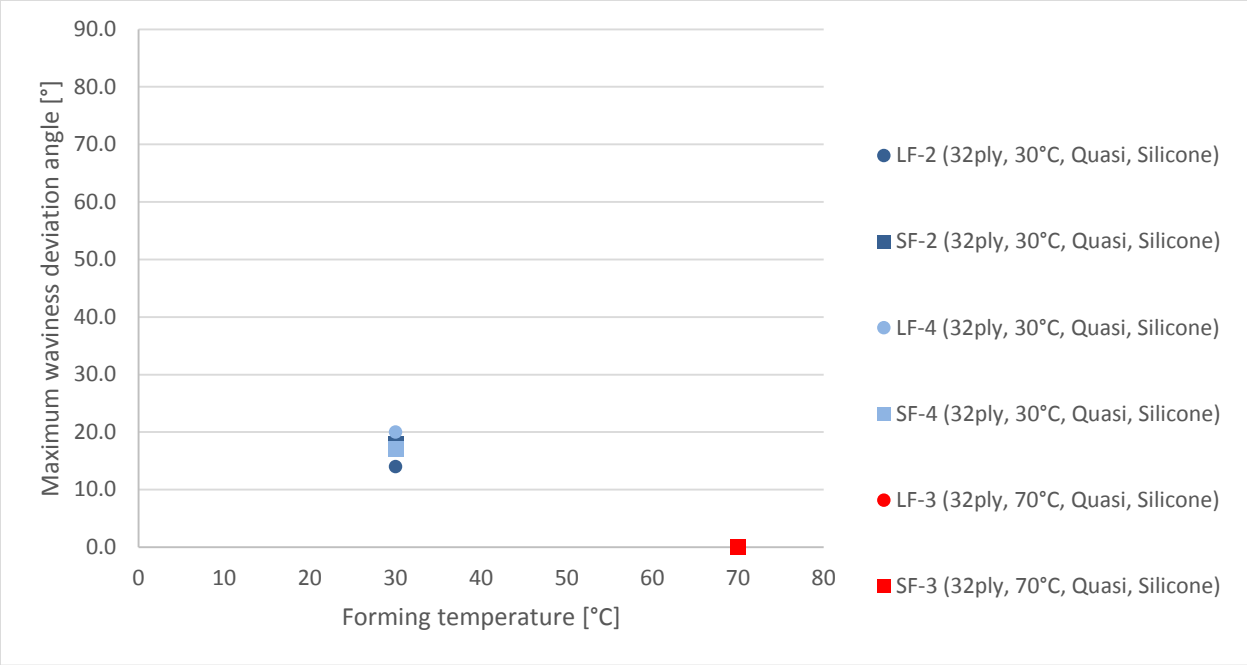

Figure C.3-1. Chart illustrating the impact of the forming temperature on the full-ply waviness deviation angle for the Quasi ply sequence ($[90/+45/-45/0]_{4S}$).

In the case of the *Offset* ply sequence ($[0/-45/+45/90]_{4S}$) parts, the 30°C-formed long flange '*LF-8*' shows very severe full-ply waviness in its mould-side ply (ply #1 overall) showing a maximum deviation angle of 61°. It also contains appreciable full-ply waviness in its following 0° ply (ply #5 overall) that had previously shown wrinkling. The short flange '*SF-8*' also showed significant wrinkling on the order of 30° misalignment, but over a shorter span and closer to the mid-corner (columns M and K). Unlike the 30°C-formed short flanges, the 70°C-formed short flange '*SF-9*' showed waviness, albeit minor (<10° misalignment, as per column L). Similarly, the long flange '*LF-9*' only showed minor waviness: a sharp contrast to the 30°C-formed long flange. A comparison of the forming temperature and the maximum waviness deviation angle for the *Offset* ply sequence is shown in Figure C.3-2.

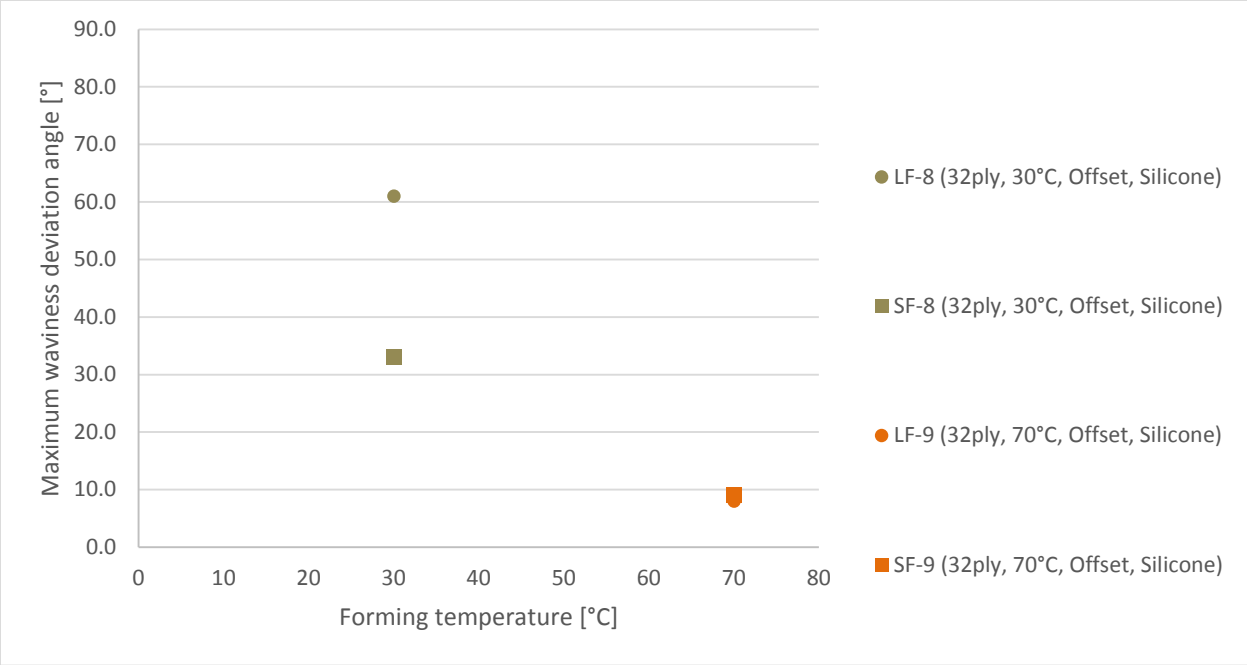

Figure C.3-2. Chart illustrating the impact of the forming temperature on the full-ply waviness deviation angle for the Offset ply sequence ($[0/-45/+45/90]_{4S}$). Data refers to the mould-side ply (ply #1 overall)

Effect of flange length

The effect of flange length on full-ply waviness can be determined by comparing each short flange to its long flange counterpart. Most long-and-short flange pairs show similar maximum deviation angles (column L) to each other, but the long flanges all show greater region spans (column M). The long flange waviness regions also typically appear slightly farther into the flange, on the order of 5-10 mm, than the short flanges which appear closer to the mid-corner; the exception being the 70°C-formed *Offset* flanges (‘*LF-9*’ and ‘*SF-9*’) who show similar waviness region locations. This relationship is plotted in Figure C.3-3.

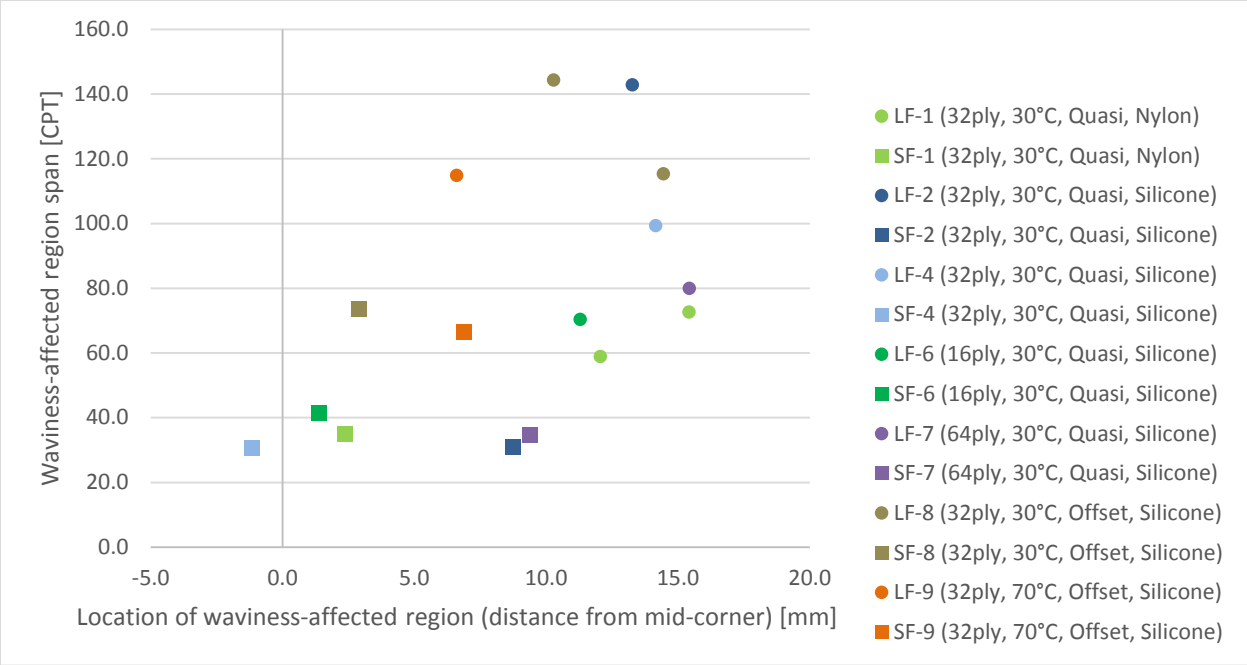

Figure C.3-3. Point cloud illustrating the impact of flange length on the location and span of waviness regions, showing distinct groupings for the long flange waves (circles) and short flange waves (squares).

Effect of ply count

The effect of ply count can be determined by comparing *Quasi* ply sequence 16-ply, 32-ply, and 64-ply trials (trials '*6*', '*2*' & '*4*', and '*7*' respectively) for the long and short flanges. With regards to the long flanges, the waviness-affected region locations (column K) show similarity but no particular trend is apparent for the region span (column M): see Figure C.3-4. Conversely, for the short flanges, the waviness-affected region locations (column K) show no similarity but the region span are quite similar (column M): Figure C.3-4.

Plotting maximum waviness deviation angle versus ply count for both the long and short flange as seen in Figure C.3-5 shows a possible inverse relationship. The thinner 16-ply flanges show the greatest maximum waviness deviation angle and the 64-ply flanges show the lowest with the 32-ply flanges showing noise in between.

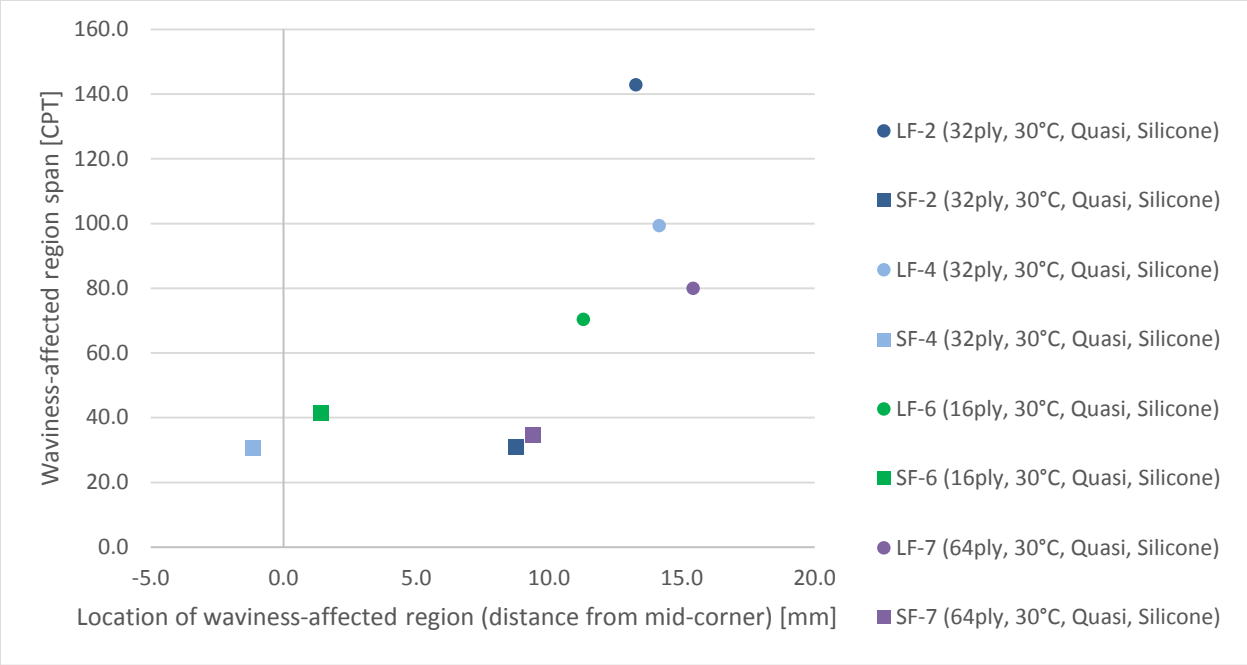

Figure C.3-4. Impact of the number of plies on the location and span of waviness regions showing an approximately vertical grouping for the long flanges and an approximately horizontal grouping for the short flanges.

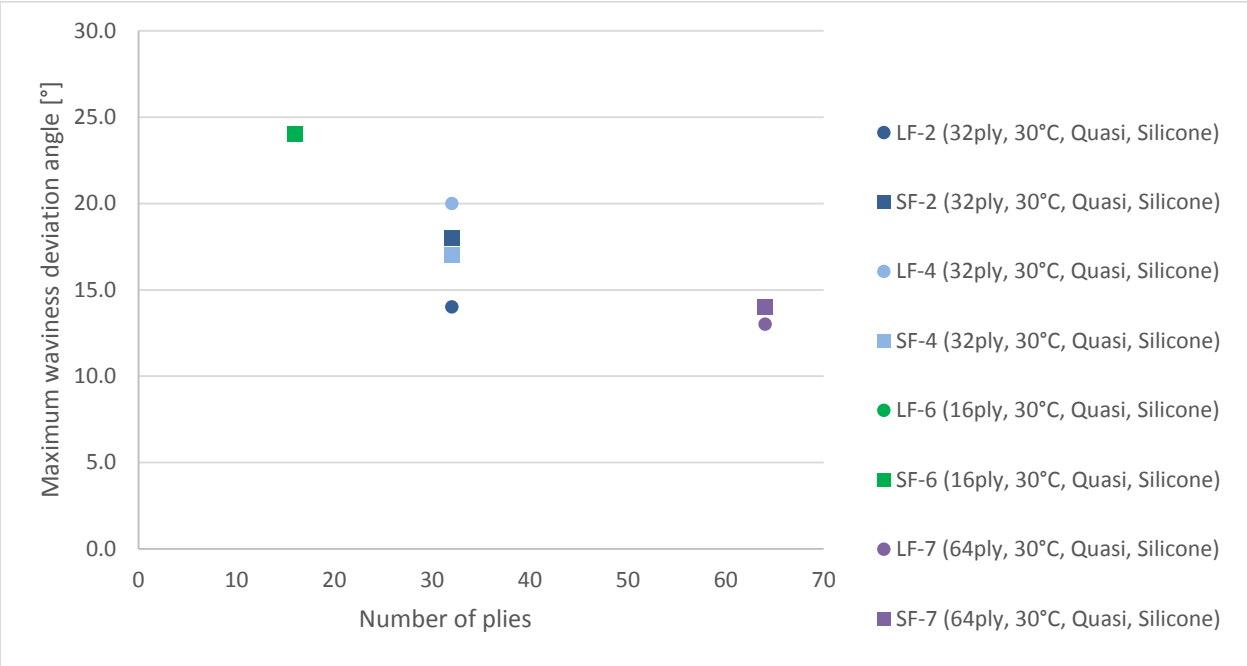

Figure C.3-5. Maximum waviness deviation angle versus ply count for both the long and short flange showing a possible downward trend

Effect of ply sequence

The effect of ply sequence on full-ply waviness can be determined by the comparison of trials '*3*' and '*9*' for the 70°C-formed parts and the comparison of trials '*2*' & '*4*' and '*8*' for the 30°C-formed parts.

With regards to the parts formed at 70°C, both *Quasi* ply sequence flanges ('*LF-3*' and '*SF-3*') showed no appreciable full-ply waviness. For the *Offset* ply sequence, both flanges ('*LF-9*' and '*SF-9*') showed measurable, albeit very minor (<10°) in-plane fibre deviation (column L).

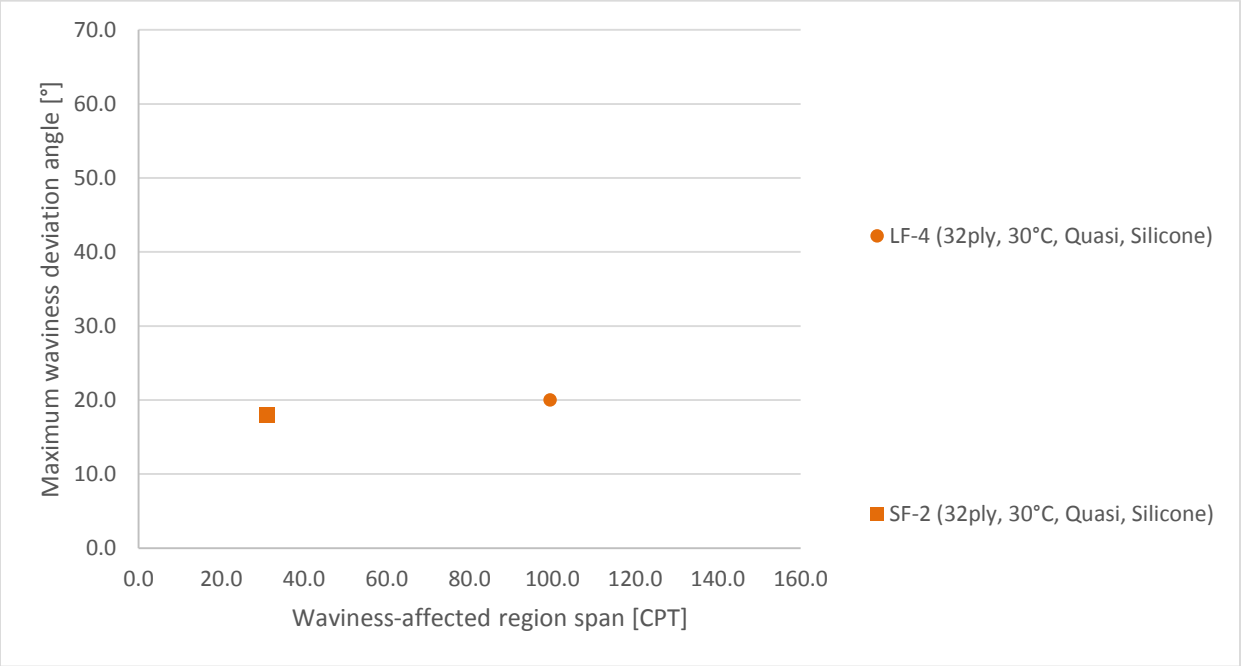

Figure C.3-6. Figure shows non-zero waviness for the Offset flanges whereas the Quasi flanges did not produce full-ply waviness. The scale corresponds to the following figure.

In the case of the 30°C-formed parts, the *Offset* ply sequence flanges ('*LF-8*' and '*SF-8*') showed significantly greater angular deviation (column L) in their mould-side ply (ply #1 overall) than both the *Quasi* ply sequence flanges ('*LF-2*', '*LF-4*', '*SF-2*', and '*SF-4*', 3rd ply overall). '*LF-8*' also showed waviness in its 5th ply overall that was of similar angular deviation angle to the *Quasi* flanges.

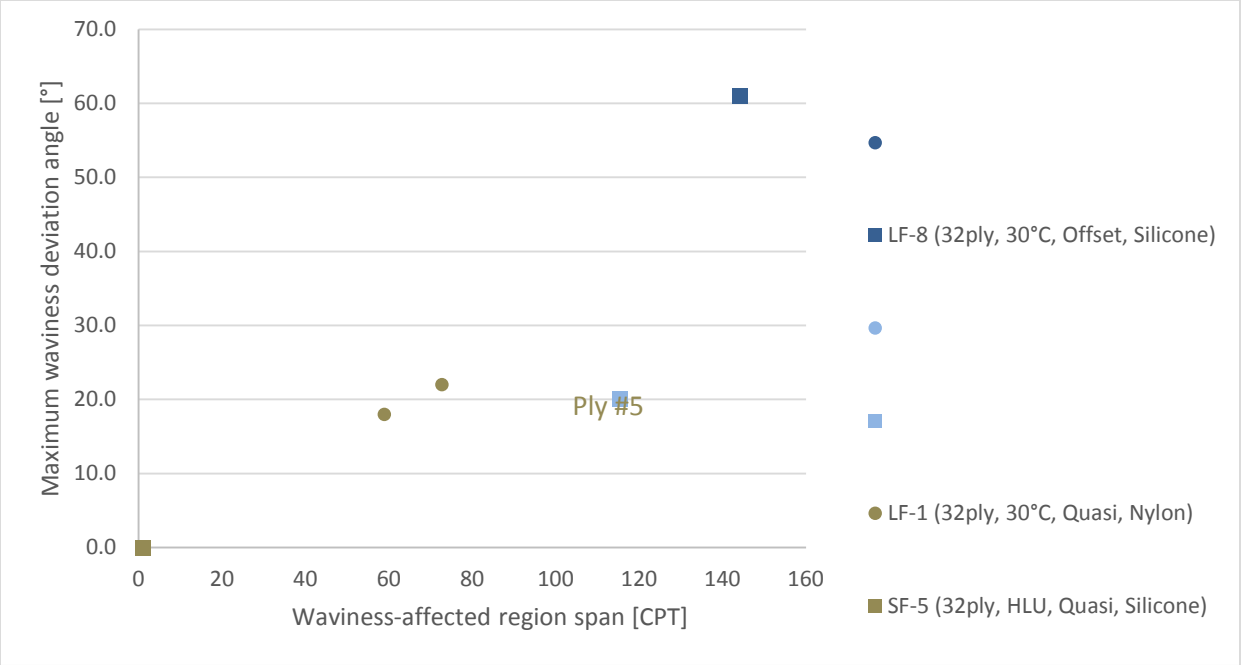

Figure C.3-7. Ply sequence impacts on the waviness region span and waviness deviation angle for the 30°C-formed samples showing greater waviness by both metrics for the Offset flanges.

Effect of forming method

The hand lay-up flanges did not show any full-ply waviness in either the long or the short flanges (‘*LF-5*’ and ‘*SF-5*’) whereas the drape-formed flanges generally did.

Combined effects of curing bag type and forming bag thickness

The Nylon-cured flanges (‘*LF-1*’ and ‘*SF-1*’) showed similar wavinuess results in all metrics (columns K, L, and M) to the comparable silicone-cured flanges (‘*LF-2*’, ‘*LF-4*’, ‘*SF-2*’, and ‘*SF-4*’).

C.4 Thickness profile

Thickness profiles are measured and plotted according to the methodology introduced in Section 4.2.2.2.

Effect of forming temperature

The effects of forming temperature on thickness profiles can be determined by comparing trials '*Part 2*' & '*Part 4*' versus '*Part 3*' for the *Quasi* ply sequence ($[90/+45/-45/0]_{xS}$) for both long and short flanges, and by comparing trials '*Part 7*' and '*Part 9*' for the *Offset* ply sequence ($[0/-45/+45/90]_{4S}$) for both long and short flanges.

With regards to the *Quasi* ply sequence parts, thickness profiles are plotted Figure C.4-1 for the 88.9 mm long flanges ('*LF*'). Generally speaking, the curve shapes appear to be quite similar for all three trials. Thinning can be seen at the corner on the order of a 10% thickness reduction. Left and right of the origin, thickness growth regions on the order of 5-7% can be seen. Thickness stabilization can be seen farther along the flange. The thickness drops off near the end of the flange. The 70°C-formed flange '*LF-3'* shows marginally better symmetry about the origin in the ± 25 mm region than the 30°C-formed flanges. The 70°C-formed flange also shows a smoother curve overall and a greater flange thickness in the 40-70 mm region. The '*LF-4*' sample shows greater skewing of peak heights on either side of the origin than the other 30°C-formed flange, '*LF-2*'.

The *Quasi* ply sequence thickness profile results are plotted in Figure C.4-2 for the 38.1 mm short flanges ('*SF*'). In this case, the three thickness profiles show much similarity in overall shape, and curve smoothness. The 30°C-formed '*LF-4*' shows marginally shorter peaks on either side of the origin and a wider flange-side peak (positive direction) than the two other trials. The 70°C-formed flange's corner region – the valley – is generally flatter than the 30°C- formed parts. All three trials have larger flange-side peaks than their web-side peaks.

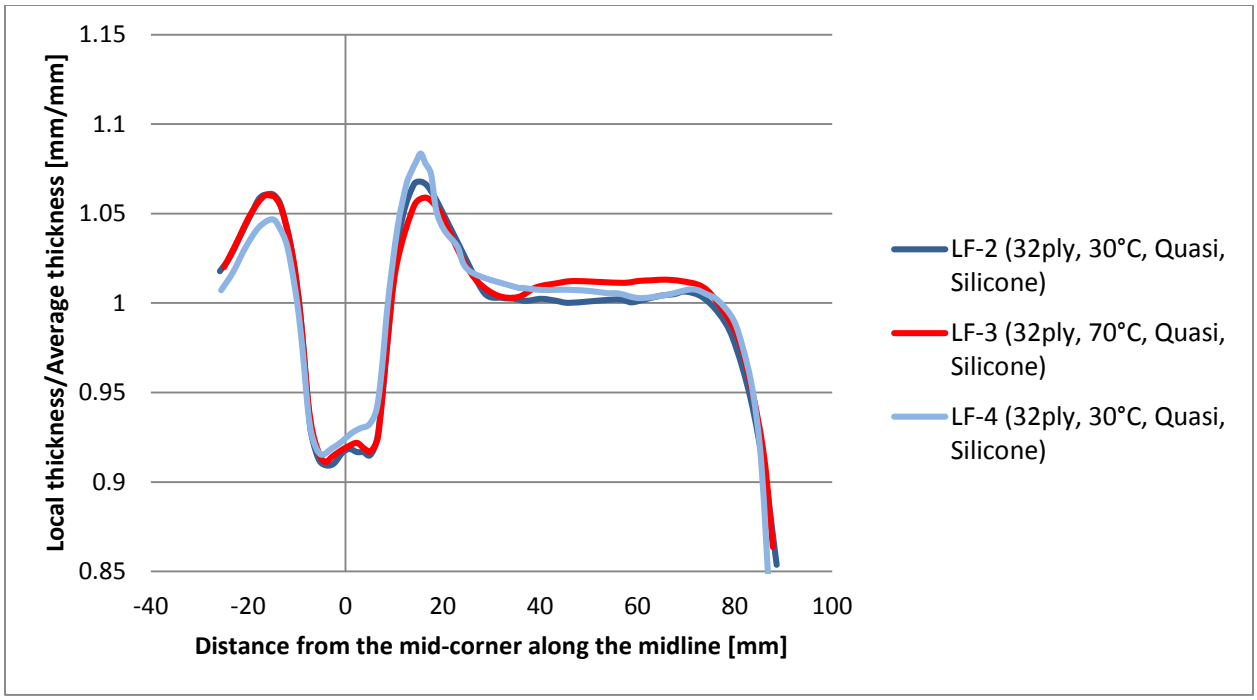

Figure C.4-1. Effect of forming temperature on Quasi long flange thickness profiles with wrinkle x-location overlays

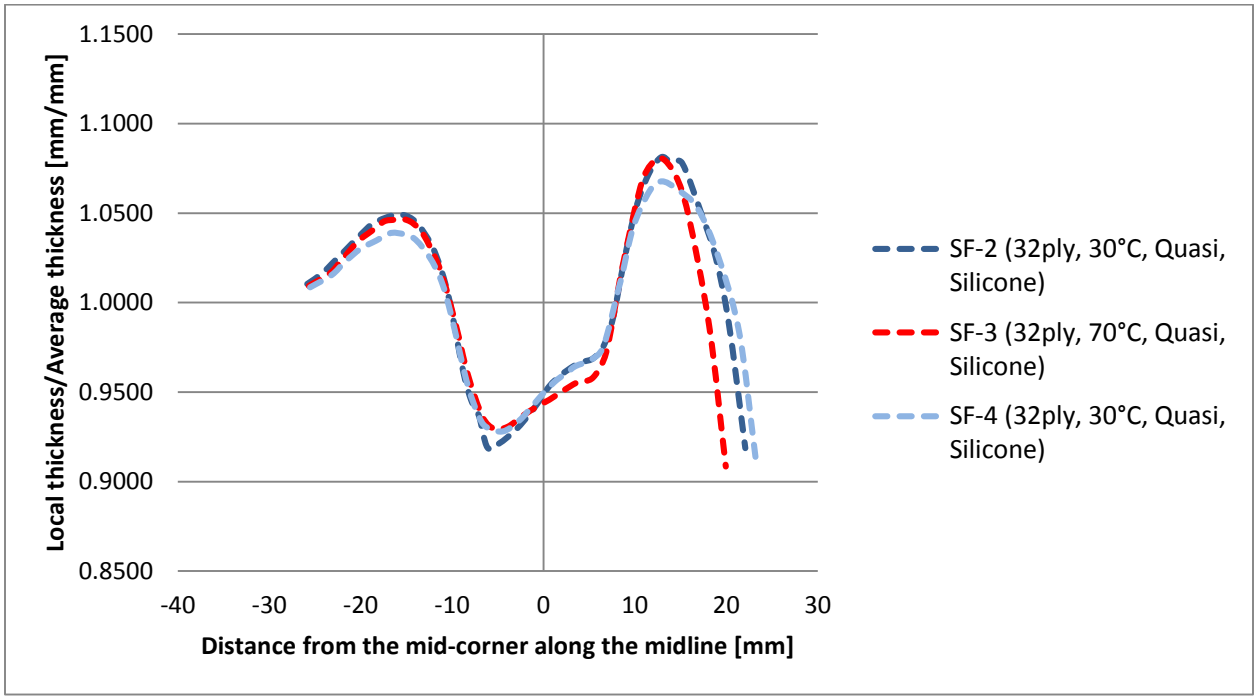

Figure C.4-2. Effect of forming temperature on Quasi short flange thickness profiles

For the 90° *Offset* ply sequence, the forming temperature effects on laminate thickness are compared in Figure C.4-3 for the 88.9 mm flanges. Both flanges see considerable corner thinning on the order of a 10% reduction. The peaks show approximately equal heights and widths on either side of the origin for both tests. The 70°C-formed flange mid-corner shows two minor valleys of similar depth whereas the 30°C-formed test shows a deeper single valley on the web-side. Both flanges show considerable noise in the flange regions between 20-75 mm from the mid-corner where the 70°C-formed flange shows two major dips (at 40 and 70 mm) and the 30°C-formed flange shows a single dip at 70 mm.

Figure C.4-4 compares the thickness profiles for the *Offset* ply sequence 38.1 mm short flanges. Both curves are generally quite smooth with peaks of similar widths. The flange-side peaks show greater height than the web-side peaks for both flanges; the 70°C-formed flange's right peak has 2% CPT greater height than that of the 30°C-formed flange. The 30°C-flange has a mid-corner valley with a steeper slope than that of the 70°C-formed flange.

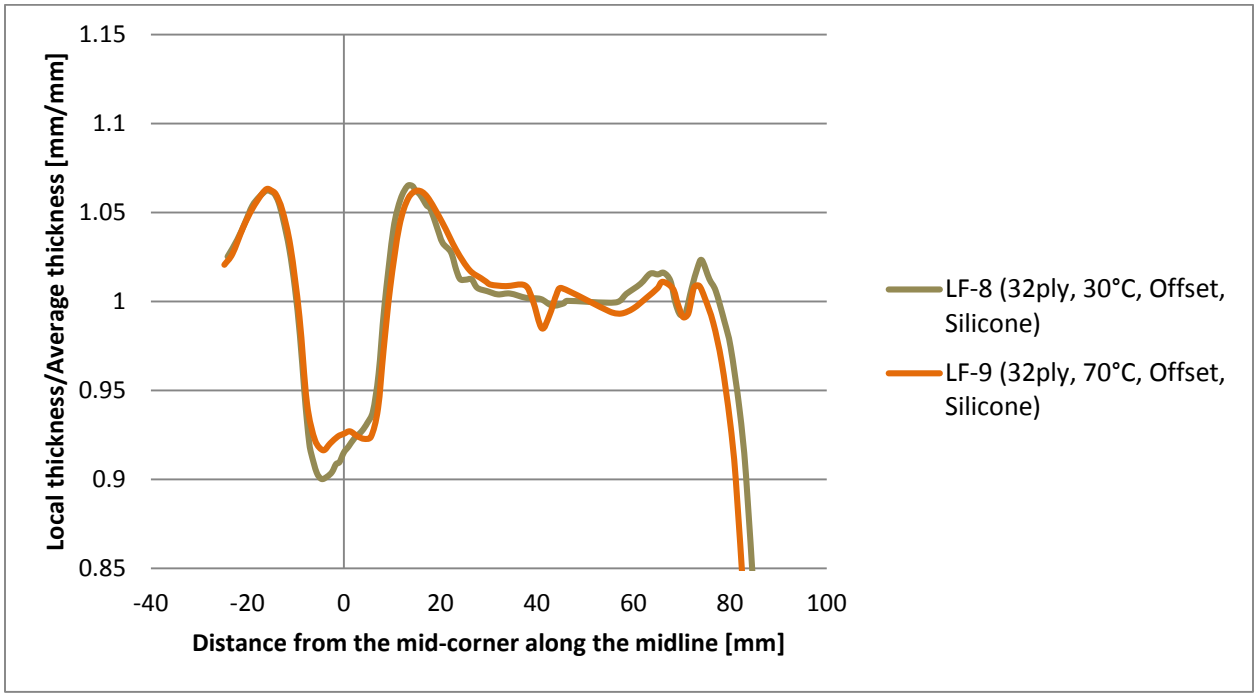

Figure C.4-3. Effect of forming temperature on Offset long flange thickness profiles

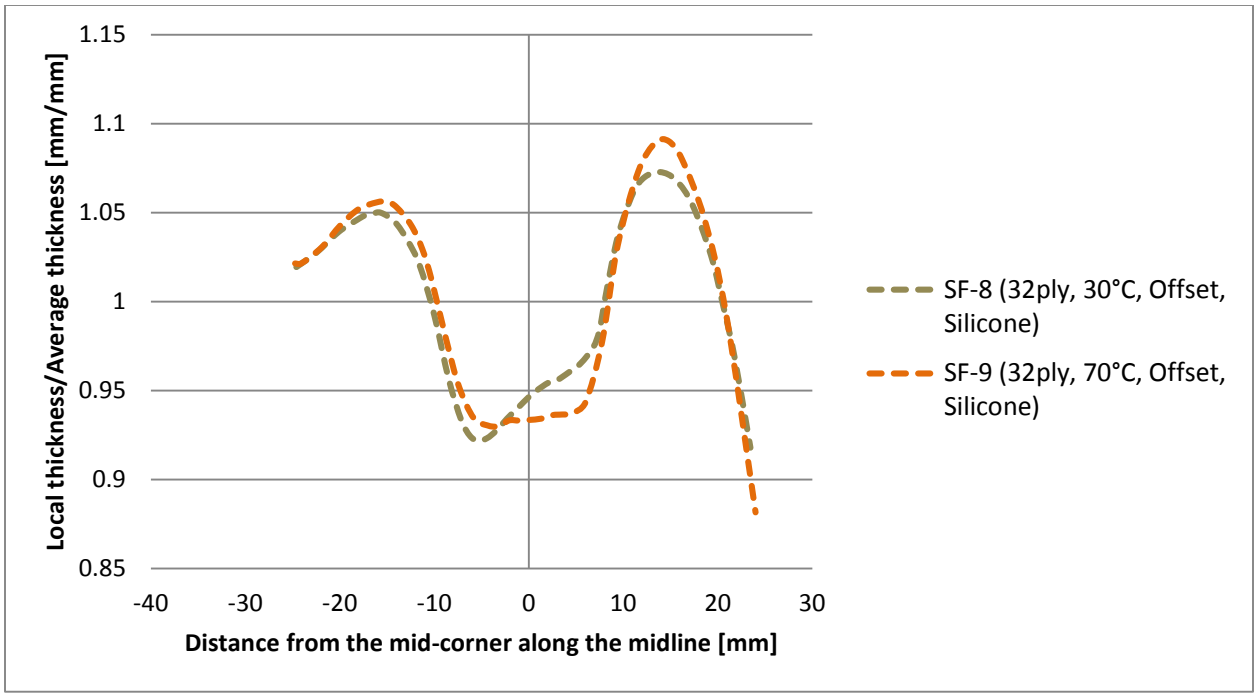

Figure C.4-4. Effect of forming temperature on Offset short flange thickness profiles

Effect of flange length

The flange length effects on thickness profiles can be investigated by comparing the long flange samples to the short flange samples from the same part (i.e. manufacturing conditions). All silicone-cured flanges are presented in Figure C.4-5, whereas the Nylon-cured flanges are presented in Figure C.4-6. For the silicone-cured parts, the long flanges show approximately uniform thickness zones in the flanges whereas the short flange thickness drops off immediately at the peak region. The long flanges generally show flatter two-valley mid-corners whereas the short flanges show raised valleys with steeper slopes up to the flange-side peaks.

In the case of the Nylon-cured part, both long and short flanges show significant bumpiness in their thickness profiles with growth changes ranging from +5% to -2% CPT. The long flange corner region shows large bumpiness before smoothing out in the length of the flange.

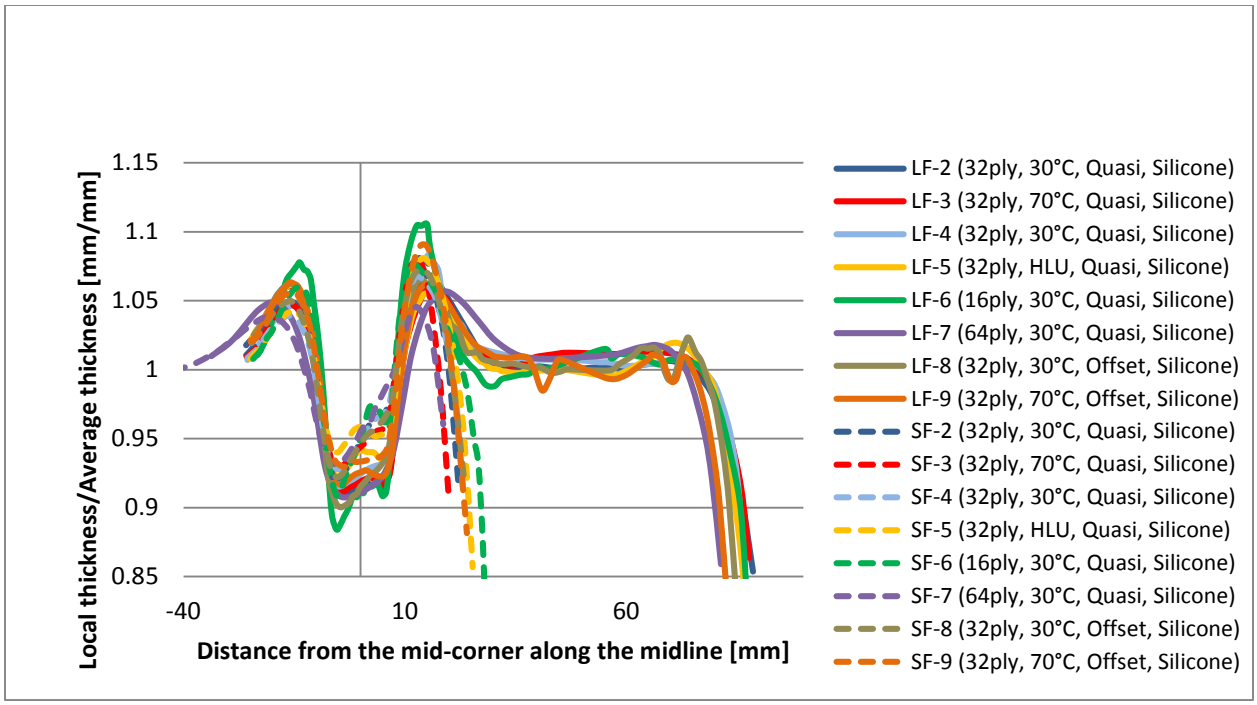

Figure C.4-5. Effect of flange length on thickness profile for all silicone-cured flanges where the solid lines represent long flanges and the dotted lines represent short flanges

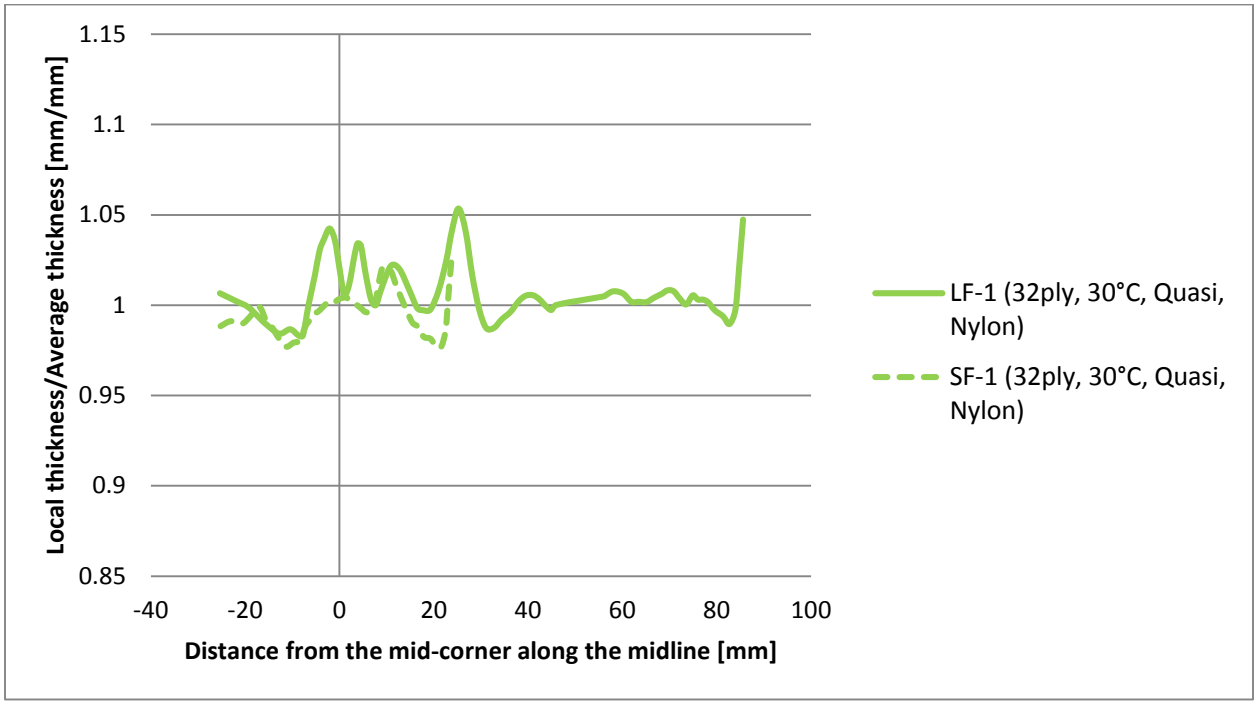

Figure C.4-6. Effect of flange length on thickness profile for all Nylon-cured flanges

Effect of ply count

The effect of ply count can be assessed for *Quasi* ply sequence by comparing the 16-ply, 32-ply, and 64-ply trials (trials '*6*', '*2*' & '*4*', and '*7*' respectively) for the long and short flanges. With regards to the long flanges, as seen in Figure C.4-7, it can be seen that corner thinning occurs at the mid-corner by approximately 8% of the total thickness of the part at its minimum, regardless of the number of plies. Contrastingly, the peaks for the 16-ply flange are tall and thin whereas the 64-ply flange is short and wide with the 32-ply flanges in between. The 16-ply flange shows the greatest bumpiness over the length of the profile, the 64-ply flange shows the smoothest profile, and the 32-ply flanges are in between. All three flanges show a thickness rise prior to the flange termination.

The trends with regards to the short flanges aren't as clear, though offer similarities in the ways that the thicker laminates show the greatest profile smoothness; the thickness profiles are plotted in Figure C.4-8. Here, all four curves show similar slopes in the mid-corner valley. Though as for the long flanges, the 16-ply short flange shows a distinct dual valley feature in the mid-corner. The 64-ply short flange flange-side peak is significantly thinner than its web-side peak though both peaks are approximately the same height. The 16-ply and 32-ply flanges show taller peaks in the flange-side.

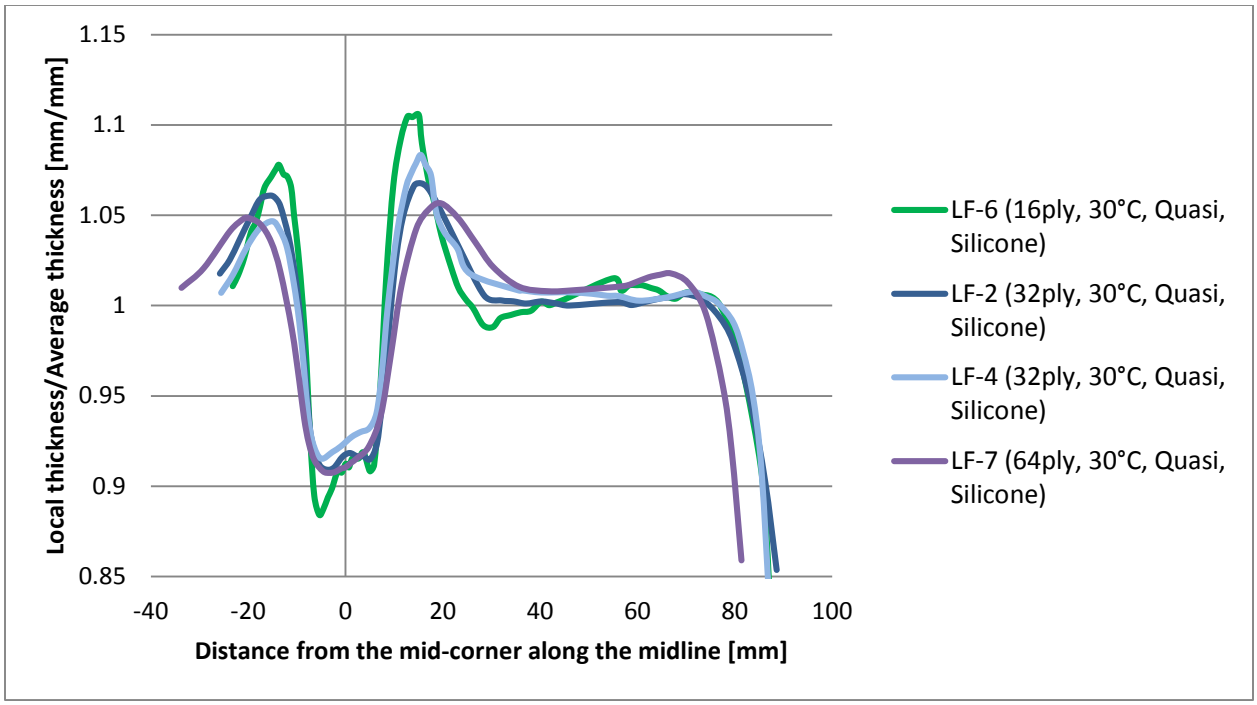

Figure C.4-7. Effect of ply count on long flange thickness profiles

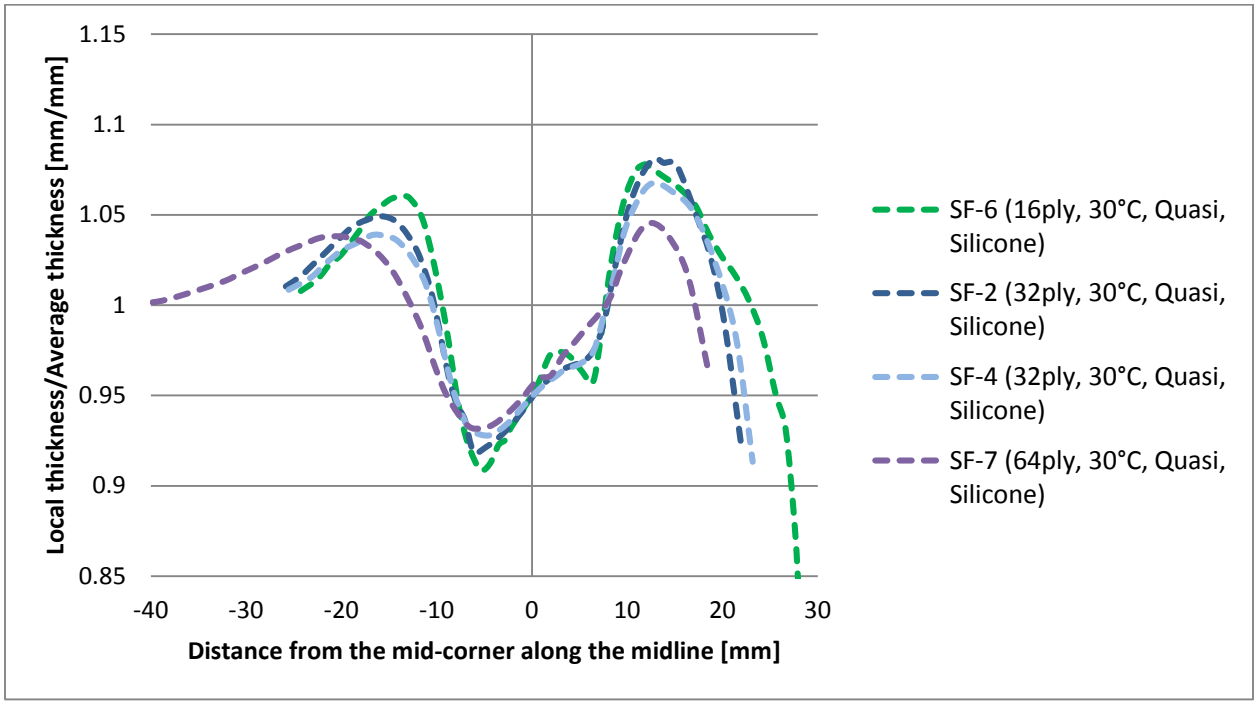

Figure C.4-8. Effect of ply count on short flange thickness profiles

It is important to note that as laminate thicknesses are varied, the method of using the midline of the between thickness measurements will artificially stretch or compress the corner's thickness

profile in the x-direction. This skewing effect can be calculated by the difference in path lengths seen in the sample mid-lines over the 90° corner. Using the 32-ply midline as a baseline, the 64-ply thickness profile sees an x-wise stretch in the corner region of approximately 6 mm (3 mm on either side of the origin) as determined by:

$$\begin{aligned}\Delta S_{64\text{ vs }32} &= \Delta R \cdot \theta \\ &= \frac{h_{64@midcorner} - h_{32@midcorner}}{2} \cdot \frac{\pi}{2} \\ &= \frac{(8.00 - 3.98) \cdot \pi}{2} \\ &= 6.31 \text{ mm}\end{aligned}$$

Similarly, the 16-ply thickness profile sees an x-wise thinning in the corner region of approximately 3 mm (1.5 mm on either side of the origin) as determined by:

$$\begin{aligned}\Delta S_{16\text{ vs }32} &= \Delta R \cdot \theta \\ &= \frac{h_{16@midcorner} - h_{32@midcorner}}{2} \cdot \frac{\pi}{2} \\ &= \frac{(1.99 - 3.98) \cdot \pi}{2} \\ &= -3.13 \text{ mm}\end{aligned}$$

Hence, with the peak locations adjusted, the locations of the maximums line up almost perfectly for the 16-ply, 32-ply, and 64-ply thickness profiles. Raw height data remains of high quality, as does the width data outside of the corner regions

Effect of ply sequence

The effect of ply sequence can be assessed by comparing the *Quasi* ply sequence ($[90/+45/-45/0]_{4S}$) parts and the *Offset* sequence ($[0/-45/+45/90]_{4S}$) parts formed at 30°C and at 70°C for the long and short flanges.

Figure C.4-9 compares the 30°C-formed long flanges for the *Quasi* and *Offset* ply sequences. The profiles are quite similar for each flange with regards to corner thinning magnitudes and peak aspect ratios; '*LF-4*' shows a slightly raised flange-side peak and a slightly reduced web-side peak. The *Offset* flange shows a significant amount of surface roughness near the flange termination. The *Offset* flange has a single valley similar to the 'LF-4' trial but with a steeper slope.

Figure C.4-10 compares the 30°C-formed short flanges for the *Quasi* and *Offset* ply sequences. These curves show no appreciable differences.

Figure C.4-11 compares the 70°C-formed long flanges for the *Quasi* and *Offset* ply sequences. The corner region show no appreciable differences but the flange section sees a smooth *Quasi* flange but an *Offset* flange with two large bumps at 40 and 70 mm. The *Offset* flange also sees a significantly more sudden thickness drop-off at the flange termination.

Figure C.4-12 compares the 70°C-formed short flanges for the *Quasi* and *Offset* ply sequences. The *Offset* flange sees a slighter greater peak than the *Quasi* flange on the flange-side. The thickness drop-off near flange termination shows the inverse trend from the long flange results, this time showing the *Quasi* sample dropping off earlier (i.e. closer to the mid-corner).

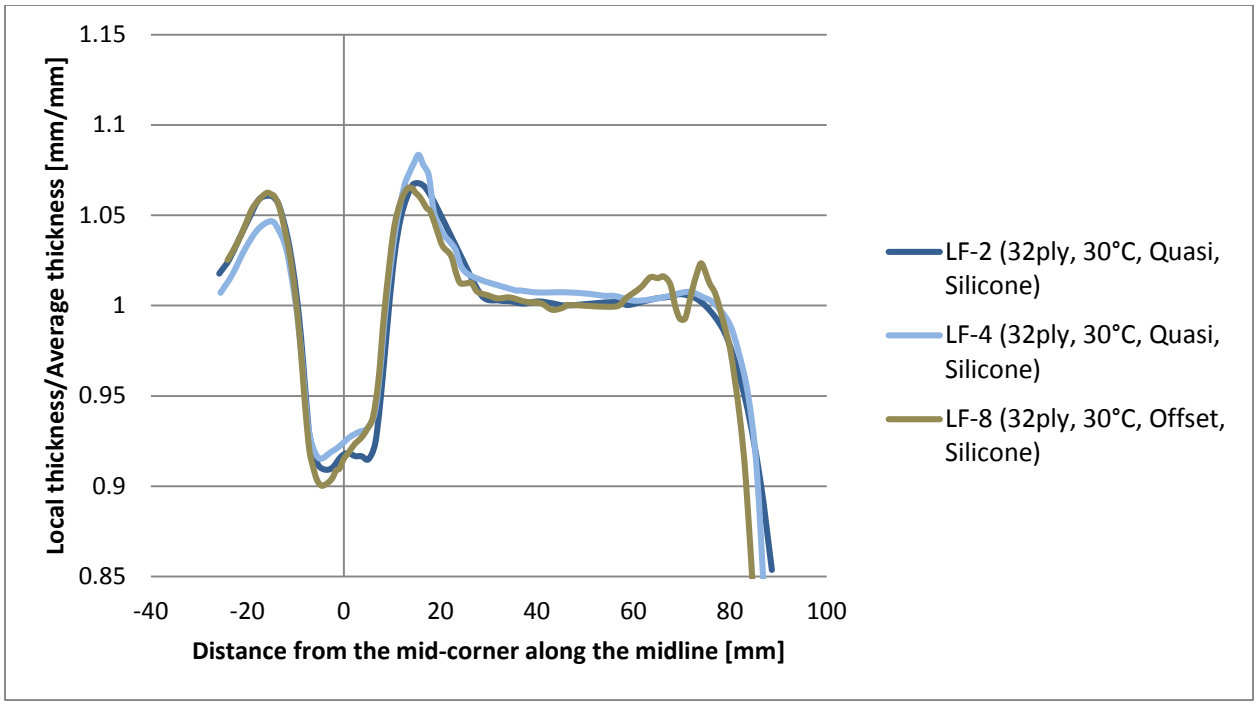

Figure C.4-9. Effect of ply sequence on thickness profile for 30°C-formed long flanges

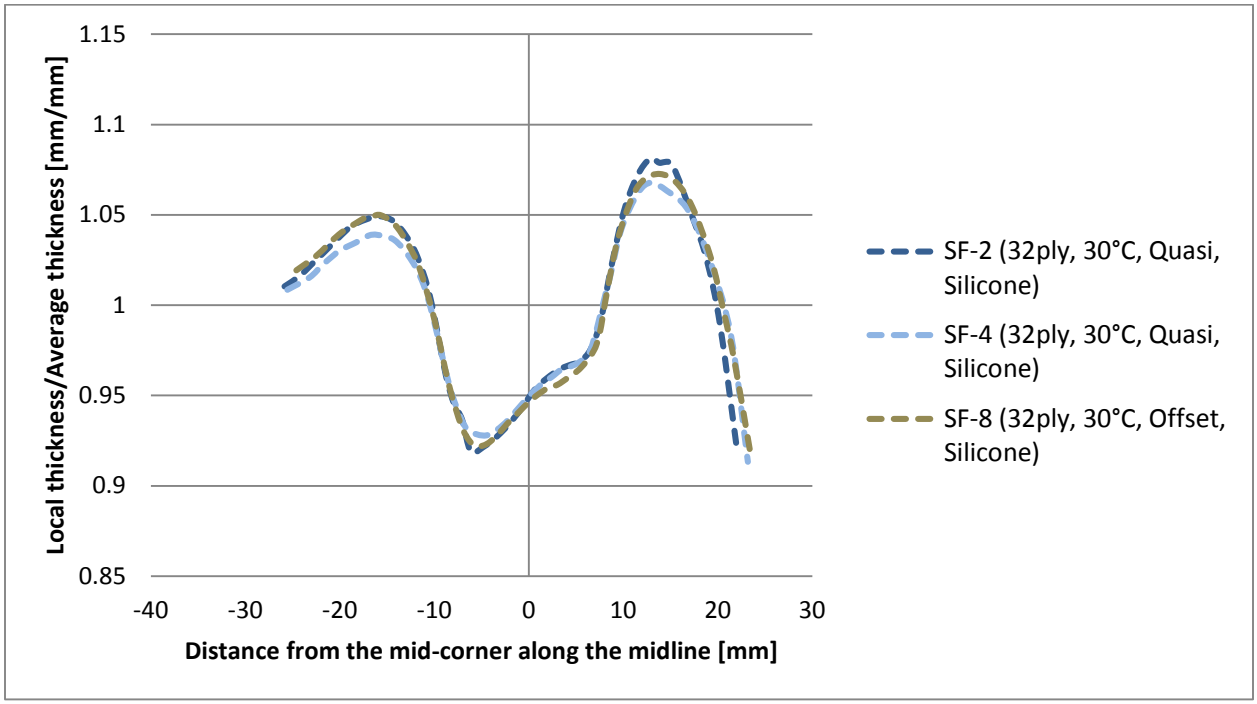

Figure C.4-10. Effect of ply sequence on thickness profile for 30°C-formed short flanges

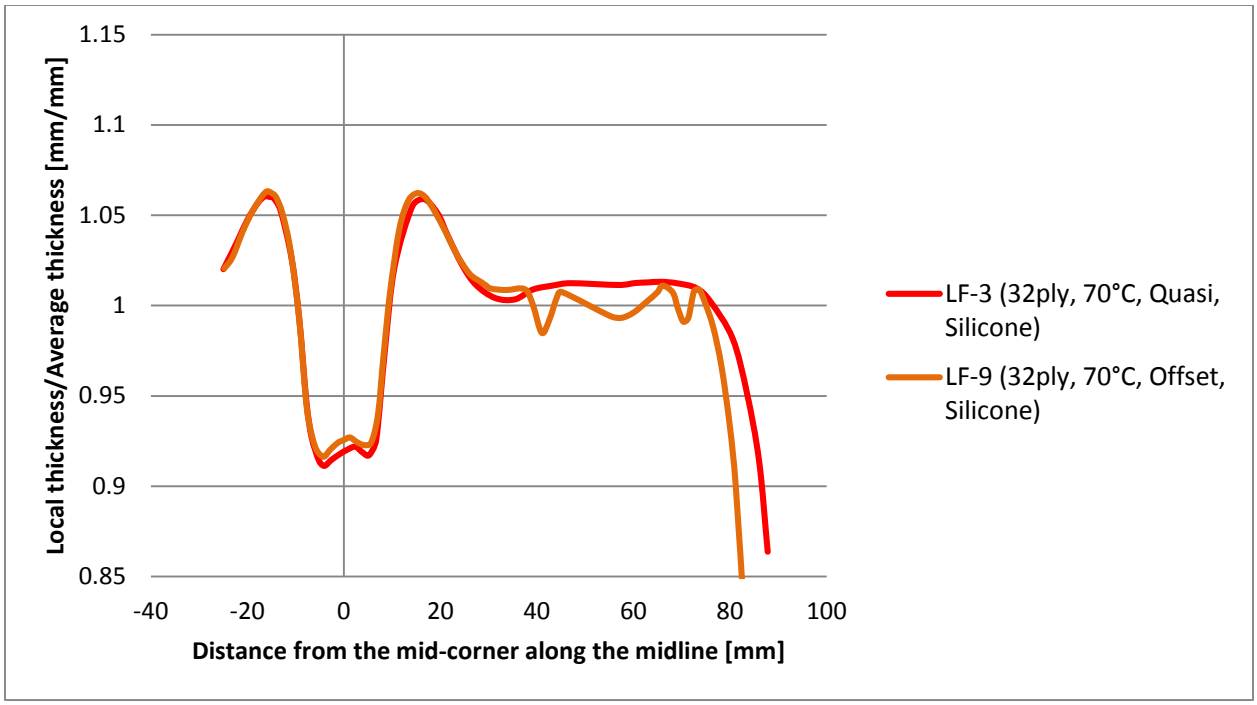

Figure C.4-11. Effect of ply sequence on thickness profile for 70°C-formed long flanges

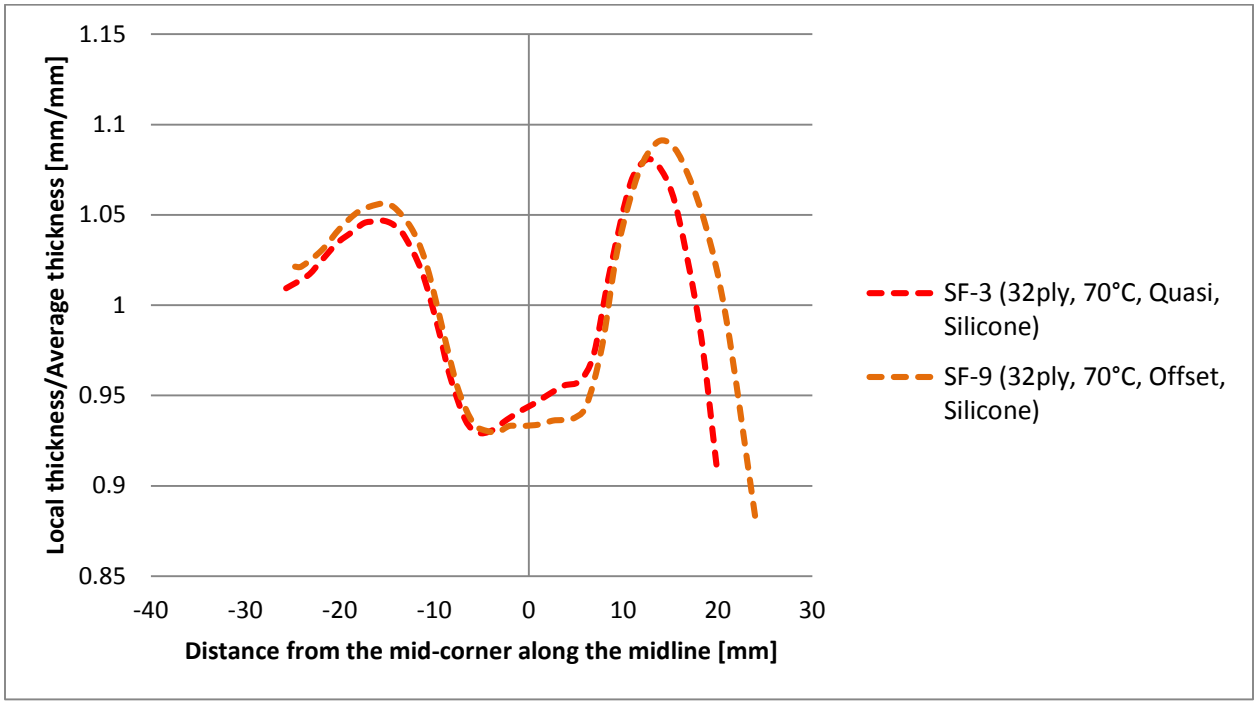

Figure C.4-12. Effect of ply sequence on thickness profile for 70°C-formed short flanges

Effect of forming method

The forming method's effects on flange thickness profile is investigated by comparing the hand lay-up part ('*Part 5*') and the 30°C drape-formed parts ('*Part 2*' & '*Part 4*').

Figure C.4-13 compares the drape-formed long flanges to the hand lay-up baseline long flange. Corner thinning is similar for all flanges, regardless of forming method. The hand lay-up flange shoes a significant rise near the flange termination that is not as pronounced in the drape-formed parts.

Figure C.4-14 compares the drape-formed short flanges to the hand lay-up baseline short flange. The hand lay-up flange has distinct dual valleys in the mid-corner but is otherwise equivalent to the drape-formed flanges.

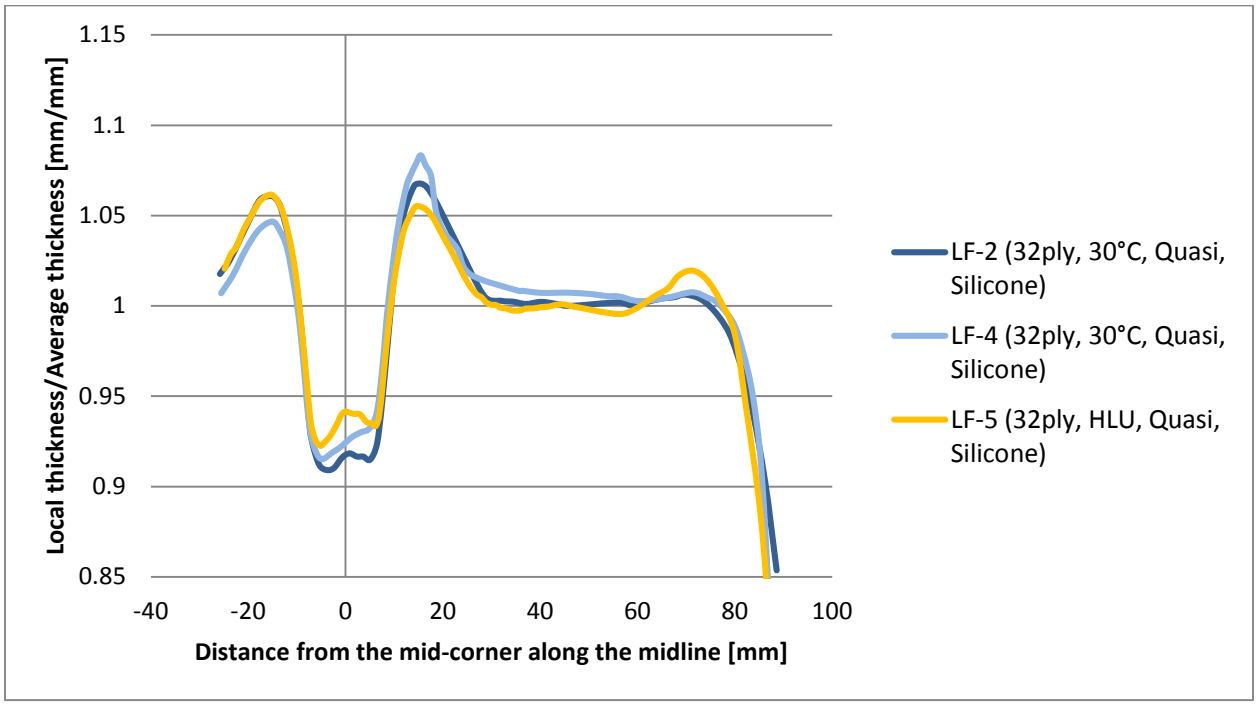

Figure C.4-13. Effect of forming method on thickness profile for long flanges

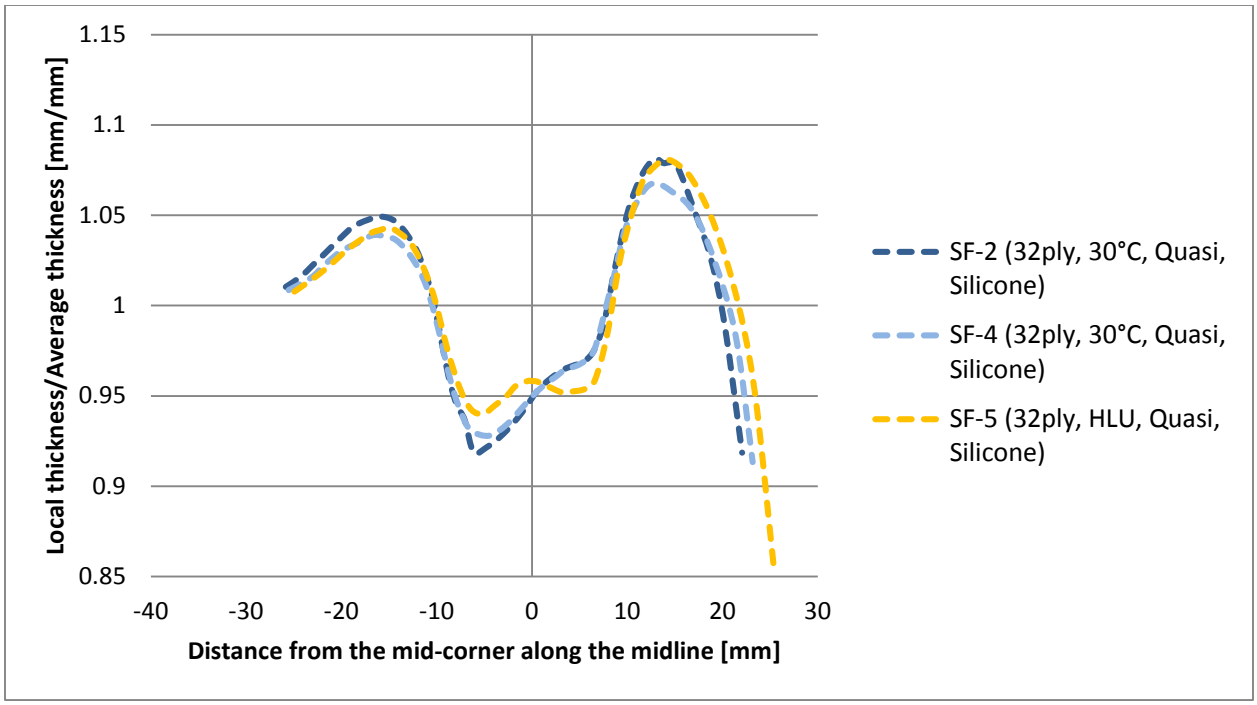

Figure C.4-14. Effect of forming method on thickness profile for short flanges

Combined effects of curing bag type and forming bag thickness

The Nylon-cured part, '*Part 1*', is compared to the equivalent silicone-cured parts, '*Part 2*' and '*Part 4*'.

Figure C.4-15 and Figure C.4-16 compare the long and short flanges, respectively. It can be seen that extreme corner thinning is seen in the silicone-cured parts, but that is not the case in the nylon-cured part which has a generally uniform thickness throughout the part. This is true of both the long and the short flanges. The silicone-cured parts show fairly smooth surfaces along the length of the flange and in the corner whereas the Nylon-cured flanges show significant bumps in the corner section. Near the flange termination, the silicone-cured flanges get thinner; the Nylon-cured flanges get thicker.

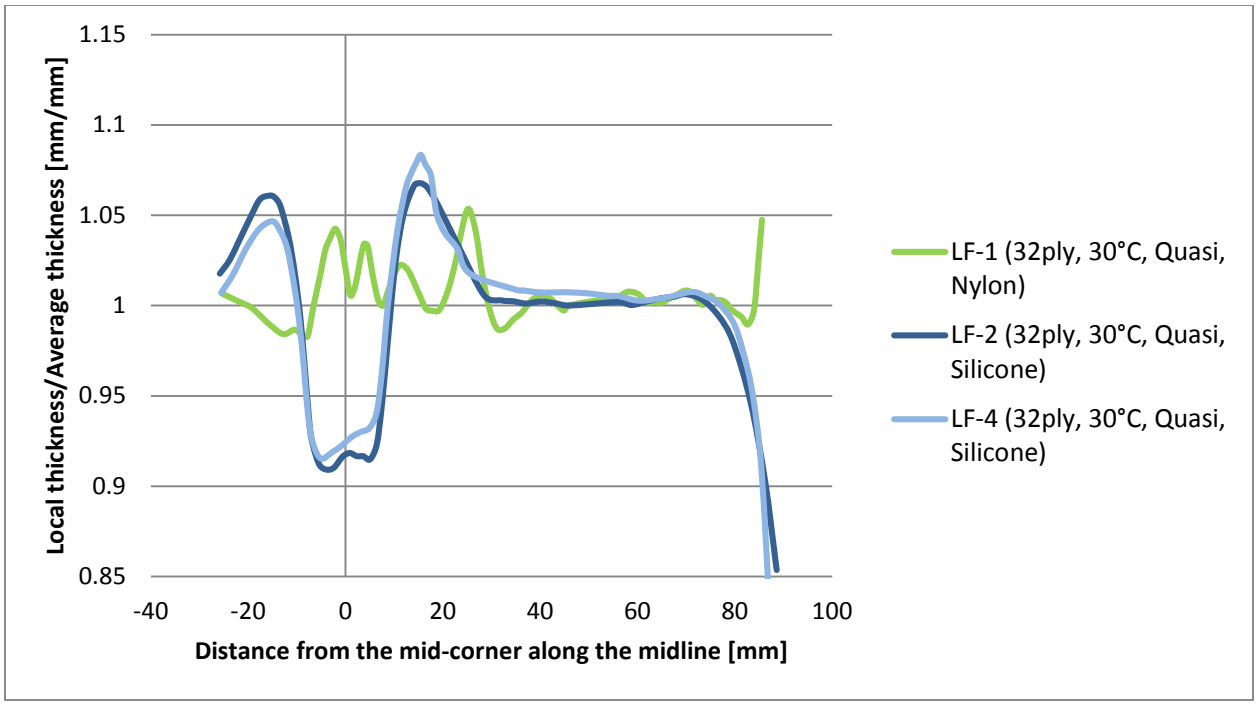

Figure C.4-15. Elastomer versus Nylon bagging during cure: Long Flange

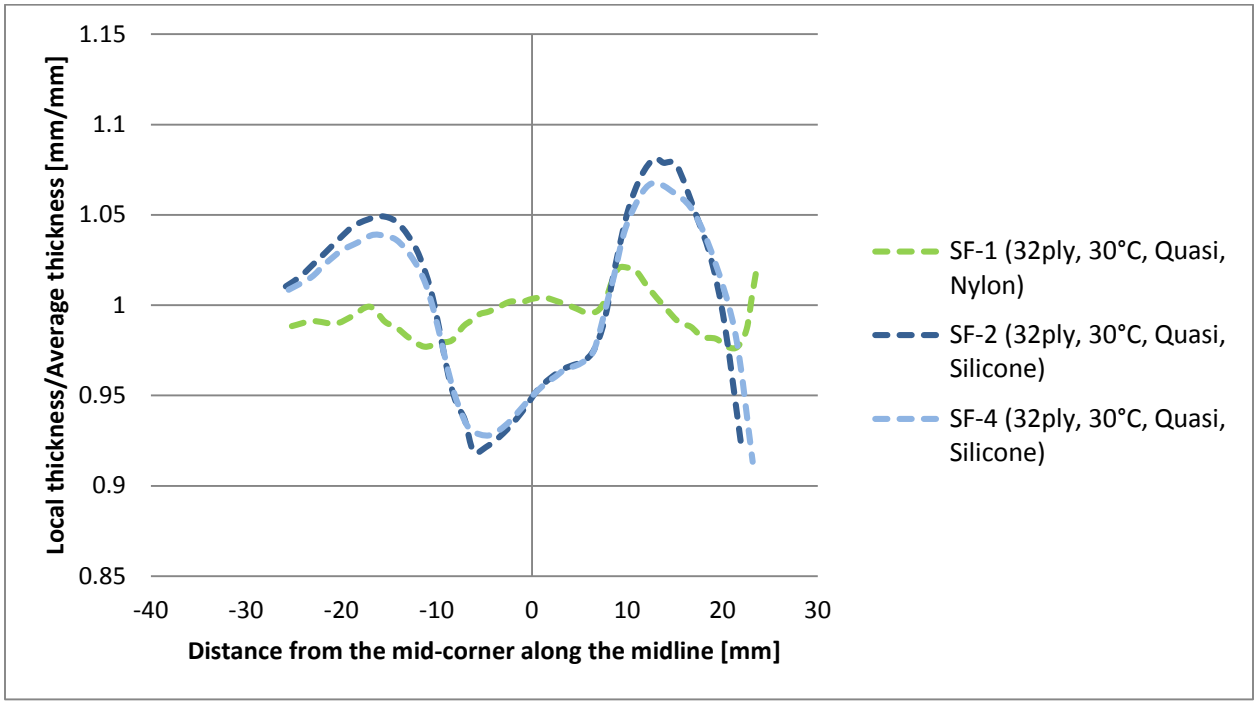

Figure C.4-16. Elastomer versus Nylon bagging during cure: Short Flange

Effect of wrinkling in short flanges

It was seen that long flange wrinkles are distinguishable in the long flange thickness profiles. However, this was not the case for the wrinkled short flange thickness profiles which showed overwhelming similarity to the non-wrinkled baseline short flanges.

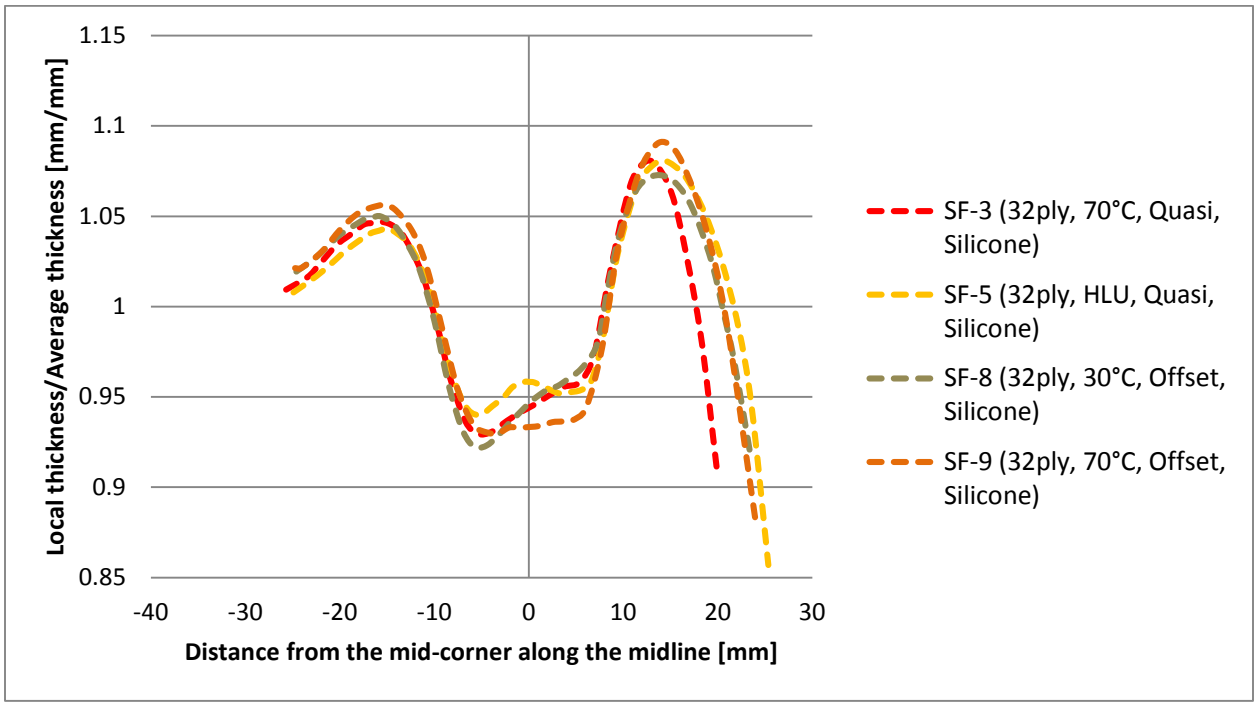

Figure C.4-17. Non-wrinkled short flange thickness profiles

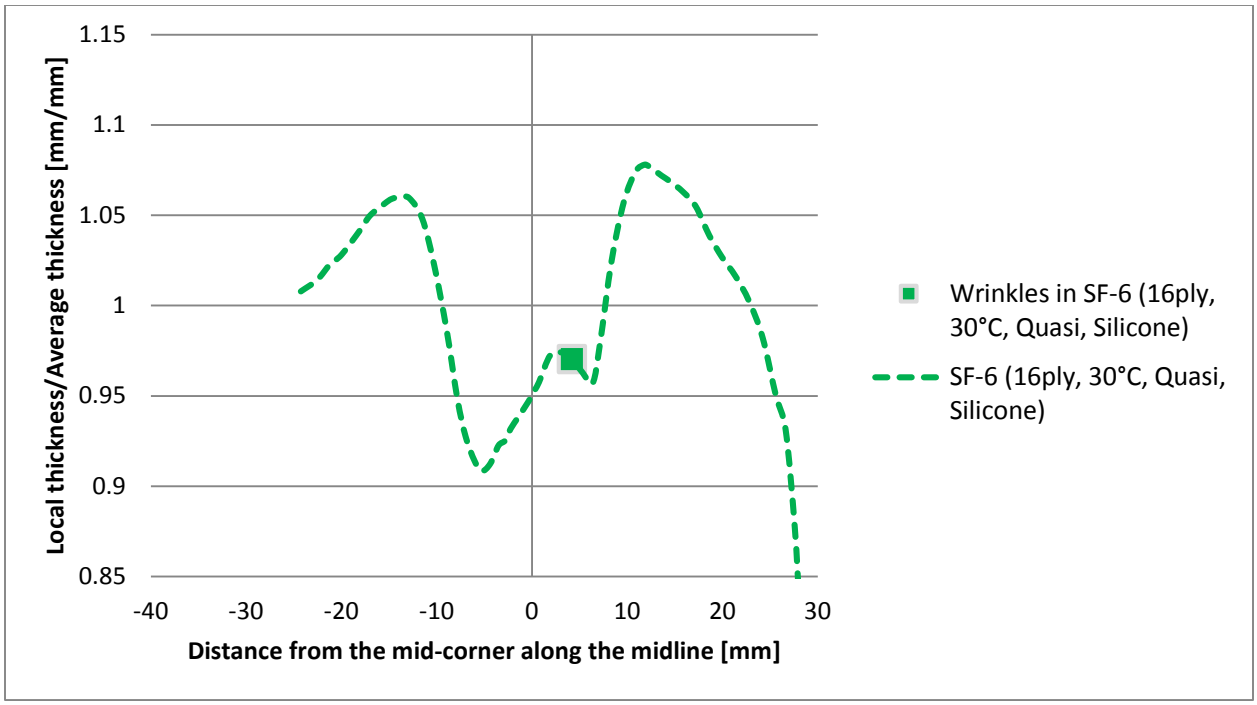

Figure C.4-18. Wrinkled 16-ply Short Flange Thickness Profile

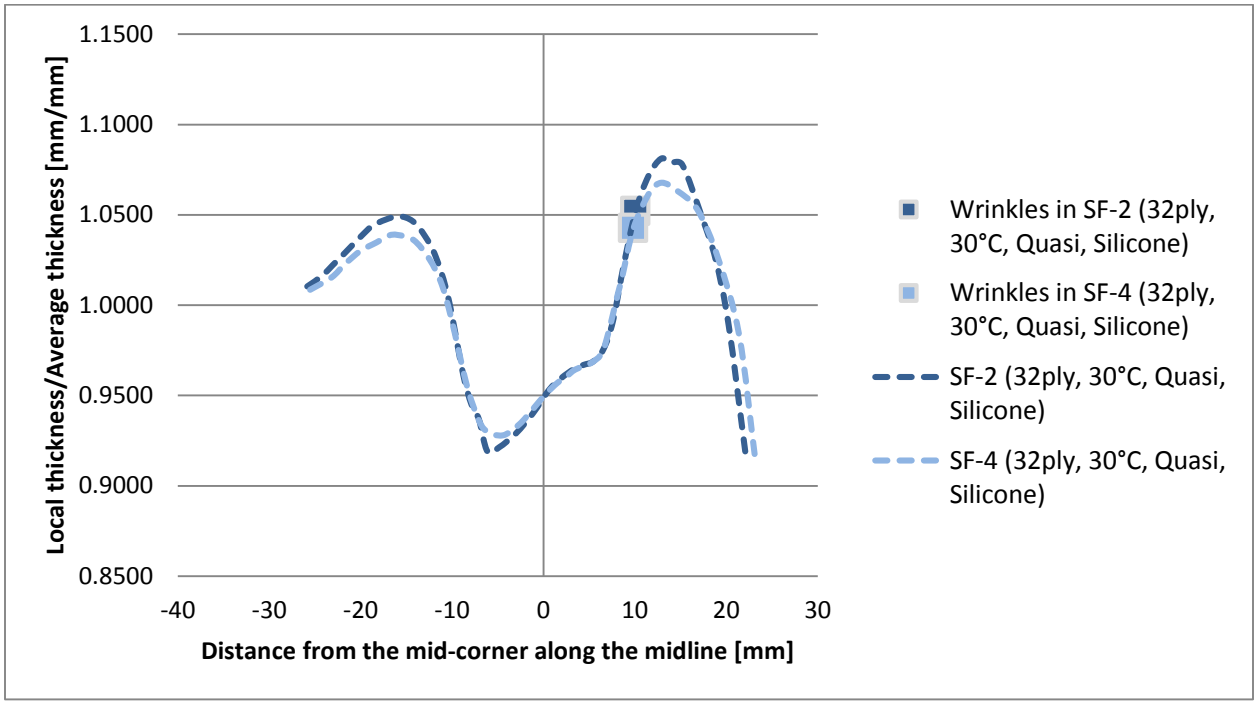

Figure C.4-19. Wrinkled 32-ply Short Flange Thickness Profile

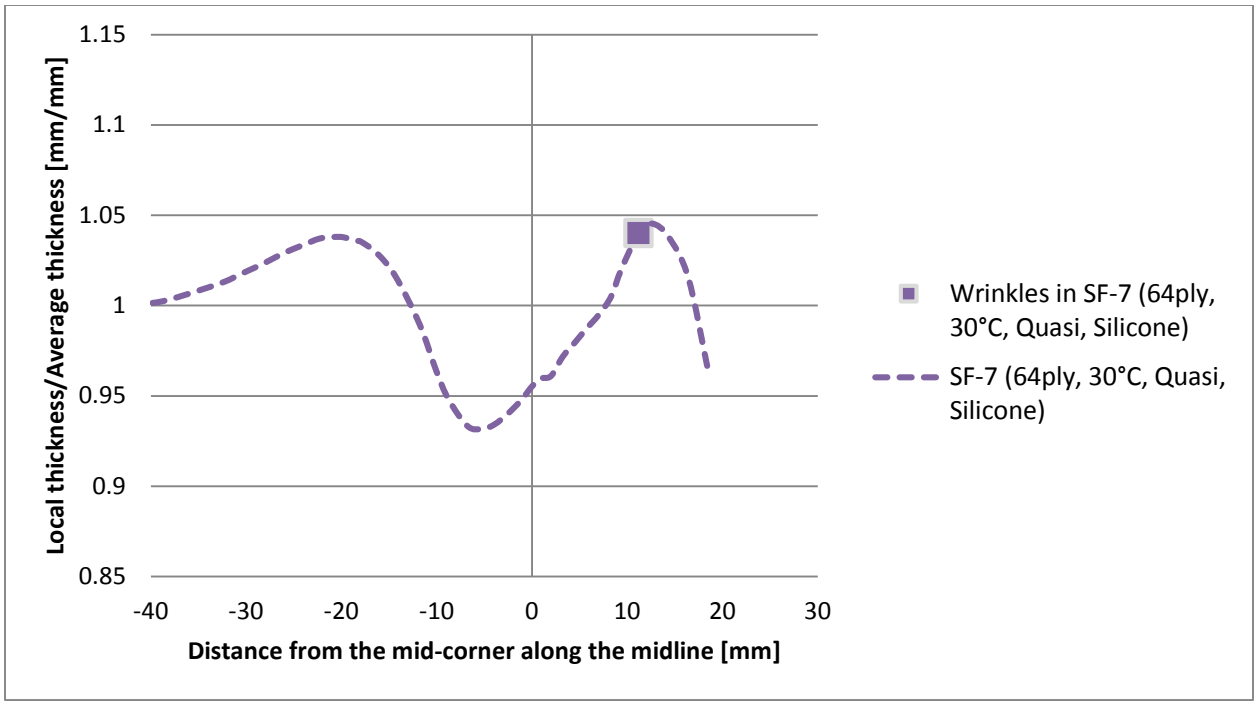

Figure C.4-20. Wrinkled 64-ply Short Flange Thickness Profile

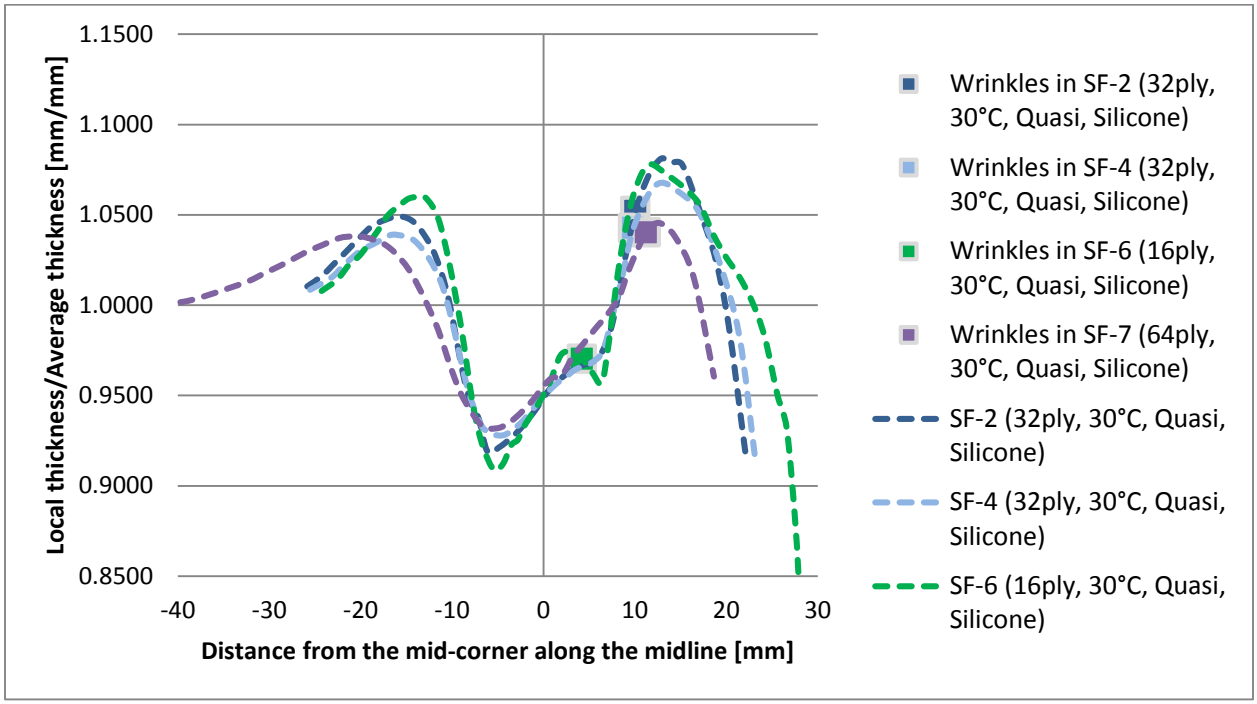

Figure C.4-21. Wrinkled Short Flange Comparison with Hand Lay-up Baseline

C.5 Termination profile

Flange termination profiles are examined under the microscope and have been measured by two methods: the ‘local method’ and the ‘end consolidation correction method’. A secondary analysis dubbed ‘part-averaging’ was performed on both measurements to address the differences in termination profiles between a cured part’s long and short flanges, as seen by comparing top and bottom micrographs. The results for both methods are presented in the following subsection where one method is chosen for further analysis.

Choice of quantification method

The data sets for are presented for the ‘*local*’ and the ‘*end consolidation correction*’ measurement methods in Figure C.5-1 and Figure C.5-2, respectively. With the data in this form, there are very subtle differences between both methods that do not make it worth choosing one method over another.

‘*Part-averaging*’ implies taking the average x-position of both flanges for the same part, as detailed in Section 4.2.2.4.3. The ‘*part-averaged*’ measurements taken with the ‘*local method*’ are shown in Figure C.5-3 and show grouping of most trials about the 27.4° line. On the other hand, the ‘*part-averaged*’ measurements taken with the ‘*end consolidation correction method*’ shown in Figure C.5-4 exhibit better linearity and better grouping for all trials. Thus, the choice of measurements has large implications over the validity of the assumptions of inter-ply deformations (slip) during cure that were discussed in Section 3.1.2.2.

Given the greater data consideration, improved linearity, and tighter grouping, the ‘*end consolidation correction method*’ was chosen as the way forward for presenting the process-condition parsed results in the following subsections.

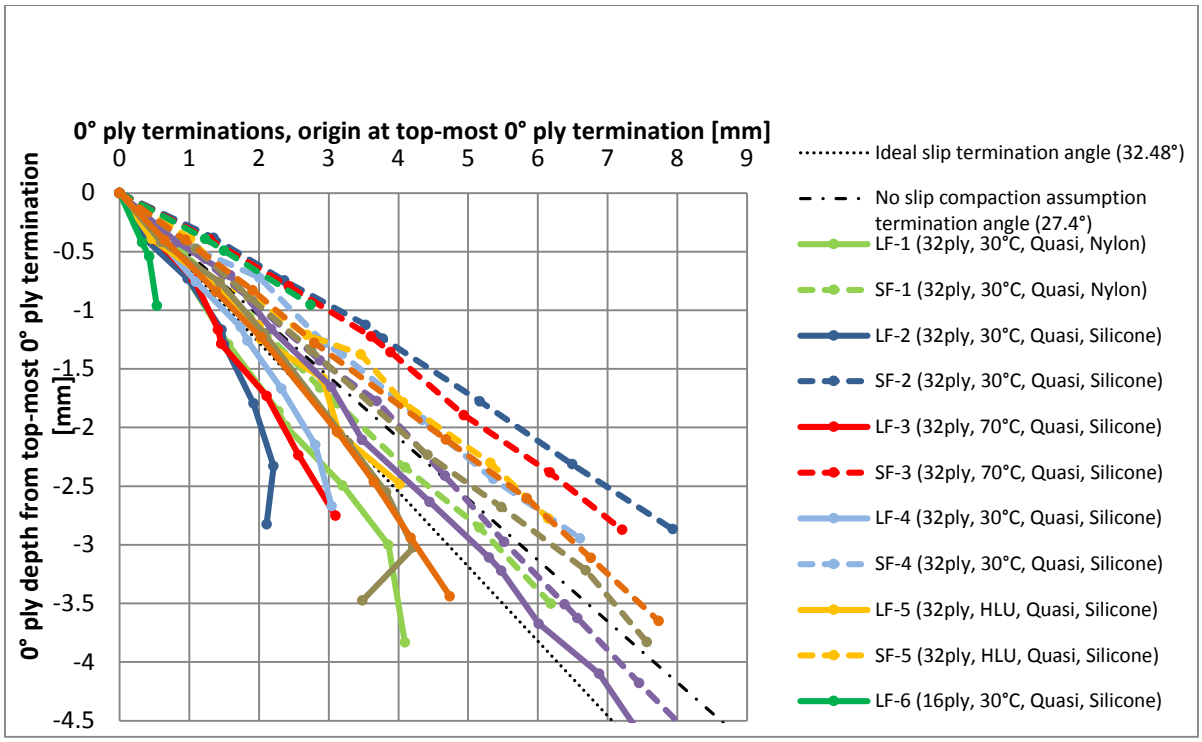

Figure C.5-1. Individual flange termination profiles via 'Local method'. All flanges are shown.

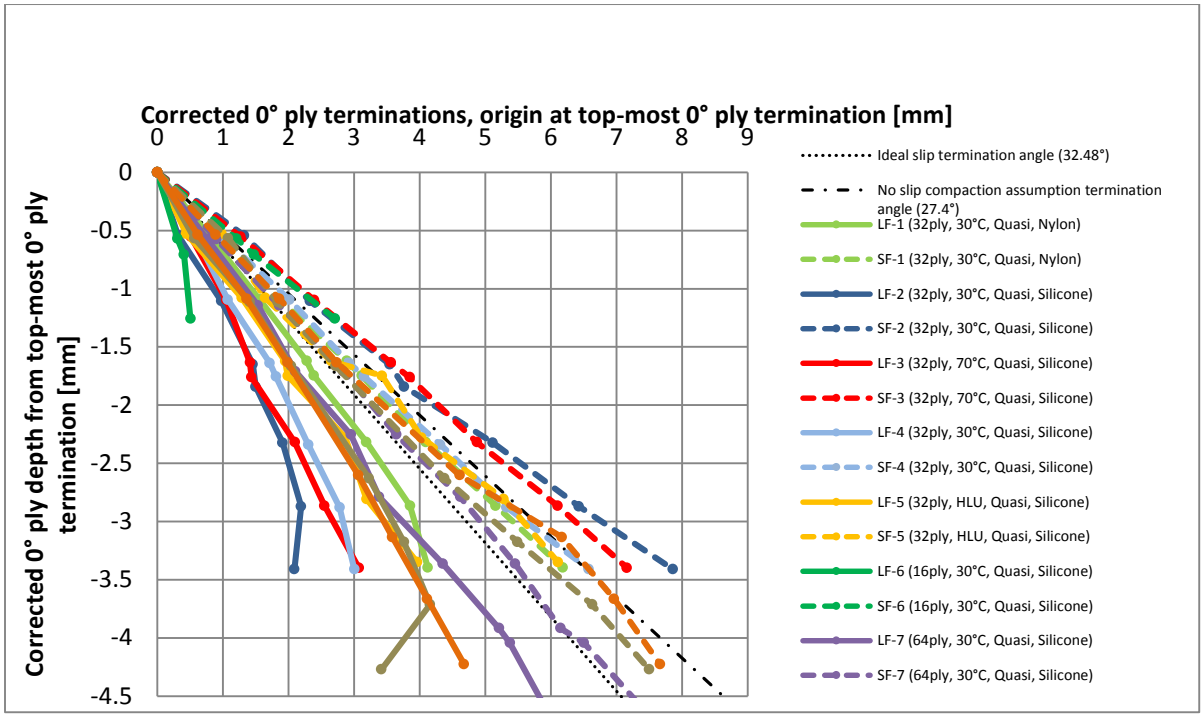

Figure C.5-2. Individual flange termination profiles via 'End consolidation correction method': All flanges are shown.

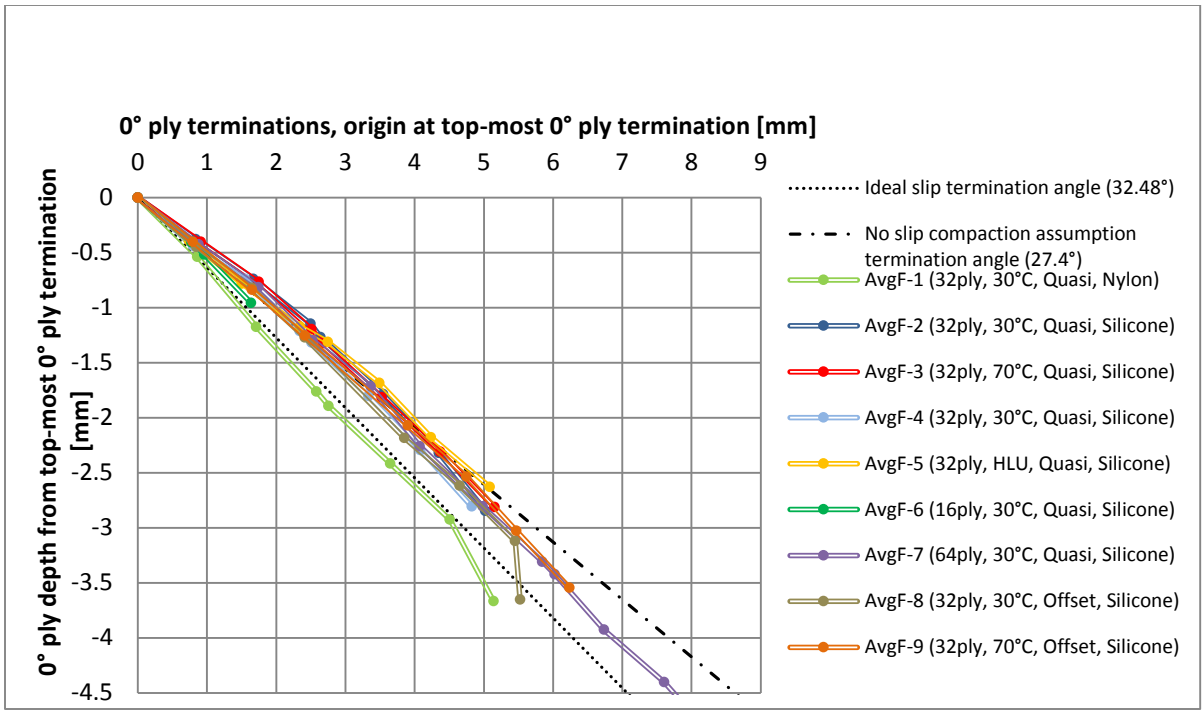

Figure C.5-3. 'Part-averaged' termination profiles via 'Local method': All flanges are shown.

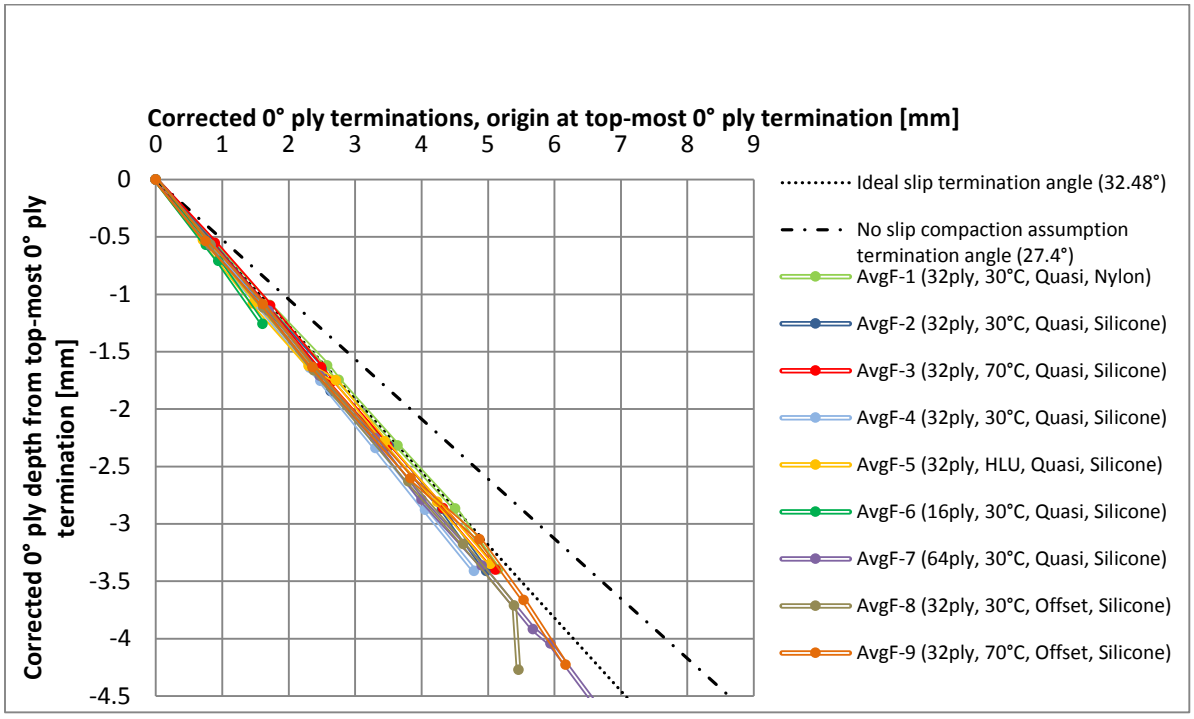

Figure C.5-4. 'Part-averaged' termination profiles via 'End consolidation correction method': All flanges are shown.

Best-case silicone-cured slip

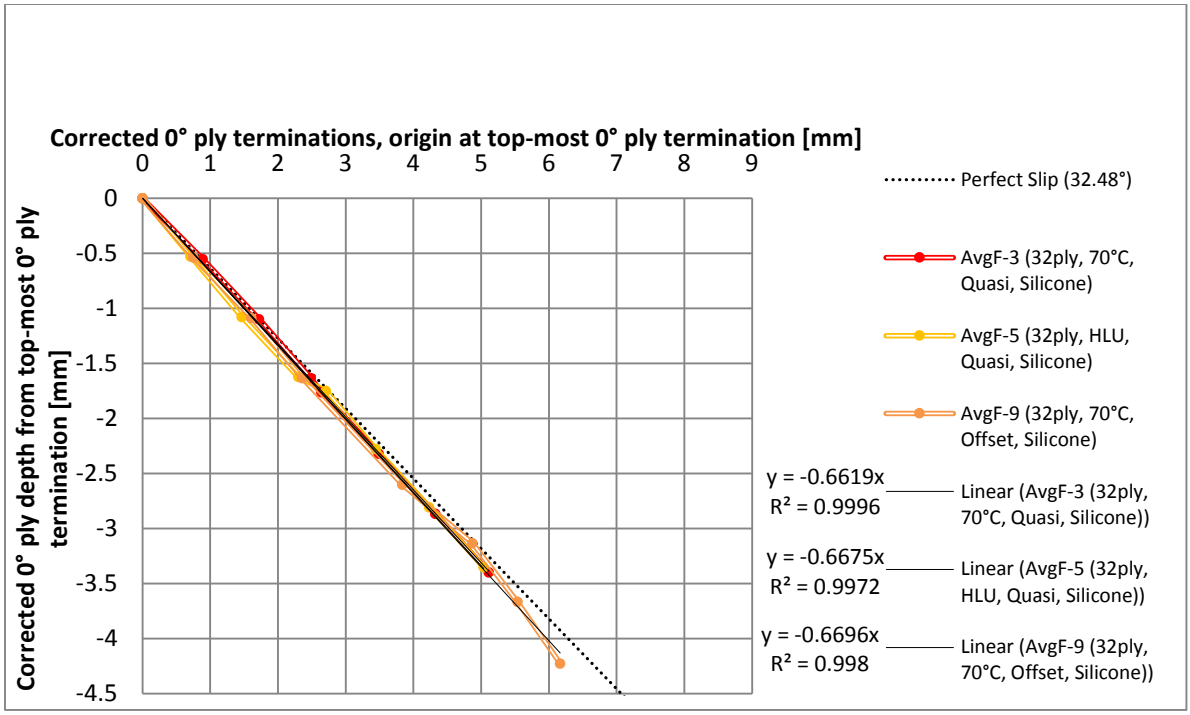

Figure C.5-5. Linear trend-fitting of best-case silicone-cured parts

However, from Figure C.5-4 it is clear that all silicone-cured parts undershot the ideal slip line. Thus, an adjusted ideal termination shape angle (‘*best-case*’) is computed. Assuming that the highest quality parts are the hand lay-up and 70°C-formed parts, an average linear fit would provide a reasonably adjusted ideal expected termination shape angle for a defect free part. This is performed in Figure C.5-5 and tabulated in the following table. An origin-intercept trend line of the part-averaged termination shape via the end consolidation correction method gives an average angle of 33.68°; a 1.2° reduction from the ideal slip angle.

Table C.5-1. Expected angle of a best-manufactured silicone-cured part by linear trend-fitting of the part-averaged termination shape

Part	Slope	R^2 value	Angle
AvgF-5 (32ply, HLU, Quasi, Silicone)	-0.6675	0.9972	-33.7231
AvgF-3 (32ply, 70°C, Quasi, Silicone)	-0.6619	0.9996	-33.5006
AvgF-9 (32ply, 70°C, Offset, Silicone)	-0.6696	0.9980	-33.8063
		|AVERAGE|	33.68°

Effect of temperature

Individual and '*part-averaged*' termination shapes are presented for both the *Quasi* and the *Offset* parts formed at 30°C and 70°C.

Figure C.5-6 shows the *Quasi* ply sequence individual long and short flanges for the 30°C and 70°C-formed samples. No clear trend can be determined with regards to the magnitude of the shift between the long and short flanges. The 30°C-formed flanges show 'tail' features in the mould-side plies (-3.4 mm ply depth) such that the x-position of the final ply does not follow the expected slope from the plies above it. Figure C.5-7 presents the same data in '*part-averaged*' form. The 70°C-formed part shows closest alignment with the ideal slip line (calculated in Section 3.1.2.2.2), though all three parts come up short of it. The '*AvgF-4*' part shows an overall steeper slope whereas the '*AvgF-2*' part shows a slope similar to that of the 70°C-formed part but with a distinct 'tail' feature.

Figure C.5-8 shows the *Offset* ply sequence individual long and short flanges for the 30°C and 70°C-formed samples. The long flanges show mostly parallel termination shapes to each other aside from a severe 'tail' feature in the bottom-most 0° ply in the 30°C-formed flange ('*LF-8*'). The short flanges show a greater divergence, particularly in the bottom four data points. All four flanges show low linearity. The '*part-averaged*' data is presented in Figure C.5-9. The 30°C and 70°C-formed parts show good alignment in the first four 0° plies (from the top) but show

increasing divergence near the mould-side. Both curves undershoot of the ideal slip 32.48° angle. The sharp 'tail'-like kink feature seen in the individual flange plot remains for the 30°C-formed part mould-side ply. The 70°C-formed sample also shows divergence from its upper half's slope but is more gradual.

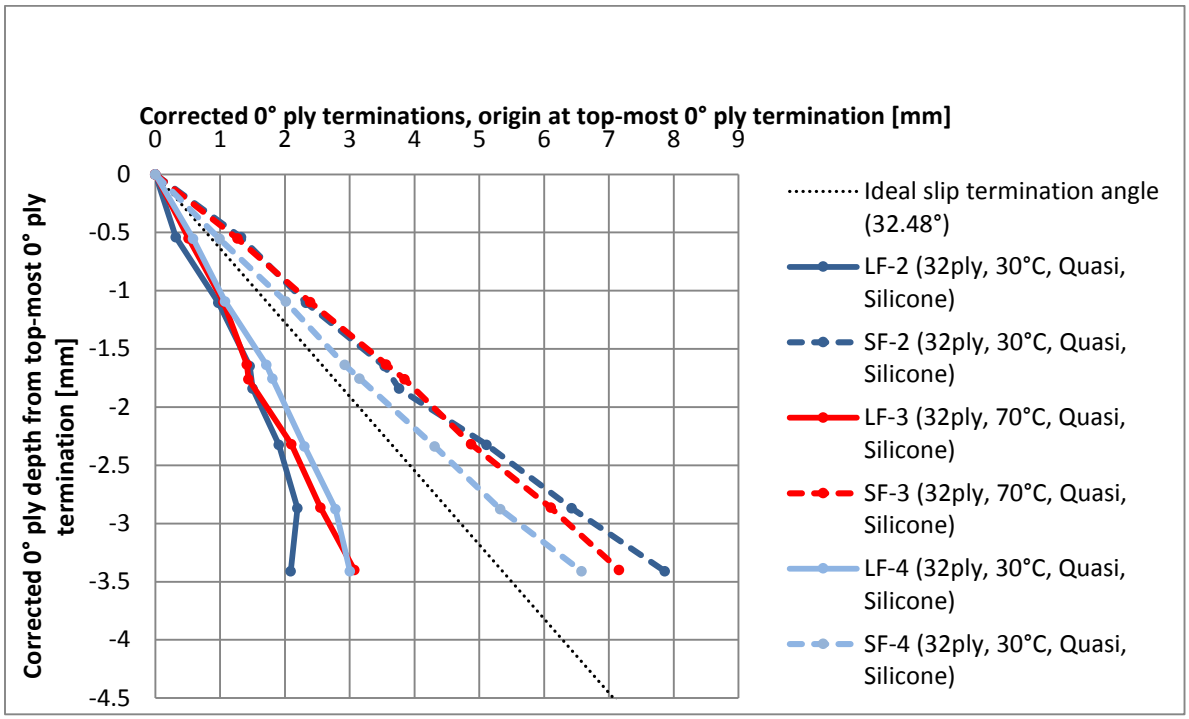

Figure C.5-6. Individual flange termination profiles for the Quasi ply sequence comparing for the 30°C and 70°C-formed parts

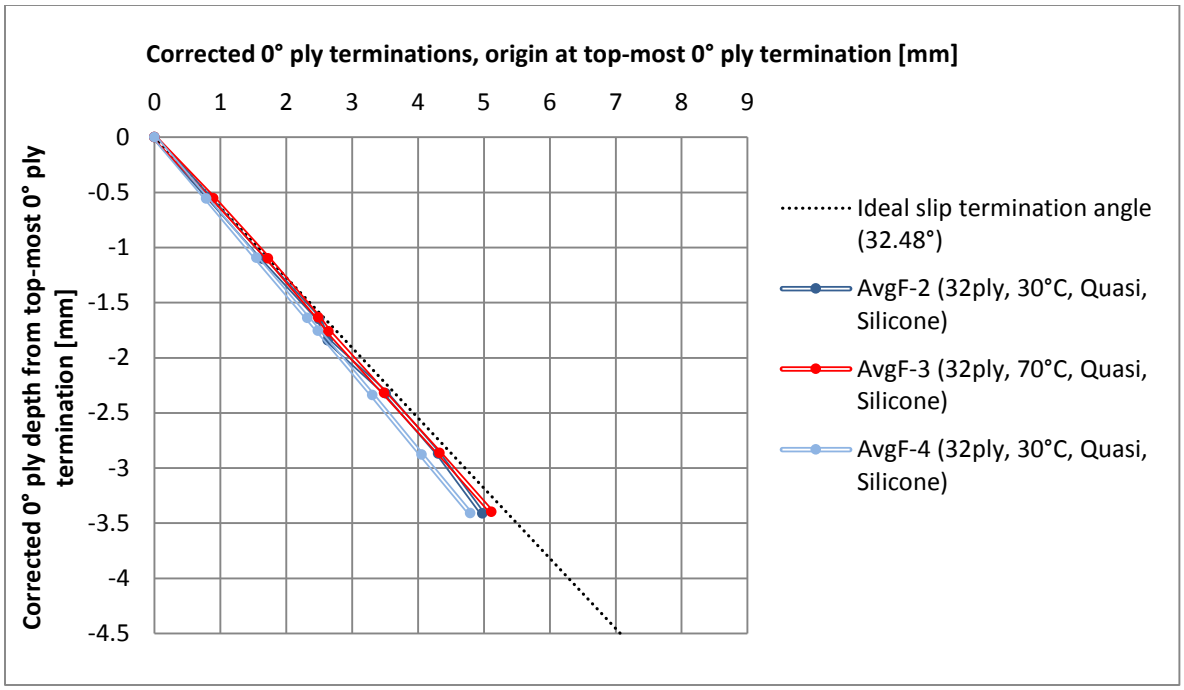

Figure C.5-7. Part-averaged 0° ply termination profiles for the Quasi ply sequence for the 30°C and 70°C-formed parts.

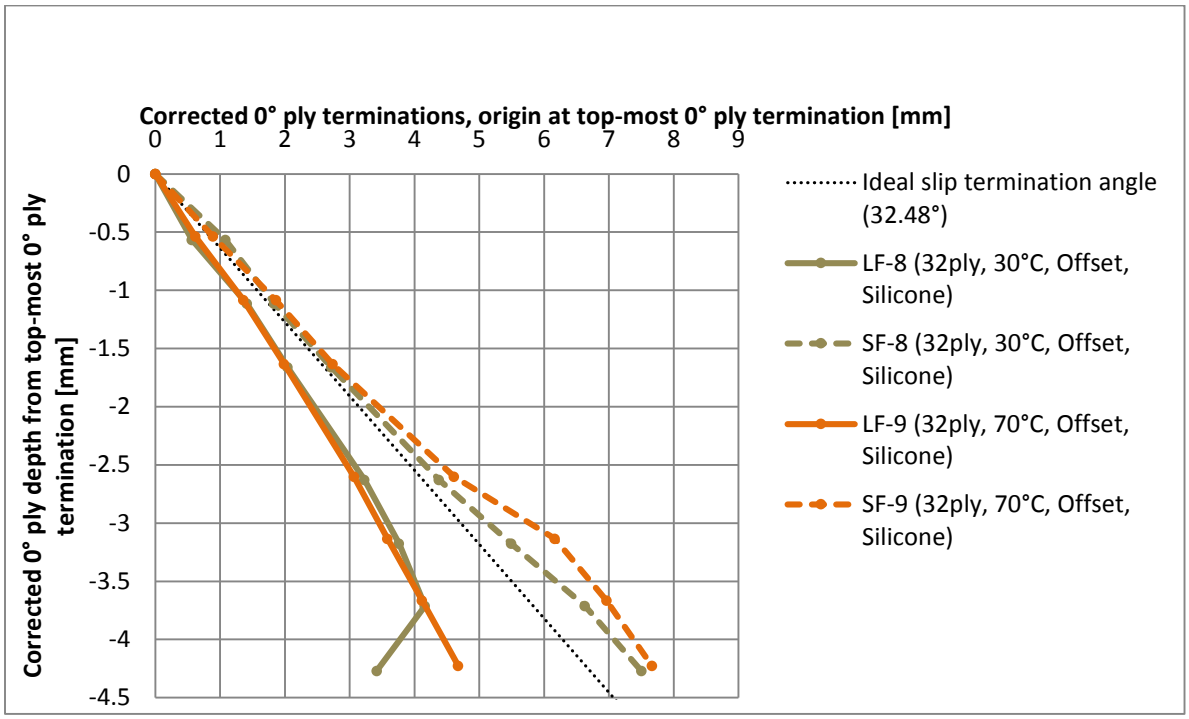

Figure C.5-8. Individual flange termination profiles for the Offset ply sequence comparing for the 30°C and 70°C-formed parts

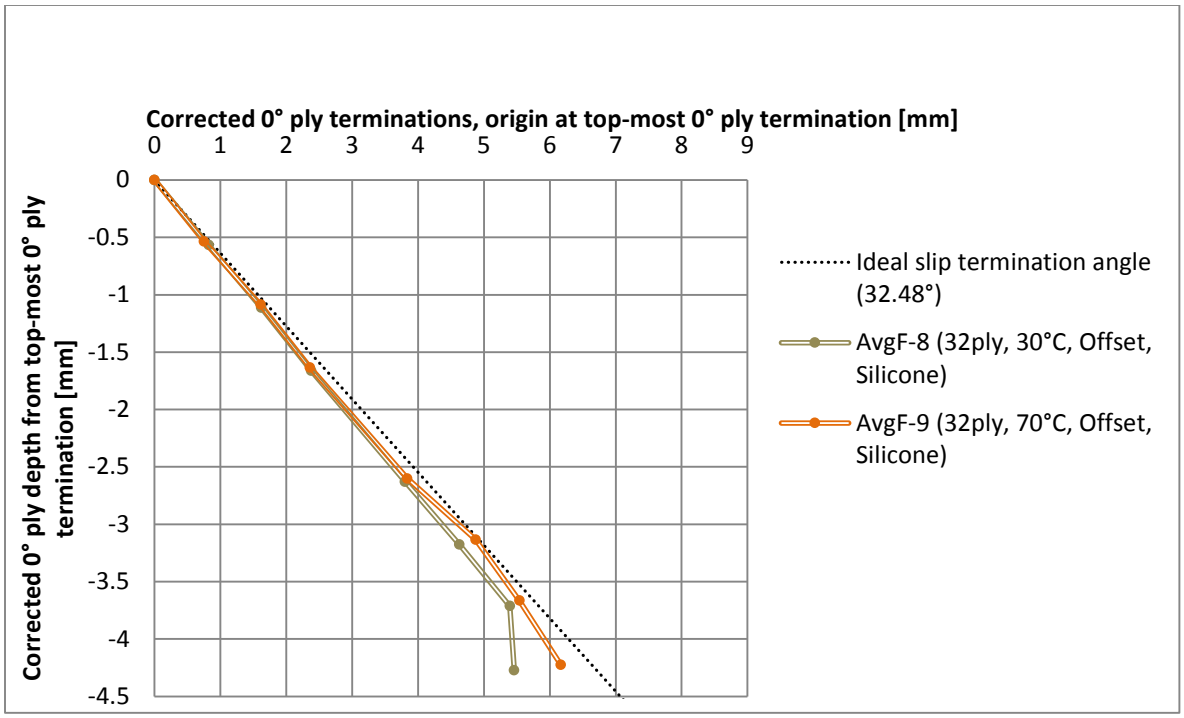

Figure C.5-9. Part-averaged 0° ply termination profiles for the Offset ply sequence for the 30°C and 70°C-formed parts.

Effect of flange length

Comparing the individual laminate termination curves for all flanges in Figure C.5-2 shows a significantly large spread of data. In particular, noticeable differences appear between the long flanges (solid lines) and short flanges (dotted lines): for all tests, the short flange laminate termination shape exhibits a smaller average termination angles than the long flanges. All short flange termination shapes show angles lesser than the ideal slip line whereas the long flanges show greater angles. Also observable from Figure C.5-2 the short flange termination shapes appear to be significantly more linear than the long flanges. However, it is important to note that the long flanges also correspond with a greater occurrence of wrinkling and waviness than the short flanges. Thus, the linearity is likely unrelated to the ply length itself, rather, it is more likely directly related to the occurrence of fibre misalignments. This is further discussed in detail in the sections below.

When comparing a particular test's long and short flanges, they appear to show similar but opposite offsets with respect to the ideal slip line, though the value of this offset is inconsistent throughout all tests. Hence, it is possible that there are unforeseen interactions between the long and short flanges during the manufacturing of the parts. To correct for any skewing, the long and short flange termination curves have been averaged and plotted in Figure C.5-4, showing a significant reduction in data spread, dubbed the '*part-averaged*' method previously outlined in Section 4.2.2.4.3. But by combining the long and short flange data, no absolute ply termination angle can be determined for any individual flange. Therefore, the '*part-averaged*' charts cannot provide information on the effect of flange length.

Effect of ply count

The impact of ply count on ply termination profiles is assessed by comparing the 16-ply, 32-ply, and 64-ply samples of the *Quasi* ply sequence flanges formed at 30°C.

Figure C.5-10 compares the individual flange 0° ply profiles. All four long flanges show tail-like features in the long flanges' mould-side plies. As for the short flanges, similar but opposite 'tail' features occur in the short flanges for the 32-ply and 64-ply flanges. The 64-ply sample shows a slightly noisy long flange profile, particularly as compared to the thinner laminates. The data spread between the long flanges and short flanges appears to be more pronounced for the thinner laminates, as illustrated by points of similar depth (for example, depths of-0.5 and -1.2 mm).

Figure C.5-11 shows the same data in part-averaged form. All four parts undershoot the 32.48° ideal slip termination angle and are fairly linear and parallel to each other.

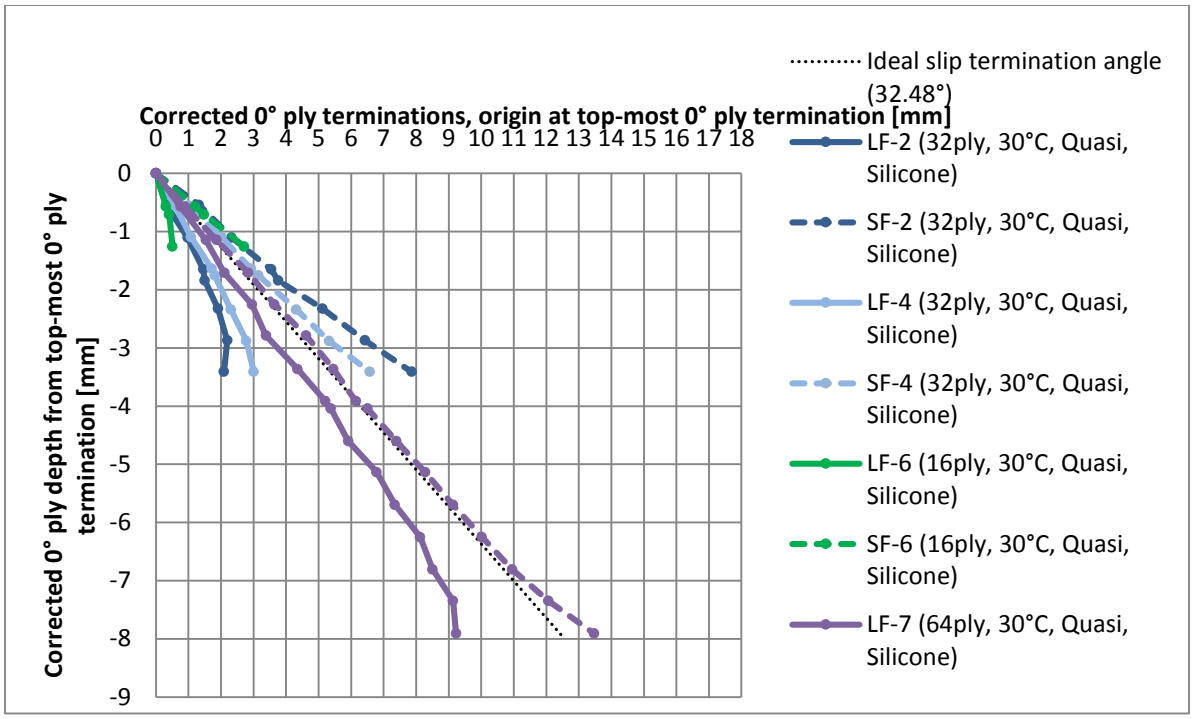

Figure C.5-10. Individual flange termination profiles for the 16-ply, 32-ply, and 64-ply laminates

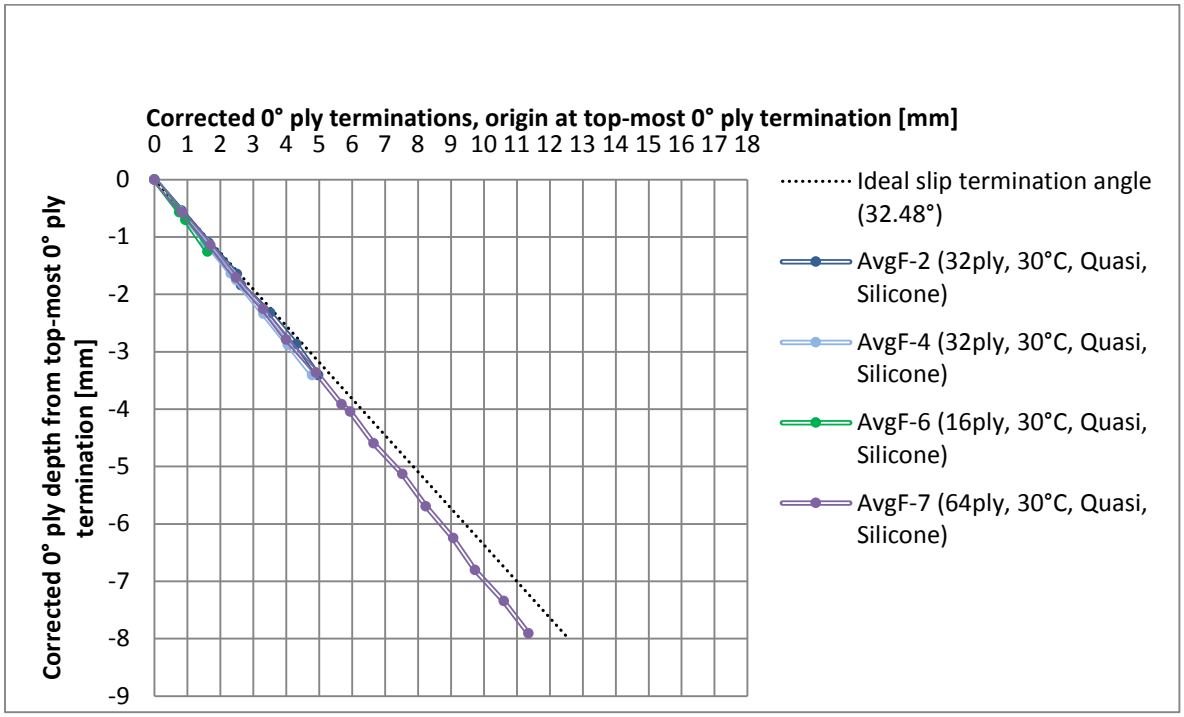

Figure C.5-11. Part-averaged terminations profiles for the 16-ply, 32-ply, and 64-ply parts.

Effect of ply sequence

The effects of ply sequence is assessed by comparing the 32-ply 30°C-formed and 70°C-formed parts for the *Quasi* and *Offset* ply sequences. Generally, the *Offset* ply sequence flange terminations appear "longer" since their 0° plies are closer to the part's top and bottom surfaces, capturing a greater proportion of the part's total thickness.

Figure C.5-12 compares the effects of ply sequence on the individual flange termination profiles for the 30°C-formed samples. The 'tail' feature is the most pronounced in the *Offset* ply sequence long flange ('*LF-8*') though can also be seen in the *Quasi* long flanges. The *Quasi* flanges show greater spread between their long and short flanges than the *Offset* flanges. The part-averaged curves in Figure C.5-13 show a severe 'tail' in for the *Offset* part but is otherwise fairly parallel to the other flanges.

Figure C.5-14compares the effects of ply sequence on the individual flange termination profiles for the 70°C-formed samples. Both long flanges and the *Quasi* short flange show good linearity. The *Quasi* parts have a greater spread between long and short flanges. Figure C.5-15 shows the *Quasi* part's '*part-averaged*' profile to be near-parallel to the ideal slip termination line. The *Offset* flange shows a measureable '*tail*' feature in its bottom ply but is otherwise near-parallel to the ideal slip line.

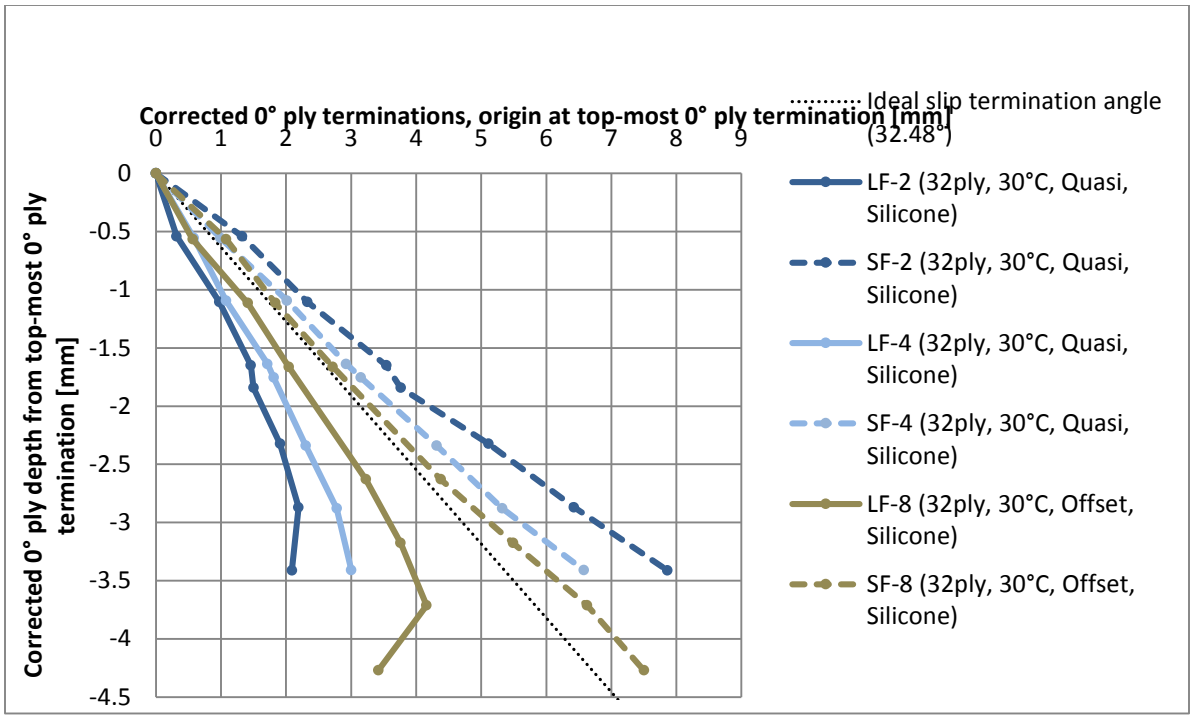

Figure C.5-12. Individual flange termination profiles for the parts formed at 30°C

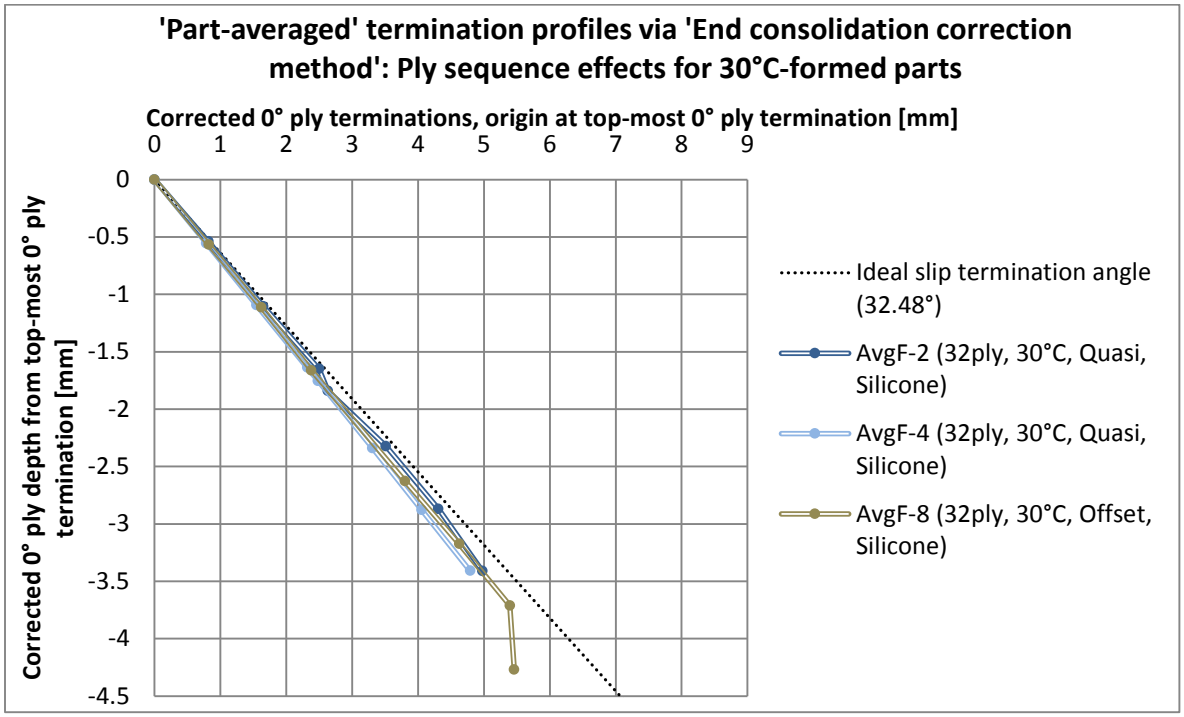

Figure C.5-13. Part-averaged termination profiles for the parts formed at 30°C

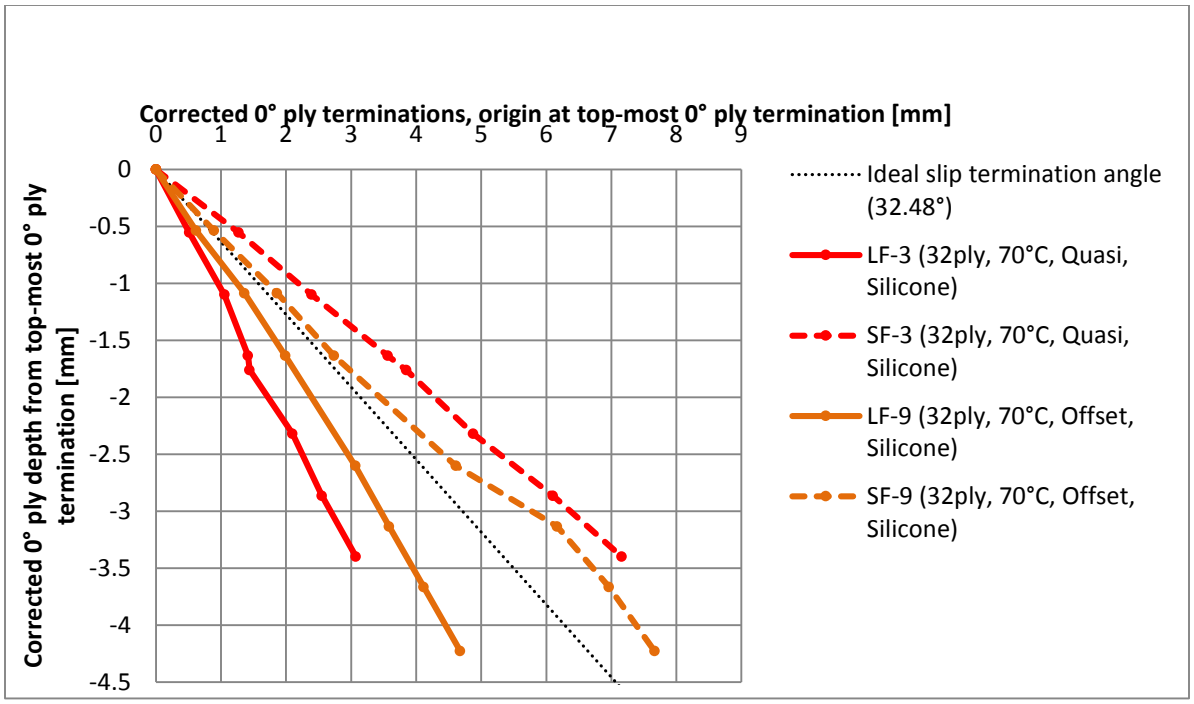

Figure C.5-14. Individual flange termination profiles comparing the effect of ply sequence when forming at 70°C

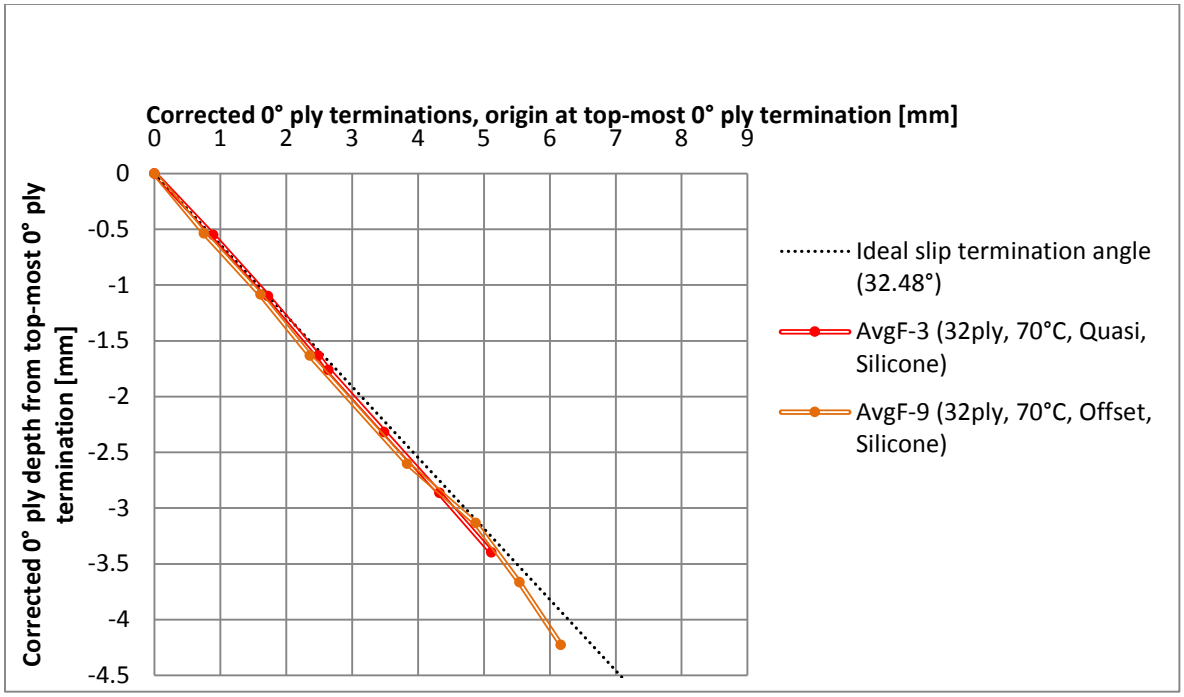

Figure C.5-15. Part-averaged termination profiles comparing the effect of ply sequence when forming at 70°C

Effect of forming method

The forming method's impact on ply termination shapes can be assessed by comparing the hand laid-up part and the drape-formed parts of the corresponding ply sequence and temperature. Figure C.5-16 compares the individual flanges for the drape-formed (at 30°C) to the hand layup baseline flanges. The hand lay-up flanges, '*LF-5*' and '*SF-5*', show significant ply termination profile jaggedness that appears to be equal and opposite for either flange length. The drape-formed flanges display improved linearity overall, though they have a larger spread between their long and short flanges.

Figure C.5-17 compares the '*part-averaged*' flange termination data for the same tests. The hand lay-up part shows reasonable linearity through the entire termination shape and is nearly parallel to the ideal slip line. The '*AvgF-4*' curve shows better linearity but undershoots the ideal slip curve in its lower half. The '*AvgF-2*' curve shows good linearity though exhibits a mould-side 'tail' feature in its last ply.

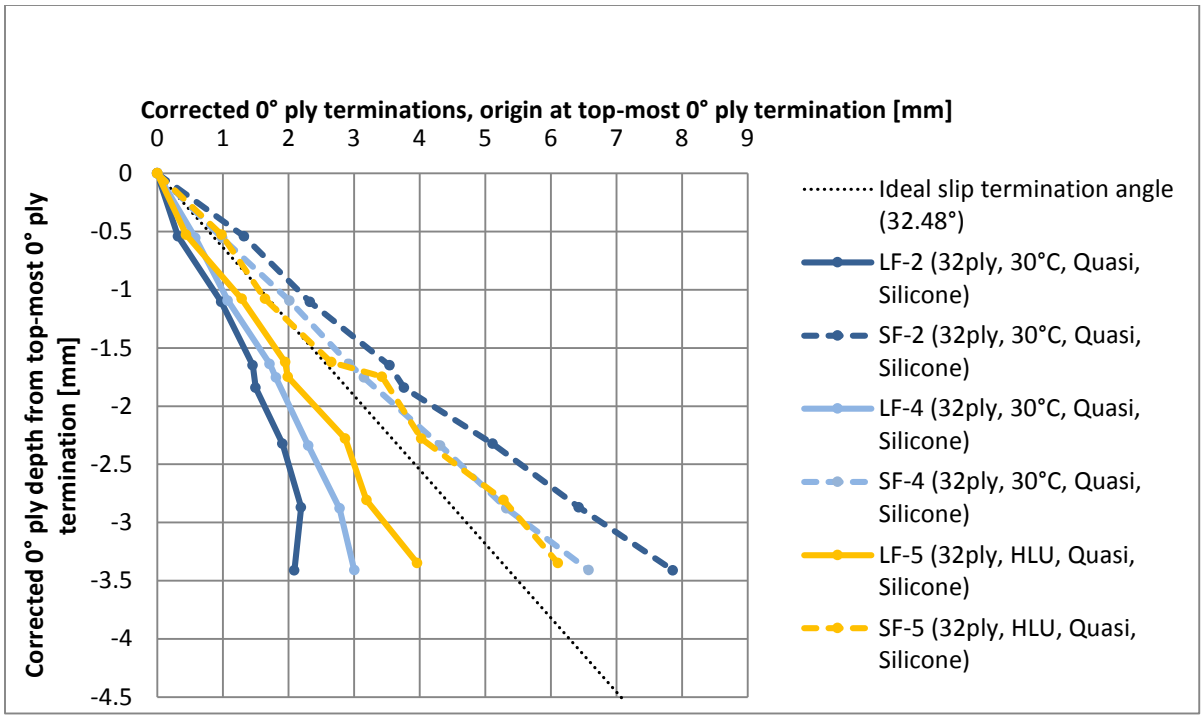

Figure C.5-16. Individual flange termination shapes: Forming method effects

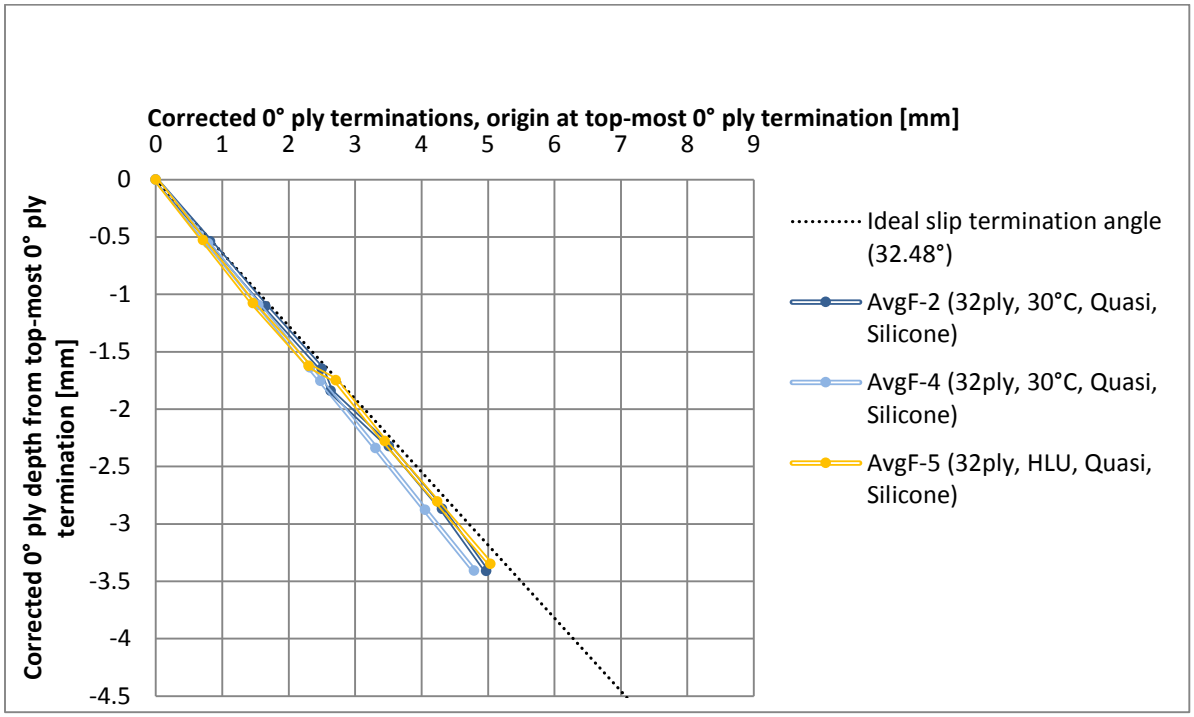

Figure C.5-17. Forming method effects on the 'part-averaged' termination profiles

Combined effects of curing bag type and forming bag thickness

The combined effects of curing bag type and forming bag thickness are investigated by comparing the Nylon-cured parts to the corresponding silicone-cured parts.

Figure C.5-18 compares the individual flange termination shapes for the nylon cured flanges (‘*LF-1*’ and ‘*SF-1*’) to the 30°C-formed silicone-cured parts (‘*LF-2*’, ‘*SF-2*’, ‘*LF-4*’, and ‘*SF-4*’). The Nylon-cured flanges show similar linearity to the silicone-cured parts, including a ‘tail’ feature in the long flange. The Nylon-cured flanges show a smaller horizontal spread than the silicone-cured parts.

Figure C.5-19 shows the same data in ‘*part-averaged*’ form. The Nylon-cured part shows remarkable agreement with the 32.48° ideal slip line with a distinct ‘tail’ feature, akin to the silicone-cured ‘*Part 2*’.

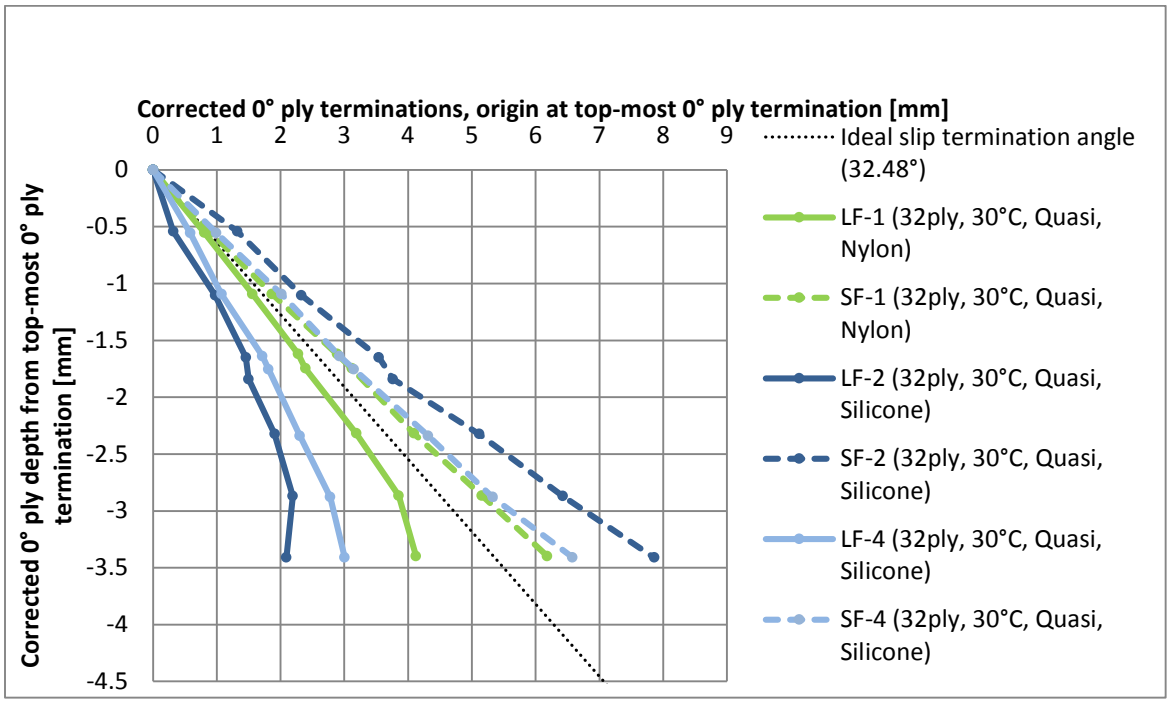

Figure C.5-18. Individual flange termination profiles comparing the combined effects of curing bag type and forming bag thickness

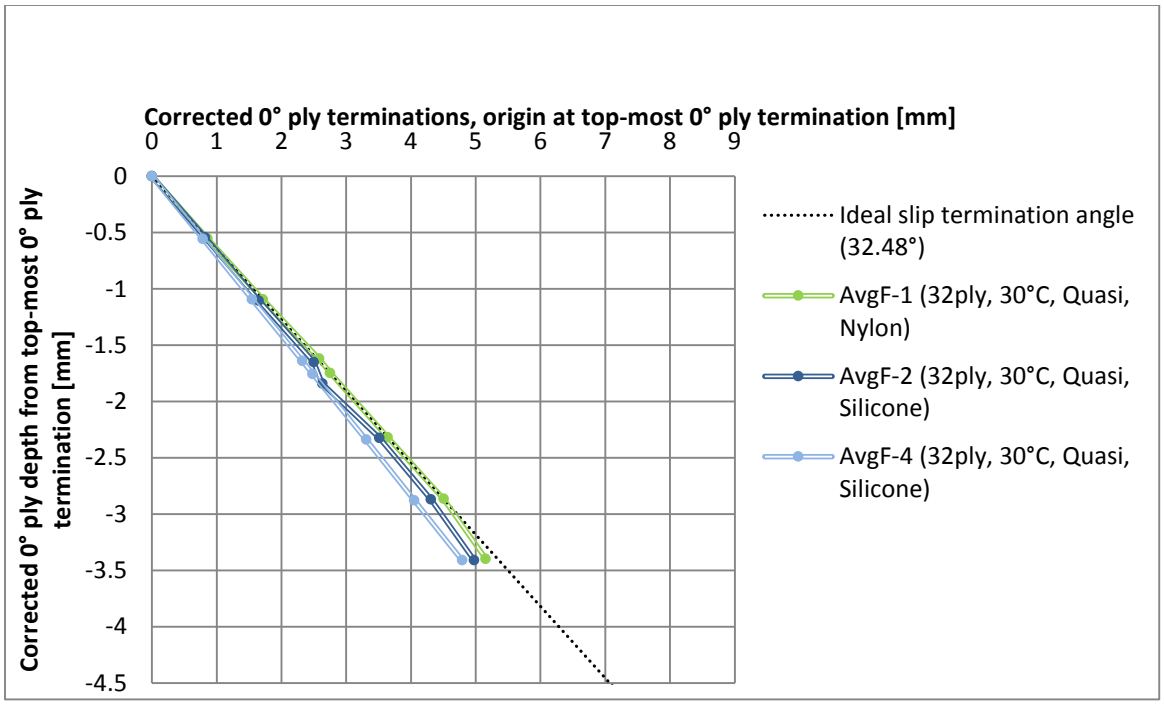

Figure C.5-19. 'Part-averaged' termination profiles comparing the combined effects of curing bag type and forming bag thickness

Individual ply terminations

Most flanges (particularly the long flanges) saw very little intra-ply deformation (shear). A few outliers exist and it appears to be significantly related to the length of the flanges. The level of intra-ply shear is presented below for each flange.

Non-sheared ends

- LF-1
- SF-2 (very partial, only in high waviness zones)
- LF-2
- LF-4
- SF-5
- LF-5
- LF-6
- LF-7
- SF-8 (high waviness AND non-sheared)
- LF-8
- LF-9

Partially sheared ends

- LF-3 (mostly non-sheared)
- SF-4 (shear – on top plies – is mostly related to end-waviness)
- SF-6 (mostly non-sheared)
- SF-9 (decent, but other plies are quite staircase-like)

Sheared ends

- SF-3 (most plies)
- SF-1 – (could be due to end-waviness)

C.6 Spring-in

Spring-in measurements for each flange were measured by the method detailed in Section B.3 and are summarized in Figure C.6-1. All values are within 1.0°.

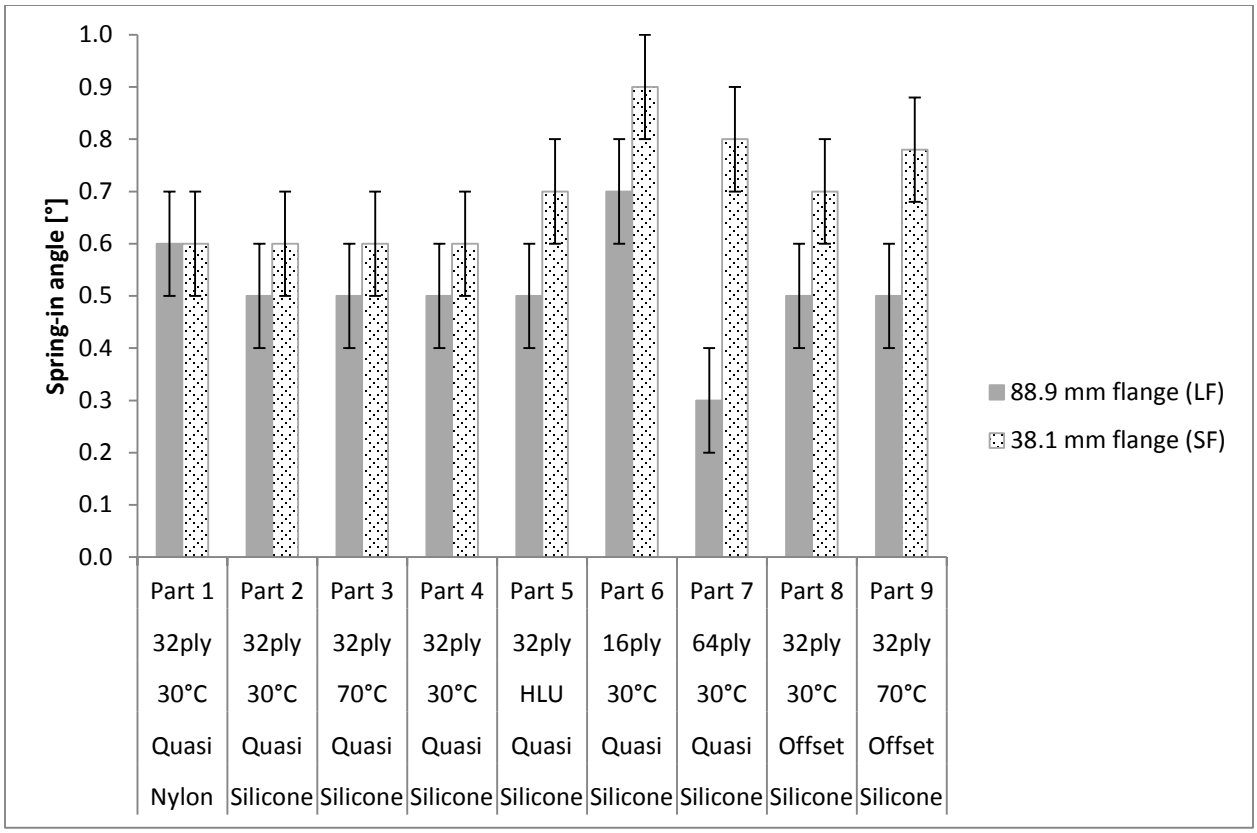

Figure C.6-1. Spring-in angle measurements for all manufactured flanges

Effect of forming temperature

The effect of forming temperature is determined by comparing '*Part 2*' and '*Part 4*' to '*Part 3*' for the *Quasi* ply sequence. In this case, the spring-in values are quite consistent and apparently show no temperature effects.

For the *Offset* ply sequence, the comparison of Part 8 and Part 9 also shows very little differences for either the short or the long flanges.

Effect of flange length

The effect of flange length appears to be the most notable as it can be readily seen that all but one short flange spring-in angles exceed the corresponding long flange spring-in angles where the largest difference is seen in the 64-ply laminate (‘*Part 7*’).

Effect of ply count

The spring-in angles for 16-ply, 32-ply, and 64-ply *Quasi* parts (‘*Part 6*’, ‘*Part 2*’ & ‘*Part 4*’, and ‘*Part 7*’ respectively) are charted with regards to ply count in Figure C.6-2. A distinct downward spring-in angle trend with increasing ply count can be observed for the long flanges. As for the short flanges, the trend appears to be more parabolic.

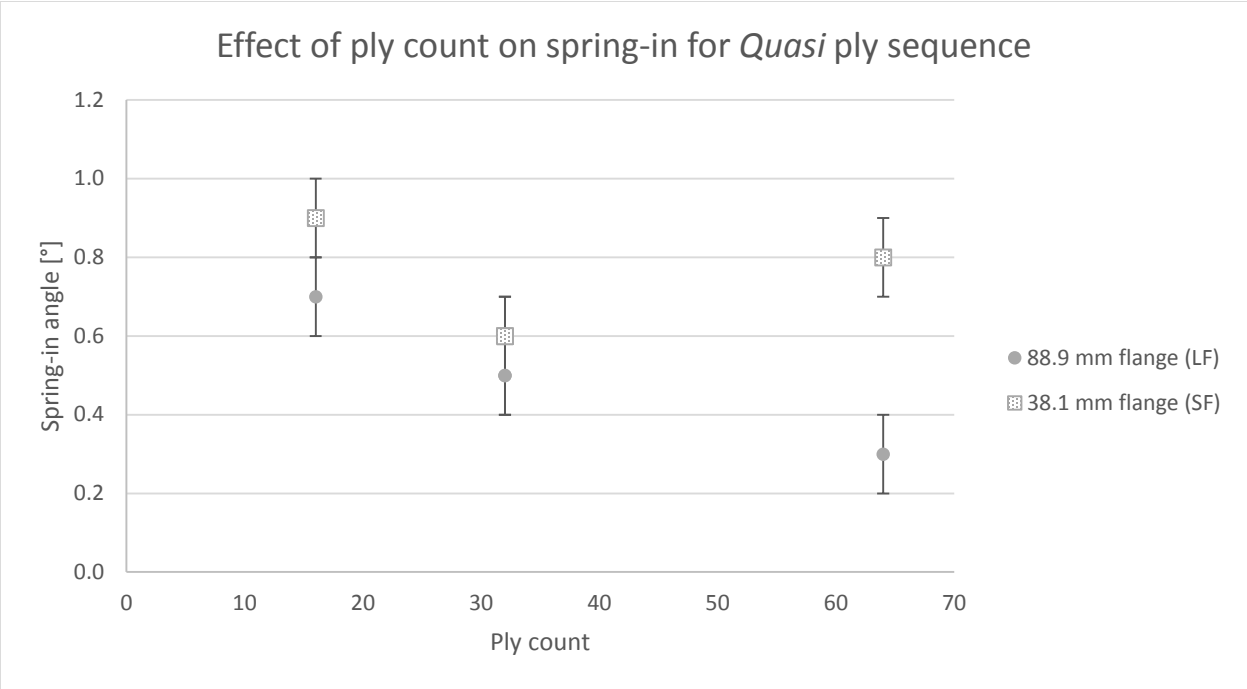

Figure C.6-2. Effect of ply count on spring-in for the Quasi ply sequence

Effect of ply sequence

The O*ffset* ply sequence (‘*Part 8*’ and ‘*Part 9*’) spring-in angles’ difference between the long flange and the short flange is slightly larger than the difference of the equivalent 32-ply *Quasi*

ply sequence parts (‘*Part 2’*, ‘*Part 4’*, and ‘*Part 3’*) for both forming temperatures. This implies a greater sensitivity to ply length for the *Offset* sequence.

Effect of forming method

The hand lay-up part (‘*Part 5*’) shows a somewhat greater spring-in angle for its short flange as compared to the comparable drape-formed parts, ‘*Part 2*’ and ‘*Part 4*’. The long flange spring-in angles don’t appear to be affected by forming method.

Combined effects of curing bag type and forming bag thickness

When comparing the Nylon-cured part (‘*Part 1’*) to the silicone-cured parts (‘*Part 2*’ and ‘*Part 4*’), the Nylon-cured flanges show no measureable difference between long and short flanges. Similarly, taking the measurement error into account, the long and short flange spring-in angles for the silicone-cured parts aren’t considerably different.

C.7 Methods development

Sub-surface imperfection survey

The sub-surface imperfections that were consistently seen can be categorized into three distinct categories: fold lines, linear shimmers, and scattered shimmers which were corroborated with the occurrence of wrinkles, unified/full-ply waviness, and scattered/partial-ply waviness, respectively.

In-plane microscopy and waviness path reconstruction methods comparison

A flange that had been previously manufactured as a part of a proof of concept manufacturing test series was used to assess the effectiveness of the ‘*in-plane microscopy*’ and ‘*path reconstruction*’ waviness detection and quantification methods. The flange in question was a 16-ply $[90_2/0_2/+45_2/-45_2]_S$ quasi-isotropic flange that was drape-formed and cured – specific

manufacturing details can be found in [30]. Cross-sectional micrographs revealed significant waviness in wrinkle zones.

The waviness measurements results are presented in terms of path deviation amplitude in Figure C.7-1, respectively. On inspection, both methods show agreement with regards to peak and valley locations, though the amplitudes of the curves are significantly greater for the path reconstruction method. At worst, the '*path reconstruction method*' shows a difference of +29% in amplitude and a difference of +%59 in angular misalignment.

With the '*in-plane microscopy*' being a direct measurement method and less sensitive to both image and measurement resolution – further discussed in (discussion) – it has been chosen as the method to be used in order to proceed with this project's sample set.

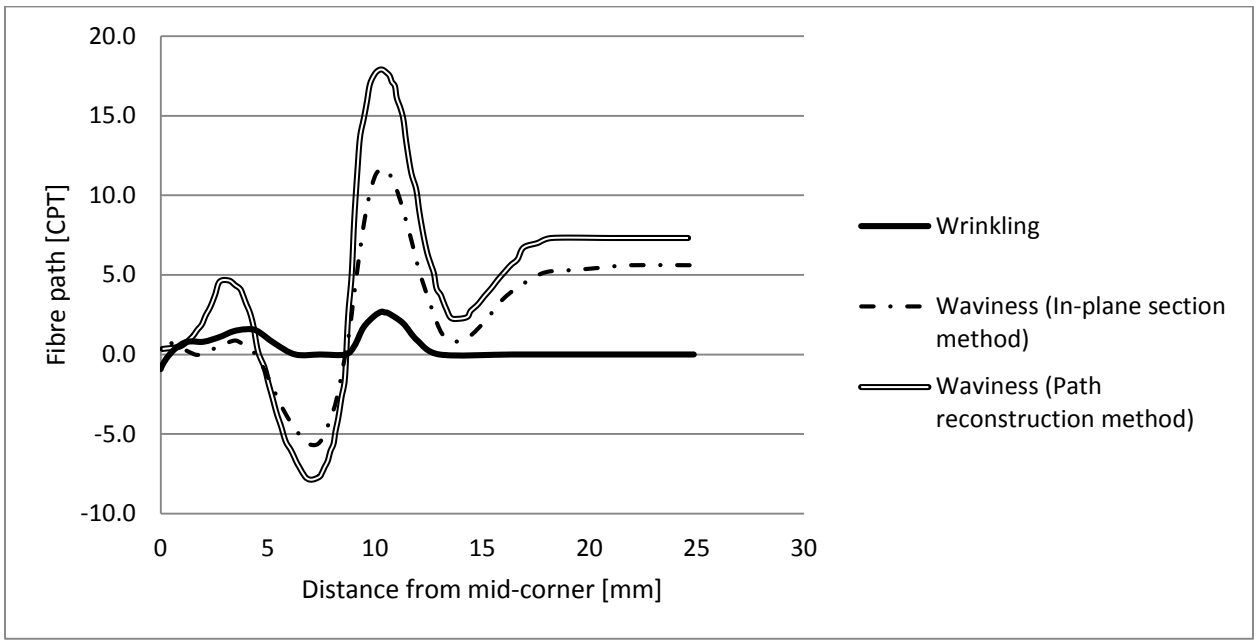

Figure C.7-1. Fibre path deviation amplitudes with respect to the nominal path, as measured by the 'in-plane section' and 'path reconstruction' methods for waviness. Wrinkling information is overlaid.

In-plane microscopy of select trials

Two samples were chosen to be analyzed using the '*in-plane microscopy*' method – samples '*LF-2*' and '*LF-08*'. From the in-plane micrographs, waves were traced and characterized by the method detailed in Section B.3. The measurement data is tabulated in Table C.7-1. Individual wave characterization from in-plane microscopy. Comparisons can be made with the measurements that were captured using the original wave characterization method detailed in Section B.2 and tabulated in Table A.4-1. Data of interest are length span (columns M and R) and maximum deviation angle (columns L and Q). The comparison is shown in Table C.7-1. All data show comparisons of similar order though significant discrepancies exist. Particularly, in the waviness region length span where the '*in-plane microscopy*' method undershoots the '*ellipse survey method*'. The maximum deviation angle shows significantly better agreement between both methods.

Table C.7-1. Individual wave characterization from in-plane microscopy

	N	O	P	Q	R	S	T
	Location of minimum [CPT]	Location of maximum [CPT]	Wave amplitude [CPT]	Maximum deviation angle [°]	Length span [CPT]	Waviness excess length per wave [CPT]	Waviness total excess length in flange [CPT]
LF-2 (32ply, 30°C, Quasi, Silicone)	140.2	132.6	0.4	6.7	35.7	0.1	0.6
	116.6	93.7	2.7	18.1	42.9	0.6	
LF-8 (32ply, 30°C, Offset, Silicone)	127.4	101.8	7.1	51.3	73.8	8.3	11.9
	80.3	*unavailable*	6.4	26.4	30.0	3.6	

Table C.7-2 Comparison of the 'in-plane microscopy method' to the 'ellipse survey method' for length span and maximum deviation angle.

	Length span		Maximum deviation angle	
	Ellipse survey method	In-plane microscopy method	Ellipse survey method	In-plane microscopy method
LF-2 (32ply, 30°C, Quasi, Silicone)	143 CPT	79 CPT	14°	18°
LF-8 (32ply, 30°C, Offset, Silicone)	144 CPT	104 CPT	61°	51°

Appendix D Additional Discussion

D.1 Wrinkle morphology

With regards to the morphology of the post-forming external bumps that were seen on the bag-side of 30°C-formed flanges, all were linear through the width of the part. Although no data can explicitly explain the mechanism governing this outcome, it is possible that it was due the composite's high shear modulus at 30°C: at low temperatures, wide wrinkles were seen in single 0° ply tests, due to the high composite shear modulus, linking adjacent tows within the prepreg to buckle in the same location [30]. By the same logic, it is also possible that the interfacing off-axis plies may have further linked 0° tows to buckle in unison through the width of the part.

The post-cure micrographs indicated regions of 90° ply thickness variations beneath the wrinkled 0° ply at the mould-side for the *Quasi* ply sequence wrinkles (Figure 5-10). Assuming the 0° ply initiated the wrinkle due to its higher stiffness in the forming direction and its greater propensity to buckle, its arch-like geometry would have shielded the region below the wrinkle from consolidation pressure during the cure cycle. Since flow is driven by high and low pressure region gradients (by definition), the shear-susceptible 90° plies are likely to have flowed into the

cavity created by the 0° ply arch early into the cure cycle, resulting in a thickened 90° ply. Though, the thickened adjacent 45° plies show significantly higher fibre volume fractions between the top of the thickened 90° ply and the wrinkled 0° ply's maximum. This may be explained by the conversion of wrinkling to waviness later in the cure cycle that would have significantly reduced the load-carrying ability of the 0° ply arch. The geometry of the arch, particularly as it was seen from the curing bag from the part's exterior, could have intensified the applied pressure at the arch maximum's location, thus squeezing resin along the flange's length where fibre volume fraction is seen to be significantly lower in the 45° plies.

D.2 Corner thinning due to taut silicone bagging

The forces imparted onto the corner by the silicone bag under tension are compared to the forces in a flat section in Figure 6-7. In flat regions, the stretched elastomer sheet's tension vectors are equal and opposite in the parallel plane to the laminate. Therefore, the resultant pressure applied to the laminate is simply the atmospheric pressure. Hence, the elastomer sheet's tension offers no contribution to laminate consolidation.

In contrast, the sheet tension forces over the corner region of the mould add up to an increase in pressure seen at the corner as a function of the tension within the silicone bag. The consolidation contribution over a 90° angle mould from the silicone bag tension can be computed from the stress-strain relation, assuming uniform tension through the length of the bag.

$$\sigma_{tension} = E_b \varepsilon_b \tag{7–3}$$

$$\varepsilon_{sheet} = \frac{\Delta l}{l_o} \tag{7–4}$$

where E_b is the sheet's elastic modulus, ε_b is the sheet's strain under vacuum, Δl is the sheet's deformation under vacuum, and l_o is the sheet's original length. Multiplying Equation (7–3) by the cross-sectional elastomer membrane area, we get the internal tension force:

$$F_{tension} = E_b \varepsilon_b \cdot h_b w \tag{7–5}$$

where h_b is the nominal silicone sheet thickness and w is its width. For the test fixture in question, the sheet's deformation can be measured from the internal topology of half (due to symmetry) of the vacuum box since the elastomer deforms and moulds itself to this cavity (from

the top-center of the mould to the edge (51 mm), down the mould (102 mm), across to the bottom plate (135 mm), up the ramp (100 mm), and up the riser (10 mm) for a total of 398 mm). The unstretched silicone sheet half-length is 260 mm.

$$\varepsilon_{sheet} = \frac{398\text{ mm} - 260\text{ mm}}{260\text{ mm}}$$
$$= 0.531$$

Since the vacuum box is a square, the true elongation will be larger due to stretch in the corners, but the parts were formed away from the corners to minimize this effect. This estimation is therefore conservative. From the Torr Technologies specification sheet, Young's modulus is 830 kPa (120 psi) for the EL80 sheeting material at 50% elongation. The tension force in the silicone sheet can be obtained via Equation (7–5) for a nominal silicone bag thickness is 0.001016 m (0.040 in):

$$F_{tension} = E_b \varepsilon_b \cdot h_b w$$
$$= (830\ 000\ \text{Pa})(0.53) \cdot (0.001016\ \text{m}) w$$
$$= 447 \cdot w\ [\text{N}]$$

From the sum of forces over the corner element, we may obtain the consolidation force oriented normal to the bag surface contributed by the silicone sheeting material under tension over a 90° convex corner:

$$F_{elastomer} = \sqrt{2}\, F_{tension} \tag{7–6}$$

Converting Equation (7–6) to pressure units,

$$P_{elastomer} = \frac{\sqrt{2}\, F_{tension}}{A_{outer}} \tag{7–7}$$

For the given test set-up, Equation (7–7) becomes:

$$P_{elastomer} = \frac{F_{elastomer}}{A_{outer}}$$
$$= \frac{\sqrt{2}\, F_{tension}}{S_b w}$$
$$P_{elastomer} = \frac{\sqrt{2}\, F_{tension}}{(R + h + h_b)\frac{\pi}{2} w} \tag{7–8}$$

where S_b is the arc length of the corner on the outside of the sheeting material. For a mould radius R of 0.009525 m, unconsolidated laminate thickness h of 5.32×10^{-3} m, nominal silicone sheet thickness h_b of 0.001016 m is and tensile force of 447·w [N], the equivalent pressure in units of atmospheric pressure is determined from Equation (7–8):

$$P_{elastomer} = \frac{\sqrt{2}\, 447 \cdot w}{(0.015861)\frac{\pi}{2} w}$$
$$= 25\ 367\ [\text{Pa}]$$
$$P_{elastomer} = 0.250 \cdot P_{atm}$$

In comparison, the corner effect of pressure increase can be determined from the forces seen by the top of the elastomer bag, F_{outer}, and the bottom of the laminate at the mould surface, F_{inner}:

$$\Sigma F_{inner} = \Sigma F_{outer}$$

$$P_{inner} A_{inner} = P_{outer} A_{outer}$$

$$P_{inner} = P_{outer} \cdot \frac{A_{outer}}{A_{inner}}$$

$$P_{inner} = P_{outer} \cdot \frac{S_b w}{S_m w} \tag{7–9}$$

$$P_{inner} = P_{outer} \cdot \frac{(R + h + h_b)\frac{\pi}{2}}{R\frac{\pi}{2}}$$

$$P_{inner} = P_{outer} \cdot \frac{(R + h + h_b)}{R} \tag{7–10}$$

where $S_m$is the arc length of the mould corner. For a mould radius R of 0.009525 m, unconsolidated laminate thickness h of 5.32×10^{-3} m, and nominal silicone sheet thickness h_b of 0.001016 m subjected to atmospheric pressure, the internal pressure resulting from the reduced corner area is:

$$P_{inner:corner\ effect} = 1.665 \cdot P_{atm}$$

By the same procedure, we can determine the increase in pressure seen at the inner surface due to the elastomer:

$$P_{inner:elastomer} = 0.416 \cdot P_{atm}$$

Therefore, with silicone bagging for this test, the total corner forces can be summed.

$$F_{corner:total(elastomer)} = P_{inner:corner\ effect} A_{inner} + P_{inner:elastomer} A_{inner}$$

$$\frac{F_{corner:total(elastomer)}}{A_{inner}} = P_{inner:corner\ effect} + P_{inner:elastomer}$$

$$P_{corner:total(elastomer)} = P_{inner:corner\ effect} + P_{inner:elastomer} \tag{7–11}$$

Considering the obtained values from Equation (7–11), the total intensified corner pressure, $P_{corner:total}$, is

$$\boxed{P_{corner:total(elastomer)} = 2.081 \cdot P_{atm}}$$

In the case of the nylon bagging where the bagging material thickness is neglected and where no tension is applied, the inner radius is the pressure seen at the corner is:

$$P_{corner:total(nylon)} = P_{outer} \cdot \frac{S_b w}{S_m w}$$

$$= P_{atm} \cdot \frac{(R+h)}{R}$$

For a mould radius R of 0.009525 m and unconsolidated laminate thickness h of 5.32×10^{-3} m,

$$\boxed{P_{corner:total(nylon)} = 1.558 \cdot P_{atm}}$$

In flat sections, the applied pressure is simply atmospheric where bag tension offers no contribution to consolidation:

$$\Sigma \mathrm{F}_{y:\,flat} = P_{atm} A$$

$$\boxed{P_{flat} = P_{atm}}$$

Thus, for the silicone-cured parts, the pressure difference between the corner and the flat regions was

$$\Delta P_{elastomer} = P_{corner:total(elastomer)} - P_{flat}$$

$$\Delta P_{elastomer} = 1.081 \cdot P_{atm}$$

For the nylon tests,

$$\Delta P_{nylon} = P_{corner:total(nylon)} - P_{flat}$$

$$\Delta P_{nylon} = 0.558 \cdot P_{atm}$$

Therefore, the silicone bag-induced pressure gradient between the corner and the flat sections has been shown to be nearly two times greater than that of the nylon bagging in this scenario. This suggests that the driver for increased thinning in the taut silicone-cured parts in comparison to the nylon-cured bag is in fact the tension in the silicone sheet.

While the nylon-cured part does see an increase in pressure at the corner with respect to the flat sections, the manufactured flange did not show any appreciable proof of thinning. Though this may be due to defects in the corner induced by pinching of the thick nylon bag and nearby ply wrinkling, it could also be due to the pressure difference being too little to overcome the shear modulus of the composite.

D.3 Spring-in

Spring-in angles were less than 1.0° degree for all manufactured flanges. The long flanges showed reductions in spring-in angle when compared to the short flange manufactured from the same C-channel, where the thicker flanges showed decreasing spring-in angles, with the exception of the 64 ply short flange.

Should the flange length's relationship with spring-in angle be significant, it is possible that the 64 ply short flange '*SF-7*' showed an greater angle than a linearly decreasing trend would suggest because that particular flange is effectively shorter than the nominal flange length. Since flange lengths were defined by their "sheared length" – the length over which slip and shear act during forming – the 64-ply sample's full-thickness length (the portion of the flange that does not include the ply drops the termination) is shorter than that of the 32-ply flanges when measured orthogonally from the web. As defined, a particular sheared length will relate to the final resting position of the mould-side ply (on a male mould) while the rest of the equilength plies' individual path lengths over the radius will land short. Thus, considering the 'SF-7' full-thickness flange length, it would be considered shorter than the other tests, having the consequential effect of an increased spring-in angle.

The impact of flange length appears to be least pronounced for the Nylon-cured samples. Where the corner thickness profile was approximately the same for the short and long pleated Nylon-cured flanges, the taut silicone-cured flanges showed increased backfilling of the flange-side valley for the short flanges (see Section 5.3). This anisotropy through the angle of the corner could have contributed to the difference seen between long and short flange spring-in angles of the silicone-cured flanges. The difference in web-side and flange-side peak profiles in the corners could also help explain the effect of ply count on spring-in angle seen in (figure 3.40*). The forming temperature did not appear to contribute any effects to the spring-in angle. While the *Offset* ply sequence did showed an increased spring-in angle for the short flanges, the long flanges were equivalent to the *Quasi* long flanges. Additionally, the occurrence of fibre misalignments did not appear to affect the measured spring-in angles (unlike Çınar and Ersoy's results, which however experimented with 4-ply L-shapes and unlike Salomi et al. who also saw

effects of fibre misalignments on spring-in values though whose wrinkles spanned a much greater proportion of the part's thickness than those seen in the current study) for long flanges, likely since the most significant wrinkles and waves that were seen were typically found outside of the corner [36], [37]. Though, since the short flange *Offset* flanges did show increased spring-in angle, it may be that the increase waviness seen in those samples when compared to the *Quasi* flanges could have played a part. Hence, the waviness seen in this study may only affect shorter corners if at all.

Given the importance of the corner's morphology on the occurrence of spring-in, the differences in the shape of the web-side and valley-side peaks for the 16-ply, 32-ply, and 64-ply flanges' corners could be the driver for the differences in spring-in angles.

Key takeaways: spring-in

- Spring-in angles were less than 1.0° degree for all manufactured flanges.
- Wrinkling and waviness did not show major effects on spring-in angle.
- The flange length and number of plies each showed inverse relationships with spring-in angles.
- The forming temperature did not show any appreciable effects on spring-in angle.
- The relative influence of each input parameter on the spring-in angles are summarized in the figure below:

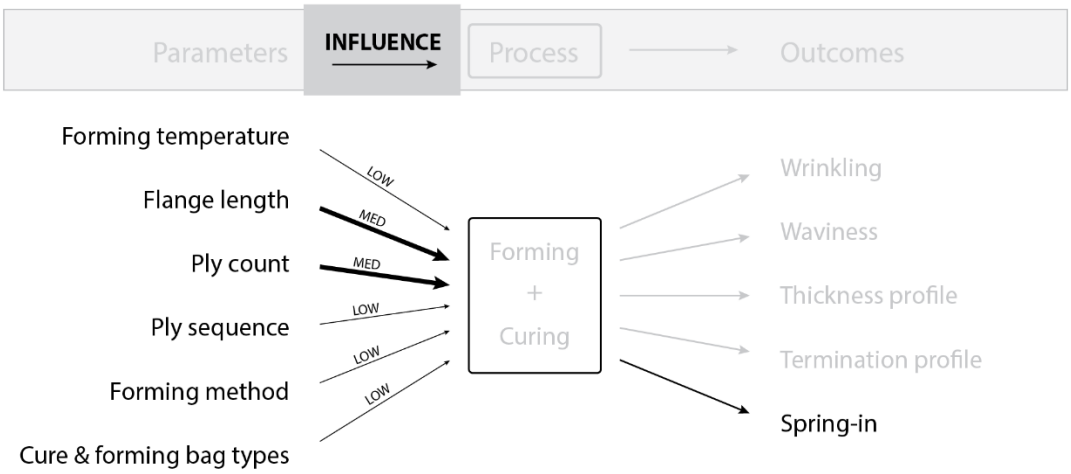

Figure D.3-1. Process input parameter influences on Spring-in outcome

D.4 Methods development

Over the course of this study, previously unpublished methods of measuring waviness, termination profiles, and sub-surface defects were developed. This section examines the effectiveness and shortcomings of each method by listing the upsides and downsides of each method.

Subsurface imperfection survey

The sub-surface defect survey was detailed in Section 4.2 where long exposure photography was performed at specific lighting angles in order to produce high contrast surface images. It proved to be an effective means of locating and identifying defects on in the mould-side surface plies without destroying the sample. The sub-surface imperfections that were repeatedly seen can be categorized into three distinct categories were fold lines, linear shimmers, and scattered shimmers which were later attributed to the occurrence of wrinkles, unified waviness, and scattered waviness, respectively. However, this method could not provide any information on the internal structure of the defects in question.

Strengths:

- Non-destructive
- Relatively quick
- Part can be curved
- All mould-side ply defects were detected

Weaknesses:

- Line-of-sight process – no through-thickness information can be obtained
- Surface quality dependence – it may not be an adequate means of detection for bag-side surface
- Optimal part-camera angle for the highest contrast images is variable, depending on the defect type and severity

D.5 Waviness analyses

In-plane microscopy

The in-plane microscopy method was detailed in Section B.3 where optical microscopy was performed in the flange's 1-2 plane. It allowed for the direct observation of waves in the flange, though was limited to flat viewing planes.

Strengths:

- Direct imaging of through-width wave morphology
- Works for fibres with non-circular cross-sections

Weaknesses:

- Destructive inspection method
- Only useful for flat parts; cannot perform this type of microscopy on curved parts
- Unable to track waviness in heavily wrinkled parts since the ply deviates out of the chosen viewing plane.
- Difficult preparation for microscopy with regards to aligning the sample's grinding plane to the intended viewing plane

Wave path reconstruction

The waviness path reconstruction method was detailed in Section B.5 where fibre paths were reconstructed from fibre ellipses obtained from cross-sectional micrographs. This method assumed wave uniformity through the width of the part, but showed that it is plausible to determine a wave's shape from a side profile obtained from the part's edge.

Strengths:

- Less destructive than in-plane microscopy – can be performed from part edges

Weaknesses:

- Assumes through-width wave uniformity – it is an indirect visualization technique
- Highly sensitive to *image resolution*, particularly at high misalignment angles – see Appendix Section D.2 for full explanation
- Sensitive to *measurement resolution* (frequency of measurements) – see Appendix Section D.2 for full explanation
- Sensitive to vertical position of chosen ellipses within the ply due to partial-ply waviness gradients
- Invalid for non-circular fibres

Resolution sensitivity of wave path reconstruction method

The wave path reconstruction method detailed in Section B.5 showed a high sensitivity to image and measurement resolution.

The difference in aspect ratios between 45° and 55° fibre ellipse major diameters is much larger than between 5° and 15° fibre ellipse major diameters. The aspect ratio and fibre angle relationship follows the $\frac{1}{\sin\omega}$ function, as shown in Figure D.5-1 and illustrated in Figure D.5-2. Therefore, as the misalignment angle increases, the accuracy of the the measurement becomes reliant on image resolution. In the case of the 200x magnification images taken in this study, each fibre diameter was only represented by an average of 10 pixels. Thus, measurement resolution errors for the diameter represents 20% of the measurement – one pixel on either side – which is quite low. The fibre misalignment angles and path lengths in this study showed high sensitivity to measurement error.

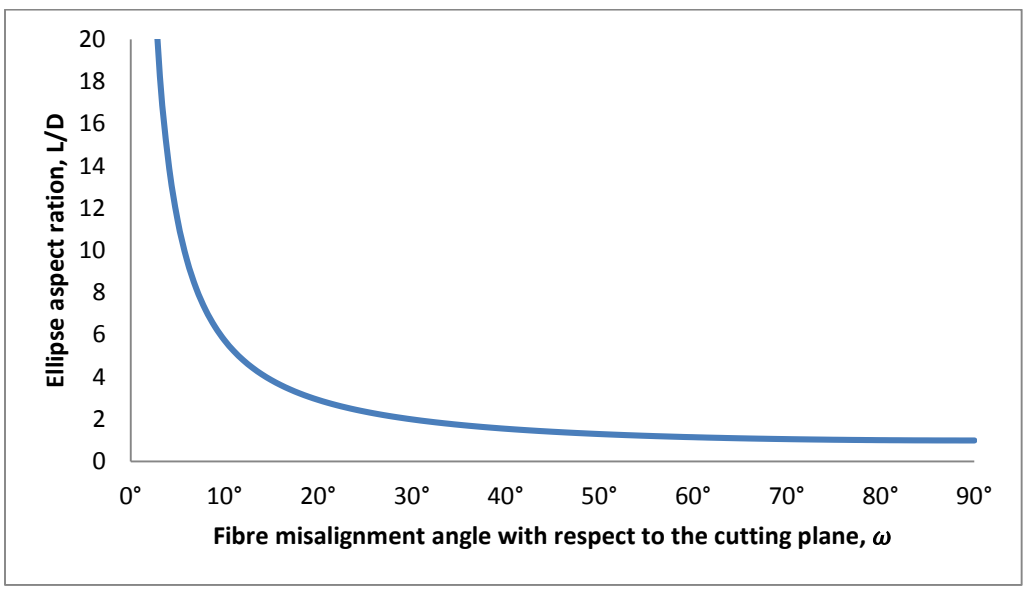

Figure D.5-1. Relationship between the ellipse aspect ratio and the fibre diameter, as per the $\frac{L}{D} = \frac{1}{\sin(\omega)}$ function.

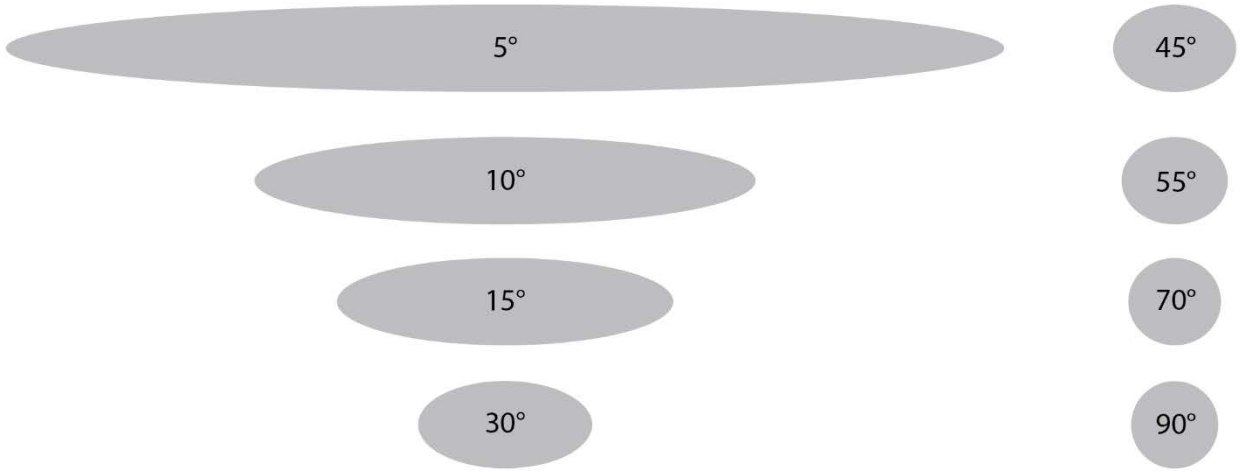

Figure D.5-2. Illustration of the non-linear relationship between fibre angle and ellipse length to diameter aspect ratio.

Additionally, since the path of each measurement segment is added to the previous segment, the *measurement resolution*, or the *frequency the taken measurements*, plays a big role in the accuracy of this method. The measurement resolution must be related to a size that is many times smaller than the smallest detectable feature.

The resulting wave path was also sensitive to the depth of the chosen ellipses. Partial-ply waviness often combined with the full-ply waviness regions which resulted in significantly different excess length measurements that were obtained using the upper half of the ply as compared to the lower half. For the FE-02 long flange example, the trapped excess length based on measurements of upper half of the ply was 0.24 CPT whereas the lower half was 1.16 CPT.